The University of Sheffield

Analysis of High-Speed Permanent Magnet Machines

Yu Wang

A thesis submitted for the degree of Doctor of Philosophy

Department of Electronic and Electrical Engineering
The University of Sheffield
Mappin Street, Sheffield, S1 3JD, UK

23 October 2019

Abstract

High-speed permanent magnet machines (HSPMM) are a competent candidate for high-speed applications due to its better efficiency, power factor, and utilization factor in comparison to other types of high-speed electrical machines. In this thesis, both the electromagnetic and mechanical issues of HSPMM including rotor split ratio optimization, rotor stress analysis, and parasitic effects such as rotor eddy current loss and UMF are investigated elaborately by means of analytical and finite element analyses, together with experimental validation.

Firstly, the optimal rotor split ratio of HSPMM is investigated analytically with consideration of stator iron loss as well as rotor mechanical stress. The influence of design parameters such as air gap length and rotor pole pairs on the optimal split ratio is investigated. Both analytical and finite element analyses reveal that the optimal split ratio for HSPMM will be significantly reduced when stator iron loss and mechanical constraints are taken into consideration.

Secondly, the rotor eddy current loss of the four-pole HSPMM with alternate stator winding configuration is investigated. The contribution of each harmonic in the production of magnet loss, either from PM field or armature field, is determined by the proposed method with consideration of stator slotting effect. In addition, the armature reaction induced magnet losses with different stator winding configurations are compared as well. It is found that the value of magnet loss is dependent on both the penetration depth and the amplitude of asynchronous spatial harmonic, which are determined by the specific slot and pole number combination.

Following from this, the existence criterion of UMF in PM machines with odd number stator slot is determined. In addition, the influence of slot and pole number combination on the rotor UMF is investigated.

Finally, a novel HSPMM design methodology considering both electromagnetic and mechanical issues is illustrated. The rotor stress is firstly analysed with consideration of PM segmentation effect. The corresponding worst operating scenarios and influential factors are then investigated. Based on the stress analysis of the HSPMM, the mechanical stress limitation is incorporated as the geometric constraints in the electromagnetic design so that the mutual influence of two different design aspects can be considered.

Acknowledgements

I give my most sincere thanks to Prof. Z. Q. Zhu for his professional and inspiring supervision during my PhD study. His encouragement helped me through the toughest time of my PhD study. His excellence as a role model will be a treasure to me for the rest of my life.

I would also like to express my gratitude to the members of the Electrical Machines and Drives Group at the University of Sheffield, particularly Dr. Liren Huang, Dr. Shaoshen Xue, Dr. Peilin Xu, Dr. Wenqiang Chu, Dr. Yue Liu, Mr. Shun Cai, Mr. Rui Zhou and Mr. Kai Zhang for their many constructive suggestions and selfless help. Further thanks to the technical staff in the Department of Electraonic and Electrical Engineering for their help.

I also would like to acknowledge CRRC ZhuZhou Institute Co. Ltd for the PhD studentship via Sheffield CRRC Electric Drives Technology Research Centre.

Finally, I would like to thank my parents for their wise counsel and sympathetic ear. You are always my strongest backing.

Contents

Nomenclature

α	Steinmetz coefficient	
a_0	Initial rotor position	rad
a_n	Numerical constant related with problem boundaries	
α_r, α_θ	Radial and tangential coefficients of thermal expansion	/C°
A_{Fe}	Slot iron area	m^2
A_s	Slot area	m^2
A_i	Amplitude of the *i*th harmonic	A
B	Iron flux density	T
B_α	Tangential flux density	T
B_{arm}	Flux density due to armature reaction	T
B_{Fe}	Flux density in iron	T
B_g	Air gap flux density	T
B_m	Maximum flux density in iron	T
B_r	PM remanence	T
B_r	Radial flux density	T
C_f	Coefficient of rotor skin friction	
C_{s1}, C_{s2}	Integration constants of sleeve	
C_{m1}, C_{m2}	Integration constants of magnets	
D_o	Stator outer diameter	m
D_s	Stator bore diameter	m
D_r	Rotor outer diameter	m
E	Young's modulus	Pa
E_r , E_θ	Radial and tangential Young's modulus	Pa
E_m	Young's modulus of magnets	Pa
E_b	Young's modulus of back-iron	Pa
f	Frequency	Hz
$F_{ABC}(\alpha,t)$	Three-phase MMF	A
F_h	Amplitude of each MMF harmonic	A
F_r	Radial force	N
F_α	Tangential force	N
F_x	Unbalanced magnetic force in horizonal direction	N
F_y	Unbalanced magnetic force in vertical direction	N

g	Effective air gap length	m
h	Thermal heat transfer coefficient	W/(m^{2}·K)
h_b	Thickness of sleeve	m
hm	PM thickness	m
i	Harmonic order (i=1,3,5…)	
I_{a}	RMS of phase current	A
j	Harmonic order (j=1,2,3…)	
k	Stress safety factor	
k_e	Coefficient of eddy current loss	
k_{ex}	Coefficient of excess loss	
k_h	Coefficient of hysteresis loss	
k_s	Slot packing factor	
k_w	Winding factor	
l_a	Axial core length	m
l	Axial rotor length	m
m_{Fe}	Mass of iron	kg
N_s	Slot number	
N_{w}	Serial turns of each phase	
p	Rotor pole pairs	
p_{b}, p_{m}	Pressures of magnets and sleeve due to centrifugal force	Pa
p_c, p_{Fe}	Iron loss	W
$P_{contact-pressure}$	Contact pressure	Pa
P_{limit}	Heat limitation	W
P_0	DC component of air gap permanence	H
$P(\alpha)$	Permanence function	H
p_w	Windage loss per unit	W
R_{mo}	Rotor outer radius	m
R_{mi}	Rotor inner radius	m
R_{si}	Sleeve outer radius	m
R_{bo}	Back-iron outer radius	m
r_b, r_{m}	Average radius of selected sleeve and magnets	m
SCF	Stress concentration factor	
T	Output torque	Nm
t	Machine periodicity	

u	Radial displacement	m
μ_1	Mass in per unit length	Kg/m
μ_0	Permeability of free space	H/m
u_{mr}	Radial displacement of magnets	m
u_{br}	Radial displacement of back-iron	m
v	Harmonic order	
v_c	Rotor peripheral speed	m/s
υ_m	Maximum allowed temperature	℃
$\nu_{\theta r}$, $\nu_{r\theta}$	Radial and tangential Poisson's ratios	
ν_m	Poisson's ratio of magnets	
ν_b	Poisson's ratio of bandage	
w	Angular speed	rad/s
w_n	Natural frequency	Hz
ω_r	Mechanical angular frequency	Hz
ω_s	Electrical angular frequency	Hz
W_{Fe}	Iron loss in watts per kilogram	W/kg
δ	Physical air gap length	m
γ	Flux density ratio	
$\boldsymbol{\Omega}$	Rotating speed	rad/s
θ_r	Rotor position in rotor reference frame	rad
θ_s	Rotor position in stator reference frame	rad
λ	Rotor split ratio	
λ_p	Optimal split ratio of HSPMM	
ε_r , ε_θ	Radial strain and tangential strain of sleeve material	
ρ	Material mass density	Kg/m^3
ρ_b	Mass density of sleeve	Kg/m^3
ρ_m	Mass density of magnets	Kg/m^3
ρ_{cu}	Resistivity of copper	S/m
ρ_{Fe}	Resistivity of iron	S/m
σ_t	Total tangential stress	Pa
$\sigma_{t,prestress}$	Pre- tangential stress	Pa
$\sigma_{t,w}$	Tangential stress due to rotation	Pa
σ_{limit}	Tangential stress limit	Pa
σ_{sr} , $\sigma_{s\theta}$	Sleeve radial and tangential stresses	Pa

σ_{mr} , $\sigma_{m\theta}$	Magnet radial and tangential stresses	Pa
σ_{br} , $\sigma_{b\theta}$	Back-iron radial and tangential stresses	Pa
ΔD	Interference fit	m
ΔT	Temperature rise	℃

Chapter 1 General Introduction

1.1 Introduction

High-speed electrical machines (HSEM) have been widely used in various applications such as high-speed spindles [ZWY09], turbochargers for more electric engines [GER14], micro-gas turbines [FER95], [GOL03], flywheel energy storage system [TSA03], and compressors and air blowers [KOL11], [ZHA16], [HUA16]. They have been gaining increasing interest from machine designers in the past twenty years. There are at least two benefits for increasing operating speed of electrical machines. One of the commonly acknowledged advantages of HESMs lies in the reduction of overall mass and volume for the same power requirement. This is particularly desirable for applications which demand a high system power density. The second advantage of adopting high-speed machines is the enhancement of system robustness and lower maintenance due to elimination associated accessories such as gearboxes.

The high-speed permanent magnet (PM) machine (HSPMM) is a competent candidate for high-speed applications due to its better efficiency and power factor, compared to other HSEMs [BIA04]. However, there are still many challenges and obstacles in terms of both mechanical and electromagnetic aspects for HSPMM which are summarized in the following paragraphs.

Under the high-speed rotating, all components in the rotor will suffer significant centrifugal force and tangential stress, which can be further aggravated by the rotor temperature rise [BIN06]. As the most vulnerable part, the rotor magnets are rather brittle with small tensile strength [DU19], [ZHA16]. Sleeves are therefore adopted to retain the magnets in surface-mounted PM (SPM) machines. Hence, rotor stress analysis is a key issue for the design of HSPMMs in order to keep the maximum induced rotor stress within the material strength limits, especially for PMs [BIN07].

On the other hand, for low to medium speed operating electrical machines, the rotor dynamics are typically not a significant issue since the operating speed range is normally far below the first critical speed. For HSPMM, the rotor dynamic issue becomes more crucial and challenging in that resonant vibration could easily happen with an improper rotor design [ZHU02].

Compared with high-speed induction machines, the HSPMMs are equipped with a more

compact size featuring high power density and loss density, thus imposing a great challenge on the cooling system design. The stator core loss and AC copper loss should be accounted under the high-speed operation. Meanwhile, a significant amount of rotor magnet loss and sleeve loss if applicable will be induced. This would cause severe rotor temperature to rise which may cause the PM irreversible demagnetization. On the other hand, the potential unbalanced magnetic force (UMF) in HSPMM with an odd number of stator slots may deteriorate the high-speed bearing wear which is vital for the rotor robustness. Hence, the electromagnetic issue in the analysis of HSPMM consists at least two aspects: (a) Understanding the generation mechanism of electromagnetic loss and UMF, as well as their precise prediction, especially at the worst operating scenario; (b) reasonable selection of machine topologies and other measures for the electromagnetic loss and UMF reduction.

It should be noted that the electromagnetic issues and the mechanical issues in HSPMM are not independent. They are strongly coupled to one another due to the link of rotor geometry. Both considerations from electromagnetic and mechanical aspects should be accounted for the HSPMM rotor design. Furthermore, the influence of one aspect on the other becomes more obvious in HSPMM, compared to low speed machines. The optimal design in one domain may be altered when the other issue is considered, which will be addressed in Chapter 2 and Chapter 5.

In summary, the essence of HSPMM analysis is a multiple iteration process which incorporates the electromagnetic, mechanical and other factors. Usually, design trade-offs must be made between different aspects according to the specific case. The aim of this chapter is to provide a systematic overview of the key design considerations and tradeoffs for HSPMM with regard to the aforementioned aspects.

This chapter will firstly discuss the definition of high-speed and summarize the alternate high-speed machine technologies. Advantages and disadvantages of each high-speed machine type will be identified. Then, both the electromagnetic issues and mechanical issues in HSPMM will be reviewed in detail. Finally, the main contribution and future work will be presented.

1.2 High-speed Machine Technologies

In this section, the definition of high-speed is firstly discussed. Then, the high-speed machine technologies are classified into three typical groups: induction machines (IM), switched

reluctance machines (SRM), and permanent magnet (PM) machines. The operating power as well as the speed of each type of machines are compared so that the suitable applications for different high-speed machines can be determined.

1.2.1 Definition of High-speed

As shown in Fig.1.1, the operating speed and power ranges of different types of high-speed machines are very wide. However, the boundaries are simply defined by two special types of high-speed machines. One type of machine is featured with ultra-high operating speed but relatively lower power rating [ZWY05], [SHE06], [PFI10], [HON12]. On the contrary, the other type of machine exhibits much higher power rating but relatively lower operating speed [ZHA15], [LUI14], [DU19]. Both should be considered as high-speed machines. Therefore, it is not wise to take either the maximum operating speed or the power rating as the only criterion for the definition of high-speed.

The definition of high-speed should be considered mainly from the perspective of the challenges the machine is faced with. Hence, the peripheral speed is normally adopted to identify high-speed machines [SIL16]. This criterion initiates from the constraints of rotor mechanical stress. As is well known, the rotor tangential stress due to rotation is proportional to the square of circumferential speed. Classification according to the peripheral speed could easily identify the realization difficulties of mechanical robustness. Similar criterion is also reported in [GER14]. HSEM is defined as electrical machines with r/min$\sqrt{}$kW over 1×10^5 and operating speed over 10kr/min. This definition is still mechanical difficulties oriented. It provides a quick and reliable guide number to access from the combinations of speed and power the likely severity of dynamic problems such as critical speed. High values of bearing DN and sensitivity to good balancing [MIL91]. In [BIN07], the HSEM is defined as the inverted-fed machines with fundamental frequency up to several kHz. This criterion focuses more on the control difficulties of high-speed machines. Another way of high-speed definition is concerned with correlations between operating speed and power rating [RAH04].

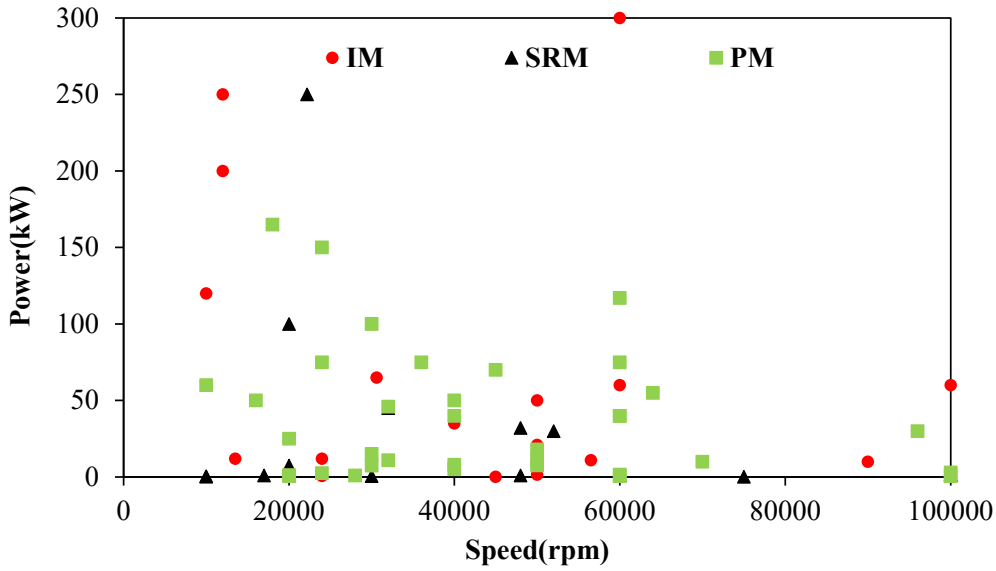

Fig.1.1. Operating power and speed of high-speed machines in literature [GER14].

1.2.2 High-speed Machine Types for Various Applications and Specifications

Over the last two decades, numerous overviews on HSEM topologies have been published [REI95], [RAM04], [BIN07], [MOG14], [GER14], [TEN14], [XIA15], [SIL16]. This section will summarize and analyse high-speed machines found in literature. The targets mainly focuses on high-speed induction machines (IMs), high-speed switched reluctance machines (SRMs) and high-speed PM machines (HSPMMs). Emphases are put on the rotor structures for each type of high-speed machines in terms of dealing with rotor stress and loss. In addition, a schematic comparison between different topologies in terms of reachable power and maximum operating speed will be made in order to identify the suitable cases for each topology.

A. High-speed IMs

IMs equipped with simple and robust rotor are normally adopted in applications such as compressors and spindles. Table 1.1 illustrates the high-speed IMs in literature. The table is sorted according to the value of peripheral speed (v_c). The highest achievable peripheral speed of IMs has reached 367m/s with a solid coated rotor in [SAA94] whilst the maximum power can reach 8MW for compressor applications in [PYR10].

It is obvious that the solid-rotor type is more favourable because of highest mechanical stiffness. Generally, there are four solid rotor topologies for IMs, namely smooth solid rotor, slitting solid rotor, solid rotor with copper coat and solid rotor with cages. The smooth solid rotor is the simplest and most robust. However, the lack of low impedance path for the rotor

current makes it relatively low efficiency. Hence, the axially slitting solid rotor was proposed to push the fundamental flux into the rotor while reducing the rotor eddy current [AHO07]. The slitting technology has also applied to the containing sleeve of high-speed SPM machines for the eddy current loss reduction [SHE13]. [ARU16] also proposes a high-speed IPM machine with solid slitting rotor. Fundamentally, the slits in rotor reduce the eddy current loss significantly. The friction loss, however, could be increased accompanied with reduction of mechanical strength.

To further improve the rotor, the solid rotor coated with the copper layer is proposed in [SAA94]. Such a design will retain the high robustness compared with the simple solid rotor whilst exhibiting high efficiency as well. The maximum peripheral speed achievable in Table1.1 is realised with this topology. The trade-off of this topology is the increase of effective air-gap length, thus inducing poor power factor. [LAH02] investigates the application of a squirrel caged solid rotor. This topology tries to integrate the robustness of solid rotor with the electromagnetic performance of squirrel cage rotor.

Several papers compare the laminated–rotor topology with alternate kinds of solid rotor configuration [IKE90], [BOG92], [LAH02], [LAT09]. It is widely acknowledged that the laminated rotor can be adopted when it is mechanical endurable because of the significantly higher overall efficiency by reduction of iron loss.

The operating power and speed of IMs are illustrated in Fig.1.2, Fig.1.3 and Fig.1.4. A few findings can be summarized as:

(1) Most of high-speed IMs operate below the speed of 60krpm.
(2) MW-level high-speed IMs account for a significant part of the working region.
(3) The value of r/min$\sqrt{}$kW for most of high-speed IMs drops below 8×10^5.

Table 1.1 High-speed IMs in literature

Power (kW)	**Speed (r/min)**	**v_c (m/s)**	**r/min√kW ($\times 10^5$)**	**Rotor Type**	**Ref.**
60	100000	367	7.74	Solid coated	[SAA94]
300	60000	342	10.39	Solid coated	[GIE12]
2000	15000	290	6.70	Laminated	[CAP05]
60	60000	283	4.64	Solid coated	[LAH02]
8000	12000	250	10.73	Laminated	[LAT09]
50	50000	236	3.53	Solid caged	[LAH02]
8000	12000	204	10.73	Solid slitted	[PYR10]
2610	11160	193	5.70	Solid caged	[WOO97]
100	30000	185	3	Laminated	[VIG92]
6000	10000	182	7.74	Laminated	[HON97]
10	90000	180	2.84	Laminated	[GER12]
6.3	120000	177	3.01	Solid	[BUM06]
35	40000	168	2.36	Laminated	[SIE90]
65	30600	144	2.46	Laminated	[LAH02]
11	56500	138	1.87	Laminated	[KIM01]
21	50000	134	2.29	Laminated	[SOO00]
250	12000	126	1.89	Solid slitted	[HUP04]
200	12000	126	1.69	Laminated	[IKE90]
12	24000	124	0.83	Solid caged	[PYR96]
1.5	50000	120	0.61	Laminated	[LAR03]
120	10000	102	1.09	Solid slitted	[AHO07]
0.7	24000	63	0.20	Solid coated	[LAH02]
12	13500	62	0.47	Solid slitted	[PYR96]
0.075	45000	60	0.12	Laminated	[ANB96]

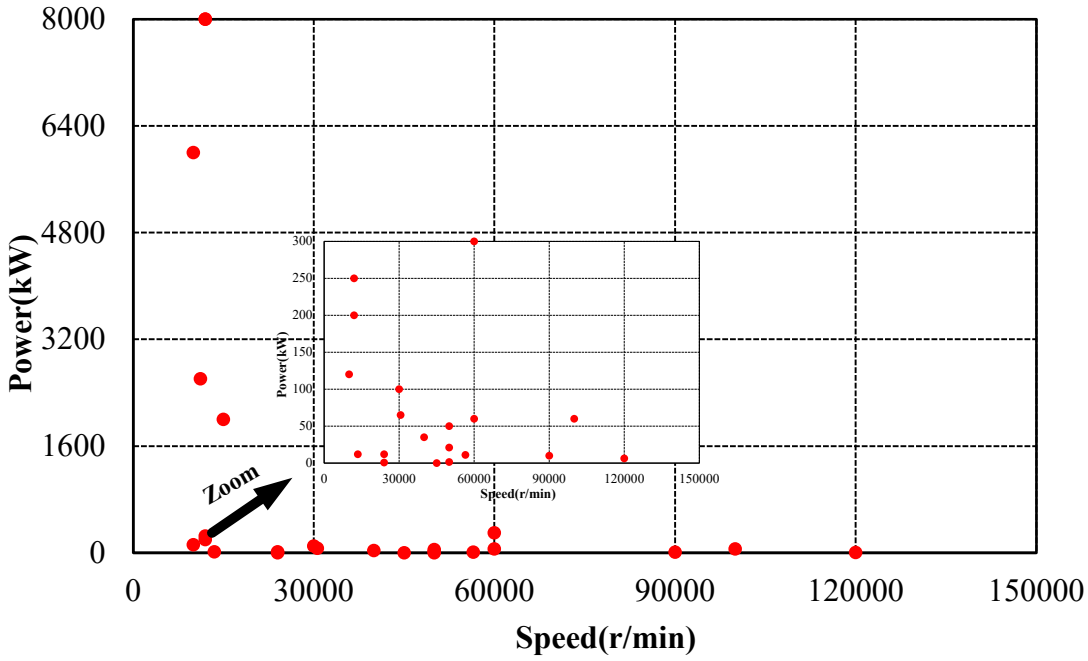

Fig.1.2. Power versus speed of IMs in literature (Table 1.1).

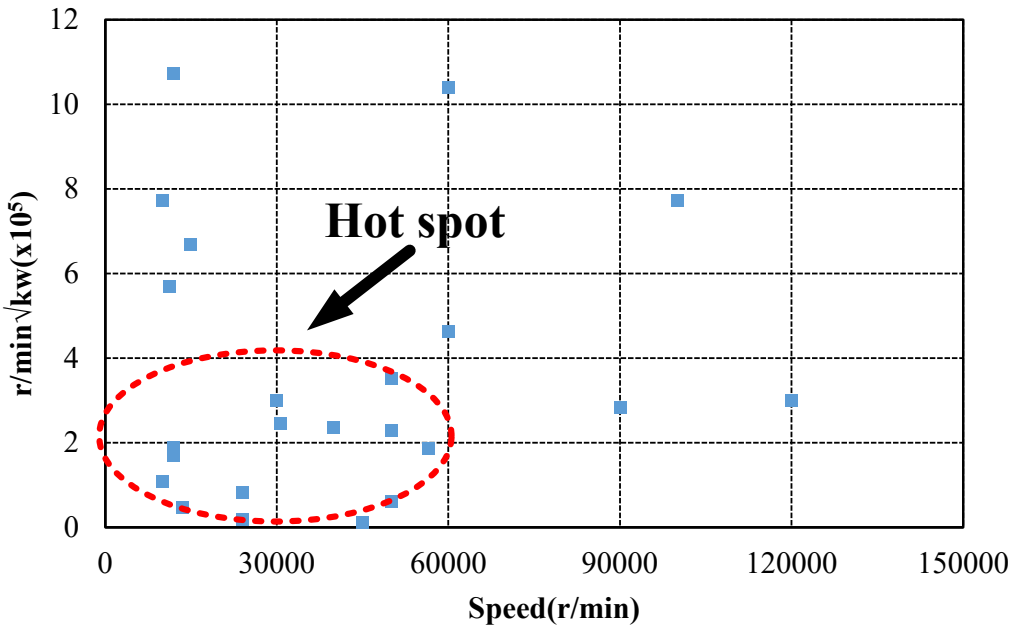

Fig.1.3. r/min √kW versus speed of IMs in literature (Table 1.1).

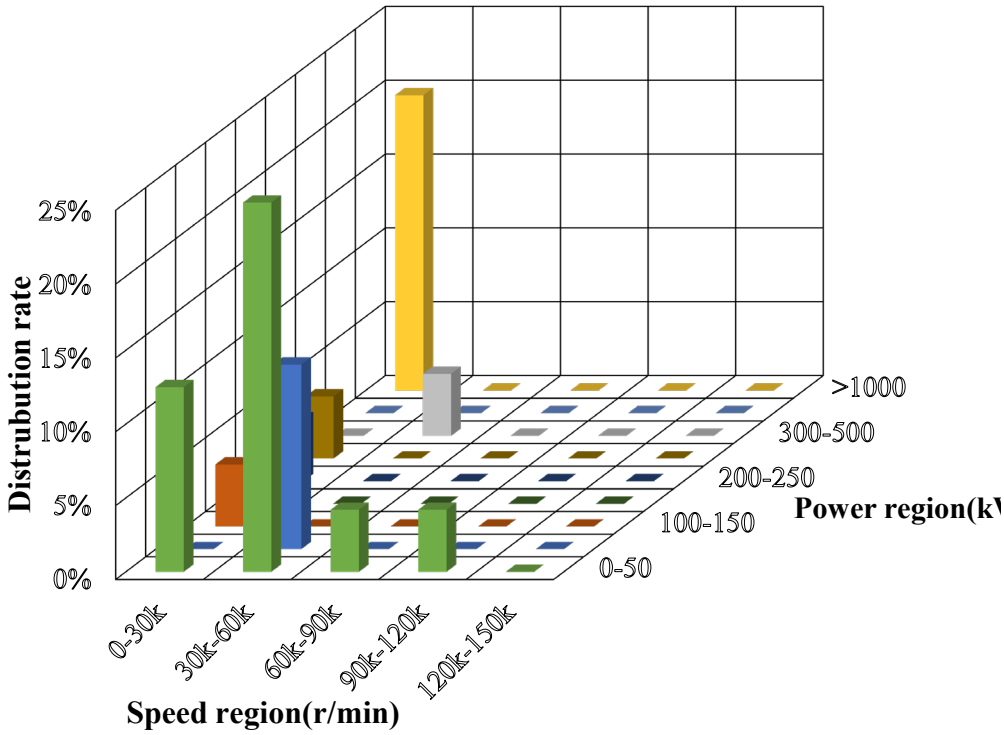

Fig.1.4. Distribution of IM working region (Table 1.1).

B. High-speed SR machines

Switched reluctance machines (SRM) are advantageous for their simple and robust structure. There are neither windings nor permanent magnets on the rotor. Thus, this type of machine is inherently suitable for high-speed applications. Table 1.2 lists the development of high-speed SRMs in literature and industry. The maximum power achievable for SR machines is 250kW with the rated speed of 22000rpm. The maximum operating speed achievable for SR machines has reached 200000rpm. The following findings can be summarized:

(1) Ultra-high-speed SRMs (>90krpm) account for a significant part.

(2) The majority of high-speed SRMs power rating is normally less than 250kW.

(3) The value of r/min$\sqrt{}$kW for most of high-speed SRMs drops below 3×10^5.

One typical application for SRM is low cost applications low power such as home appliances [BRA11], [KIM08], [LEE13]. They are commonly constructed with two-phase, four-slot-two-pole configuration. Another typical application for high-speed SR machines is the integrated starting generator in aero-power system [RIC97], [FER95].

On the other hand, the most challenging issues for high-speed SRM are the significant windage loss resulting from small air gap and uneven rotor surface and the torque ripple. Hence, in [DAN15], a rotor flux bridge is adopted to reduce the windage loss. For the reduction of torque ripple, several literature can be found on the method of rotor shape profiling [LEE13], [HUA18].

Table 1.2 High-speed SRMs in literature

Power (kW)	**Speed (r/min)**	**v_c (m/s)**	**r/min√kW ($\times 10^5$)**	**Air-gap length (mm)**	**Ref.**
0.1	750000	235.5	0.24	0.35	[KUN12]
45	32000	197.6	2.15	0.64	[BAR14]
1	130000	176.8	1.3	0.2	[ZHO09]
100	20000	153.0	2	2.00	[IKA14]
1.5	100000	136	1.22	0.2	[JIN09]
0.3	100000	136	0.547	0.2	[SUN07]
7.5	20000	125.6	0.55	0.25	[FAN06]
1.6	100000	110.9	1.26	0.15	[PEI13]
0.6	30000	46.315	0.23	0.25	[LEE13]
1	17000	32.91	0.17	0.35	[ZHU14]
250	22200	N/A	3.51	N/A	[RIC97]
32	48000	N/A	2.72	N/A	[RAH04]
30	52000	N/A	2.85	N/A	[FER95]
1	200000	N/A	2	0.4	[MOR00]
1	60000	N/A	0.6	0.3	[BRA12]
1	48000	N/A	0.48	N/A	[KIM08]

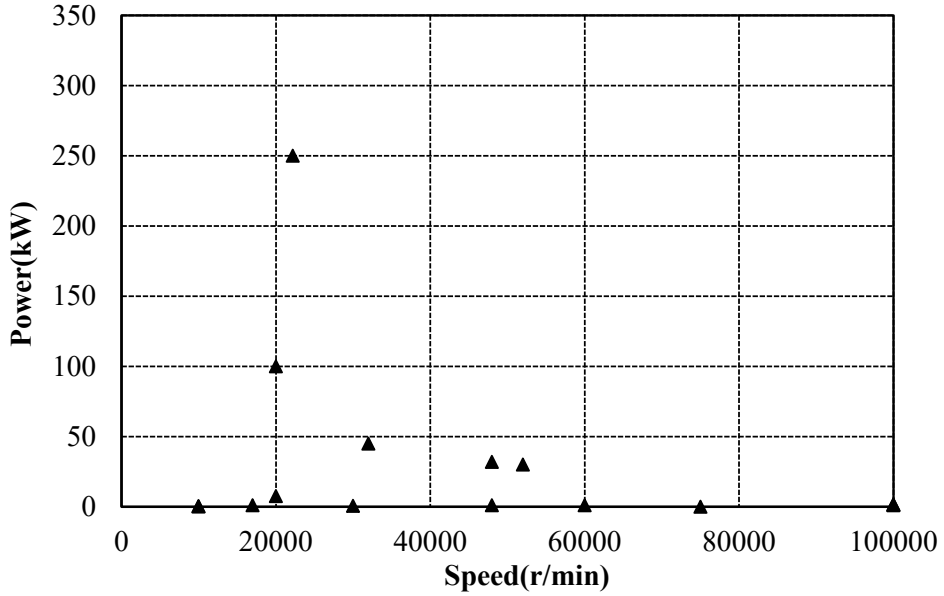

Fig.1.5. Power versus speed of SR machines in literature (Table 1.2).

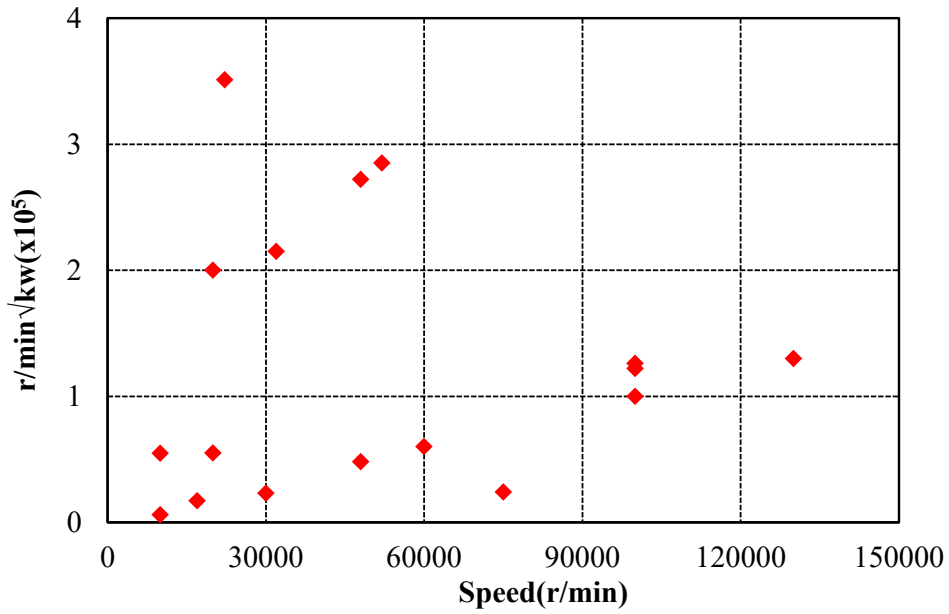

Fig.1.6. r/min √kW versus speed of SR machines in literature (Table 1.2).

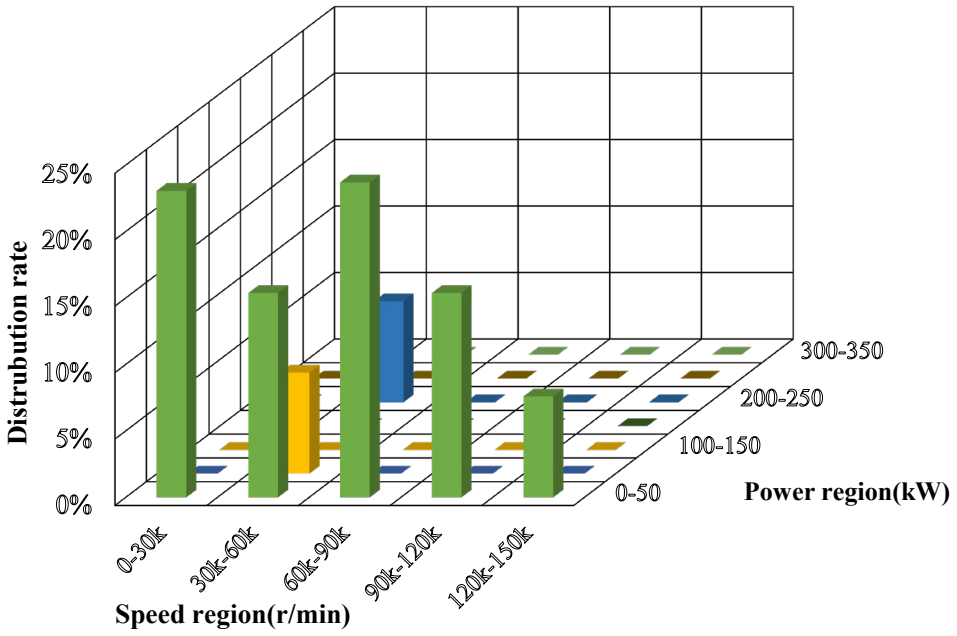

Fig.1.7. Distribution of SR machine working region (Table 1.2).

C. High-speed PM machines

PM machines are becoming more popular in recent years due to their high-power density as well as high efficiency, which are highly desirable for high-speed operation. Table 1.3 lists current HSPMMs published in literature and industry. As can be seen, the maximum power achievable for HSPM machines has reached 8 MW with the rated speed of 15000r/min [BAI09]. The proposed machines equipped with SPM construction are designed for a gas turbine. On the other hand, the maximum operating speed achievable for HSPM machines is proposed and tested in [ZWY05]. This machine is adopted in mesoscale gas turbine at the speed of 500000r/min.

Table 1.3 High-speed PM machines in literature

Power (kW)	Speed (r/min)	v_c (m/s)	r/min$\sqrt{}$kW ($\times 10^5$)	Rotor Type	Retaining sleeve	Ref.
1500	20000	314	7.7	SPM	Carbon fiber	[PAU04]
22	120000	294	5.63	SPM	Alloy	[WAN10a]
2	220000	288	3.11	SPM	Carbon fiber	[NOG07]
N/A	200000	280	N/A	SPM	Carbon fiber	[BOR10]
1	500000	261	5	SPM	Titanium	[ZWY05]

8000	5000	250	13.4	SPM	Carbon fiber	[BAI09]
11	50000	233	1.66	IPM	Laminated	[HON97]
15	120000	220	4.65	SPM	Inconel78	[HON09]
117	60000	207.2	6.49	SPM	Alloy	[LI14]
5	240000	201	5.37	SPM	Alloy	[SHI04]
1100	30000	200	9.95	SPM	Carbon fiber	[GER14]
75	60000	190	5.20	SPM	Non-magnetic Steel enclosure	[XIN10]
5	120000	188	2.68	SPM	Alloy	[GER14]
2.3	150000	188	2.27	SPM	Alloy	[SHE12]
1120	18000	180	6.02	SPM	Carbon fiber	[FEN15]
2	200000	172	2.83	SPM	Alloy	[PFI10]
0.5	400000	167	2.83	SPM	Alloy	[HON13]
40	40000	161	2.53	SPM	Carbon fiber	[BIN06]
0.1	500000	157	1.58	SPM	Alloy	[ZWY05]
46	32000	154	2.17	SPM	Alloy	[FER14]
50	16000	135	1.13	IPM	N/A	[HSU08]
10	70000	125	2.21	SPM	Alloy	[SHE13]
150	24000	111	2.94	SPM	Alloy	[DON14]
0.5	60000	92	0.42	SPM	Carbon fiber	[SCH08]
0.5	100000	91	0.71	SPM	Alloy	[JIA11]
2.5	24000	84	0.37	SPM	Alloy	[UPA09]
1.5	60000	82	0.73	SPM	Carbon fiber	[HWA14]
8	40000	74	1.13	IPM	N/A	[KIM12]
25	20000	56	1.0	SPM	Alloy	[PAP14]
1	28000	51	0.28	SPM	Alloy	[CHO06]
1.3	20000	38	0.23	SPM	Alloy	[ZHU97]
5000	15000	N/A	10.6	SPM	Carbon fiber	[GON14]
1000	15000	N/A	4.74	SPM	Carbon fiber	[RAH04]
640	10000	N/A	2.52	SPM	Carbon fiber	[LUI14]
100	30000	N/A	3.0	SPM	Alloy	[SMI10]
75	36000	N/A	3.11	SPM	GH4169(Alloy)	[DON14]
70	45000	N/A	3.76	SPM	N/A	[RAH04]
60	10000	N/A	0.77	SPM	Alloy	[BOU14]

55	64000	N/A	4.74	SPM	Alloy	[JAN04]
50	40000	N/A	2.83	SPM	N/A	[YON12]
40	60000	N/A	3.79	SPM	N/A	[LON98]
30	96000	N/A	5.26	SPM	Alloy	[XIA15]
18	50000	N/A	2.12	SPM	Alloy	[HAS14]
11	32000	N/A	1.06	IPM	Alloy	[CHO06]
7.6	50000	N/A	1.38	SPM	N/A	[NAG05]
5	150000	N/A	3.35	SPM	Carbon fiber	[TAK94]
3	150000	N/A	2.59	SPM	Alloy	[HU14]
1.85	136000	N/A	1.85	SPM	Alloy	[LIN08]

Fig.1.8. 100-W 500000-r/min high-speed PM machine [ZWY05].

From Table 1.3, the maximum peripheral speed for SPM machines with carbon fibre has reached 314m/s whist the figure for those employing metallic sleeve is 294m/s. A higher peripheral speed can be realised for IPM machines by means of exotic steel laminated rotor or solid rotor [HON97], [ARU16].

Fig.1.9. High-speed IPM machine with slitting solid rotor [ARU16].

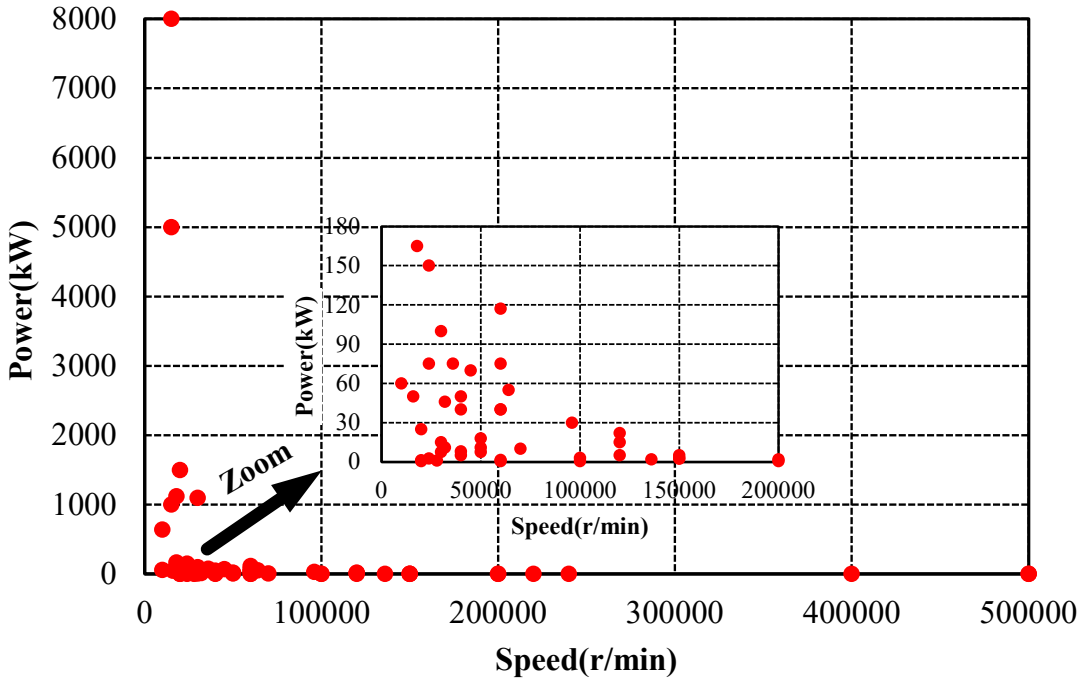

Fig.1.10. Power versus speed of PM machines in literature (Table 1.3).

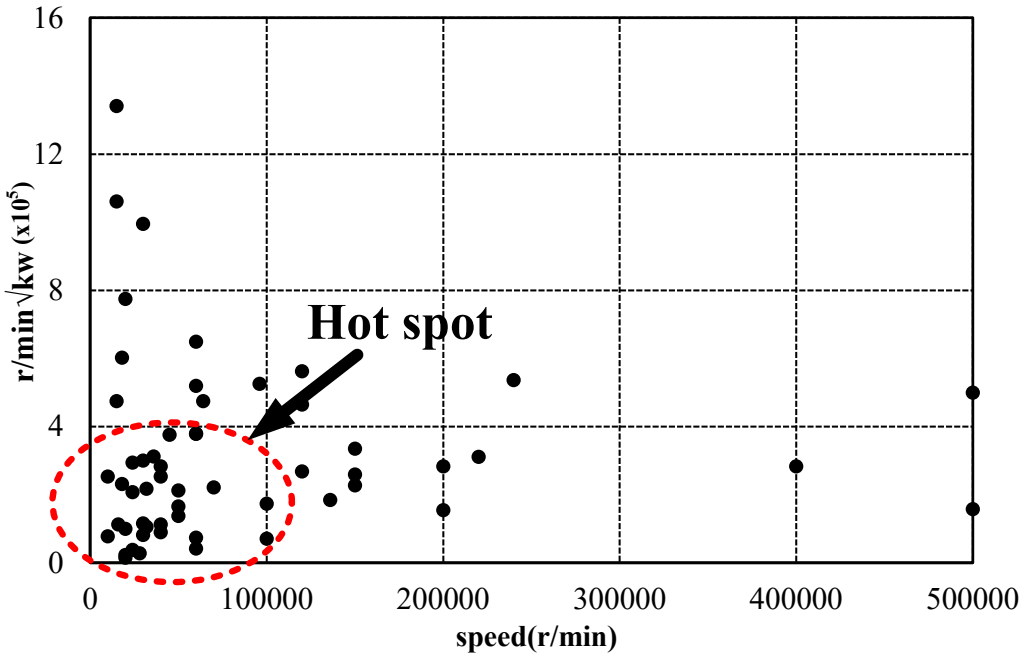

Fig.1.11. r/min √kW versus speed of PM machines in literature (Table 1.3).

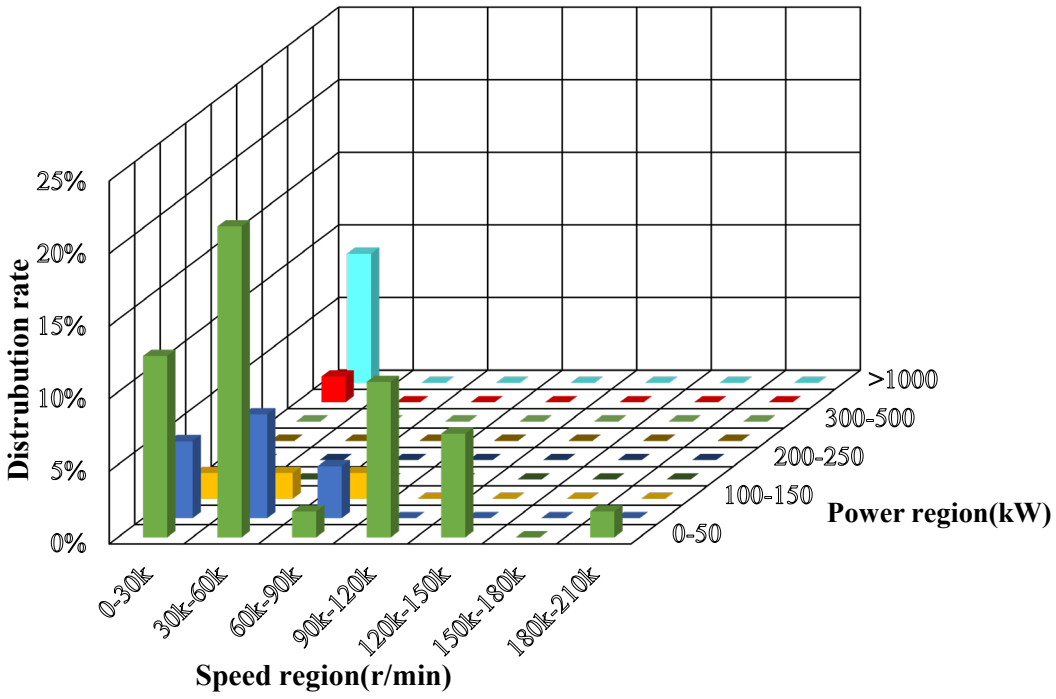

Fig.1.12. Distribution of high-speed PM machines working region (Table 1.3).

Table 1.4 summarizes key parameters of the feasible topologies of high-speed electrical machines. A few observations can be concluded:

1) The maximum peripheral speed can be realized with solid-rotor IM topology, followed with the SPM machine with carbon fibre sleeve. These two topologies are the most selected solutions in the MW level high-speed applications.

2) The IM with strengthened laminated rotor shares equal value of r/min√kW with SPM machine with a metallic sleeve. However, the maximum power achievable for SPM machines is only 150kW which is far behind that of IMs. This can be attributed to the thermal limits of the permanent magnet under the protection of thermal limits. The induced sleeve loss imposes a great threat on the magnet, thus restricting the improvement of power level.

3) Switched reluctance machines are relatively advantageous in the tolerable operating speed thanks to its unique rotor structure. However, the large iron loss and windage loss make them not so competitive with SPM machines and IMs.

Table 1.4. Summary of key parameters for feasible topologies of HSEM

Machine Type		Max. power (kW)	Max. speed (r/min)	Max. r/min√kW ($\times 10^5$)	Max. peripheral speed (m/s)	Ref.
IMs	Solid-rotor IMs	60	10000	7.74	367	[SAA94]
	IMs using high-strength sheet steels for rotor	2000	15000	6.70	290	[CAP05]
	IMs with conventional laminated rotor	280	90000	3.0	185	[GER12]
SPM	SPM machines with carbon fiber	8000	220000	13.4	314	[PAU04]
	SPM machines with metallic sleeve	22	120000	5.63	294	[WAN10a]
IPM	IPM machine with high strength laminated rotor	11	50000	1.66	233	[HON97]
	IPM machines with normal laminated rotor	50	40000	1.13	135	[HSU08]
SRM	SRMs	250	220000	3.51	210	[RIC97]

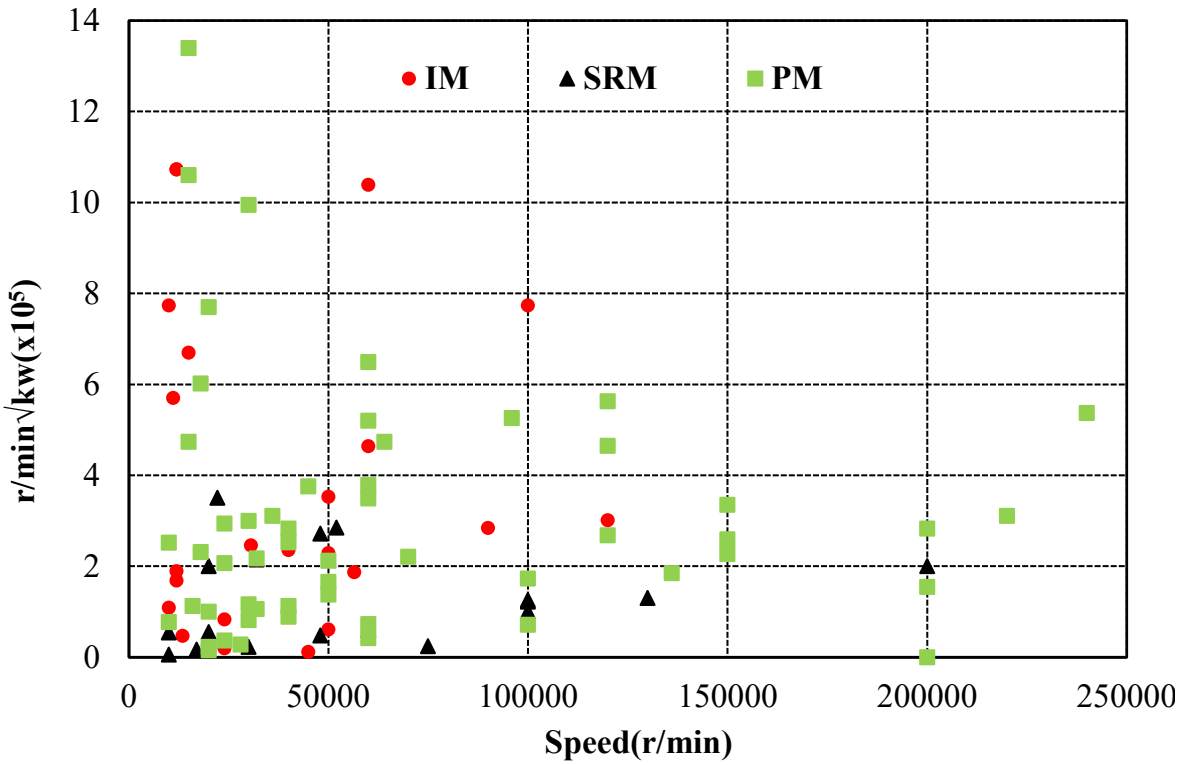

Fig.1.13. r/min √kW versus speed of different types of HSEMs in literature (Table 1.1, Table 1.2, and Table 1.3).

To conclude, the PM machine is superior to the SRM and IM in terms of power density and efficiency, whilst sacrificing the rotor mechanical stability and the temperature endurance capabilities. By contrast, SRM has the superior mechanical robustness, high durability in harsh environment due to its unique rotor topology, but at the expense of high torque ripple, high iron loss, high windage loss, and thus low efficiency and complicated inverter. IM has a robust and cheap construction, ensuring high reliability in the harsh environment. However, the trade-offs lie in the lowest power density and sophisticated power converter for both control and field excitation. Table 1.5 illustrates the advantages and disadvantages of feasible topologies of high-speed electrical machines. This thesis will focus on the issues related with high-speed PM machines

Table 1.5 Advantages and disadvantages of feasible topologies of HSEMs

Machine Type	Advantages	Disadvantages
Induction machines	Robustness and low maintenance	High rotor loss thus low efficiency Low power factor
Radial PM machines	Large airgap length (SPM) High efficiency High power factor High power density thus compact size	Rotor robustness Rotor eddy current loss (SPM) PM temperature endurance (SPM)
Axial PM machine	High power factor and efficiency Low rotor loss Large airgap length	Increased cost Complicated structure
Homopolar machine	High power factor Easy field adjustment Simple rotor structure	Large windage loss Large iron loss
Claw-pole machine	High power factor Easy field adjustment	Complicated 3D rotor structure High rotor loss and leakage flux thus low efficiency
Switched reluctance machine	Fault tolerant due to lack of PMs Robust and simple rotor	Low torque density High torque ripple Small airgap required
Synchronous reluctance machine	Fault tolerant due to lack of PM Relatively robust rotor structure	Low power density Small airgap length needed

1.3 Electromagnetic Issues in High-speed PM Machines

The electromagnetic analysis of HSPMM has never only been about the improvement of efficiency and power density. Instead, design guidelines in terms of topology such as slot and pole number combination should be considered more from the loss and stress point of view. This section will discuss various aspects of electromagnetic design considerations which is quite interdependent on the rotor thermal stability and mechanical robustness, reflected by the electromagnetic loss and unbalanced magnetic force.

1.3.1 Machine Topologies

There are several factors related to machine topologies of HSPMM. This section mainly focuses on three aspects: stator topologies, including slot and pole number combinations; and winding configurations and the rotor configurations, especially for the location of magnets. Table 1.6 gives the stator and rotor configurations as well as winding design in existing literature.

Table 1.6 Stator and rotor configurations of HSPMM in literature

Power (kW)	Speed (r/min)	Stator-pole	Rotor-pole	Winding configuration	Rotor Type	Ref.
1500	20000	12	8	Non-overlapping	SPM	[PAU04]
18	50000	Ironless	8	Overlapping	SPM	[HAS14]
50	16000	48	8	Overlapping	IPM	[HSU08]
60	10000	48	8	Overlapping	SPM	[BOU14]
100	30000	8	6	Non-overlapping	SPM	[SMI10]
8000	15000	48	4	Overlapping	SPM	[BAI09]
5000	15000	48	4	Overlapping	SPM	[GON14]
1120	18000	27	4	Overlapping	SPM	[ZHA15]
55	64000	24	4	Overlapping	SPM	[JAN04]
640	10000	Slotless	4	Overlapping	SPM	[LUI14]
7.6	50000	24	4	Overlapping	SPM	[NAG05]
25	20000	6	4	Non-overlapping	SPM	[PAP14]
0.5	60000	6	4	Non-overlapping	SPM	[SCH08]
117	60000	36	2	Overlapping	SPM	[LI14]
5	240000	6	2	Non-overlapping	SPM	[SHI04]

75	60000	24	2	Toroidal	SPM	[XIN10]
1	500000	Slotless	2	Overlapping	SPM	[ZWY08]
5	150000	-	2	-	SPM	[TAK94]
75	36000	24	2	Toroidal	SPM	[DON14]
2	220000	6	2	Non-overlapping	SPM	[NOG07]
150	24000	24	2	Toroidal	SPM	[DON14]
2	200000	Slotless	2	Non-overlapping	SPM	[PFI10]
0.5	400000	6	2	Non-overlapping	SPM	[HON13]
3	150000	24	2	Overlapping	SPM	[HU14]
40	40000	-	2	-	SPM	[BIN06]
2.3	150000	12	2	Overlapping	SPM	[SHE12]
10	70000	12	2	Overlapping	SPM	[SHE13]
1.85	136000	24	2	Overlapping	SPM	[LIN08]
11	50000	-	2	-	IPM	[HON97]
0.1	500000	Slotless	2	Toroidal	SPM	[ZWY05]
8	40000	18	2	Overlapping	IPM	[KIM12]
11	32000	24	2	Overlapping	SPM	[CHO06]
1.5	60000	3	2	Non-overlapping	SPM	[HWA14]
0.5	100000	12	2	Overlapping	SPM	[JIA11]
2.5	24000	24	2	Overlapping	SPM	[UPA09]
1	28000	24	2	Overlapping	SPM	[CHO06]
1100	30000	-	-	-	SPM	[GER14]
30	96000	-	-	-	SPM	[XIA15]
1000	15000	-	-	-	SPM	[RAH04]
15	120000	-	-	-	SPM	[HON09]
40	60000	-	-	-	SPM	[LON98]
70	45000	-	-	-	SPM	[RAH04]
50	40000				SPM	[YON12]
5	120000	-	-	-	SPM	[GER14]
46	32000	-	-	-	SPM	[FER14]

A. Stator configurations

Both the stator and the stator winding of HSPMMs are immersed in the high frequency variable magnetic field. Hence, the design of stator parts should be considered more from the perspective of loss reduction and heat dissipation.

Generally, the stator configuration of HSPMM can be classified into two kinds: slotted stator and slotless stator, as shown in Fig.1.14. For the HSPMM with slotted stator, the spatial harmonics caused by stator slotting effect would induce a significant amount of eddy current loss in the rotor of SPM machines which will be discussed in detail in Chapter 3. On the other hand, the number of stator slot number also makes a difference to the slotting effect. In [XIN10], it was pointed out that the rotor loss will be significantly reduced with the increasing slot number due to weakened slotting effect.

In order to fully eliminate the influence of slotting effect, slotless stator structure can be found in several papers [BIA04], [BIA05], [PER10], [LUI14], [CHE15]. A few features of this type of stator can be summarized as:

1) The rotor loss due to the PM field pulsation is fully eliminated. This is quite desirable for high speed machines with lower number of stator slots, where slot harmonics order is relatively low thus penetrating into the rotor magnets easily. The cogging torque has been mitigated as well. From Fig.1.15, for the machine with slotted stator, significant flux distortion appears in the air gap, which will yield parasitic effects such as rotor loss or UMF. On the other hand, the open-circuit air gap flux density is quite sinusoidal for in HSPMM with a slotless stator. However, this merit is at the expense of a lower torque density. A lower amplitude of fundamental flux due to the increased reluctance will be observed in slotless machines. Hence, normally, the Halbach magnetization will be adopted together with the slotless structure to compensate for the reduced flux density [JAN01], [JAN03], [PRA12], [LUI14].

2) The stator core loss will be significantly reduced due to decreased iron volume and stator flux density.

3) The relatively large equivalent air gap also acts as a double-edged sword. On the one hand, the armature reaction is negligible, thus having a lower demagnetization risk and lower rotor eddy current loss. On the other hand, the phase inductance will be significantly reduced,

making the high-speed machine more difficult to be controlled due to the increased current ripple and distortion [BIA06a].

4) The elimination of stator slot provides more freedom for the configuration of air gap winding, especially in the axial direction. On the other hand, for the air gap winding, due to the direct exposure in the variable field, AC loss should be more concerned compared with the slotted winding. Moreover, the winding thermal dissipation will also become an issue. The winding configuration in slotless stator will be discussed in the following section.

Table 1.7 illustrates the advantages and disadvantages of HSPMM with the slotted and slotless stators. It should be noted the term of high or low is only applicable in the comparison of two machines.

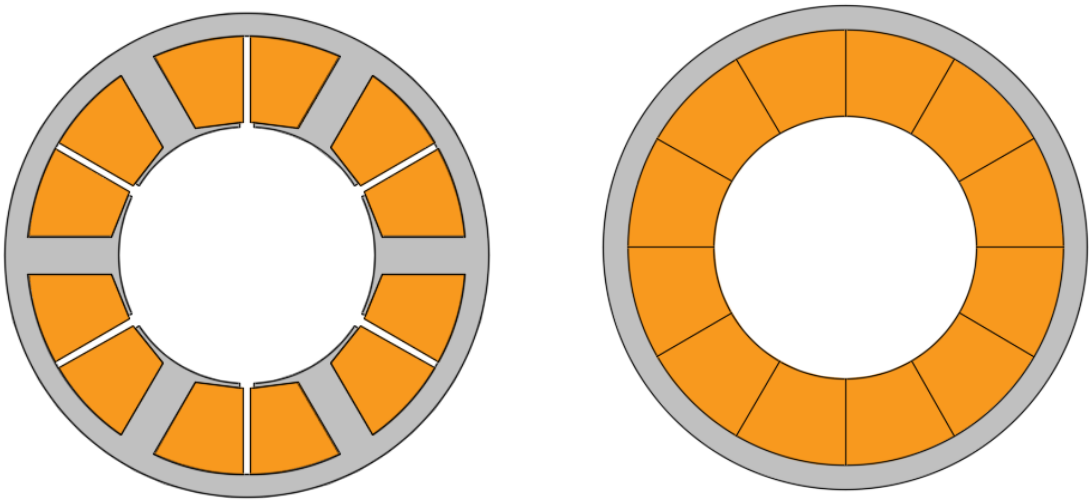

(a) (b)

Fig.1.14. Stator configuration for 6-slot 4-pole high-speed PM machines. (a) Slotted stator. (b) Slotless stator.

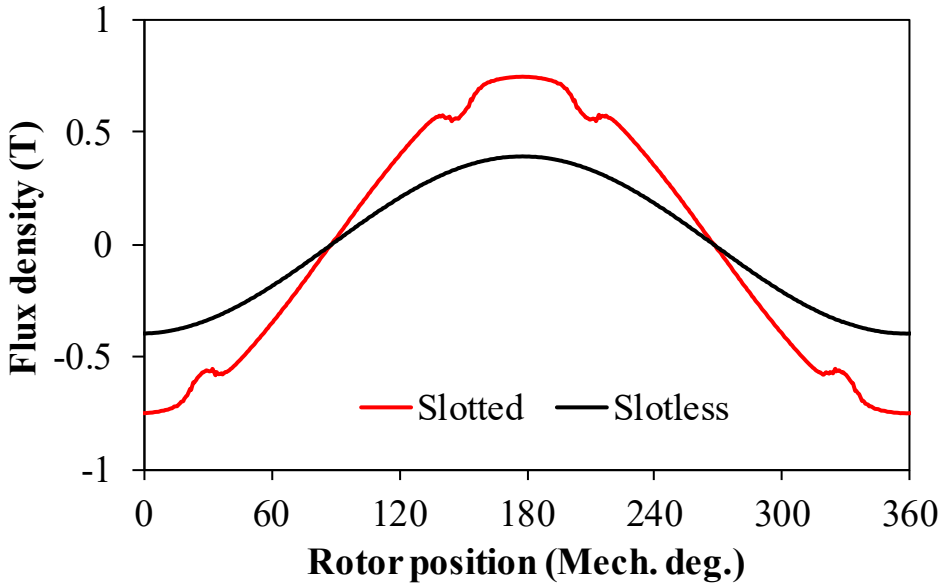

Fig.1.15. Open-circuit air gap flux density of different types of stator.

Table 1.7. Comparison of HSPMM with slotted and slotless stator

Stator Type	Slotless	Slotted
Open-circuit flux density	Low	High
Torque density	Low	High
Armature reaction	Weak	Strong
Demagnetization risk	Low	High
Stator iron loss	Low	High
Stator AC copper loss	High	Low
Stator DC copper loss	High	Low
Winding embedding	Complex	Easy
Stator thermal dissipation capability	Weak	Strong
Rotor eddy current loss	Low	High
Control difficulties	High	Low

B. Winding configurations

Typically, the stator winding of HSPMM can be classified as overlapping winding and non-overlapping which are quite related with the specific slot and pole number combinations. Normally, the HSPMMs with an integer number of slots per phase per pole (SPP) will employ the overlapping winding [JAN04] [BAI09], [KIM12], [SHE13], [LI14]. Typical slot and pole

number combinations are 12-slot/2-pole, 18-slot/2-pole, 24-slot/2-pole, 12-slot/4-pole, 48-slot/4-pole. On the other hand, the HSPMMs with a fractional number of SPP will normally employ the non-overlapping winding also known as fractional-slot concentrated winding (FSCW) [REF10]. Typical slot and pole number combinations are with the classical 3s/2p series such as 3-slot/2-pole [ZHU97], [MA19], 6-slot/4-pole [SCH08], [PAP14], 12-slot/8-pole [PAU04].

The advantages and disadvantages of overlapping and non-overlapping windings have been heavily reported in literature [BIA06b], [BOG09], [REF10], [PFI10]. For HSPMM, the concern is how these two winding configurations make a difference in terms of aforementioned rotor loss and rotor mechanical robustness. To be more specific, attention should be paid on the produced MMF harmonics as well as the end-winding length of these two types of windings. The rotor loss is significantly dependent on the produced MMF. The rotor critical speed will be significantly increased with the enlarged end-winding length. There is no doubt that the overlapping winding is superior in terms of spatial harmonic contents and the non-overlapping winding is more preferred due to shorted end-winding length. Hence, the selection of the winding type should take the requirement of operating speed and power into consideration. From Table 1.6, it is obvious to find that the overlapping winding is more preferred in the HSPMM with high power rating [BAI09], [GON14], [LUI14], [ZHA15] in which the rotor loss is quite an issue. By contrary, the non-overlapping is more inclined to be adopted in HSPMM with ultra-high speed [SHI04], [NOG07], [PFI10]. This basic rule is also capable of explaining the increasing popularity of 6-slot/2-pole HSPMM with non-overlapping winding in the recent decades [UZH16], [WAN18], [MA18]. Although the winding factor of this configuration is only half of that in non-overlapping configuration, the reduced end-winding length is more advantageous for ultra-high-speed application.

Another typical method to reduce the end-winding length is the adoption of toroidal winding as shown in Fig.1.16. The overlapping winding or non-overlapping winding is wound in the stator yoke instead of stator teeth. The advantages of this type of winding includes three aspects: better thermal dissipation; increased machine integrity due to short end-winding length, and easy manufacturing compared with the overlapping winding. Accordingly, there are also at least two applications suitable for the adoption of the toroidal winding in HSPMM:

1) Compared with overlapping winding, the end-winding length is significantly reduced; and the stator thermal dissipation capability is greatly strengthened. Hence, in the high-power

high-speed application, where the integral number of SPP is needed from the point of view of loss reduction, the toroidal overlapping winding is normally adopted [XIN10], [DON14], instead of the conventional distributed tooth-wound overlapping winding. It resembles the merits of distributed winding in terms of MMF and the non-overlapping winding in terms of shortened end-winding length.

2) The stator thermal dissipation capability is significantly increased due to the direct contact with the stator housing and the presence of the extra air-duct. Hence, it is quite suitable to be adopted in a slotless stator where the winding heat dissipation is an issue. A few pieces in literature reported a combination of slotless stator and toroidal winding [ZWY05], [BOR09] [GIL16], [TUY17].

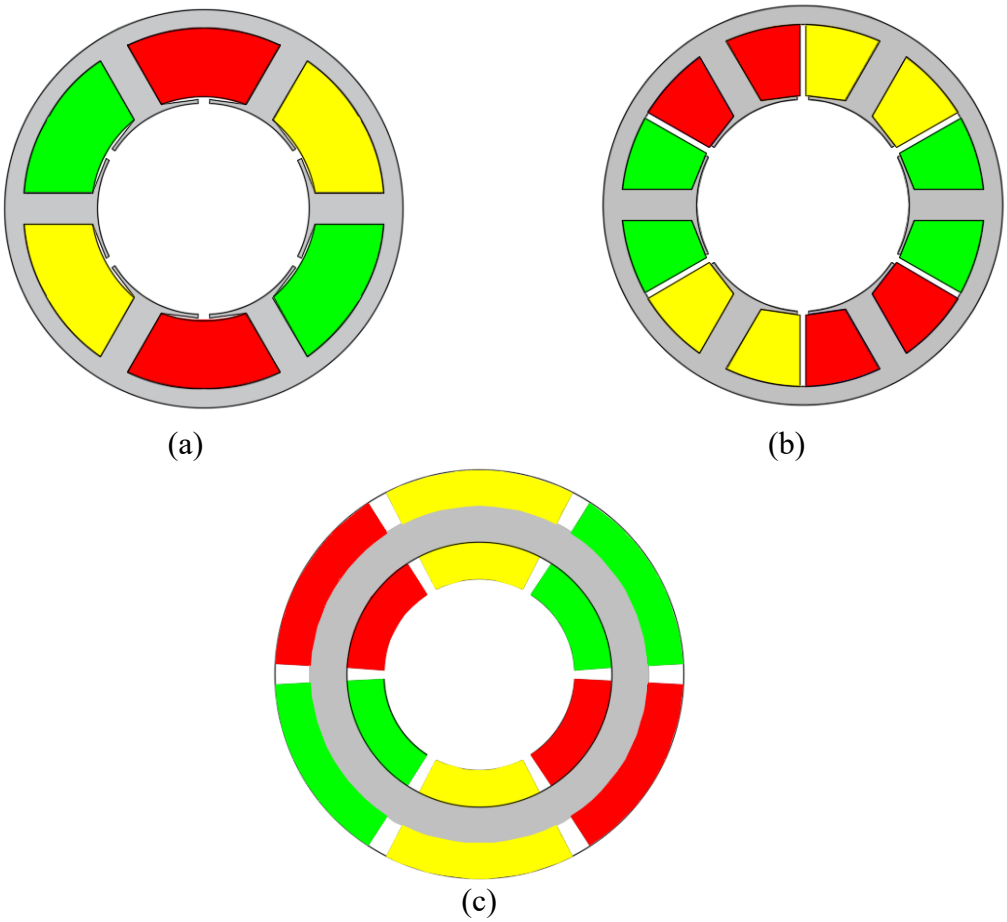

Fig.1.16. Winding configurations for 6-slot 2-pole high-speed PM machines. (a) Overlapping winding. (b) Non-overlapping winding. (c) Ring-wound (Toroidal) winding.

C. Rotor configurations

The selection of rotor topologies for HSPMM is a vital issue which is involved with both electromagnetic and mechanical problems such as magnet utilization and protection. The electromagnetic performance, such as power density and efficiency, and mechanical robustness of HSPMM are quite dependent on the rotor design. Basically, the rotor design of HSPMM can be regarded as the search for a reasonable combination of magnets, rotor iron and retaining sleeve if applicable, by making trade-offs between the PM containment for mechanical robustness and PM utilization for high efficiency.

This section will briefly summarize and give a schematic analysis of the rotor configurations of HSPMM and try to discover the reasons behind it. From Table 1.6, it can be seen that the SPM machines with the retaining sleeves are widely used for high speed applications. On the other hand, the IPM machines with strengthened material together with the magnetic bridge and shaping techniques are also gaining popularity in the last decade [KIM12], [JIA15], [ARU16].

(a) High-speed SPM machines

As proven in the previous section, the SPM machines are more favored due to mechanical robustness. Normally, the HSPMM rotor topologies can be grouped into two categories according to the rotor pole number. The rotor pole number of HSPMM is usually selected to be 2 or 4. Generally, the 2-pole rotor is more preferred due to lower fundamental frequency which is extremely desirable for ultra-high-speed applications. The rotor configurations for the 2-pole HSPMM are illustrated in Fig.1.17. The solid magnet type is the most adopted configuration due to the easy manufacturing and magnetization [ZWY05], [XIN10], [JIA10], [PFI10], [HON13]. The cylindrical magnets are diametrically magnetized so that the sinusoidal back-EMF can be acquired. In addition, the solid magnet ensures the rotor integrity. Meanwhile, this will induce the significant magnet loss, making it unsuitable for the high-power applications.

Another popular 2-pole rotor topology is the hollow magnet type shown in Fig.1.17 (b) [NAG05], [SHE13]. This configuration increases the utilization rate of the magnets in solid magnet type whilst still maintaining a sinusoidal air gap flux density. The parallel magnetized PMs naturally can be regarded the 2-pole Halbach array.

On the other hand, the 4-pole rotor is more inclined to be adopted for high-power high-speed

applications due to reduced end-winding length and stator copper loss, which are quite advantageous for stator thermal equilibrium in high power applications [JAN04], [BIN06], [LUI14], [ZHA15].

Fig.1.18 (a) shows a typical 4-pole rotor for the SPM machine [PAU04], [HUY09]. The parallel magnetized magnets are bread-loaf shaped to obtain the sinusoidal air gap field. The rotor eddy current loss can be maintained to a relatively low level. However, the biggest issue for this configuration is the localized rotor mechanical stress in the inter-pole gap. The unique shape of magnets results in the geometry discontinuity, which finally leads to the stress concentration in the retaining sleeve [BIN06].

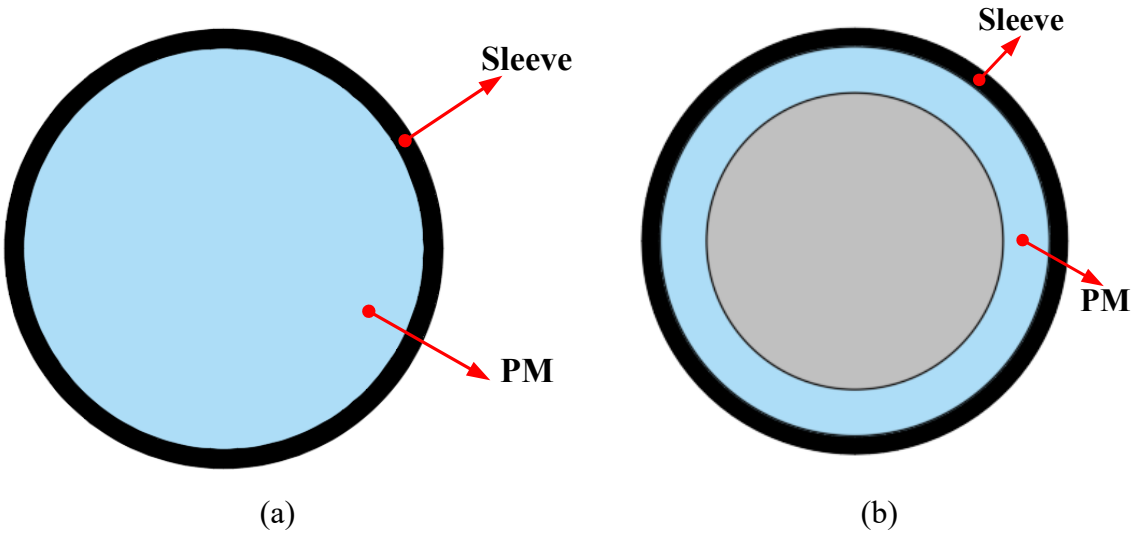

Fig.1.17. Rotor configurations for 2-pole high-speed SPM machines. (a) Solid magnet type. (b) Hollow magnet type.

In order to facilitate the sinusoidal PM field as well as mitigating the concentrated sleeve stress, the segmented magnets are evenly distributed in the circumferential rotor surface, together with the inter-pole filler is reported in much of the literature [BIN06], [WAN10b], [YON12], [LI14], [HWA14], [FEN15], [ZHA16], [DU19]. The ratio of pole arc to pole pitch is selected to be less than 1 so that the inter-pole leakage flux can be suppressed and more sinusoidal PM field can thereby be obtained. On the other hand, the non-magnetic pole fillers such as stainless steel are inserted into the gaps between the adjacent poles in order to reduce to concentrated stress in the sleeve. The magnets are segmented so that the reduced PM eddy current loss is expected. Overall, this rotor configuration is the most widely adopted for 4-pole HSPMM.

As mentioned in the previous section, the Halbach array is normally adopted in the slotless stator for production of stronger air gap field [HON97], [MYE03]. The inherent self-shielding property and sinusoidal air gap field distribution is quite desirable for the rotor of 4-pole HSPMM [JAN04], [LUI04]. The inter-pole gap can be eliminated while a much stronger and sinusoidal air gap field can be obtained. The rotor magnet loss is also significantly lower because of magnet segmentation and sinusoidal field. The main challenges for this type of configuration are the massive consumption of magnets and high manufacturing cost.

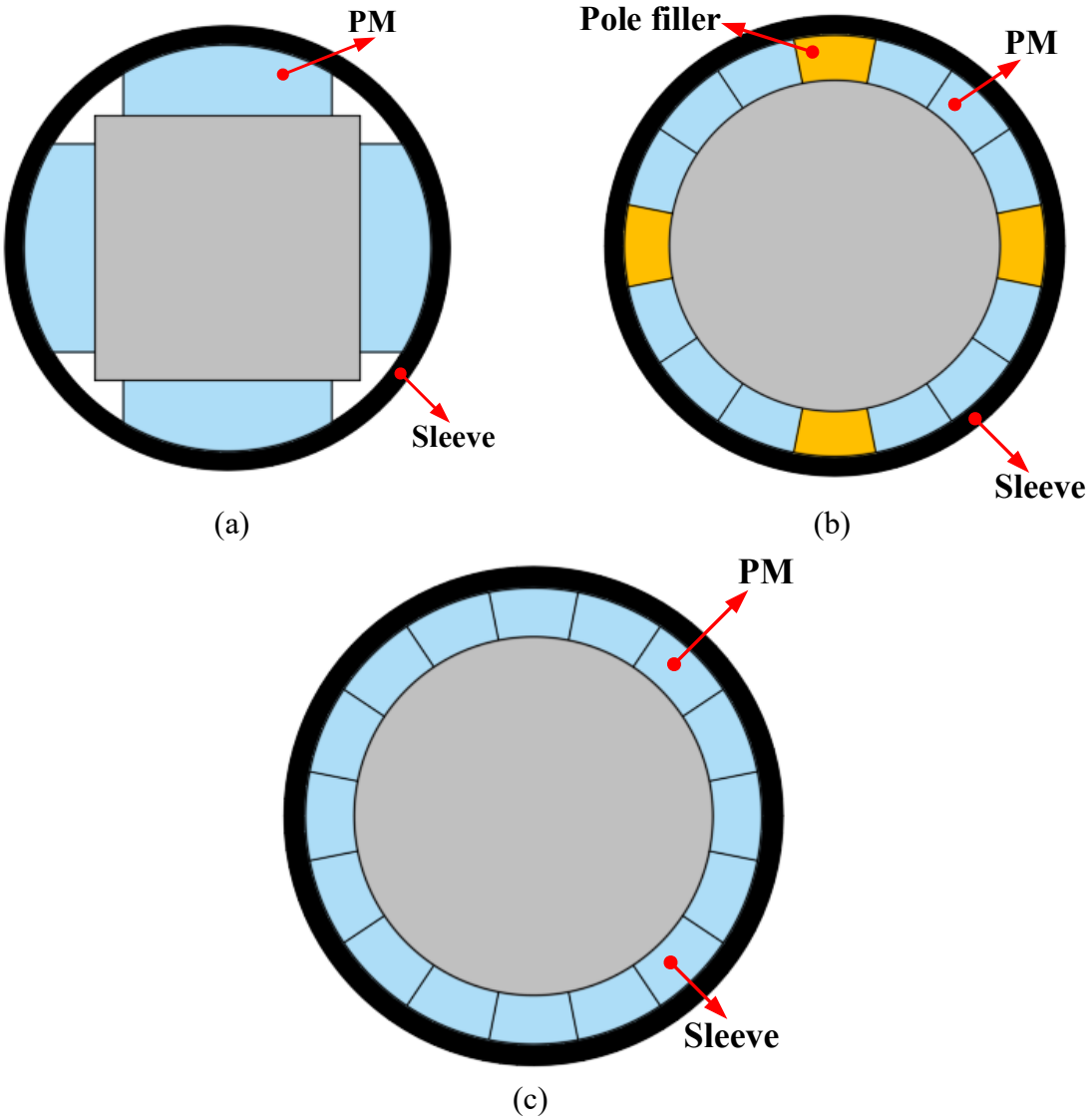

Fig.1.18. Rotor configurations for 4-pole high-speed SPM machines. (a) Broad-loaf magnets type. (b) Segmented magnets with inter-pole filler. (c) Halbach magnetized magnets.

(b) High-speed IPM machines

Although IPM machines are not typical design solutions for high speed application, they are still gaining increasing attention due to the outstanding flux-weakening performance [DEG96] and lower rotor losses [YAM09], especially at high speed. More importantly, the magnets are naturally protected by the rotor iron bridge to withstand the huge centrifugal force. Retaining sleeve is no longer needed so that a much smaller air gap can be expected. Thus, the main concern in terms of mechanical robustness becomes the rotor iron bridge where the Von Mises stress will be concentrated, instead of the magnets in SPM machines. The iron bridge, the thinnest area in rotor core, is mechanically the weakest point and the shape of the bridge significantly affects leakage flux and determine the electromagnetic performance to a large extent [JUN12]. Hence, trade-offs have to be made in the design of the iron bridge.

Typical methods for rotor robustness improvement can be concluded as increasing bridge thickness [JUN12], making dual or triple bridge [KIM12] and bridge corner shaping [ARU16]. However, these methods either sacrifice the electromagnetic performance due to more linkage flux or increase the manufacturing difficulties, which is not suitable for mass production.

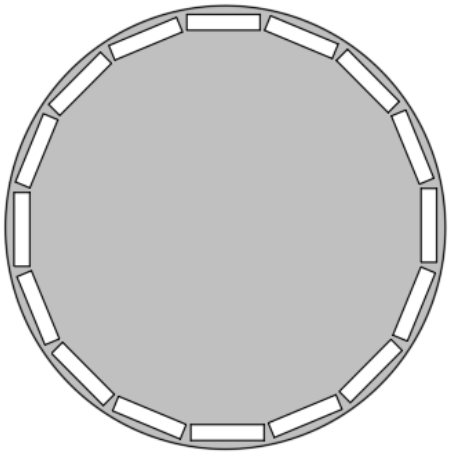

Fig.1.19. High-speed IPM machines with buried magnets [DEG96], [BIN06].

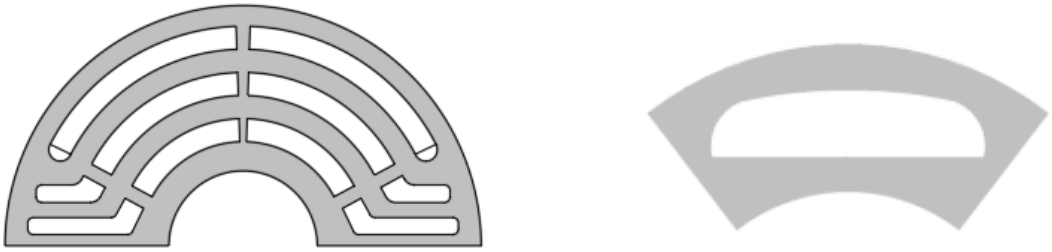

(a) (b)

Fig.1.20. Techniques for rotor stiffness improvement of high-speed IPM machines. (a) Multiple bridges. (b) Iron bridge edge shaping.

In recent years, the “hybrid” concept is gaining substantial attention in the rotor stiffness improvement of IPM machines. In [JIA15], a hybrid rotor configuration is reported for high-speed interior permanent magnet motors, as shown in Fig.1.21. The rotor stiffness is enhanced with the inter-stacked silicon sheet and high-strength stainless sheet. In [ARU16], a novel IPM machine with circumferentially slitting solid rotor is proposed in order to overcome this mechanical constraint in high speed region as shown in Fig.1.9. The solid rotor exhibits much stronger mechanical stiffness than that of laminated one. Meanwhile, the slitting technique is adopted in order to reduce the significantly larger eddy current loss in the rotor iron.

Overall, the speed limit of high-speed IPM machines has always been pushed forward with the development of high-strength steels and manufacturing techniques. However, compared with high-speed SPM machines, IPM machines still exhibit quite a limitation in terms of maximum operating speed, which is demanding in certain applications such as spindles. Hence, although this thesis would only focus on the design guidelines of high-speed SPM machines, it is also helpful and provides more insights to also study the design of high-speed IPM machines.

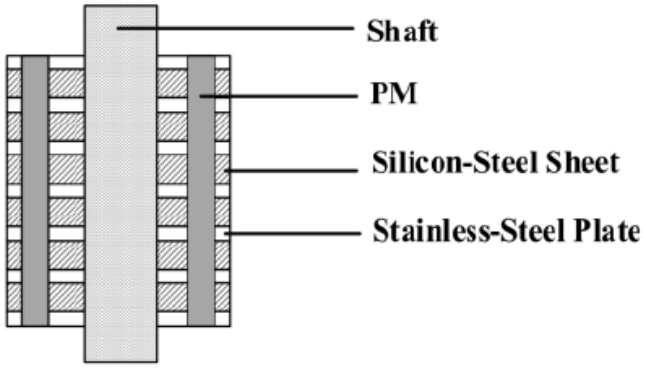

Fig.1.21. High speed IPM machines with inter-stacked rotors [JIA15].

1.3.2 Stator AC Copper Loss

There are generally two types of loss in high speed PM machines, electromagnetic loss including stator copper loss and rotor eddy current loss and mechanical loss including aerodynamic loss and bearing loss. These losses result from the high-frequency pulsated flux and high-speed friction, respectively. Both can be dominant depending on the specific speed and power. In ultra-high-speed application [ZWY05], the mechanical loss dominates the total loss. In MW-level high speed application [BIA09], the rotor eddy current loss is significant. For HSPMM, the accurate loss calculation is extremely important due to the low thermal

endurance of the rotor magnets. Meanwhile, the mechanical stress is also affected by the thermal expansion [BIN06]. The understanding of loss production mechanism and precise prediction will lay a solid foundation for the proposal of targeted loss mitigation strategy. This section will try to give a brief analysis of the losses and summarize the alternate techniques for reduction in the existing literature.

Under high-speed operation, the stator AC copper loss will rise rapidly as a result of the skin effects and proximity effect [SUL99]. The skin effect refers to the trend for high-frequency currents to travel on the conductor skin; whereas the proximity effect refers to the inclination for current to flow in a non-uniform pattern on the cross-section of conductors. These undesirable patterns tend to form the concentrated current loops because of the nearby magnetic field.

There are several papers involved with the calculation of AC copper loss under high-speed operation. In [LUO09], an analytical model is reported to predict the AC copper loss of a 100W, 50krpm slotless PM machine. In [THO09], a simple analytical model is established to estimate the proximity loss in high-speed flux switching machines. Those analytical methods could give a rough evaluation of stator losses. However, the accuracy is not satisfying due to the negligence of the non-linear factor, slot opening flux leakage and other theoretical assumptions. Hence, in [RED08], the 2-D analytical model is proposed for predicting strand-level proximity losses with consideration of the slotting effect. In [RED10], the stand-level and bundle-level proximity loss due to both armature reaction field and PM field can be predicted with an integrated analysis tool.

In order to cope with the significant AC copper loss in HSPMM, [MEL06] points out that the reasonable arrangement of conductors will significantly mitigate the proximity effect. The stator winding should be placed in the rear parts of stator slot with the minimized radial height. On the other hand, the skin effect can be suppressed with the adoption of smaller conductor strands. Hence, Litz wire, consists of hundreds of smaller conductors, is typically one of the most preferred techniques [SUL99]. However, this will also reduce the slot packing factor and thermal dissipation capability. Meanwhile, the high cost of Litz wire is the main issue for its massive implementation. Hence, use of transposed wire bundles as an alternative method of proximity loss reduction is investigated in [RED09] [RED11]. 3-D FE method is adopted for the investigation of the influence of different strand number and transposed degrees.

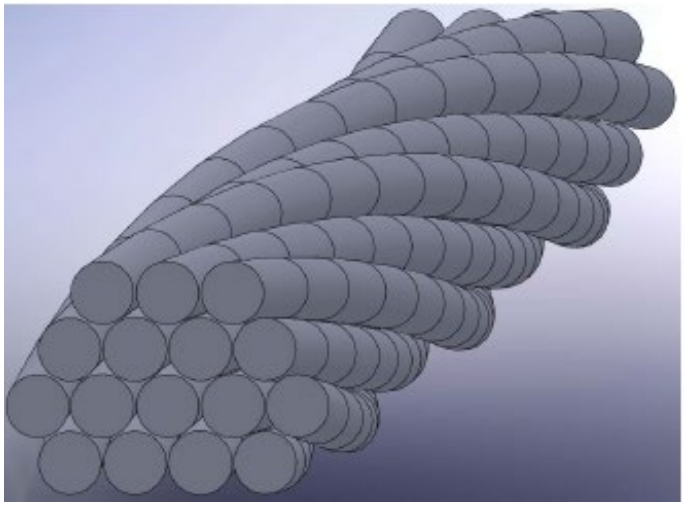

Fig.1.22. Transposed wire bundles [RED09].

1.3.3 Iron Loss

Due to high fundamental and switching frequency, the stator iron loss of HSPMM is significantly increased compared with that in low to medium speed operating PM machines. Hence, the estimation of stator iron loss in HSPMM is quite necessary to provide more accurate basis for the following thermal analysis.

The well-known Steinmetz equation is widely adopted for the rough prediction of iron loss [BER88], [ATA92], [BOG03], [ION07]:

$$p_c = k_h B^{\alpha} + k_e (Bf)^2 + k_{ex} (Bf)^{1.5} \tag{1.1}$$

where α is the Steinmetz coefficient and B is the iron flux density; f denotes the frequency; k_e is the coefficient of eddy current loss; k_h denotes the coefficient of hysteresis loss; k_{ex} represents the coefficient of excess loss.

It should be noted that this equation is under the hypothesis of strictly sinusoidal field. However, in real cases, the existence of flux distortion and DC basis makes the loss coefficients no longer constant. Hence, several modified equations have been reported with the consideration of aforementioned factors [ION06], [MTH06], [POP07], [YAM10a]. Furthermore, in [XUE18a], the influence of temperature on the coefficient of hysteresis loss and coefficient of eddy current loss is investigated.

The material properties of stator lamination also affect the value of stator loss to a large

extent. While the frequency and stator core flux density is given, the iron loss is mainly dependent on the lamination thickness and the final annealing method. Electrical steels with 0.1mm thickness, yielding extremely low iron losses have been reported in [HAY09], [CHI11]. In recent years, the amorphous alloy is gaining more popularity for certain applications due to significant reduction of core losses [LUO09], [HON13]. [DEM14] reported a high-speed induction motor with stator core made of amorphous material, as shown in Fig.1.23. However, this material is rigid and brittle, and thus only suitable for stator lamination. In addition, soft magnetic materials (SMC) with low permeability is also raising attention due to the elimination of core eddy current loss in high frequency [BIA06b], [CHE09].

Fig.1.23. Stator core made from the amorphous material [DEM14].

1.3.4 Rotor Eddy Current loss

The issue of rotor eddy current loss has always been the concern for HSPMM. Generally, the generation of rotor eddy current loss can be attributed to the field variation seen by the rotor. This field variation results from the following reasons: (a) nonsinusoidal stator MMF distribution due to stator winding disposition. (b) permeance variation due to slotting effect and local saturation. (c) nonsinusoidal phase current due to BLDC control and PWM. The existence of spatial and temporal harmonics in the air gap field will yield a significant eddy current loss in the rotor magnets, the rotor yoke as well as the metallic sleeve for magnet retaining. The risk of demagnetization will be increased due to the difficulties of rotor cooling, especially for the rotor magnets sheltered by the sleeve with low thermal conductivity such as carbon-fiber.

Hence, the accurate estimation of rotor eddy current loss is of great importance to the thermal

equilibrium of HSPMM. The calculation methods for rotor eddy current loss can be found in several papers [ZHU93], [ZHU04], [WAN10b], [LAZ10], [JUM15]. Those methods can be divided into the analytical and finite element analysis (FEA) method. The analytical solution is always applied in SPM machines. The permeance variation resulting from slotting effect is ignored. The permeability of iron core is assumed to be infinite. The stator winding is represented by an equivalent ampere-conductor distribution over the stator slot openings. A typical analytical model with consideration of the eddy current reaction field is reported in [ZHU04], shown in Fig.1.24.

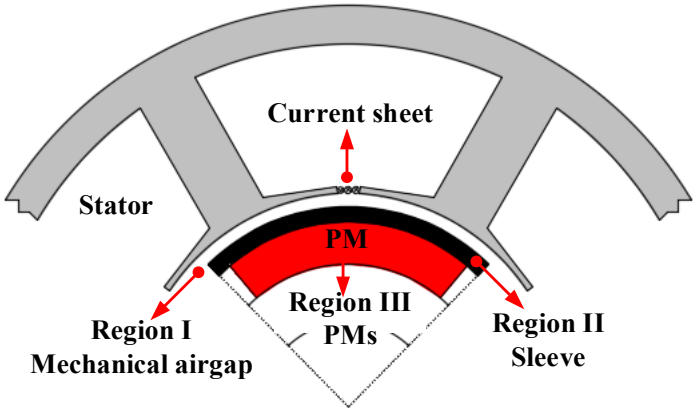

Fig.1.24. Models for analytical prediction of rotor eddy current loss [ZHU04].

The analytical method is more preferred at the preliminary design stage due to its convenience and rapidness. It provides a rough evaluation of the rotor eddy current loss, which distinguishes the bad electromagnetic designs from the good ones in terms of rotor loss. However, it makes a lot of hypothesis which is not the real case. The accuracy of results cannot be ensured. Hence, 2-D FEM is more popular in the prediction of eddy current loss with acceptable accuracy. The computation time is also acceptable with the development of advanced business software. The problem for the 2-D FEM is the ignorance of the end-effect and segmentation effect. It is obvious that the 3-D FEM would solve this problem at the cost of computation time. Hybrid solutions which combine the 2-D FEM and 3-D FEM are proposed in [SAB06], [YAM09]. Nevertheless, the evaluation of rotor eddy current loss ensures a better understanding of the loss generation mechanism so that the corresponding reduction techniques can be taken.

Fundamentally, the methods for eddy current loss reduction can be classified into three groups according to their different aims. One group of methods aims to suppress the spatial or

time harmonics which are the sources of the rotor eddy current loss, [ZWY05], [BIN07], [REF08], [XIN10], [MA19]. Another group of methods aims to increase the resistance of the eddy current flowing loop [YAM09], [SHE13], [HUN15]. The other group of methods aims to shelter the magnets from the penetration of asynchronous harmonics thanks to shielding effect of the coated copper layer [VEE97], [SHA06], [ETE12], or the metallic sleeves such as Inconel or Titanium [ZHO06], [LI14].

Normally, the MMF spatial harmonics can be effectively suppressed by choosing reasonable stator slot/pole combination as well as winding configuration. A typical example is the structure with 2 poles, 6 slots and overlapping/non-overlapping windings, which performs far better than the common structure with 2 poles, 3 slots and non-overlapping windings in terms of rotor eddy current loss [ZHO06]. In [MER15], the 2-pole HSPMMs with alternate stator winding configuration are compared with the consideration of PWM influence, as shown in Fig.1.25. However, all these observations focus on the 2-pole HSPMM only; there is few literature concerned with the 4-pole HSPMM with alternate stator configurations, although the 4-pole, 27-slot HSPMM with overlapping winding configuration is reported in [ZHA15], [DU19]. The influence of different stator winding configurations and the resultant MMF on the rotor eddy current loss remains to be systematically investigated. Hence, in Chapter 3, the analysis of the rotor eddy current loss of 4-pole HSPMM with alternate stator slot number and winding configuration is conducted.

Essentially, the winding technique has been widely used in PM machine with fractional-slot concentrated winding for the cancelation of sub-harmonic. Typical methods are multi-phase winding [PAT14], [CHE14], multi-layered winding as shown in Fig.1.26, [ALB13], [WAN15], winding connection alternation [ZHO18]. These techniques can be applicable for the spatial harmonic elimination in HSPMM with mild influence on the amplitude of the working harmonic. Although few publications can be found on the application of winding techniques for the rotor loss reduction in HSPMM. It is believed to be one of the most favorable ways for the higher efficiency of HSPMM. In addition, no changes are needed in the rotor, which is quite desirable from the mechanical point of view. In [ZHA19], a split phase winding configuration is proposed for the rotor loss reduction of HSPMM.

Other harmonic mitigation techniques include the rotor surface shaping [YAM10b], rotor or stator slitting [CHO16], stator dummy slot [MA19] or dummy teeth, stator flux barriers [DAJ14]. The common principle of those methods is creating a flux path with increased

reluctance for the loss contributing spatial harmonics. However, the fundamental harmonic is reduced to some degree. The rotor loss reduction is at the expense of loss of electromagnetic torque. The loss of power outweighs the gain of rotor loss reduction, especially for the low-power, ultra-high speed HSPMM [MA19]. The overall efficiency is reduced.

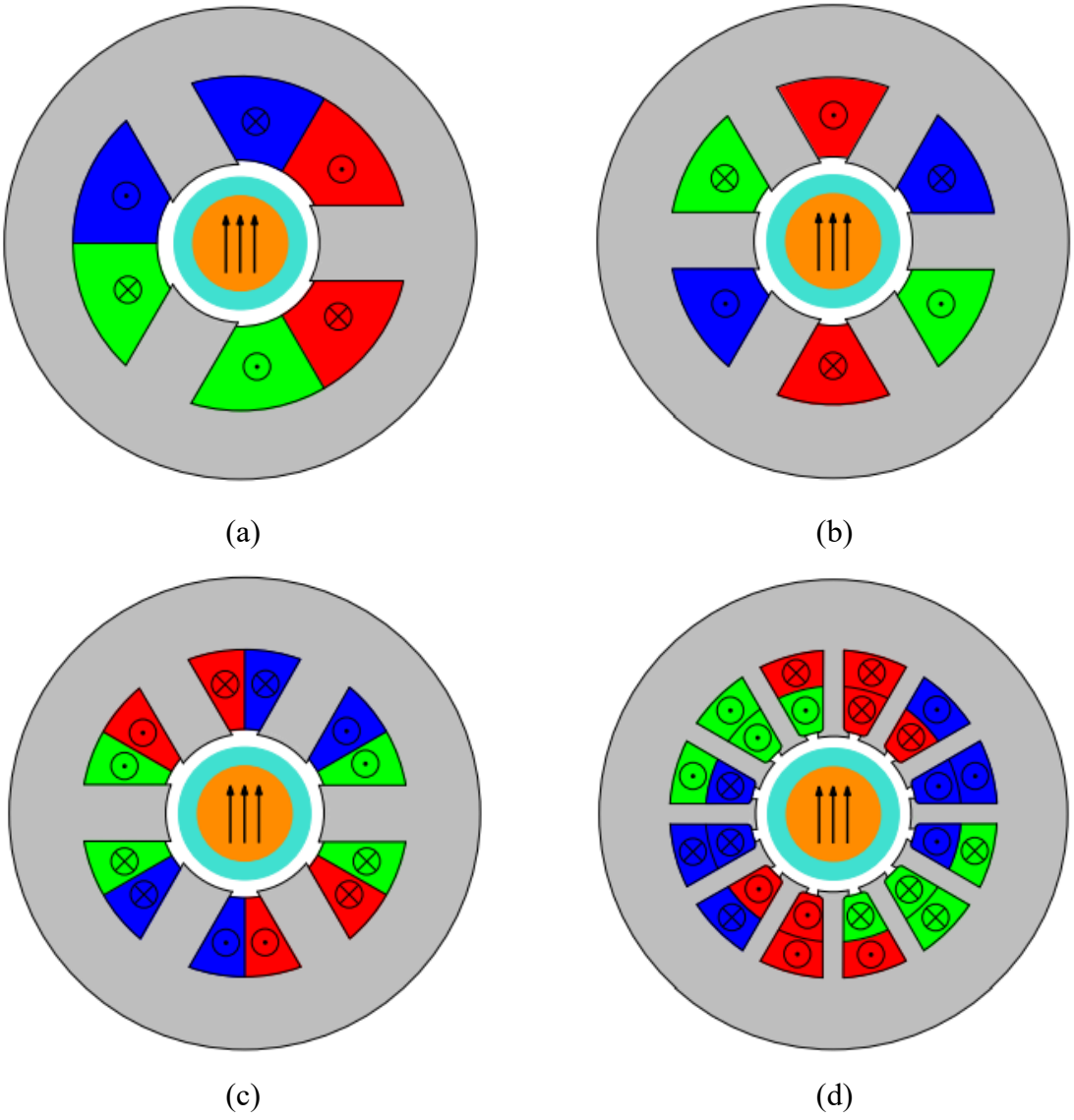

Fig.1.25. 2-pole HSPMMs with alternate stator winding configurations [MER15]. (a) 3-slot/2-pole with non-overlapping winding. (b) 6-slot/2-pole with overlapping winding. (c) 6-slot/2-pole with non-overlapping winding. (d) 12-slot/2-pole with overlapping winding.

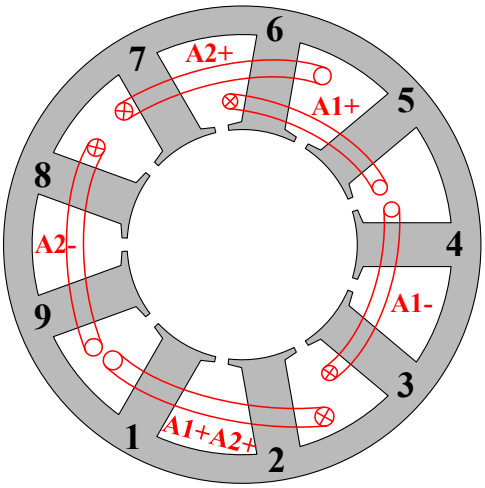

Fig.1.26. Multi-layered winding technique in FSCW machine [ALB13].

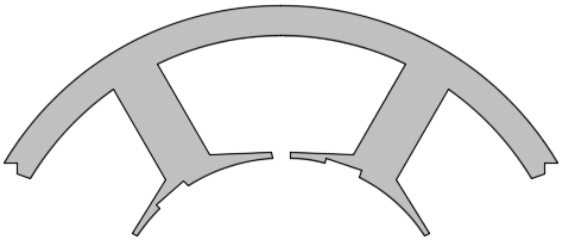

Fig.1.27. Dummy slot for HSPMM [MA19].

For the reduction of slot harmonics resulting from the slotting effect, small slot openings of the stator core are reported in [TOD04], or even the closed slot opening [PAP14] and the slotless configuration [BIA04], as shown in Fig.1.28. However, smaller slot openings or closed slot openings increase the difficulties of winding embedding. Meanwhile, the linkage flux will be increased as well. Extra ohmic loss as a result of significant skin effect and proximity effect will also be induced. The slotting effect on the rotor eddy current loss due to both the PM harmonics and armature reaction harmonics will be discussed in detail in Chapter 3.

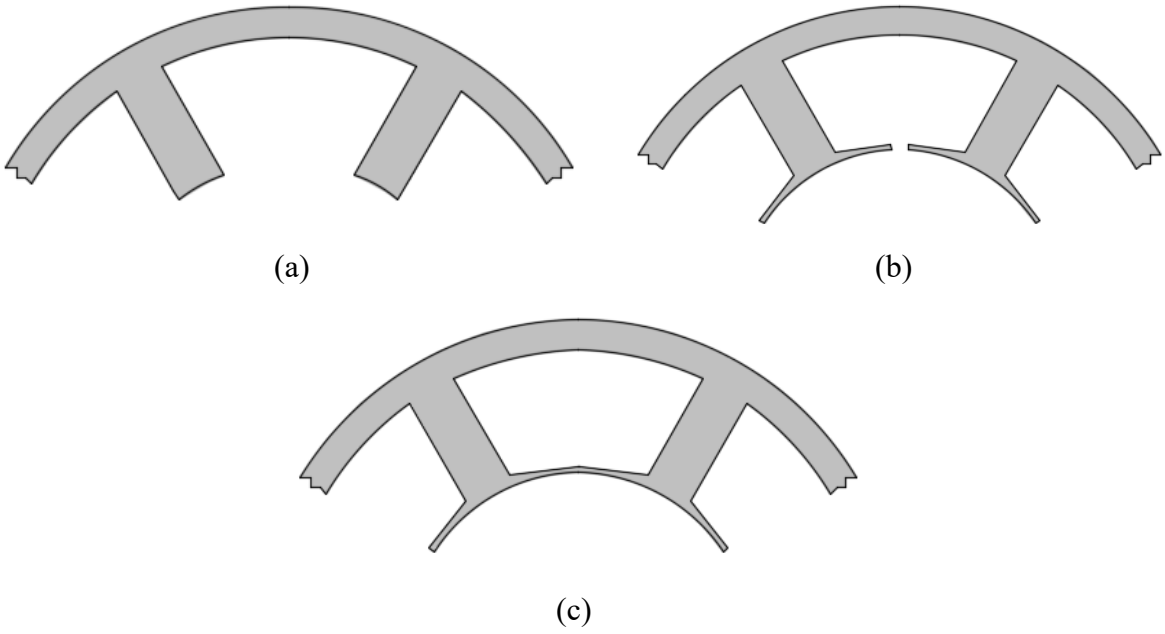

Fig.1.28. Stators of HSPMM with different slot shape. (a) Open slot. (b) Small open slot [TOD04]. (c) Closed slot [PAP14].

As for temporal harmonics, the combination of a dc/dc converter, a dc link filter and a non-PWM inverter instead of a single PWM inverter, as combined drive isolates the PWM harmonics from motor in [SHE13]. In [BIN07], [ZWY08] a novel three-level inverters to reduce at a given switching frequency the current ripple by about 50% with respect to conventional 2-level inverters.

The principle of a second group of methods for rotor eddy current loss reduction is the physical isolation of eddy current. Hence, the magnet segmentation [BIN06], [YAM09], [WAN10b], [YON12], [LI14], [ZHA16] and the sleeve slitting [JUN15] or grooving [SHE13] must be the most efficient way. In [YAM09], it is pointed out that the axial PM segmentation, is more preferred than the circumferential one for SPM machines, whereas the effects of these segmentation methods are nearly identical in the IPM machine. For the metallic sleeve slitting or grooving, the mechanical robustness should be considered.

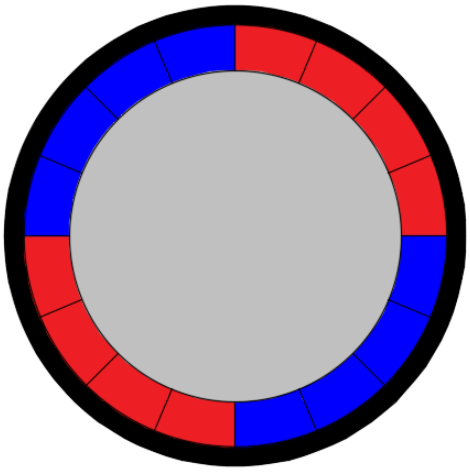

Fig.1.29. Circumferential magnet segmentation for HSPMM [YAM09].

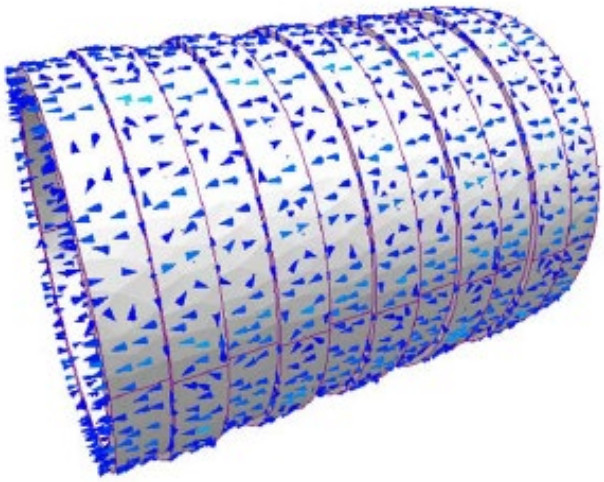

Fig.1.30. Sleeve grooving for eddy current loss reduction [SHE13].

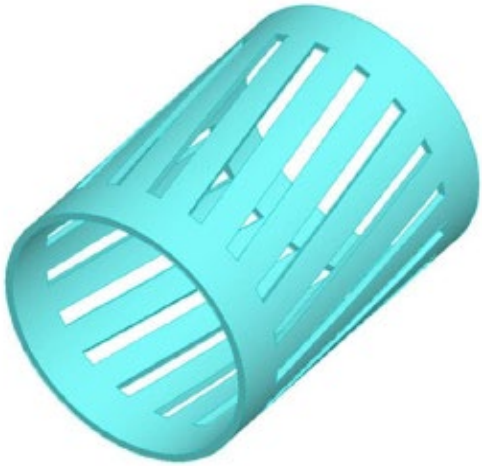

Fig.1.31. Sleeve slitting for eddy current loss reduction [JUN15].

Another widely adopted method for rotor eddy current loss reduction is copper shielding [VEE97], [ZHO06], [SHA06], [REF08], [NIU12], [ETE12], [LI14]. The idea of a conducting copper shield dates at least to the days when the superconducting field windings were considered in the rotor [VEE97]. There are two purposes for the copper layer: mechanical oscillation damping and field shielding for super-harmonics. The influence of copper layer on the working harmonic is negligible. The copper layer acts as the field shielding between the permanent magnet and retaining sleeves. This is extremely desirable in SPM machines with carbon-fiber sleeve, as shown in Fig.1.32 (a). In addition, the copper shielding can also be clapped into the surface of the metallic sleeves such as Inconel and Titanium [SHA09], as shown in Fig.1.32 (b).

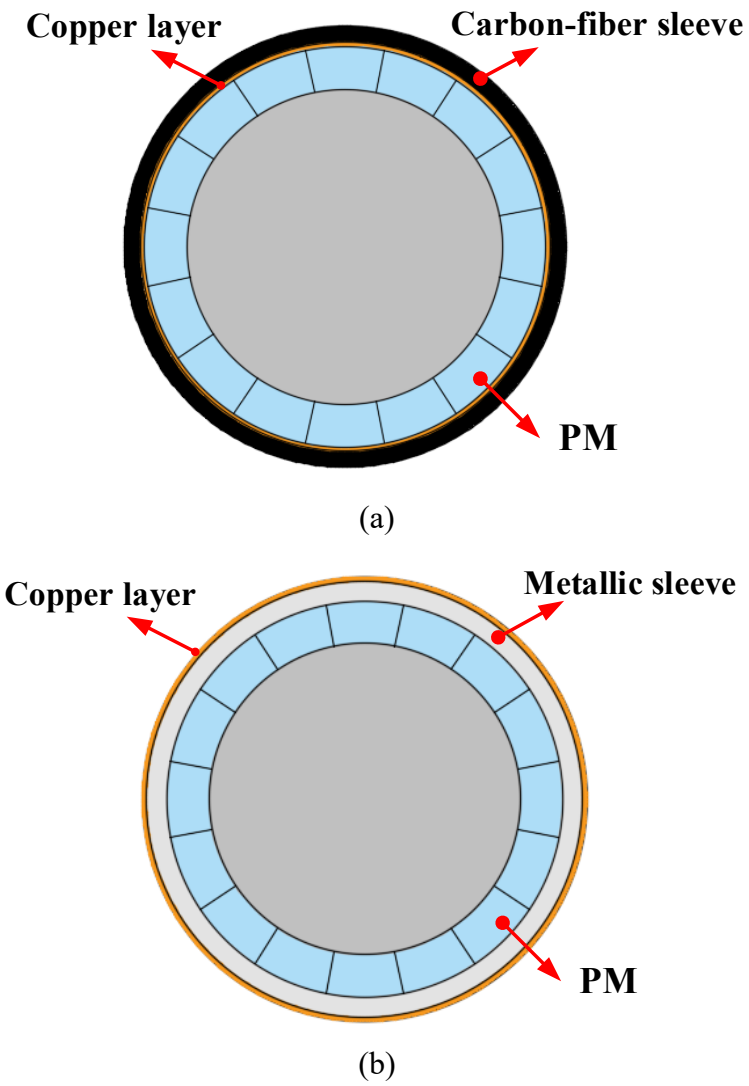

Fig.1.32. Copper shielding technique for rotor eddy current loss reduction.

1.3.5 Rotor Unbalanced Magnetic Force

Unbalanced magnetic force (UMF), one of the machine parasitic effects which jeopardises the bearing life and yields noise and vibration, may occur in fractional-slot machines with odd number of stator slots, even when there are no rotor eccentricities or other manufacturing tolerances [BI97], [DOR08], [LI09], [ZHU07b]. However, this is not a typical issue for HSPMMs without rotor eccentricity since almost all the HSPMMs employ an even number of stator slots as can be seen in Table 1.6, except for the 3-slot 2-pole HSPMM which can be applied in ultra-high speed applications [ZHU97], [MA19]. In [ZHU97], it is pointed out that mechanical resonance may be induced as a result of the UMF. Meanwhile, there is no doubt that the existence of rotor eccentricity will yield significant UMF due to asymmetric field distribution.

The production and characteristics of UMF in different types PM machines with and without rotor eccentricity are comprehensively studied [JAN96], [JAN03], [MIC14] [MAH15], [KIM16]. On the one hand, the UMF in the 2-pole HSPMM has been widely investigated [JAN03], [KIM16], [MA18]. In [JAN03], it is pointed out the Halbach magnetized rotor exhibits lower radial force under the rotor eccentricity scenarios compared with that of the radial magnetized rotor. In [KIM16], an analytical model for the prediction of UMF in a toroidally wound high-speed BLDC motor is developed. In [MA18], the auxiliary slots are inserted in the 3-slot/2-pole HSPMM, ensuring over 90% reduction the on-load UMF. However, the effectiveness of the proposed method is quite dependent on the load.

On the other hand, in recent decades, the HSPMMs with an odd number of stator slots for certain applications are emerging [RED11], [ZHA15], [ZHA17], [DU19]. However, the existing literature only focuses on the electromagnetic performances such as rotor eddy current loss or mechanical performances such as rotor stress. It is unknown how the UMF will be affected in these fractional-slot PM machines with lower pole number. In Chapter 4, a comprehensive investigation will be conducted on HSPMM machines with an odd number of stator slots.

1.4 Mechanical and Aerodynamic Issues in High-speed PM Machines

In high speed applications, the mechanical issues are second to none with respect to electrical ones. The structural challenges of rotor component as well as rotor dynamics are key issues that should be taken into consideration. In this section, all these mechanical design considerations will be addressed.

1.4.1 Rotor Stress

Due to the huge centrifugal force in the high-speed operated rotor, stress analysis is the key issue for mechanical robustness of HSPMMs. The most important issue is how to obtain the exact value of stress in all rotor parts. Then, the maximum stress induced in each component of the rotor should be ensured within the material strength under all operating speed and temperature, especially for PMs. In addition, the contact pressure pointing to the inner side should always exist so that the electromagnetic torque can be transferred to the shaft. These two conditions are fundamental requirements for the safe running of high-speed PM machines.

The methods for stress calculation can be classified into analytical and numerical ones. Several papers on the analytical calculation of rotor stress can be found [BIN06], [WAN07], [BOR10], [BUR17]. [BIN06] proposed a simplified analytical model for stress calculation with the hypothesis that the rotor is strictly rotational symmetry. In [WAN07] and [BOR10], the displacement technique was adopted for the stress calculation of the HSPMM with the nonmagnetic alloy sleeve. In [BUR17], a 3D analytical model considering the axial stress was established for both solid and hollow magnet rotors in the plane strain condition. Although all these analytical solutions can provide a fundamental insight from the stress generation to reduction, as pointed out in [BIN06], the non-linear factor such as geometry discontinuity and edging effect cannot be considered in the analytical model. A derivation can still be generated in the analytical models. Hence, in order to obtain the exact value of rotor stress, 2D or 3D FEA are more widely adopted in the calculation of rotor stress with complicated structure or other non-linear factors. In Chapter 5, the limitation of analytical calculation will also be highlighted.

Another important issue which needs to be considered is the localized rotor stress occurring at the magnet edges. In [BIN06], it is pointed out that the inter-pole should be avoided due to

the presence of concentrated sleeve stress which may degenerate the life of sleeves as shown in Fig.1.33 (a). Hence, the final design eliminates the inter-pole gap in order to ensure an evenly distributed sleeve stress, as shown in Fig.1.33 (b). However, the main issue for this rotor configuration lies in the non-sinusoidal air gap flux which will yield many parasitic effects such as extra current harmonics and rotor loss. Thus, in [ZHA15], in order to obtain the sinusoidal air gap field as well as the elimination of concentrated stress, the inter-pole gap is filled with pole fillers made of non-magnetic material with similar Young's modulus and coefficient of thermal expansion (CTE) with the permanent magnet.

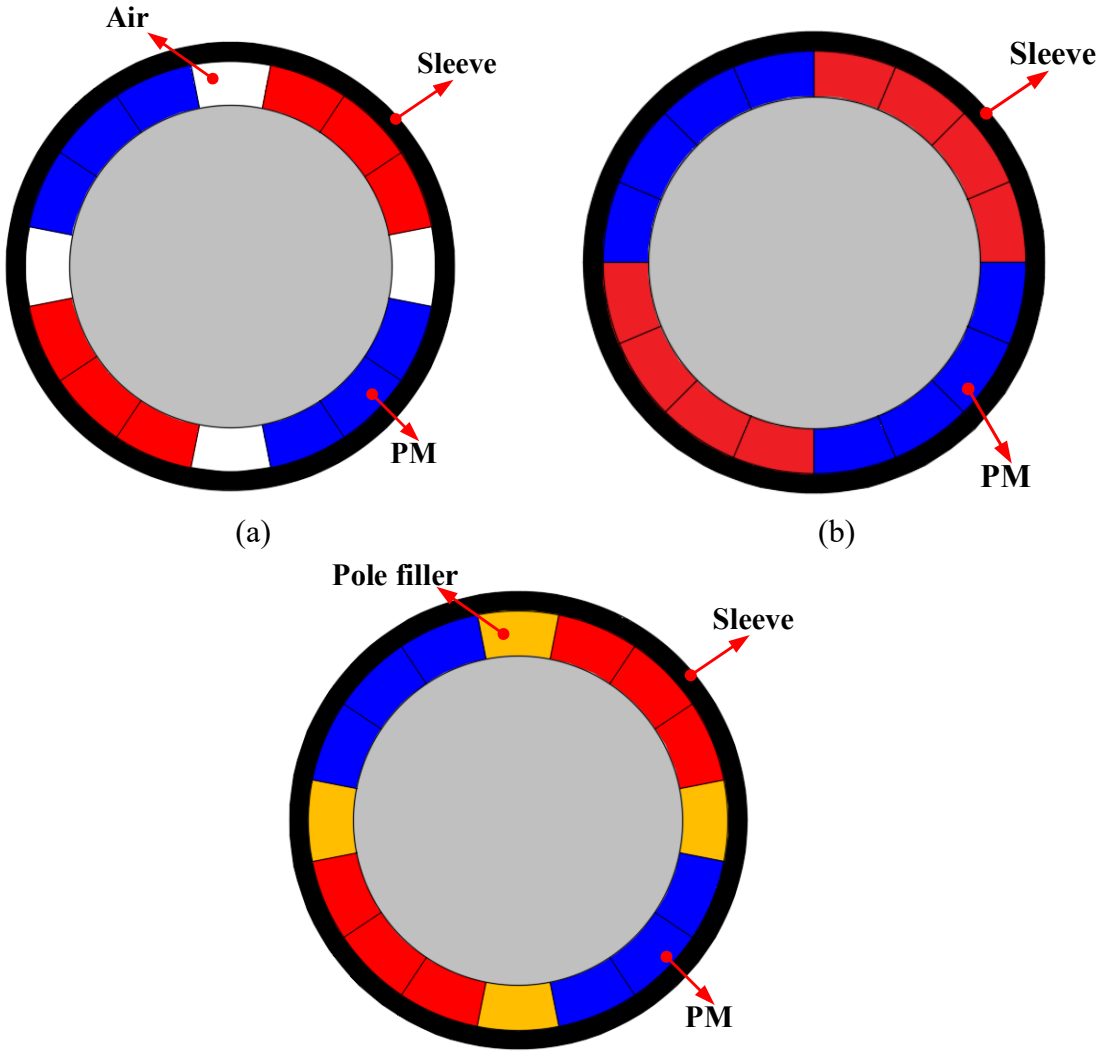

Fig.1.33. Different rotor configurations in HSPMMs. (a) Rotor with inter-pole [BIN06]. (b) Rotor without inter-pole. [BIN06]. (c) Rotor with inter-pole fillers [ZHA15].

1.4.2 Rotor Dynamics

For low-speed electrical machines, the rotor dynamics are normally not an issue as the operating speed range is far away from the critical speeds. However, for high speed machines, the rotor dynamics analysis plays a pivotal role for the safe operating of rotors. In fact, HSPMMs normally consist of the magnets and a retaining sleeve. These parts may aggravate the rotor dynamic performance since they increase the rotor mass whilst making no contribution to the rotor robustness.

The most common analysis methods that are used in rotor dynamics can be divided into two kinds: the so-called transfer matrix method and the finite-element method (FEM) as shown in Fig.1.34. The former has a small amount of calculation, but at the cost of large error and possibility of lost root phenomenon, with the development of modern computing technology, the analytical method has already lost its value. On the other hand, in the last two decades, there are many publications in which FEM is successfully applied in the area of rotor dynamics as in [ZHU02], [ZWY05], [GER09], [HWA16].

It is reported that three different bending and vibration modes exist for the rotor which will occur at three specific natural frequencies. In [ZHU02], the analytical equations for the three natural frequencies is given as

$$w_n = a_n \sqrt{\frac{EI}{\mu_1 l^4}} \tag{1.2}$$

where E represents the Young's Modulus, I denote the inertia of rotor, μ_1 is the mass in per unit length, l denotes the rotor axial length, and a_n is the constant obtained by the Rayleigh method, which is related with the boundary conditions. It is obvious that the axial length reduces the natural frequency significantly. Hence, the non-overlapping winding is more preferred for the ultra-high-speed application.

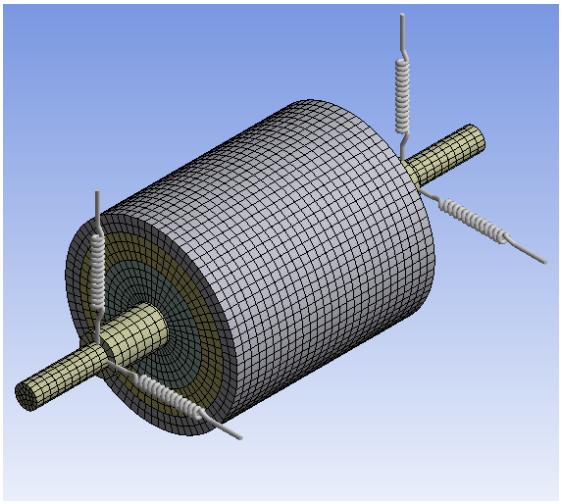

Fig.1.34. 3-D beam FE model for rotor dynamic analysis [ZHU02].

1.4.3 Aerodynamics Loss

For high speed electrical machines, the friction forces due to high speed rotation become strong enough to produce significant mechanical loss which cannot be ignored. Aerodynamics loss is defined as the losses produced by the viscous shear stress and the aerodynamic effects in the end windings surrounding areas. It can be the dominant loss for HSPMM operating in ultra-high-speed applications [ZWY10], [PFI10]. The general estimation of aerodynamics loss at the radial surface of the rotor can be written as [GER09]:

$$P_w = \pi C_f \rho r^4 \omega^3 L \tag{1.3}$$

where C_f denotes the coefficient of rotor skin friction, which can be calibrated from the experimental data. However, due to the existence of turbulence in the air flow and the axial cooling flow, the accuracy of (1.3) cannot be assured.

The recent improvements in numerical computing such as Computational Fluid Dynamics (CFD) allowed the analysis of complex airflow to be easier to perform.

1.5 Research Scope and Major Contributions

1.5.1 Outline of Thesis

In this thesis, the analysis of high-speed PM machine with particular focus on both the electromagnetic and mechanical issues is conducted. For the electromagnetic issue, the rotor eddy current losses of the 4-pole HSPMM with alternate stator configurations are analysed in depth. In addition, the existence criterion of unbalanced magnetic force in PM machine with an odd number of stator slots is determined. The influence of slot and pole number combination on the unbalanced magnetic force is investigated. As for the mechanical issue, the rotor mechanical stress considering the PM segmentation is analyzed. Following from this, the worst-case operating scenario is determined. Finally, the influence of the mechanical issue on the electromagnetic one is discussed with the focus on the optimal split ratio of rotor outer diameter to stator outer diameter, considering mechanical stress constraints. This thesis is organized as follows. Fig.1.35 shows the structure of the thesis.

Chapter 1 reviews alternate high-speed machine technologies, covering both electromagnetic and mechanical issues.

Chapter 2 investigates the optimal split ratio of HSPMM with consideration of stator iron loss and rotor mechanical stress constraints.

Chapter 3 investigates the rotor eddy current loss in the 4-pole HSPMM with alternate stator configurations. The contribution of both the armature reaction harmonics and the PM harmonics as well as the slotting effect are quantified.

Chapter 4 investigates the unbalanced magnetic force in PM machines with an odd number of stator slots. The existence criterion of UMF in PM machines is determined. The influence of slot and pole number combinations on UMF is discussed in detail.

Chapter 5 investigates the rotor mechanical stress of HSPMM with the consideration of PM segmentation. In addition, a novel design methodology of HSPMM considering both electromagnetic and mechanical issues is proposed.

Chapter 6 makes a conclusion of the work in this thesis and discusses the future work.

APPENDIX A shows the engineering drawings of the four prototyped PM machines.

APPENDIX B lists the publications in the PhD study.

1.5.2 Major Contributions of the Thesis

The major contributions of this thesis include:

1) The influence of mechanical constraints on the electromagnetic issue of HSPMM is firstly clarified. A novel design methodology considering both the electromagnetic issue and mechanical issue is proposed. The optimal split ratio of HSPMM considering the stator iron loss and the rotor mechanical stress constraints is determined.

2) Both the armature reaction and PM field induced rotor magnet losses in HSPMM are determined. The contribution of each harmonic due to armature reaction, PM field and slotting effect is quantified. The impact of the winding configuration on the resultant MMF harmonics and rotor magnet loss is discussed in depth.

3) The existence criterion of PM machine with an odd number of stator slots is clarified. In addition, the UMF in PM machines with both an odd number of stator slot and lower pole number is investigated.

4) The rotor mechanical stress is firstly analysed with the consideration of PM segmentation. Rotor stress concentration due to PM segmentation is firstly revealed. The corresponding worst-case operating scenarios and influential factors are then summarized.

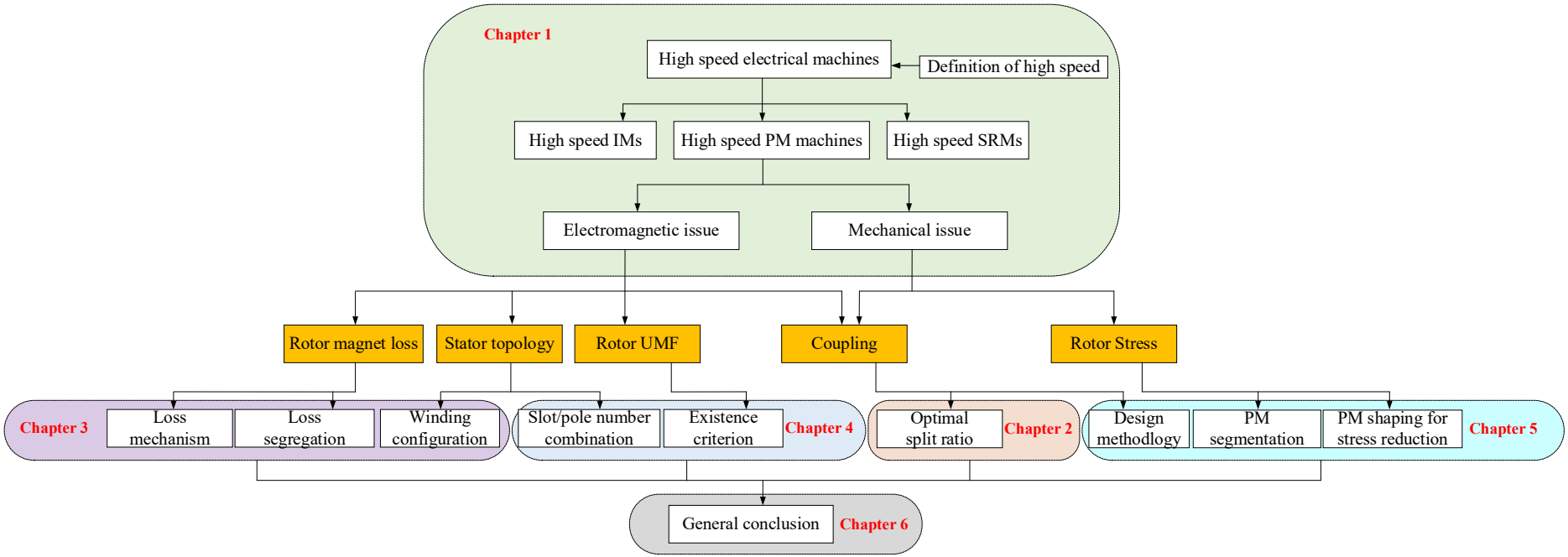

Fig.1.35. Structure of thesis.

Chapter 2 Rotor Split Ratio Optimization for High Speed PM Machines with Consideration of Stator Iron Loss and Mechanical Stress Constraints

The split ratio, i.e. the ratio of rotor outer diameter to stator outer diameter, is one of the most vital design parameters for PM machines due to its significant impact on the machine torque or power density. However, it has been optimized analytically in existing papers with due account only for the stator copper loss, which is reasonable for low to medium speed PM machines. For high speed PM machines (HSPMM), the ignorance of stator iron loss and the mechanical stress on the rotor will lead to a deviation of optimal split ratio and actual torque capability. In this chapter, the optimal split ratio of HSPMM is investigated analytically with consideration of the stator iron loss as well as the rotor mechanical stress. The influence of design parameters such as air gap length and rotor pole pairs on the optimal split ratio is elaborated. Both the analytical and finite element analysis reveal that the optimal split ratio for HSPMM will be significantly reduced when stator iron loss and mechanical constraints are considered.

This chapter is based on the author's own papers [WAN18], [FEN19], [XUE18b].

2.1 Introduction

High-speed electrical machines have been widely used in a variety of applications including domestic appliances, electrical spindles, turbochargers, electrical turbo-compounding systems, and have been attracting increased interest from both industry and academia, particularly in the past two decades [ANC10], [GUR13], [BIA04], [BOR10].

As a competent candidate, the high-speed permanent magnet (PM) machines (HSPMM) are a very promising design alternative for high-speed applications due to high power density as well as high efficiency and compactness compared with other types of electrical machines such as induction machines and switched reluctance machines [ZHU97], [BIN07], [LUO09], [KOL09], [GER14].

However, the inherent high speed and induced high frequency will yield a huge centrifugal force and a significant electromagnetic loss in the rotor and stator. These two limitations

impose a great constraint on the capability of power density and efficiency [BIA04], [YAM13]. Under high-speed operation, the rotor components will suffer huge centrifugal stress, making the magnet retaining extremely important [BIN06]. The centrifugal stress is influenced by a few factors, including the rotor diameter. On the other hand, the split ratio, the rotor outer diameter to the stator outer diameter, is also an important design parameter for any PM machine. It has a great impact on the torque/power capability and efficiency for the given frame size. [CHA94] derived a simple analytical expression of optimum split ratio for maximum torque density. In [PAN06], the optimal split ratio of both brushless AC and DC motors with either overlapping or non-overlapping windings were investigated. In addition, the influences of air gap flux density waveforms, stator tooth-tips as well as the end-winding on the optimal split ratio were discussed. In [WU10a], the optimal split ratio as well as the flux density ratio were analyzed both individually and globally in a fractional-slot IPM machine.

For HSPMM, the design of the split ratio is even more important. Not only is the torque density of HSPMM significantly influenced by this parameter, but also the mechanical stress of the rotor and stator iron loss are greatly impacted by this ratio. Hence, it is necessary to investigate the optimal split ratio for HSPMM. In [EDE01], the stator iron loss was considered in the analysis of optimal split ratio of a high-speed PM machine. It was found that the optimal split ratio is slightly reduced compared to that with a fixed copper loss only. [REI13] introduced the current density as the local thermal constraint which is reasonable only when considering the local overheat in stator end-windings [BOG09]. In [FAN16], the thermal network was adopted in order to obtain the winding temperature rise of HSPMM directly and a more accurate value of optimal split ratio could be acquired. However, compared with the stator temperature, the temperature rise in the rotor should be more of a concern for HSPMM since the permanent magnets are vulnerable to the temperature rise resulting from the induced PM eddy current loss.

In summary, in existing papers, the split ratio of HSPMM has been optimized with the consideration of thermal constraints only. The mechanical constraints, including the stress limit and rotor dynamics issues are ignored, leading to the deviation of the optimal split ratio and actual torque/power capability. In this paper, the optimal split ratio for HSPMM is obtained with the consideration of the mechanical constraints, with particular focus on the rotor stress. The stator iron loss is also considered. The impact of the sleeve material and maximum operating speed on the optimal split ratio is elaborated. In addition, the influence of the flux

density ratio, i.e. the ratio of stator lamination flux density to airgap flux density on the optimal split ratio is analyzed.

The chapter is organized as follows. In section 2.2, the optimal split ratio for maximum torque is investigated with due account of copper loss constraints only. Then, the influences of stator iron loss on optimal split ratio as well as actual maximum torque are analyzed in section 2.3 which further clarifies why and how the optimal split ratio for actual maximum torque will change when both copper loss and stator iron loss are taken into consideration. Section 2.4 aims to illustrate how the mechanical stress constraints including the tangential and radial stress limitation make an impact on the actual optimal split ratio. Finally, in section 2.5, both the rotor stress constraints and the stator iron loss are considered simultaneously in the determination of optimal split ratio of HSPMM with the conclusions in section 2.6.

2.2 Optimal Split Ratio Accounting for Copper Loss Only

Fig.2.1 shows the structure of a typical HSPMM with 6s/4p-non-overlapping winding configuration. The permanent magnets are protected by the retaining sleeve in order to withstand the huge stress resulting from high speed. The specifications of the machine are given in Table 2.1. Generally, when the air gap flux distribution is uniform, the armature reaction is ignored and the phase back-EMF is in phase with the current, the electromagnetic torque of a three-phase brushless PM motor can be expressed as [PAN06], [LI18]:

$$T = \frac{3\sqrt{2}}{2} D_s l_a N_w k_w I_a B_g \tag{2.1}$$

where D_s is the stator bore diameter. l_a is the active stack length and N_w represents the serial turns of each phase. k_w denotes the winding factor. I_a is the RMS of the phase current and B_g is the air gap flux density. It should be noted that the split ratio for HSPMM in this chapter refers to the ratio of rotor outer diameter to stator outer diameter which is different from definitions for low-speed electrical machines. The influence of air gap length on optimal split ratio for HSPMM is significant and will be addressed in this section. Hence, λ denotes the split ratio which is defined as:

$$\lambda = \frac{D_r}{D_o} \tag{2.2}$$

where D_r is the rotor outer diameter and D_o is the stator outer diameter. The stator bore diameter can be expressed as:

$$D_s = \lambda D_o + 2g \tag{2.3}$$

where g denotes the total air gap length. The torque can be further given as [PAN06]:

$$T = \frac{3\sqrt{2}}{2}\sqrt{A_s}(\lambda D_o + 2g)\sqrt{\frac{P_{cu}k_s N_s l_a}{36\rho_{cu}}}k_w B_g \tag{2.4}$$

where A_s is the slot area and k_s is the slot packing factor. N_s is the slot number and ρ_{cu} is the resistivity of copper. On the other hand, ignoring the effect of saturation, flux-leakage as well as slotting effect, the air gap flux density B_g can be accordingly expressed as [LIP11]:

$$B_g = \frac{h_m}{h_m + g}B_r \tag{2.5}$$

where h_m is the PM thickness. When (2.5) is substituted into (2.4), the electromagnetic torque can be derived as:

$$T = \frac{3\sqrt{2}}{2}\sqrt{A_s}(\lambda D_o + 2g)\frac{h_m}{h_m + g}B_r k_w\sqrt{\frac{P_{cu}k_s N_s l_a}{36\rho_{cu}}} \tag{2.6}$$

where

$$A_s = \frac{\pi D_o^2}{4N_s}\left\{\begin{array}{l}(\lambda + \frac{2g}{D_o})^2\left[\frac{\pi}{3p}(\frac{\pi}{3p}+2)\gamma^2 + 2\gamma - 1\right] \\ -2(\lambda + \frac{2g}{D_o})(\frac{\pi}{3p}+1)\gamma + 1\end{array}\right\} \tag{2.7}$$

where p is the rotor pole pairs and N_s denotes the stator slot number and γ represents the flux density ratio which is defined as:

$$\gamma = \frac{B_g}{B_{\max}} \tag{2.8}$$

where B_{max} is the maximum flux density in the stator iron. Hence, the electromagnetic torque with respect to the split ratio can be expressed as:

$$T \propto f(\lambda) = \sqrt{A_s}(D_o\lambda + 2g) \tag{2.9}$$

The optimal split ratio for maximum torque can be obtained by solving the following differential equation:

$$\frac{\partial f(\lambda)}{\partial \lambda} = 0 \tag{2.10}$$

The optimal split ratio can be given as:

$$\lambda_p = \frac{b_p - \sqrt{b_p{}^2 - 4a_p}}{a_p} - \frac{2g}{D_o} \tag{2.11}$$

where

$$a_p = 8\left[\frac{k\pi}{p}\left(\frac{k\pi}{p} + 2\right)\gamma^2 + 2\gamma - 1\right] \tag{2.12}$$

$$b_p = 6\left(\frac{k\pi}{p} + 1\right)\gamma \tag{2.13}$$

$k = \frac{1}{3}$ for motors with stator non-overlapping winding (2.14)

While the split ratio increases, the tooth width and yoke thickness will become larger correspondingly when the air gap length and the flux density ratio are confirmed. The resultant slot area will decrease with the increase of split ratio. Hence, there will always exist an optimal split ratio at which the electromagnetic torque reaches maximum. The minimum air gap length (g=2mm) is obtained with the usage of the empirical equation in [PYR08]. A suitable value for the length of the air gap of an inverter fed, high-speed machine (the peripheral speed of the rotor>100 m/s), can be calculated as:

$$\delta = 0.001 + \frac{D_r}{0.07} + \frac{v}{400} \tag{2.15}$$

where D_r denotes the rotor outer diameter and v denotes the peripheral speed of the rotor.

The copper loss is fixed to ensure the same thermal performance. As for the value of copper loss, when the machine frame size is given, the total heat transferred through the external surface depends on the specific cooling type. This heat source, namely electromagnetic loss,

can be written as [BIA04]:

$$P_{\text{limit}} = h\upsilon_m \pi D_o l_a \tag{2.16}$$

where h denotes the thermal heat transfer coefficient and υ_{m} denotes the maximum allowed temperature corresponding to specific insulation level.

On the other hand, the range of feasible split ratio is significantly limited by the geometrical restrictions. The maximum split ratio depends on the air gap length and flux density ratio when the stator outer diameter is given.

Fig.2.2 shows the variation of torque with split ratio and air gap length. The optimal split ratio for maximum torque is significantly reduced with the increase of flux density ratio. This can be attributed to the increase of stator teeth and back iron due to larger flux density ratio. Thus, the slot area is accordingly reduced. The split ratio is then reduced to make up for the shrink of space so that the copper loss can be constant.

From (2.11), it is obvious that the optimal split ratio is also influenced by the air gap length. Fig.2.3 illustrates the variation of torque versus split ratio with respect to different air gap length. The optimal split ratio will be significantly reduced with the increase of air gap length when the flux density ratio is constant. The slot area is reduced with the increase of air gap length. The split ratio will accordingly be reduced in order to keep the copper loss constant. Fig.2.4 shows the variation of analytical and FE calculated electromagnetic torques with split ratio, for the machine having a 6s/4p (N_s/2p) with a non-overlapping winding. It should be noted that the stator and rotor iron permeability is assumed infinite and the flux leakage is ignored in the analytical results. The analytical result agrees well with the FE predicted one.

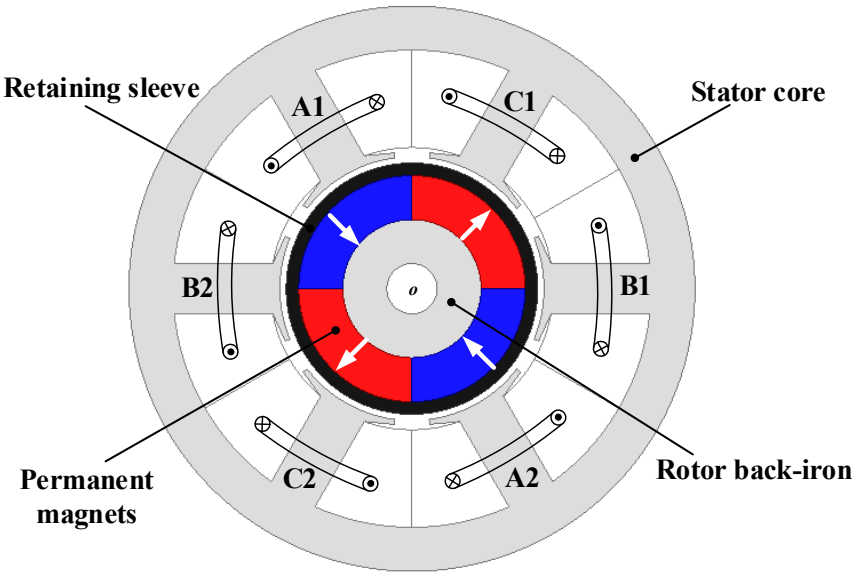

Fig.2.1. Cross-section of a typical HSPMM.

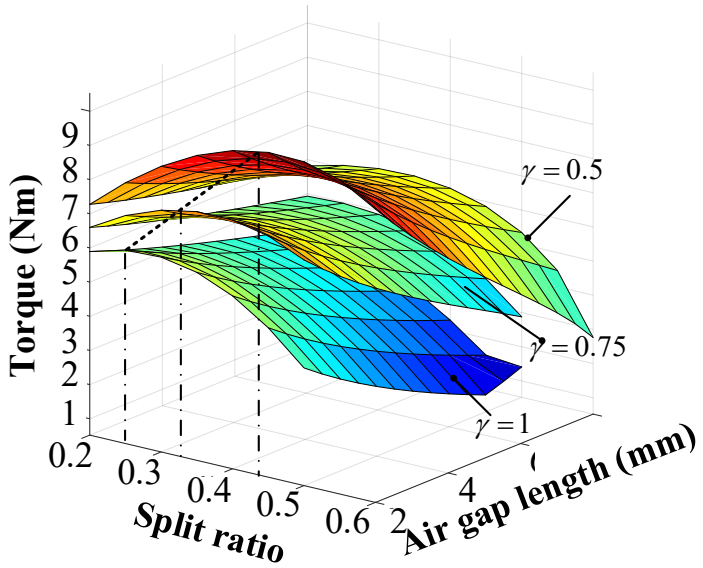

Fig.2.2. Electromagnetic torque versus split ratio and air gap length with respect to different flux density ratio (p=2, Ns=6, Do=90mm, la=55mm, copper loss=100W γ=0.5).

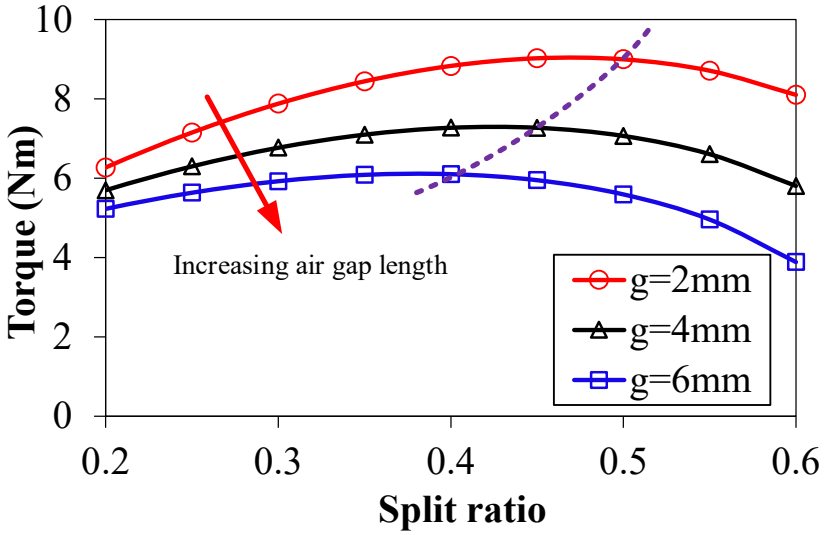

Fig.2.3. Variation of electromagnetic torque with split ratio for different air gap length.

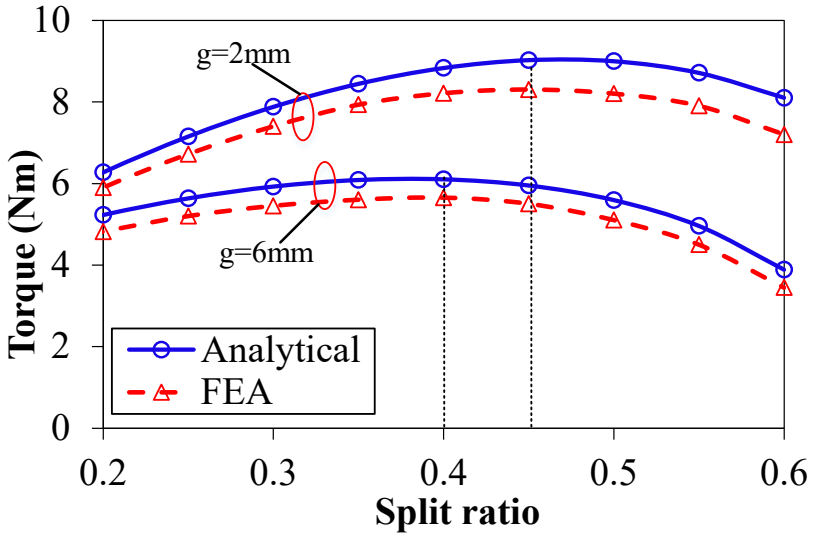

Fig.2.4. Analytically and FE predicted variations of torque with split ratio and air gap length.

Table 2.1 Specifications of High-speed PM Machine

Parameters		Parameters	
Stator outer diameter (mm)	90	Stator yoke thickness (mm)	4.4
Stator bore diameter (mm)	39.5	Stator teeth width (mm)	8.8
Split ratio	0.35	Packing factor	0.6
Rotor outer diameter (mm)	31.5	Stack axial length (mm)	55
Sleeve thickness (mm)	2	Number of turns per phase	20
PM thickness (mm)	8		

2.3 Optimal Split Ratio Accounting for Copper Loss and Stator Iron Loss

Compared with low speed PM machines, the stator iron loss of HSPMM cannot be ignored due to the inherent high frequency. This iron loss can even be dominant for HSPMM operating at ultra-high speed (>100krpm). In this section, the optimal split ratio of HSPMM considering copper loss and the stator iron loss will be investigated in detail.

2.3.1 Optimal Split Ratio Considering Stator Iron Loss

Generally, a two-term iron loss model can be adopted for calculating the iron losses with the acceptable accuracy, while the classic loss and excess loss in the three-term model are combined into a global eddy current loss [BOG03], [LIN04], [ION07]. This model can be expressed as:

$$W_{Fe} = k_h f {B_{Fe}}^2 + k_e f^2 {B_{Fe}}^2 \tag{2.17}$$

where W_{Fe} denotes iron loss in watts per kilogram, k_e and k_h represent the hysteresis coefficient and eddy current coefficient, respectively. f denotes the frequency of magnetic field. B_{Fe} denotes the maximum flux density in the stator iron.

On the other hand, the stator iron flux density can be expressed as:

$$B_g = \gamma B_{Fe} \tag{2.18}$$

where γ denotes the flux density ratio and B_g denotes the air gap flux density. Hence, the stator iron loss can be further written as:

$$P_{Fe} = W_{Fe} m_{Fe} = B_g^2 \gamma^{-2} \rho_{Fe} A_{Fe} l_a (k_h f + k_e f^2) \tag{2.19}$$

where ρ_{Fe} denotes the mass density of stator iron, A_{Fe} denotes the stator lamination area and l_a represents the stack length.

On the other hand, in HSPMM, the stator electromagnetic loss mainly consists of stator iron loss and winding copper loss. Thus, when the cooling type, stator outer diameter and stack length are given, the allowable stator copper loss can be expressed as:

$$P_{cu} = P_{\text{limit}} - P_{Fe} = P_{\text{limit}} - K_{Fe} A_{Fe} \tag{2.20}$$

Where

$$K_{Fe} = B_g^2 \gamma^{-2} \rho_{Fe} l_a (k_h f + k_e f^2) \tag{2.21}$$

It can be seen that both stator iron loss and copper loss are closely related with the stator lamination area A_{Fe} which is determined by the split ratio, the stator teeth width and the back-iron thickness. Fig.2.5 illustrates the variation of stator iron loss and copper loss of a typical HSPMM with 6s/4p-Non-overlapping winding configuration. The stator iron loss becomes larger with the increase of split ratio before reaching the maximum value. The same trend is observed with the variation of iron area A_{Fe} when the stator flux density is constant. The stator iron area increases at the initial stage due to the wider teeth and yoke and then decreases as a result of smaller teeth height.

On the other hand, the stator copper loss is observed with the opposite trend to the stator iron loss when the total stator loss is fixed. The copper loss decreases with the increase of split ratio until reaching the minimum value. After this specific split ratio, the stator copper loss starts to increase mildly.

In summary, when the stator iron loss is taken into consideration for HSPMM, the copper loss varies significantly with the split ratio instead of being constant. Therefore, the ampere turns will be directly affected due to the variation of copper loss. Hence, the variation of electromagnetic torque with split ratio will be eventually altered.

The torque expression for a three-phase brushless PM motor is derived in (2.4). When (2.20) and (2.21) are substituted into (2.4), the electromagnetic torque can be further expressed as:

$$T = \frac{3\sqrt{2}}{2} k_w B_g \sqrt{\frac{k_s N_s l_a}{36 \rho_{cu}}} f(\lambda) \tag{2.22}$$

$$f(\lambda) = (D_o \lambda + 2g) \sqrt{A_s (p_{\text{limit}} - K_{Fe} A_{Fe})} \tag{2.23}$$

In (2.23), both A_s and A_{Fe} are functions of split ratio which have already been derived in [PAN06]. Hence, the optimal split ratio for maximum electromagnetic torque considering stator iron loss can be obtained by solving the following differential as:

$$\frac{\partial f(\lambda)}{\partial \lambda} = 0 \tag{2.24}$$

Fig.2.6 illustrates the electromagnetic torque versus split ratio with and without consideration of stator iron loss. It can be seen that the torque would be considerably reduced when the iron loss is taken into account. This should be attributed to the reduced copper loss thus electrical loading at each split ratio. In addition, the optimal split ratio for maximum electromagnetic torque has also been reduced due to the decreasing copper loss with the increasing split ratio before reaching minimum. The optimal split ratio has to be reduced in order to make the $f(\lambda)$ maximum.

It is worth mentioning that torque variation range is relatively smaller when considering the stator iron loss. The electromagnetic torque decreases slowly after reaching the maximum value. As mentioned before, the copper loss turns to increase mildly which makes a compensation for the torque by increasing the electrical loading. Therefore, the electromagnetic torque will not drop sharply compared with that when only the copper loss is considered. As shown in Fig.2.6, although there is a slight difference between the analytical and FE predicted torques, the optimal split ratios have a good agreement which verifies the validity of previous analytical analysis.

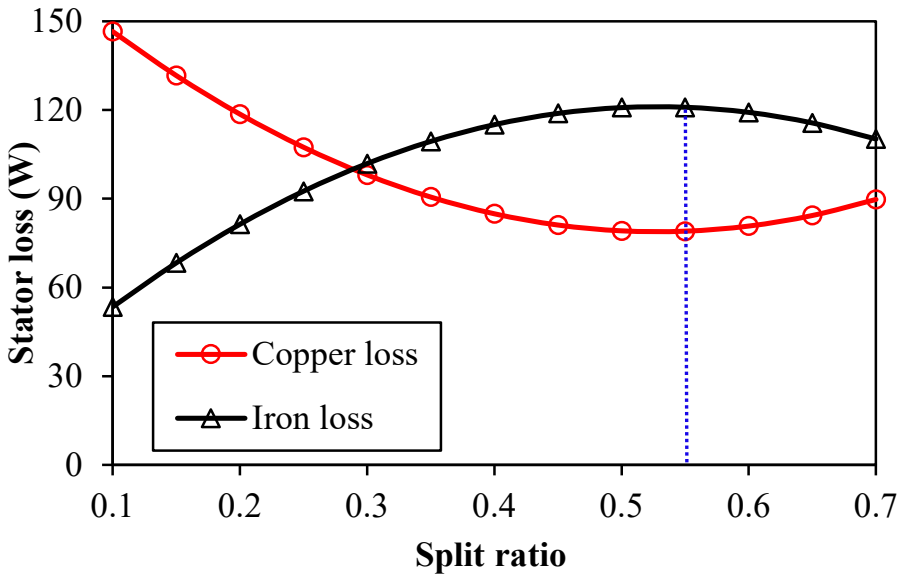

Fig.2.5. Variation of stator loss with split ratio (γ=0.5, f=2166Hz, B_g =0.85T).

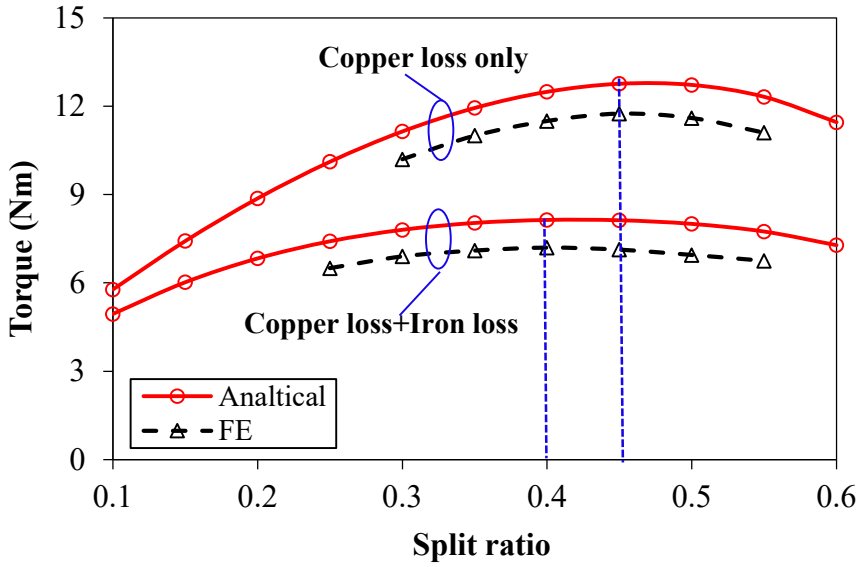

Fig.2.6. Variation of electromagnetic torque with split ratio (γ=0.5, f=2166Hz, B_g =0.85T).

2.3.2 Influence of Design Parameters on Optimal Split Ratio

As mentioned in Section 2.3.1, the optimal split ratio considering stator iron loss is closely related with the allowable copper loss variation trend versus split ratio. On the other hand, the design parameters affecting the variation of iron loss will pose the opposite impact on the allowable copper loss when the stator loss is fixed with certain cooling method. In this section, the influence of these design parameters such as air gap length as well as rotor pole pairs on the optimal split ratio will be elaborated.

A. Air gap length

For HSPMM, the air gap length is relatively larger due to the presence of retaining sleeve. When the air gap length increases, the stator iron loss will be significantly decreased due to the reduced stator flux density. Thus, the allowable copper loss will be inversely increased as shown Fig.2.7 (b). However, it changes little with the variation of split ratio when the air gap length becomes larger. This corresponds to the variation of stator iron loss with split ratio. As can be seen from (2.19), the stator iron loss depends on the stator flux density and the stator iron area when other parameters are constant. With the increase of air gap length, the stator iron loss increases more slowly due to the reduced stator flux density.

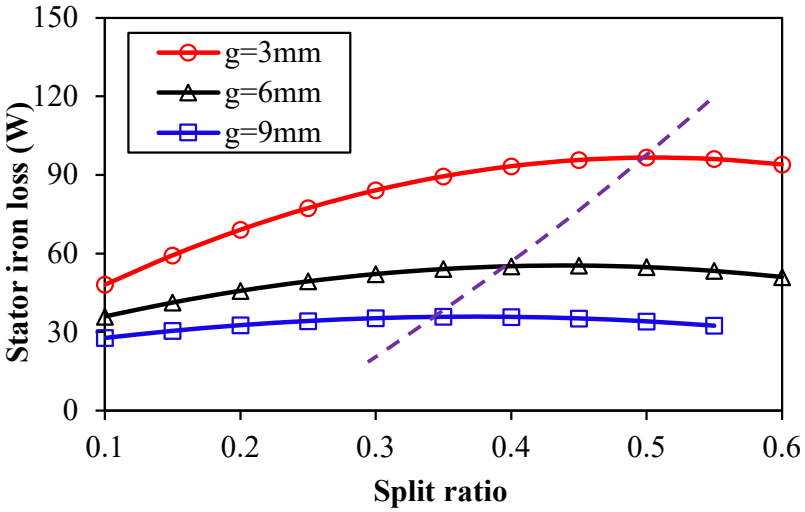

(a)

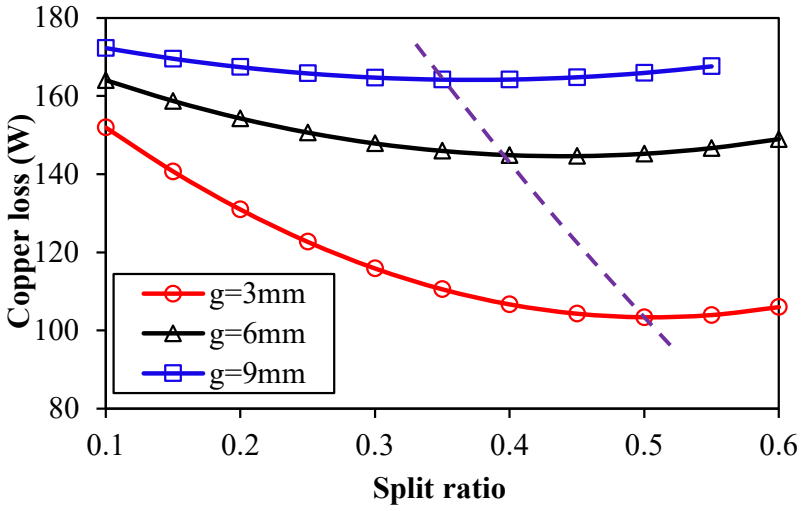

(b)

Fig. 2.7. Variation of stator loss with split ratio at different air gap length (γ=0.5, *f*=2166Hz). (a) Stator iron loss. (b) Copper loss.

Thus, with the increase of air gap length, the difference between the optimal split ratios with and without consideration of stator iron loss decrease. As shown in Fig.2.8 (b), when the air gap length reaches 9mm, the optimal split ratio almost remains constant as the copper loss changes little over the whole split ratio variation range.

However, the optimum split ratio of HSPMM considering stator iron loss will still decrease with increase of air gap length as shown in Fig.2.9. This can be attributed to the reduced slot area with the increasing air gap length. The optimum split ratio has to be reduced so that the total electromagnetic loss remains constant when the air gap length is relatively large.

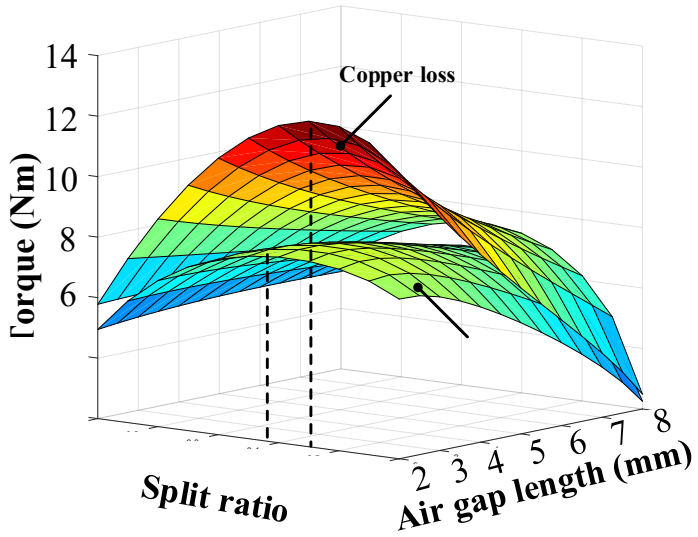

(a)

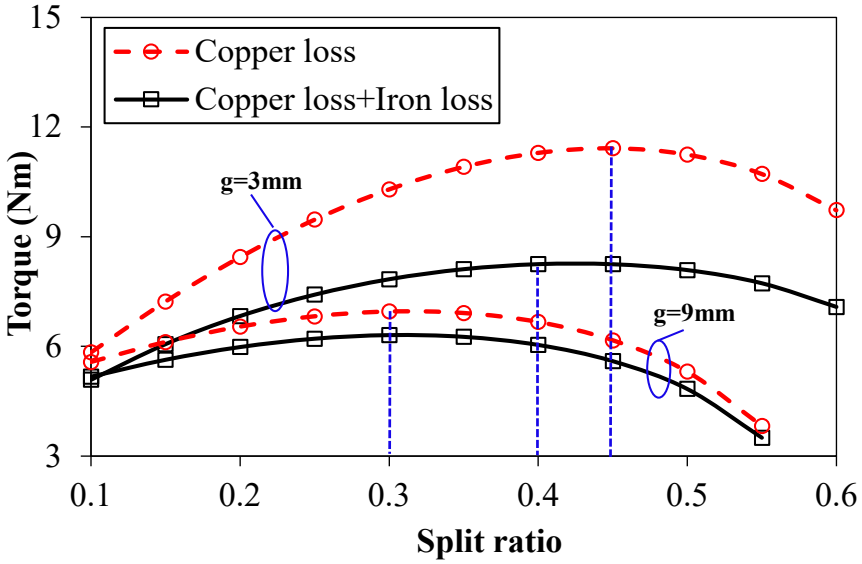

(b)

Fig.2.8. Variation of electromagnetic torque with split ratio at different air gap lengths (γ=0.5, *f*=2166Hz). (a) Variation of torque with split ratio and air gap length. (b) Variation of torque with split ratio.

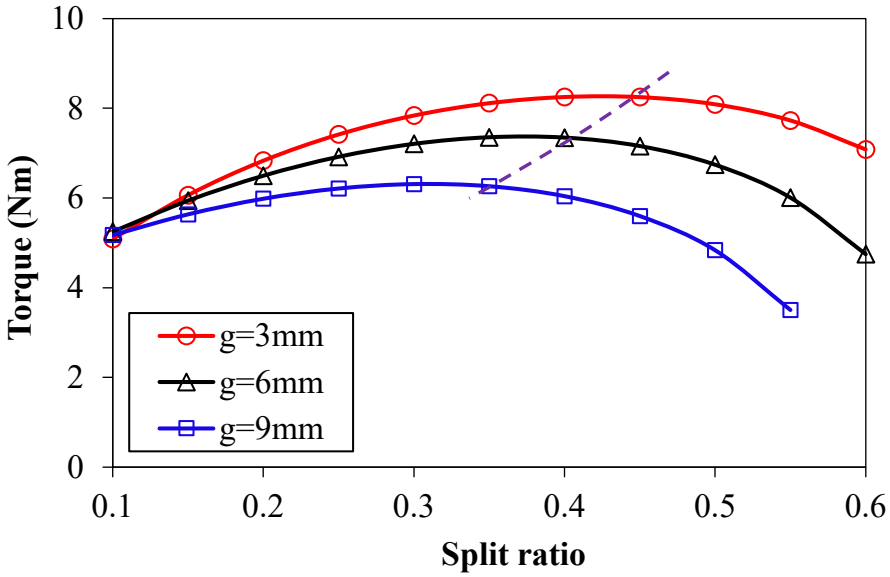

Fig.2.9. Variation of electromagnetic torque with split ratio considering stator copper loss and iron loss (γ=0.5, *f*=2166Hz).

B. Flux density ratio

The flux ratio is defined as the ratio between the stator iron flux density and air gap flux density. Hence, the flux ratio has a great impact on the stator iron loss thus the optimum split ratio when the air gap flux density is fixed. In this section，the influence of flux ratio on the optimum split ratio considering stator iron loss will be investigated.

As is shown in Fig.2.10, the stator loss will be significantly increased when the flux ratio gets larger. Accordingly, the allowable copper loss with the larger flux ratio will drop sharply to a minimum value and then start to rise. Hence, the optimal split ratio has to be reduced in order to make up for the reduction of allowable electrical loading, as shown in Fig.2.11. On the other hand, when the flux ratio is relatively small (0.25), the allowable copper loss decreases slowly with the rise of split ratio. Hence, in this case, the optimal split ratio almost remains constant when considering the stator iron loss.

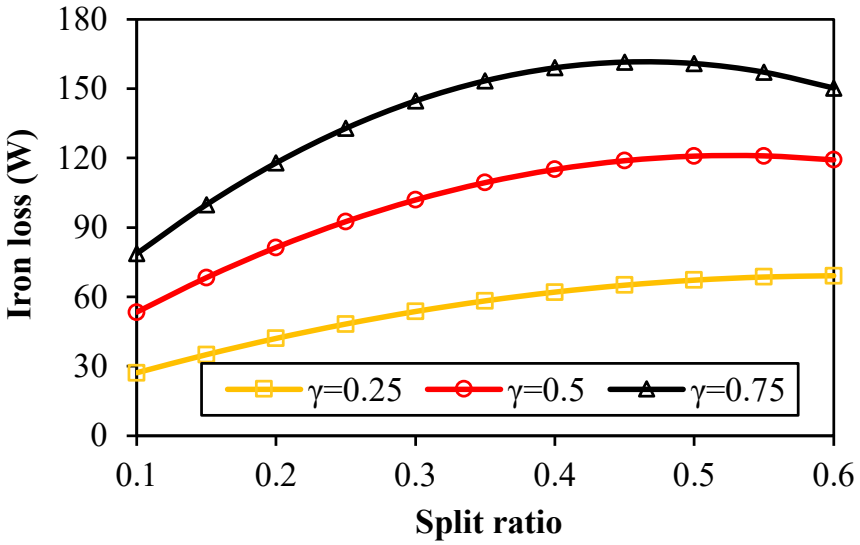

(a)

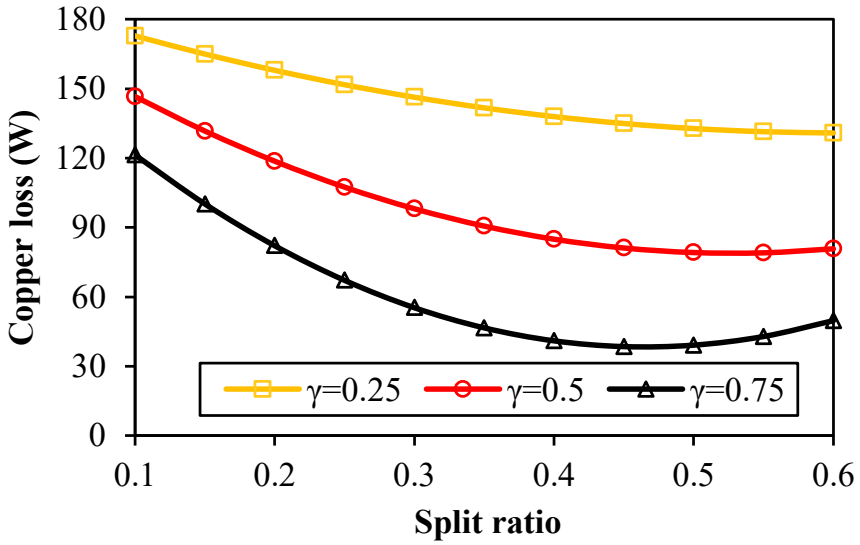

(b)

Fig.2.10. Variation of electromagnetic loss with split ratio at different flux density ratios (B_g =0.85T, f=2166Hz). (a) Stator iron loss. (b) Copper loss.

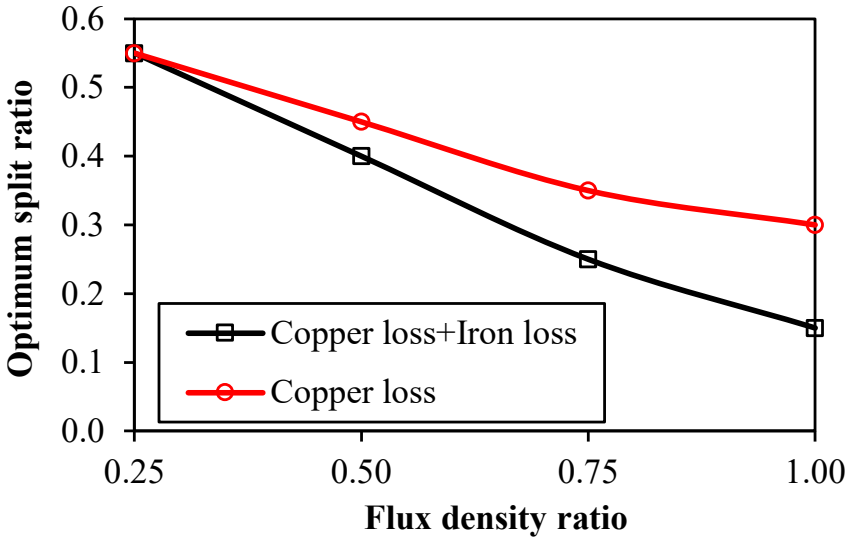

Fig.2.11. Variation of optimal split ratio with flux density ratios (B_g =0.85T, f=2166Hz).

C. Operating speed

It is obvious that the stator iron loss is significantly influenced by the operating speed. In this section, the impact of operating speed on the optimal split ratio of HSPMM is investigated. Fig.2.12 illustrates the variation of stator loss with split ratio at different operating speed. It can be seen that the operating speed exert similar effect on the stator loss compared with flux density ratio. The stator iron loss will rise rapidly to the maximum value and then decrease while the operating speed is relatively high. Thus, the allowable copper loss will drop sharply while the operating speed is large. Hence, the optimal split ratio will be reduced when the operating speed is increasing. On the other hand, when the operating speed is relatively low, the optimal split ratio remain constant compared with that without consideration of iron loss.

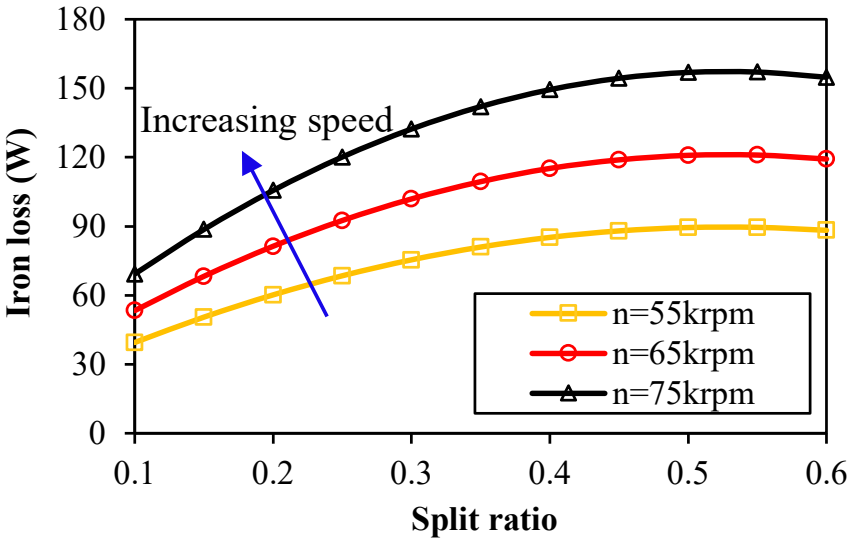

(a)

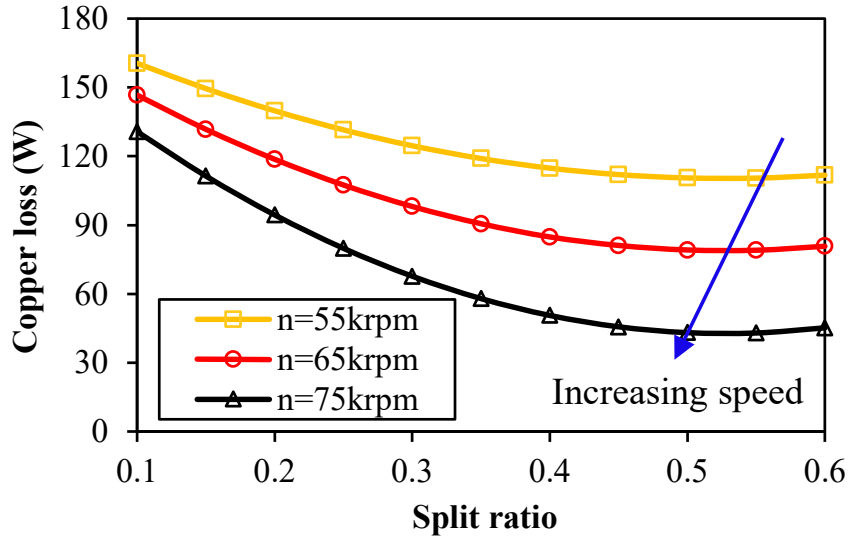

(b)

Fig.2.12. Variation of stator loss with split ratio at different operating speed (B_g =0.85T). (a) Stator iron loss. (b) Copper loss.

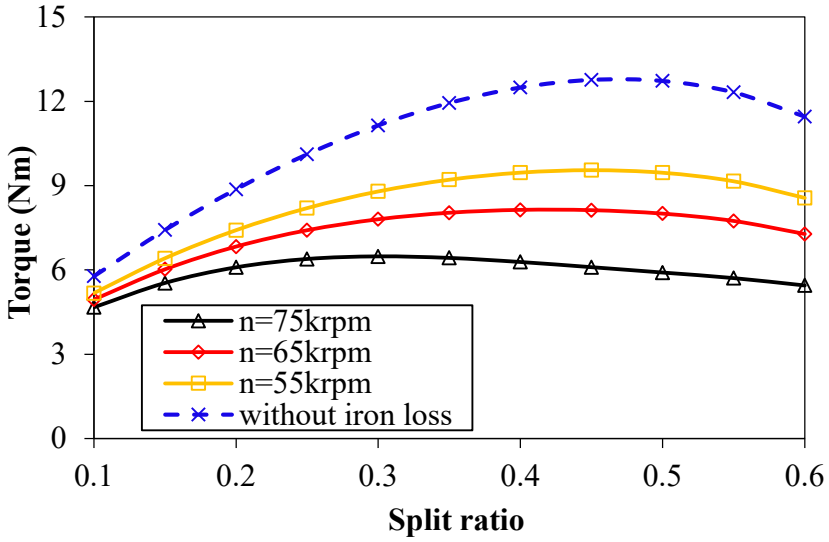

Fig.2.13. Variation of electromagnetic torque with split ratio at different speed (B_g =0.85T).

D. Rotor pole pairs

Compared with low-to-medium speed PM machines, the stator and rotor components of HSPMM, especially the permanent magnets are immersed in the high frequency variable magnetic field, yielding a significant amount of iron loss. A lower number of rotor pole pairs would not only contribute to the reduction of iron loss but also help to reduce switching loss in the inverters. Normally, the rotor pole pair of HSPMM is selected to be 1 or 2. In this section, the influence of rotor pole pairs of HSPMM on optimal split ratio is investigated.

Fig.2.14 illustrates the variation of stator loss with split ratio for the HSPMMs with 6s/4p-Non-overlapping and 6s/2p-Non-overallping configuration. It is shown that the iron loss of HSPMM with 6s/2p-Non-overlapping configuration will be much smaller than that of 6s/4p-Non-overlapping due to half of the fundamental frequency. Hence, the allowable copper loss will be larger when the total electromagnetic loss is fixed. In addition, due to the smaller fundamental frequency, the iron loss of HSPMM with 6s/2p-Non-overlapping increases more mildly than that with 6s/4p-Non-overlapping. Accordingly, the allowable copper loss decreases gently with the increase of split ratio. Hence, the optimal split ratio for HSPMM with 6s/2p-Non-overlapping winding remains almost constant when the stator iron loss is taken into consideration. As has been proved, when the stator copper loss is considered only, the optimal split ratio will be reduced when the rotor pole pair decreases from 2 to 1 due to yoke thickness increase [8]. This reduction will be smaller when the stator iron loss is taken into account as shown in Fig.2.15. In other words, the optimal split ratio for HSPMM with 6s/2p-Non-

overalpping is not as sensitive to the consideration of stator iron loss as 6s/4p-Non-overalpping configuration.

Although the allowable copper loss for 6s/2p-Non-overlapping is much larger, stator ampere turns are limited by the reduced slot area. More importantly, the winding factor of HSPMM with 6s/2p-Non-overlapping configuration is only 0.5, making the final electromagnetic torque significantly smaller than that of HSPMM with 6s/4p-Non-overlapping as shown in Fig.2.15. It should be noted that the actual torque capability is still limited by the thermal constraints resulting from rotor eddy current loss, especially for the HSPMM with 6s/4p-non-overlapping winding configuration.

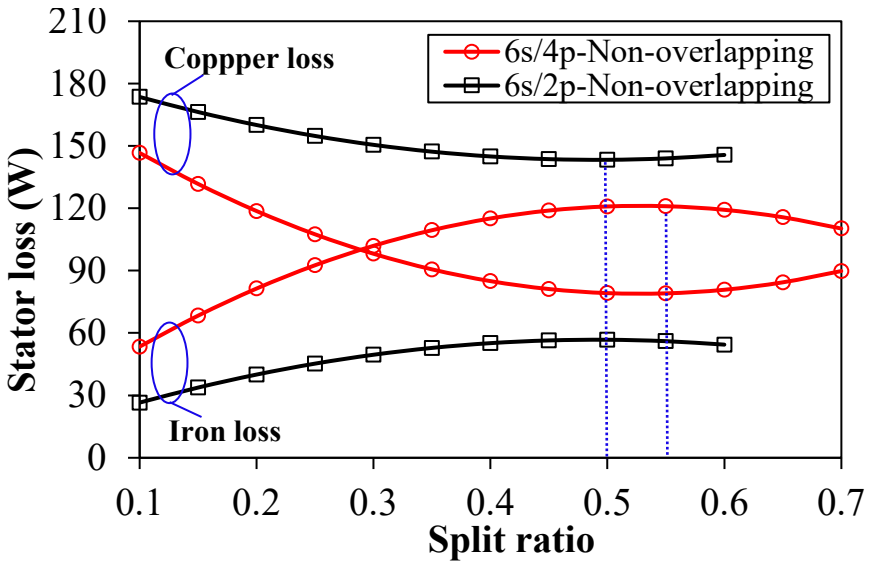

Fig.2.14. Variation of electromagnetic loss with split ratio at rotor pole pairs.

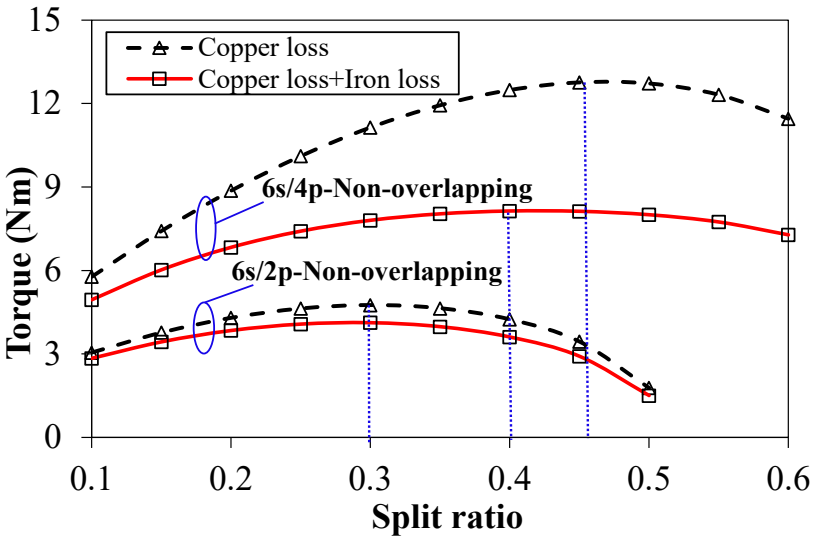

Fig.2.15. Variation of electromagnetic torque with split ratio at rotor pole pairs.

2.4 Optimal Split Ratio Accounting for Copper Loss and Mechanical Stress

The topology of HSPMM is similar to low-to-medium speed operating PM machines. In [GER14], it is highlighted that due to the requirement of mechanical robustness and thermal stability, a surfaced mounted permanent magnet (SPM) machine with a high-strength retaining sleeve is almost exclusively employed.

To obtain certain pre-stress between the sleeve and PM at high speeds, an interference fit should always exist between the PM and the sleeve so that the contact force and tangential force in the sleeve can be derived for magnet retaining. In addition, to avoid the presence of stress concentration at the magnet edges, the inter-pole air gap between magnets should be avoided [BIN06].

At the preliminary design stage, it is of vital importance to take the mechanical constraints into consideration. Generally, two fundamental conditions should be satisfied: the tangential stress in the inner surface of the sleeve should be within the material limits, and the contact pressure between PM and rotor back-iron should always be positive [BIN06].

For HSPMMs, the optimal split ratio is inevitably influenced by the aforementioned mechanical constraints. Both the tangential tensile stress and contact pressure are highly related to the rotor diameter which can be reflected by the split ratio.

2.4.1 Split Ratio Optimization with Tangential Stress Limitation

In most cases, the PMs in a HSPMM are more vulnerable to the tensile stress than the compressive stress. Both NdFeB and SmCo have strong compressive strength and flexural strength but are very weak in tensile strength. Hence, a retaining sleeve with strong tangential tensile strength is necessary. In fact, the main stress in the retaining sleeve is in the form of tangential stress which, when the sleeve is considered as the thin shell, can be expressed as [BIN06]:

$$\sigma_t = \sigma_{t,prestress} + \sigma_{t,w} = \frac{\Delta DE}{\lambda D_o} + \frac{1}{4}\rho_b w^2 \lambda^2 D_o^2 \tag{2.25}$$

where $\sigma_{t,prestress}$ refers to the pre-stress due to shrinking of retaining sleeve. $\sigma_{t,w}$ denotes the additional tangential stress due to rotation and σ_t is the total tangential stress of the specific

sleeve. ΔD is the sleeve interference fit with respect to the machine diameter D_o. ρ_b and E represent the sleeve mass density and the Young's modulus. ω is the angular velocity of the rotating rotor.

As can be seen from (2.25), the sleeve tangential stress can be expressed as the function of split ratio. The value of tangential stress depends on the sleeve material property (mass density and Young's modulus), the interference fit, the operating speed, as well as the split ratio. Fig.2.16 illustrates the tangential stress at the inner side of sleeve with the variation of different interference fits.

It can be seen that the tangential stress will increase with the increase of sleeve interference fit in the whole split ratio range. For each given sleeve interference fit, the tangential stress will drop sharply with the increase of split ratio before reaching a minimum value. After that, the tangential stress will rise slowly with the increase of split ratio.

For a given sleeve with certain tangential strength, the split ratio can be flexibly chosen by adjusting the sleeve interference fit. However, there always exists a minimum split ratio for each sleeve interference fit at which the tangential stress reaches the material limits. These minimum split ratios increase with the increase of sleeve interference fit. In addition, they are also influenced by the actual tangential stress. For illustration, two limit lines representing different values of real sleeve tangential stress are also shown in Fig.2.16. It can be seen that when the actual sleeve tangential stress reaches the material limit, the value of the minimum split ratio is the smallest. Hence, a factor *k* is defined to evaluate the stress margin with respect to the sleeve material tensile strength.

$$k = \frac{\sigma_t}{\sigma_{\text{limit}}} \tag{2.26}$$

where σ_t represents the actual value of sleeve tangential stress and σ_{limit} is the tensile strength limit of the sleeve material. Fig.2.17 illustrates the relationship between the minimum split ratio and the interference fit as well as *k*. It should be noted that the maximum operating speed at which the tangential stress is checked has been increased by 20% for the consideration of an over speed test [BIN06]. It can be seen that the widest split ratio range can be achieved when the actual tangential stress reaches the limits and the interference fit is relatively small. Hence, *k* is preferred to be 1 so that the design values for split ratio can be adequate.

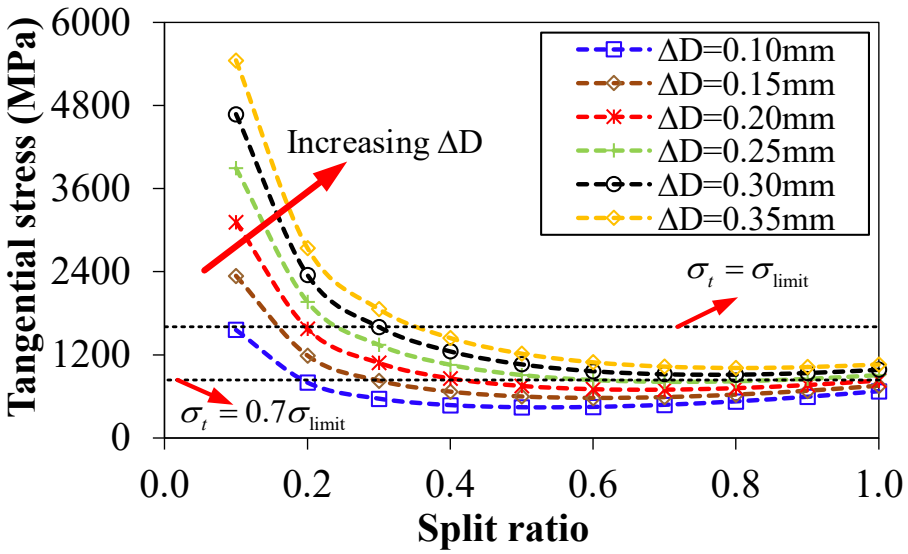

Fig.2.16. Variation of sleeve tangential stress with split ratio (carbon fibre, n_{max}=120kr/min).

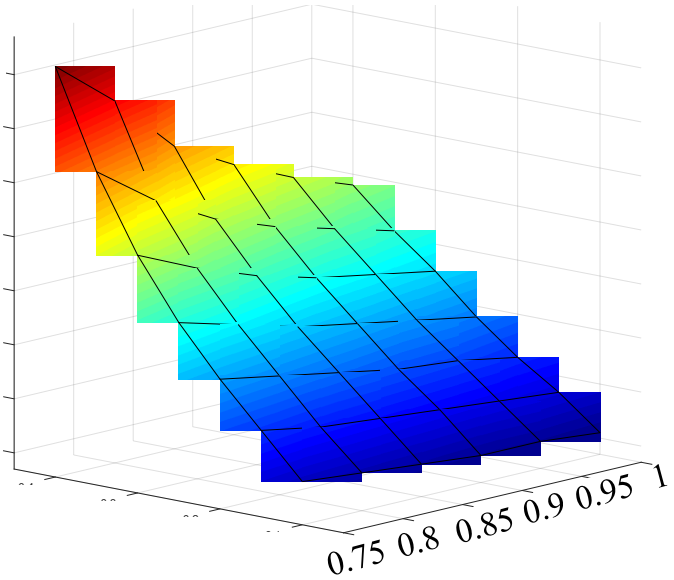

Fig.2.17. Minimum split ratio versus interference fit and factor k (carbon fibre n_{max}=120kr/min).

2.4.2 Split Ratio Optimization with Contact Pressure Limitation

The following paragraphs are from the author's own paper [FEN19].

Generally, for a simple rotor configuration with symmetrically mounted magnets, the contact pressure between the magnets and the rotor back iron can be expressed as [BIN06]:

$$P_{contact-pressure} = \frac{h_b}{r_b}\sigma_{t,prestress} - p_m - p_b \tag{2.27}$$

where h_b and r_b represent the thickness and average radius of selected sleeve. p_m and p_b represent the pressures of magnets and sleeve resulting from centrifugal force which reduces the total contact pressure between the magnets and the rotor. These pressures can be analytically determined as [BIN06]:

$$p_m = \omega^2 r_m \rho_m h_m \tag{2.28}$$

$$p_b = \omega^2 r_b \rho_b h_b \tag{2.29}$$

where h_m and r_m represent the thickness and average radius of PMs. ρ_m and ρ_b represent the mass densities of the magnets and sleeves. On the other hand, the sleeve pre-stress due to shrink fit can be expressed as the difference between the actual sleeve tangential stress and the tangential stress due to rotation. In addition, (2.28) and (2.29) can be substituted into (2.27). Hence, (2.27) can be further derived as a function of split ratio:

$$\begin{aligned} P_{contact-pressure} &= \frac{h_b}{r_b}(\sigma_t - \sigma_{t,w}) - p_m - p_b \\ &= \frac{2h_b\sigma_t}{D_o}\frac{1}{\lambda} - \omega^2(\frac{1}{2}\rho_m h_m + \rho_b h_b)D_o\lambda + \frac{1}{2}\omega^2\rho_m {h_m}^2 \end{aligned} \tag{2.30}$$

As mentioned in the previous section, the contact pressure between the rotor and the magnets should always be positive. From (2.30), it can be seen that the contact pressure decreases with the increase of split ratio. Hence, there exists a special split ratio at which the contact pressure equals zero and the actual split ratio should always be smaller than this value. This can be expressed as:

$$\lambda < \lambda_o = \frac{a + \sqrt{a^2 + 16b}}{2c} \tag{2.27}$$

where

$$a = \rho_m h_m^2 \tag{2.28}$$

$$b = \sigma_t(2\rho_b h_b^2 + \rho_m h_m h_b)/\omega^2 \tag{2.29}$$

$$c = D_o(2\rho_b h_b + \rho_m h_m) \tag{2.30}$$

For HSPMM, the main component of the sleeve tangential stress is the pre-stress due to shrink fit, especially for the carbon fibre sleeve with low mass density [BIN06]. Compared

with the tangential stress ($\sigma_{t,prestress}$) resulting from sleeve shrinking, the tangential stress due to rotation ($\sigma_{t,w}$) is much smaller. Therefore, the following condition can be applied:

$$\begin{aligned} 16b &= 16\sigma_t(2\rho_b h_b^2 + \rho_m h_m h_b)/\omega^2 \\ &>> 16\sigma_{t,w}(2\rho_b h_b^2 + \rho_m h_m h_b)/\omega^2 > a^2 \end{aligned} \tag{2.31}$$

Hence, (2.31) can be further simplified as:

$$\lambda < \lambda_o \approx \frac{4\sqrt{b}}{2c} = \frac{2k}{\omega D_o}\sqrt{\frac{\sigma_{\text{limit}}}{2\rho_b + \rho_m \dfrac{h_m}{h_b}}}\ (0 < k \le 1) \tag{2.32}$$

It has been proved that the feasible range of split ratio is the widest when *k* equal to 1. Hence, the maximum split ratio of HSPMM under contact pressure limit can be given as:

$$\lambda_{\max} = \frac{2}{\omega D_o}\sqrt{\frac{\sigma_{\text{limit}}}{2\rho_b + \rho_m \dfrac{h_m}{h_b}}} \tag{2.33}$$

It can be seen that the split ratio of HSPMM is restricted by the sleeve tensile strength, the maximum operating speed as well as the magnet mass density and the ratio of magnet to sleeve thickness. The maximum split ratio is significantly reduced with the increase of maximum operating speed and the ratio of magnet to sleeve thickness.

On the other hand, it is obvious that the air gap of HSPMM is larger than that of normal PM machines due to existence of sleeve. From (2.33) the minimum air gap length, which consists of physical air gap and sleeve, can be given as:

$$g_{\min}(\lambda) = h_{b,\min} + \delta = \frac{\rho_m}{\dfrac{4\sigma_{\text{limit}}}{(\omega D_o)^2}\dfrac{1}{\lambda^2} - 2\rho_b} h_m + \delta \tag{2.34}$$

Clearly, the sleeve material in terms of mass density and tensile strength has a significant impact on the minimum sleeve thickness which will be fully addressed in the subsequent section. In this section, the sleeve material is selected to be carbon fibre due to its low mass density and high tensile strength. Ignoring the effect of saturation, flux-leakage as well as slotting effect, the air gap flux density can be accordingly expressed as:

$$B_g = \frac{h_m}{h_m + h_b + \delta} B_r = \frac{1}{1 + \dfrac{\rho_m}{\dfrac{4\sigma_{\text{limit}}}{(\omega D_o)^2}\dfrac{1}{\lambda^2} - 2\rho_b} + \dfrac{\delta}{h_m}} B_r \tag{2.35}$$

Substituting (2.34) and (2.35) into (2.6), the electromagnetic torque of HSPMM under mechanical constraints can be derived as:

$$T(\lambda) = \frac{3\sqrt{2}}{2} f(\lambda) g(\lambda) B_r k_w \sqrt{\frac{P_{cu} k_s N_s l_a}{36\rho_{cu}}} \tag{2.36}$$

where

$$f(\lambda) = \sqrt{A_s}\left(D_o\lambda + \frac{2\rho_m}{\dfrac{4\sigma_{\text{limit}}}{(\omega D_o)^2}\dfrac{1}{\lambda^2} - 2\rho_b} h_m + 2\delta\right) \tag{2.37}$$

$$g(\lambda) = \frac{1}{1 + \dfrac{\rho_m}{\dfrac{4\sigma_{\text{limit}}}{(\omega D_o)^2}\dfrac{1}{\lambda^2} - 2\rho_b} + \dfrac{\delta}{h_m}} \tag{2.38}$$

Hence, the optimal split ratio of HSPMM under mechanical constraints can be obtained by solving the equation as follows:

$$\frac{\partial T(\lambda)}{\partial \lambda} = 0 \tag{2.39}$$

It is apparent that the equation for the optimal split ratio considering the mechanical constraints is much more complicated than that of the normal PM machines due to the presence of $g(\lambda)$. The pure analytical solution of a high order equation (2.39) is quite complicated as well. Thus, the numerical method is adopted which is much easier and convenient to solve this equation. The two equations with respect to the electromagnetic and mechanical domains have already been determined as:

$$\begin{cases} T(\lambda, g) = \dfrac{3\sqrt{2}}{2}(\lambda D_o + 2g)\dfrac{h_m B_r}{h_m + g} k_w \sqrt{\dfrac{P_{cu} k_s N_s l_a A_s}{36\rho_{cu}}} \\ g_{\min}(\lambda) = \dfrac{\rho_m}{\dfrac{4\sigma_{\text{limit}}}{(\omega D_o)^2}\dfrac{1}{\lambda^2} - 2\rho_b} h_m + \delta \end{cases} \tag{2.40}$$

Fig. 2.18 (a) illustrates the surfaces of two equations in the electromagnetic and mechanical domain, respectively. The electromagnetic surface is divided into two parts by the surface representing the mechanical constraints. For each specific split ratio, there exists a corresponding minimum air gap length. Hence, the left-side of the electromagnetic surface is valid from the mechanical point of view. In addition, it is obvious that a curve is defined by the intersection of the two surfaces. This curve represents the enveloping of valid designs in the electromagnetic domain considering the mechanical constraints.

As shown in Fig.2.18 (b), the projections for enveloping of the designs with and without the mechanical constraints are illustrated in the 2-D plane. It can be seen that the optimal split ratio for the maximum torque considering the mechanical constraints is significantly reduced from 0.45(M1) to 0.35(M2). In addition, the achievable torque has also been decreased from 9.02Nm to 7.09Nm. M3 denotes the optimal design with the same effective air gap length of M2 when the mechanical constraints are not considered. It can be seen that the optimal split ratio is reduced from 0.45(M1) to 0.41(M3) due to the increase of air gap length. When the mechanical constraint is then considered, the optimal split ratio is further reduced to 0.35(M2). This reduction can be attributed to the different level of limitation on the air gap flux density with the increasing of the split ratio.

Fig.2.19 shows the minimum required air gap length and the corresponding maximum air gap flux density with increase of split ratio. It can be seen that the flux density is dramatically decreased due to the increased air gap length. This limitation becomes more obvious with the increase of split ratio when the PM thickness is given. Hence, the shift of optimal split ratio does not only result from the increase of air gap length due to presence of the sleeve which has been proved in the previous section. More importantly, the restriction for the air gap flux density also varies with the split ratio. The difference between the restricted flux density with the unrestricted one becomes larger with the split ratio increasing. Thus, the optimal split ratio corresponding to the maximum torque has to be decreased. The maximum torque has also been decreased due to a reduction of the achievable air gap flux density. The optimization procedure

for the optimal split ratio is shown in Fig.2.20.

Fig.2.21 shows the cross sections of the optimal designs with and without consideration of mechanical constraints. Clearly, the split ratio is significantly reduced. The design parameters of each machine are given in Table 2.2.

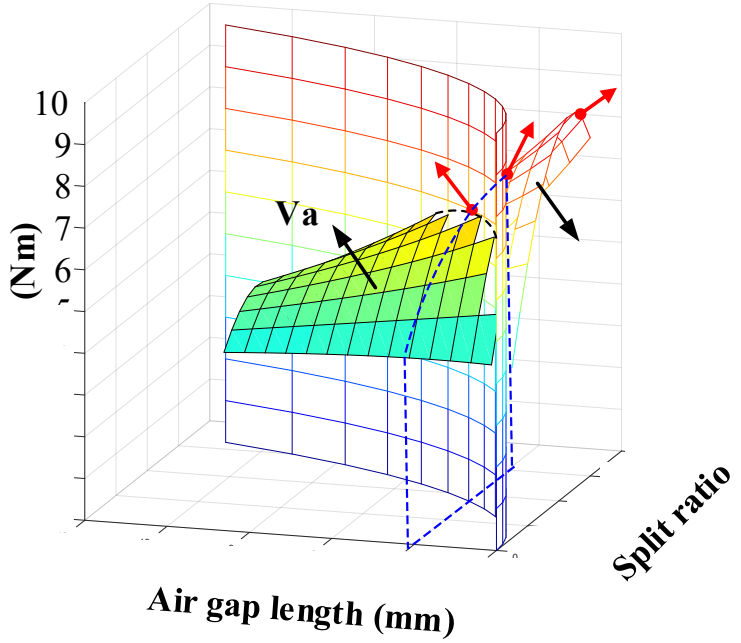

(a)

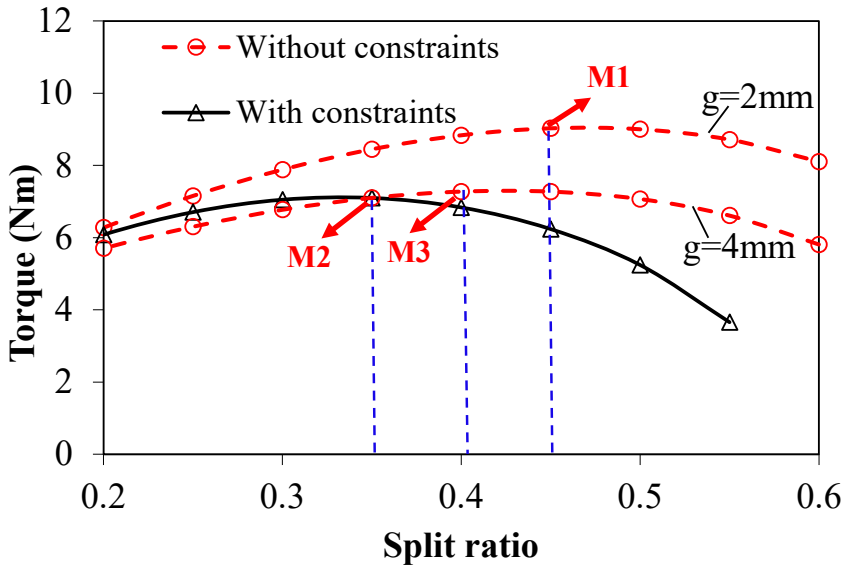

(b)

Fig.2.18. Variation of electromagnetic torque with split ratio and air gap length (γ =0.5, n_{max}=120kr/min). (a) Variation of torque with split ratio and air gap length. (b) Variation of torque with split ratio with and without constraints.

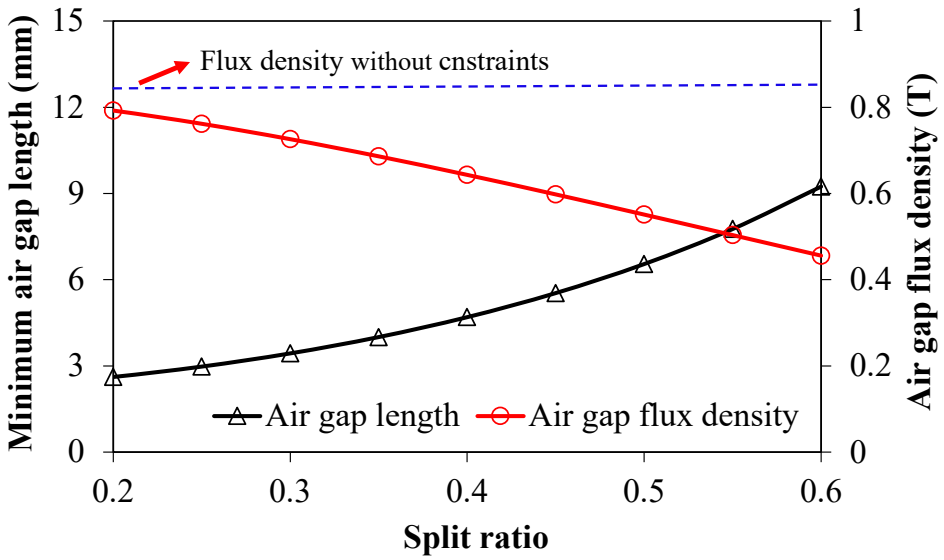

Fig.2.19. Variation of minimum air gap length and maximum flux density with split ratio.

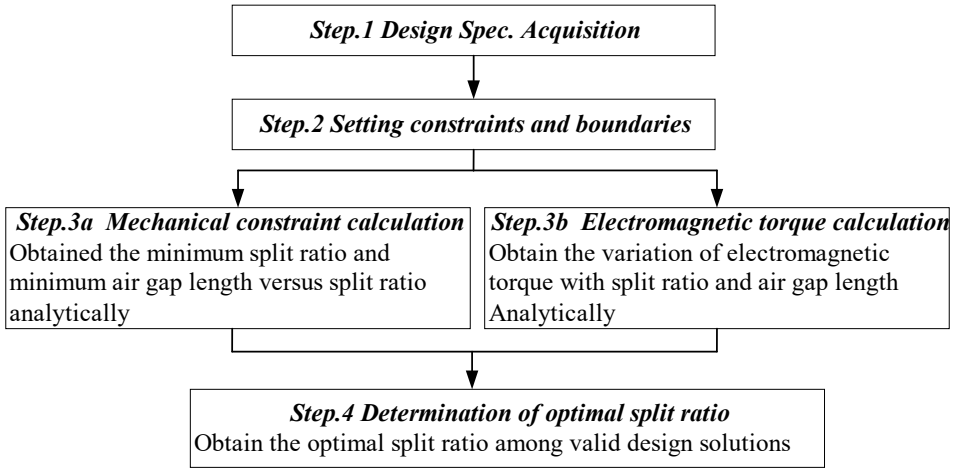

Fig.2.20. Optimization procedure for split ratio of HSPMM considering mechanical constraints.

Fig.2.22 illustrates the flux distributions of optimal designs with or without the mechanical constraints. Evidently, the design with mechanical constraints (M2) exhibits less saturation in the stator iron than the one without mechanical constraints (M1) due to increase of air gap length. On the other hand, when the total effective air gap length keeps constant, the optimal design without mechanical constraint (M3) has a similar stator as well as air gap flux density compared with that with mechanical constraint (M2).

Fig.2.23 illustrates the spectra of air gap flux densities of three optimal designs with and without consideration of mechanical constraints. Both M2 and M3 clearly exhibit much lower fundamental flux density than M1, which agrees well with the trend in Fig.2.22.

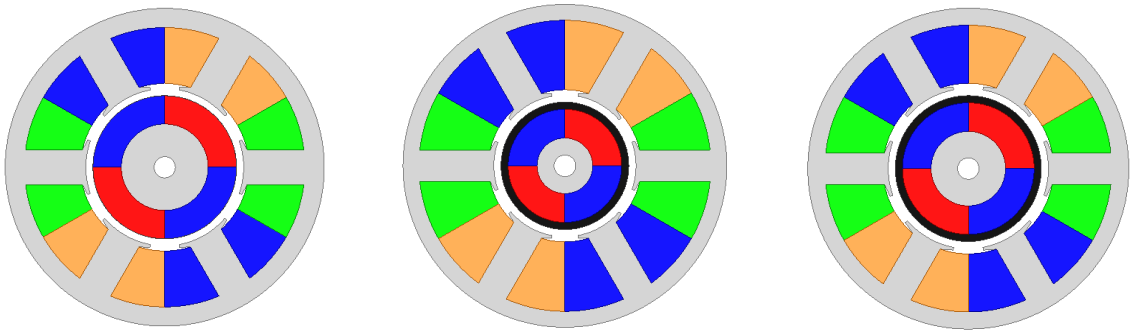

M1 M2 M3

Fig.2.21. Cross-sections of three optimal designs for maximum torque.

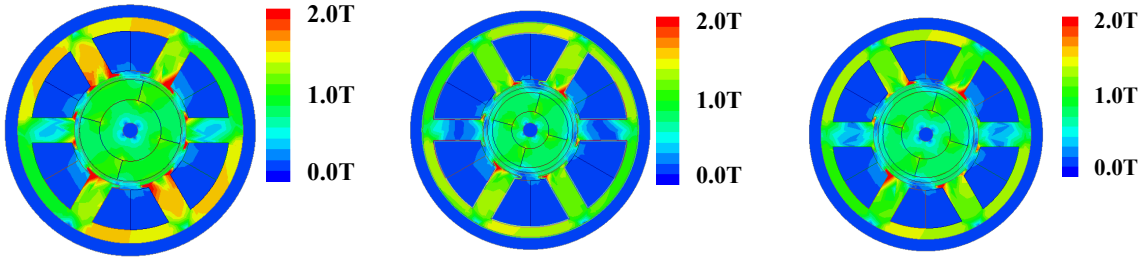

M1 M2 M3

Fig.2.22. Flux distributions of three optimal designs for maximum torque.

The contact pressures between magnets and rotor back iron for two optimal designs are shown in Fig.2.24. It should be noted that the absolute value of contact pressure represents the stress level. The negative sign represents the direction of contact pressure (points to center in the polar coordinates system). It can be seen that the minimum contact pressure lies on the surface between the permanent magnet and the rotor back iron. The minimum contact pressure for the design without consideration of mechanical constraints (M3) is 0.053MPa, making the permanent magnets finally detach from the rotor back iron. Meanwhile, the contact pressure for the optimal design considering mechanical constraints (M2) is -0.036MPa which provides a residual force for permanent magnets sticking on the rotor back iron. To conclude, M2 proves to be the most feasible design solution with the maximum electromagnetic torque when the mechanical constraints are taken into consideration. The geometrical parameters of the designed HSPMM are shown in Table 2.2.

In addition, it should be noted that the thermal constraints in terms of stator iron loss as well as AC copper loss and rotor eddy current loss also affect the split ratio of HSPMM due to the restriction of flux density. This will be studied in future research.

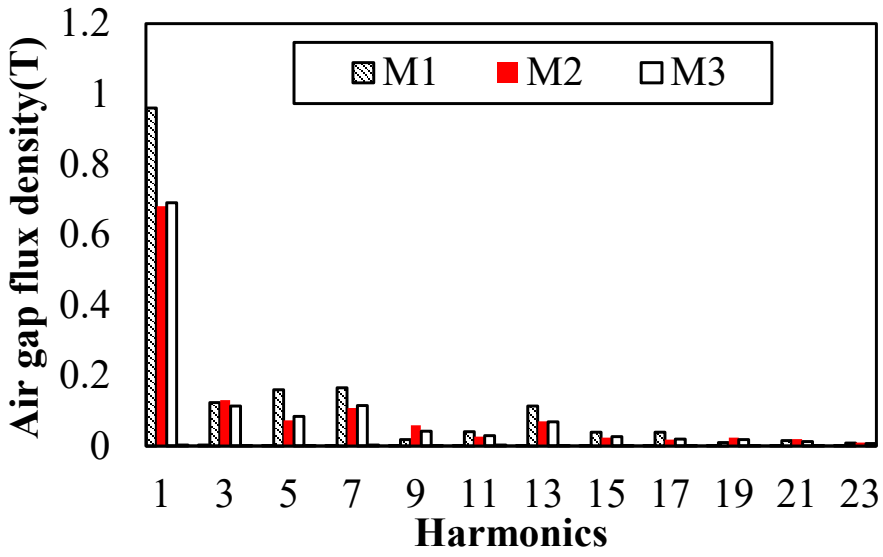

Fig.2.23. Spectra of air gap flux densities of three optimal designs for maximum torque, without/with mechanical constraints.

Table 2.2 Parameters of the Optimal Designs

Parameters	M1	M2	M3
Stator outer diameter(mm)	90		
Stator bore diameter(mm)	44.5	39.5	44.9
Split ratio	0.45	0.35	0.41
Rotor outer diameter(mm)	40.5	31.5	36.9
Rotor shaft diameter(mm)	6		
Physical air gap length(mm)	2		
Sleeve thickness(mm)	--	2	2
PM thickness(mm)	8		
Stator yoke thickness(mm)	5.5	4.4	5.2
Stator teeth width(mm)	11	8.8	10.5
Stator axial length(mm)	55		
Phase resistance(mΩ)	5.3	3.0	4.8
Phase inductance(μH)	29	30	28
Number of turns	20		
Phase Current(A)	85	105	91

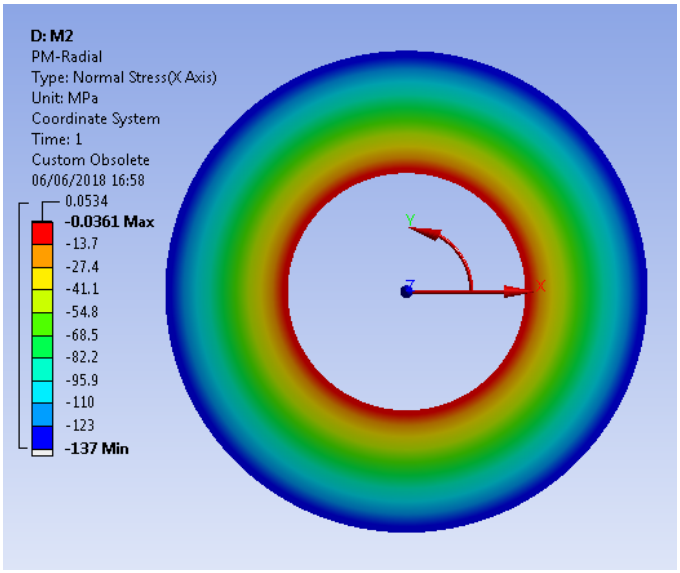

M2

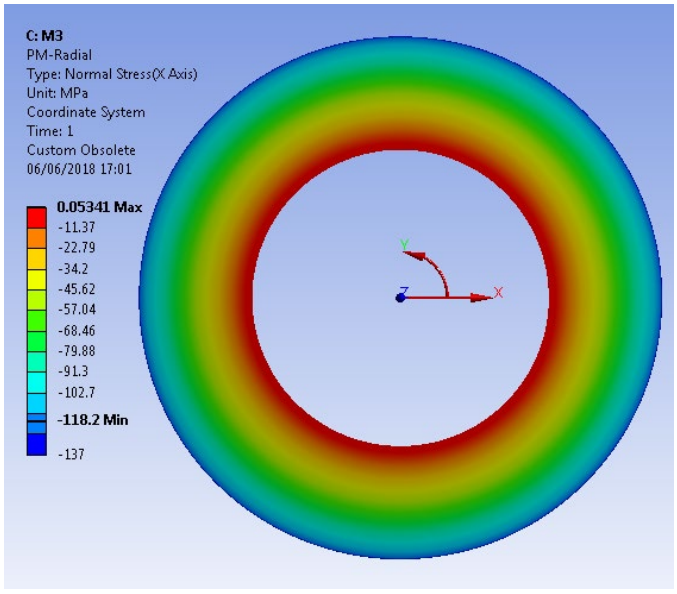

M3

Fig.2.24. Spectra of air gap flux densities of three optimal designs for maximum torque, without/with mechanical constraints.

2.4.3 Influence of Design Parameters on Optimal Split Ratio

As shown in the previous section, the optimal split ratio with a given flux ratio and permanent thickness for HSPMM can be obtained. However, from (2.33), it can be seen that the mechanical constraints are closely related with flux density ratio as well as the sleeve material physical properties and maximum operating speed. In this section, the influence of the

previous parameters on the optimal split ratio of HSPMM is investigated. It is worth mentioning that the level of limitation on flux density for magnets of different thickness will not change significantly when the split ratio increases. Thus, the magnet thickness has no significant influence on the determination of optimal split ratio.

A. Flux density ratio

From (2.37), it can be seen that the optimal split ratio considering the mechanical constraints still depends on the slot area which is closely related with the flux density ratio. Fig.2.25 illustrates the variation of optimal split ratio with flux density ratio, and clearly shows that the optimal value decreases with the increase of flux density ratio. This can be attributed to the increase of width of the slot teeth and thickness of yoke while the flux density ratio is increasing. Hence, the slot area is consequently reduced. In order to maintain the constant copper loss, the stator bore diameter has to be reduced. It can be seen that with the decrease of flux density ratio, the difference between the optimal split ratios with and without consideration of mechanical constraints increases. This can be attributed to the increasing air gap length with the increasing split ratio, when mechanical constraints are considered. Thus, the stator bore diameter increases faster, which in turn restricts the increase of optimal split ratio so that the copper loss can be constant.

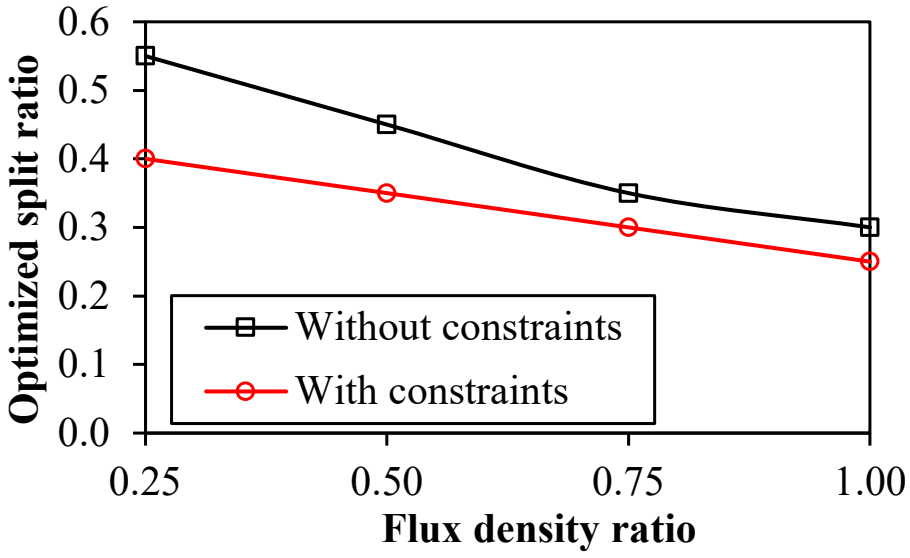

Fig.2.25. Variation of optimal split ratio with flux density ratio.

B. Maximum operating speed

In the practical design, the worst case should always be considered. The contact pressure

between the magnet and the rotor back iron turns into the minimum when the machine operates at the maximum operating speed. Hence, the optimum split ratio is quite interdependent with the maximum operating speed at which the contact pressure must be no smaller than zero. As can be seen from (29), the mechanical constraint is closely related with the maximum operating speed. The limitation on split ratio becomes more demanding with the increase of maximum operating speed. In this section, the influence of maximum speed on the optimized split ratio for HSPMMs is investigated.

Fig.2.26 illustrates the different surfaces with respect to the different maximum operating speeds. It can be seen that with the increase of maximum operating speed, the smaller valid surface of the designs than that without constraints can be obtained. On the other hand, as shown in Fig.2.27, when the maximum operating speed is relatively small, the envelop of the valid designs is almost the same as that of the design surface without constraints, which means that the optimized split ratio, as well as the maximum achievable torque, remain almost stable at lower speed. Under this circumstance, the mechanical constraints can be ignored.

As shown in Fig.2.28, the optimized split ratio keeps decreasing with the increase of maximum operating speed. On the other hand, when the maximum is below 45kr/min, the optimized split ratio almost remains unchanged compared with the one without consideration of mechanical constraints. When the maximum operating speed is relatively low, the required sleeve thickness for the selected sleeve material will not be comparable to the mechanical air gap length. Thus, the air gap flux density will only drop very slightly.

Table 2.3 Material Properties

Material properties	PM (NdFeB)	Carbon fiber	Inconel 718	Stainless Steel 304
Density (kg/m^3)	7400	1620	8200	7600
Young's Modulus (GPa)	160	140	199	196
Tensile strength (MPa)	120	1400	1100	500
Cost ($/kg)	40	150	65	2.3

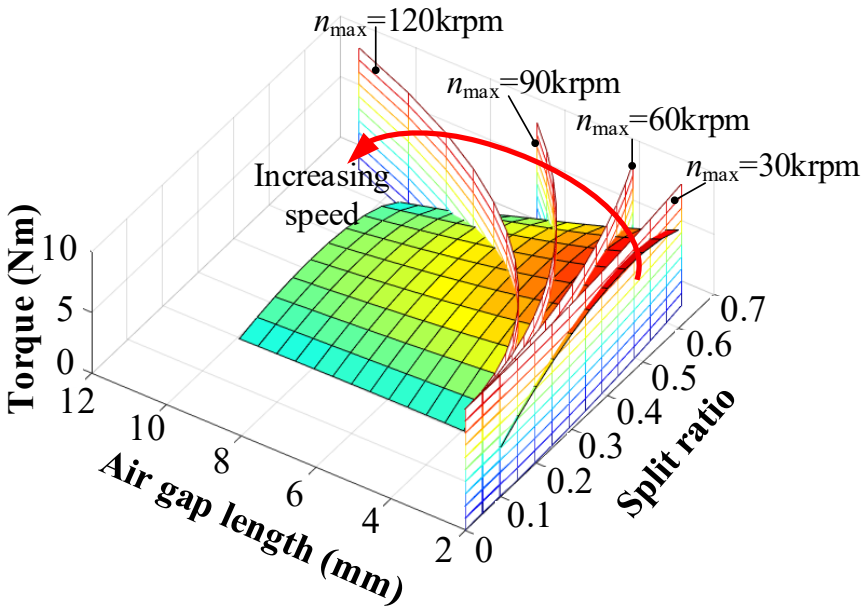

Fig.2.26. Variation of electromagnetic torque with air gap length and split ratio.

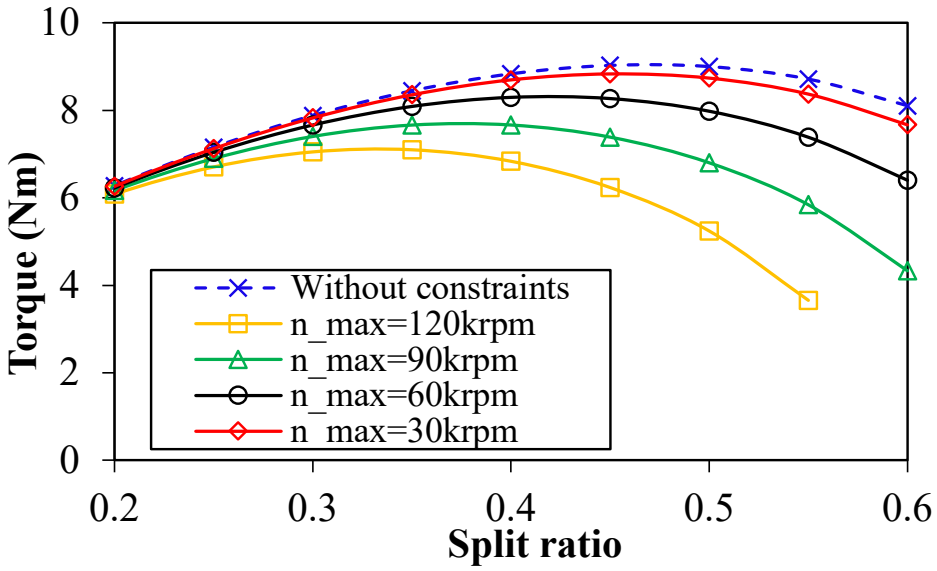

Fig.2.27. Variation of electromagnetic torque with split ratio at different operating speed.

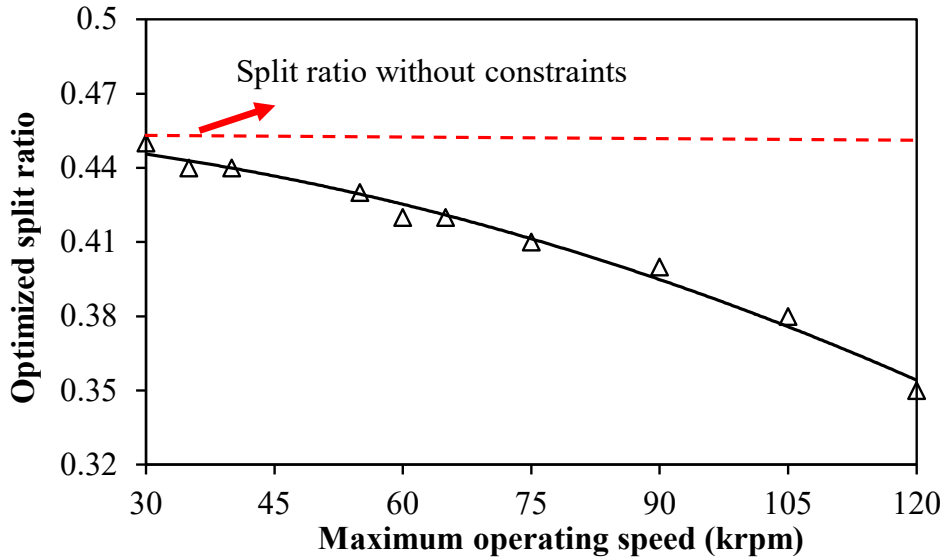

Fig.2.28. Variation of optimal split ratio with different maximum operating speed.

C. Retaining sleeve material

The sleeve material is very important to the design of HSPMM due to its strong tensile strength. The material properties of typical retaining sleeves and PMs are shown in Table 2.3. It can be seen that carbon fibre is equipped with the greatest tensile strength while the one for stainless steel has the least. However, the cost of carbon fibre is also the highest. The criteria of sleeve selection should take the cost and the electromagnetic performance as well as the mechanical robustness into consideration.

The minimum air gap length can be easily obtained from (2.34), as shown in Fig.2.29. Carbon fibre shows great advantages for its smallest sleeve thickness, especially at higher speed. Fig.2.30 illustrates the electromagnetic torque versus split ratio under the mechanical constraints with different sleeve materials at the speed of 60kr/min. It is obvious that HSPMM with carbon fibre sleeve has the highest torque density compared with the others due to the relatively larger air gap flux density. In Fig.2.32, it can be seen that the maximum air gap flux density for the design with carbon fibre is larger than the others due to a smaller effective air gap.

As mentioned before, the maximum operating speed has a significant impact on the maximum torque as well as the optimized split ratio of HSPMM. The optimized split ratios for HSPMM equipped with three different sleeve materials, respectively, are shown in Fig.2.33. With respect to maximum operating speed, the optimized split ratio for machines with carbon fibre is not as sensitive as the one for machines with Inconel and stainless steel.

In addition, as shown in Fig.2.34, the maximum achievable torque for HSPMM equipped with carbon fibre is higher than that of Inconel. This difference becomes larger with the increase of the maximum operating speed which indicates that the carbon fibre is extremely suitable for ultra-high speed applications. On the other hand, the Inconel compromises the cost and mechanical robustness, exhibiting advantages in the medium speed range.

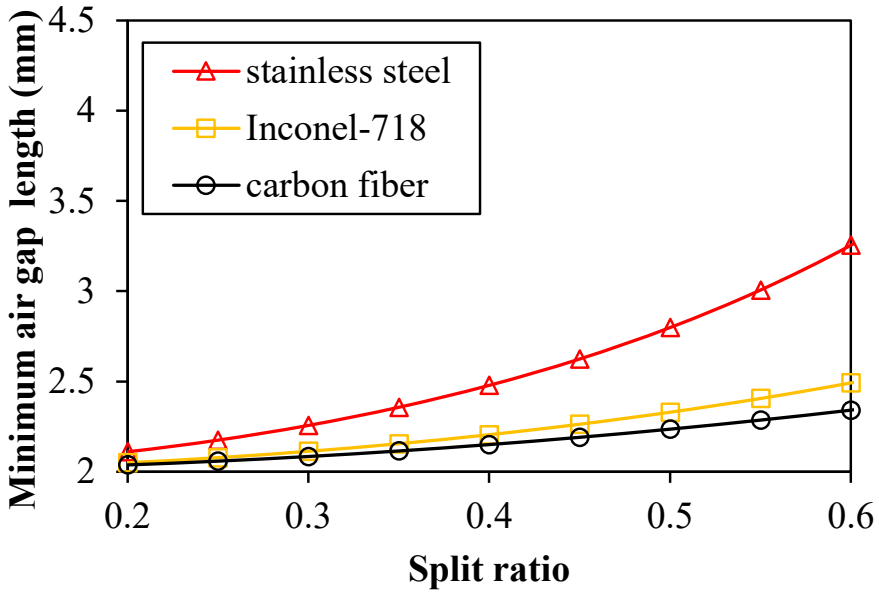

(a)

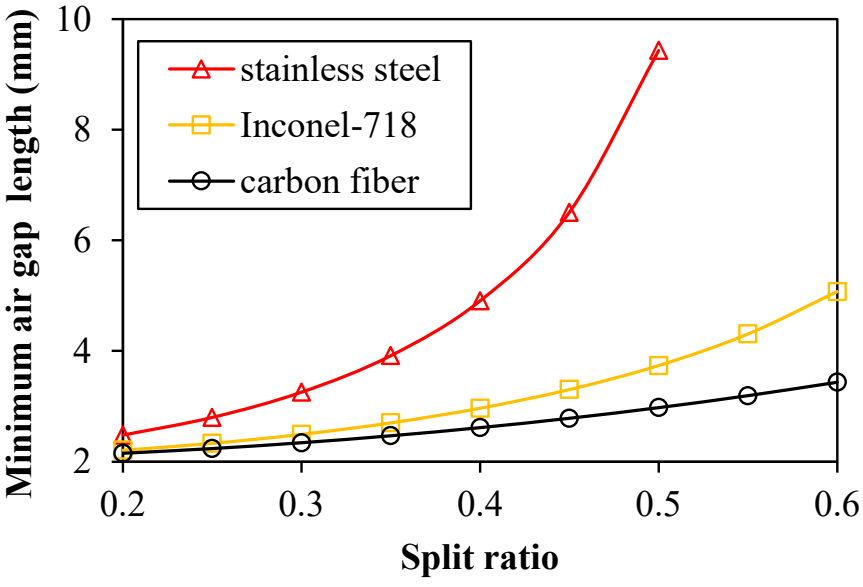

(b)

Fig.2.29. Variation of minimum air gap length versus split ratio with respect to different sleeve material.

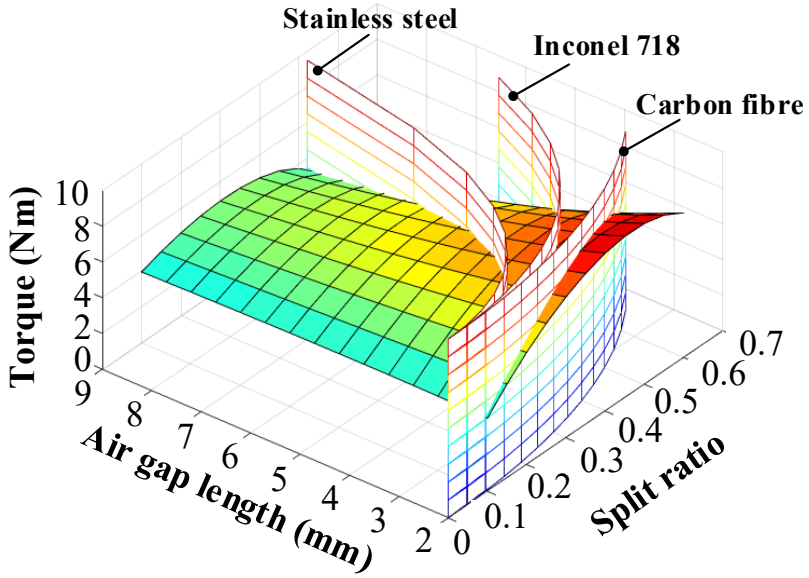

Fig.2.30. Variation of minimum air gap length versus split ratio with respect to different sleeve material.

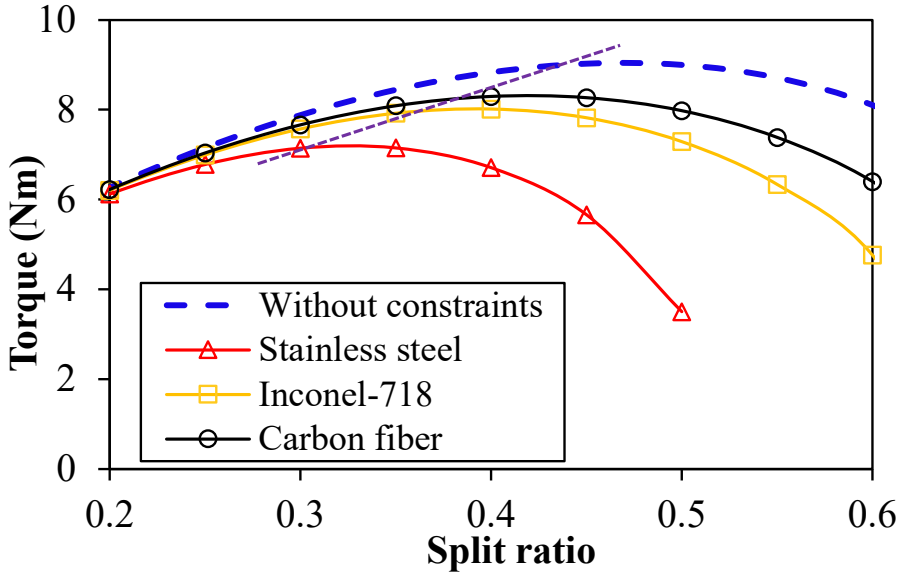

Fig.2.31. Variation of minimum air gap length versus split ratio.

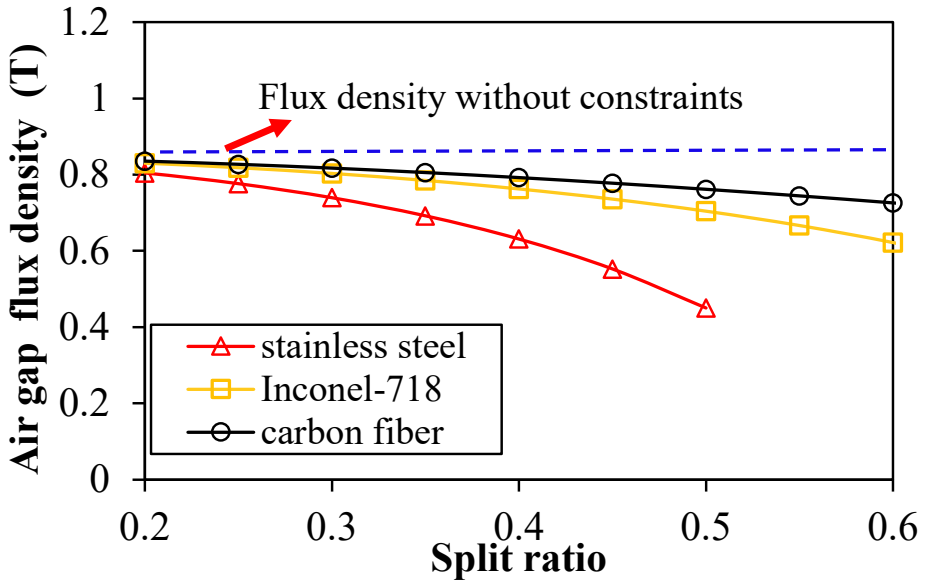

Fig.2.32. Maximum air gap flux density versus split ratio (n_{max}=60krpm).

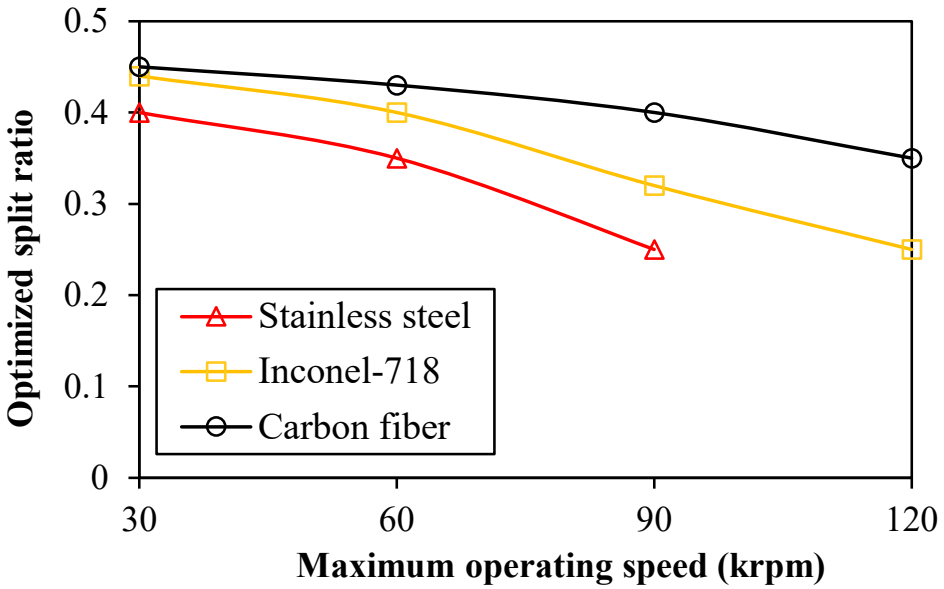

Fig.2.33. Optimal split ratio versus maximum operating speed.

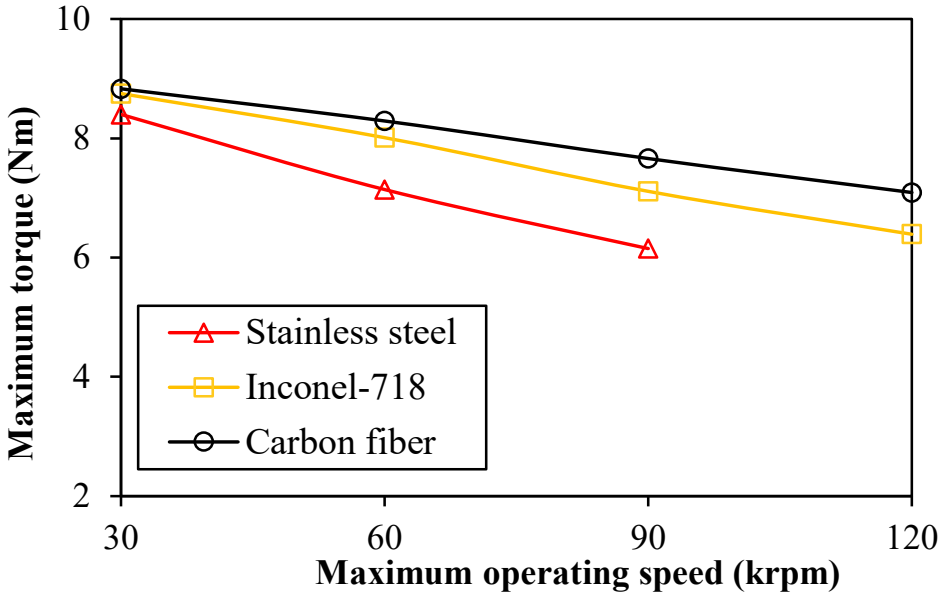

Fig.2.34. Maximum achievable torque versus maximum operating speed.

2.5 Optimal Split Ratio Accounting for Stator Loss and Mechanical Stress

In this section, both the stator iron loss and mechanical stress are considered in the determination of optimal split ratio of HSPMM. When the mechanical constraints are taken into consideration, the stator flux density will be reduced due to the extra air gap length for retaining sleeve. As shown in Fig.2.35, the minimum air gap length keeps increasing with the increase of split ratio. Hence, the limitation on air gap flux density becomes more severe with the enlarged air gap length. Accordingly, the stator iron loss will be reduced. In addition, the split ratio at which the stator iron loss reaches maximum is also decreased as shown in Fig.2.36. This shift as well as the air gap flux density reduction will eventually lead to decrease of the optimal split ratio. Fig.2.37 illustrates four curves of electromagnetic torque versus split ratio with respect to three different scenarios. It is shown that optimal split ratio is significantly reduced when the stator iron loss and mechanical constraints are taken into consideration. Although the air gap flux density is reduced in the whole split ratio range, the restriction on the iron loss enables a larger allowable copper loss thus the electrical loading, eventually making the achievable electromagnetic torque almost constant when the mechanical constraints are taken into consideration.

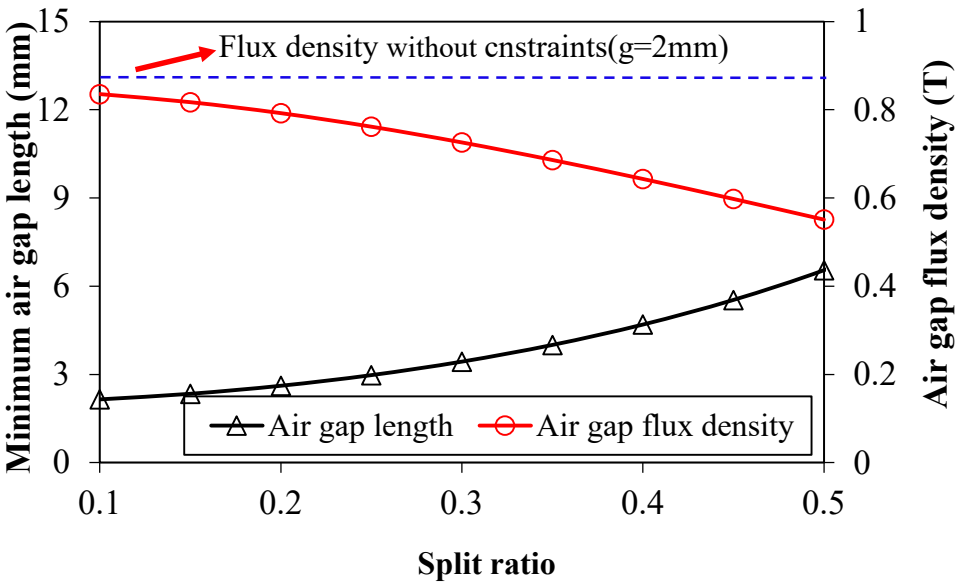

Fig.2.35. Minimum air gap length and maximum flux versus split ratio with and without mechanical constraints.

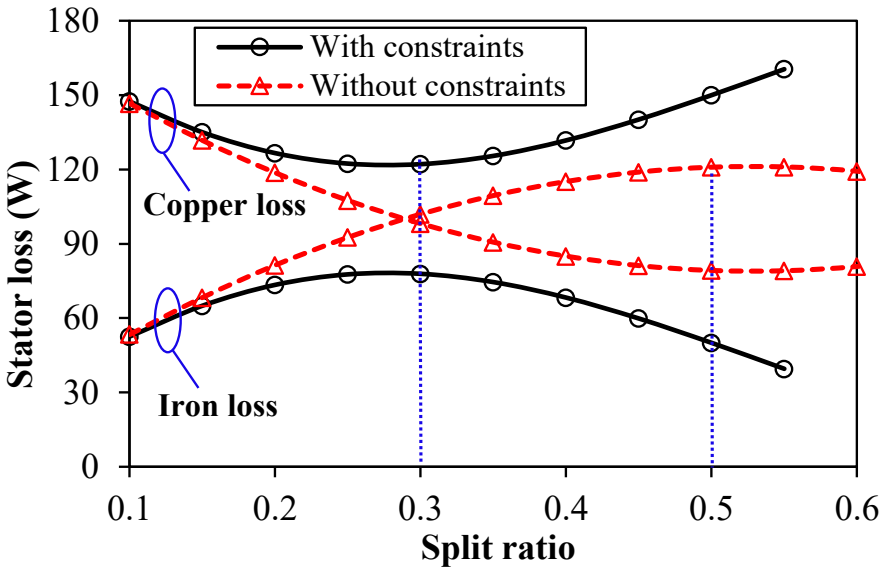

Fig.2.36. Stator loss versus split ratio with and without mechanical constraints.

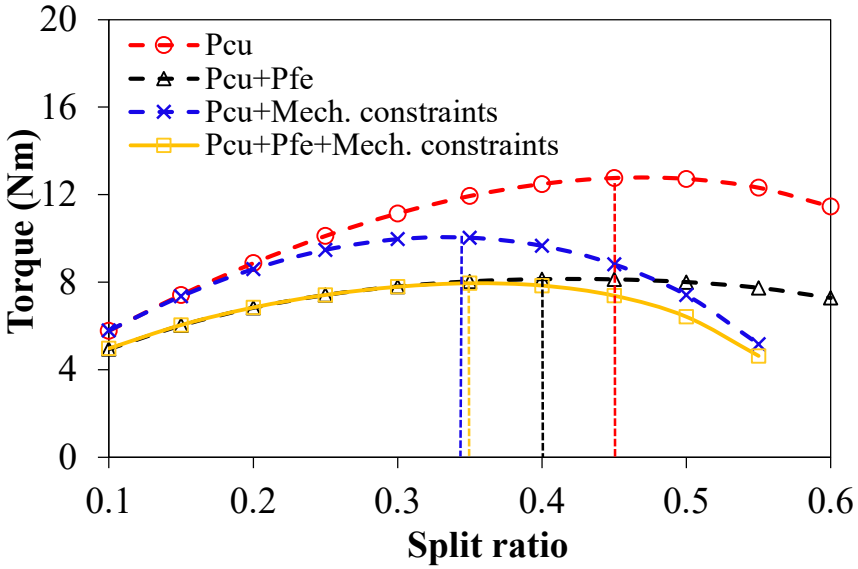

Fig.2.37. Electromagnetic torque versus split ratio with different scenarios.

2.6 Summary

In this section, the optimal split ratio for HSPMM has been analyzed with different electromagnetic and mechanical consideration including stator iron loss as well as the sleeve tangential stress limit and contact pressure requirement between the magnets and the rotor back iron. The analytical results have been verified by the finite element analyses. It has been shown that the optimal split ratio is significantly reduced when the mechanical constraints and stator iron loss are taken into account. Furthermore, the achievable torque has also been decreased sharply due to the limitation on the maximum air gap flux density. The influences of flux density ratio, as well as the sleeve material and maximum operating speed on the optimized split ratio, have also been investigated. It is shown that the optimal split ratio is reduced significantly with the increase of flux density ratio and maximum operating speed. The carbon fibre exhibits distinctive advantages among the commonly used sleeve materials with the highest torque density, making it extremely suitable for ultra-high-speed applications.

Chapter 3 Analysis of Magnet Eddy current Loss for Four-Pole High Speed PM Machines with Alternate Stator Winding Configuration

In Chapter 2, the optimal split ratio of HSPMM is determined with due account for stator electromagnetic loss and mechanical constraints. However, the electromagnetic loss on the rotor side, especially in the magnets, should also be taken into consideration. Significant rotor magnet loss will be induced under high-speed operation due to existence of both spatial and temporal field harmonics. In this chapter, the rotor magnet loss analysis is conducted on the four-pole HSPMM, with focus on the loss segregation resulting from spatial field harmonics. The contribution of each harmonic in the production of magnet loss, either from both PM field or armature, is determined with the proposed method. In addition, the slotting effect on both PM field and armature reaction field is compared and the corresponding resultant magnet loss is quantified. The literature on magnet loss due to modulated MMF harmonics is firstly reviewed. Meanwhile, the influence of stator configuration, e.g. number of stator slot and coil pitch, on the armature reaction-induced magnet loss is investigated. Finally, experimental results are provided to verify the theoretical analysis on back-EMF and torque.

3.1 Introduction

The rotor loss has always been an issue for permanent magnet brushless machines equipped with surface-mounted magnets [ATA00], [TOD04], [ZHU04], [NAK06], [SHA09], [BIA13]. Generally, the generation of rotor eddy current loss can be attributed to the field variation seen by the rotor. This field variation results from the following reasons: (a) Nonsinusoidal stator MMF distribution due to stator winding disposition. (b) Permeance variation due to slotting effect. (c) Nonsinusoidal phase current due to BLDC control and PWM. The existence of spatial and temporal harmonics in the air gap field will yield a significant eddy current loss in the rotor magnets, rotor yoke as well as the metallic sleeve for magnet retaining. The risk of demagnetization will be increased due to the difficulties of rotor cooling, especially for the rotor magnets sheltered by the sleeve with low thermal conductivity such as carbon-fiber.

Hence, the accurate prediction of rotor eddy current loss is of great importance to the robustness of permanent magnet brushless machines. A lot of analytical models can be found

for the calculation of rotor loss in the past two decades [ATA00], [ISH05], [WU12], [DUB14]. Those analytical models give more insight to the mechanism of the rotor loss generation. In addition, this also gives the guidelines for the selection of rotor loss reduction methods such as magnet segmentation [YAM09], [HUA10], [WAN10b], [MIR12], rotor pole shaping [YAM10], multi-layered or dual phase stator winding [SUN14], stator dummy teeth or dummy slot [MA19].

For the HSPMM, the rotor loss issue should be more concerned due to high frequency and abundant time harmonics in the phase current. Meanwhile, the air gap length in high speed PM machines is much larger than that of low-speed PM machines. The relatively larger air gap will impose distinct effect on the spatial harmonics with different order, which will be demonstrated in the following section. The interaction between harmonics with same frequency but different spatial orders is also affected by the relatively larger air gap [WU12]. It will be demonstrated in this chapter that the harmonic superposition method is still applicable with acceptable accuracy for the magnet loss calculation of HSPMM.

On the other hand, the rotor topology selection of HSPMM is very limited due to the consideration of rotor mechanical robustness and machine control difficulties. The permanent magnets are normally surface-mounted onto the rotor back-iron or directly bonded with the shaft, especially for very high-speed operation. The rotor pole numbers of high-speed PM machines are usually selected to be 2 or 4 depending on specific requirements and constraints. The 2-pole rotor structure is widely used in low-power ultra-high-speed applications due to lower fundamental frequency which is easier for control and beneficial to the reduction of stator iron loss and rotor PM eddy current loss [ZHO06], [ZWY05], [PFI10], [HON12]. The 4-pole rotor is more inclined to be adopted for high-power high-speed applications due to reduced end-winding length and stator copper loss, which are quite advantageous for stator thermal equilibrium in high power application [JAN04], [BIN06], [LUI14], [ZHA15]. Hence, the stator configuration such as winding disposition should be more concerned. It will be demonstrated that the number of stator slots and winding coil pitch make a huge difference to the induced stator MMF and thus the penetrated harmonics.

This chapter is organized as follows. In Section 3.2, the rotor magnet loss segregation will firstly be conducted on the 6-slot 4-pole HSPMM. The contribution of PM harmonics and the MMF harmonics to the resultant magnet loss is quantified. In addition, the validity of harmonic superposition method will be verified. Then, the magnet loss due to the slotting effect on both

the PM field and the armature reaction field are obtained in section 3.3. Furthermore, in section 3.4, the comparison is made on the armature reaction induced magnet loss in HSPMM with alternate stator configuration. The experimental results are provided in section 3.5 in order to verify the theoretical analysis. The summary is eventually given in section 3.6.

3.2 Rotor Magnet Loss Segregation of HSPMM

In this section, the rotor PM eddy current loss is segregated on a typical 6-slot 4-pole HSPMM based on the frozen permeability method. The eddy current loss due to each field harmonic, either from the PM field or armature reaction field is determined. The contributing harmonics are modelled individually, and the validity of the harmonic superposition method is confirmed.

3.2.1 Causes of PM Eddy Current Loss

Fundamentally, the rotor PM eddy current loss is caused by the magnetic field variation from different sources. Fig.3.1 illustrates the different origins that contribute to the magnetic field variation in the magnets. It is commonly known that the magnetic field in the PMs consists of the inherent PM field and armature reaction field penetrating the magnets. For the PM field, both the slotting opening effect and the local saturation in the tooth tip will lead to the permeability variation, causing PM field variation. On the other hand, although the amplitude of armature reaction field is much smaller than that of PM field in the surface-mounted PM machines, the field variation can be very significant. Abundant spatial harmonics due to specific slot and pole combination and winding configuration do exist in the armature reaction field. In addition, for high-speed PM machines, the relatively lower carrier ratio will inevitably introduce time harmonics, which consequently cause the variation of armature field.

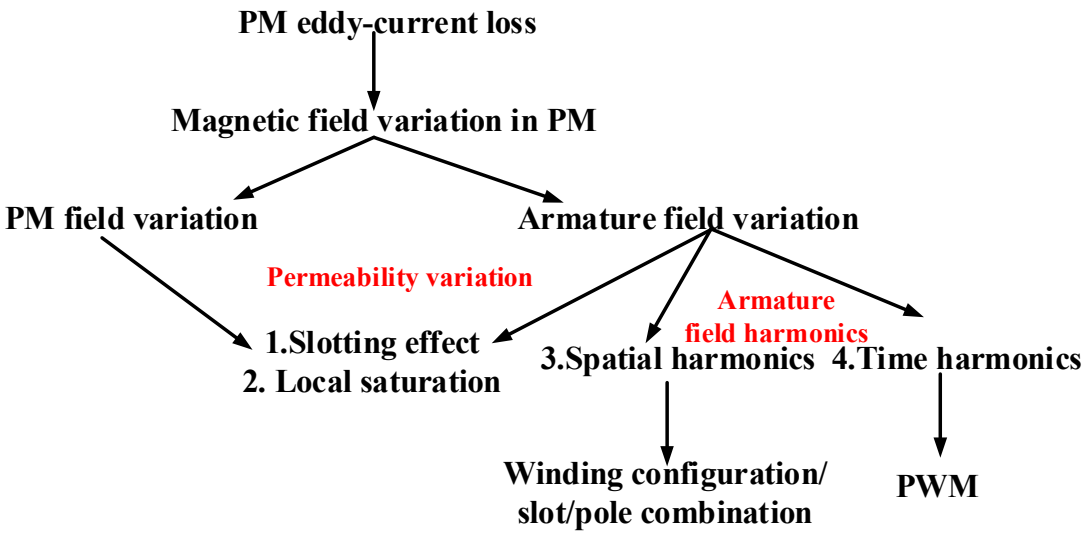

Fig.3.1. Different sources contributing to the rotor PM eddy current loss.

Hence, it is important to identify the contribution of each origin of resultant PM eddy current loss. This will provide more insight in the generating mechanism of rotor magnet loss of HSPMM so that the loss mitigation method can be accordingly adopted. In this section, special attention is paid to the determination of eddy current loss resulting from armature reaction field and PM field. Then the contribution of each harmonic in the MMF is determined based on the superposition principle.

3.2.2 Determination of Harmonic-Induced PM Eddy Current Loss Based on Frozen Permeability Method

In order to identify the harmonics due to PM field and armature reaction field, the frozen permeability method is employed in the FE computation [CHU13]. The main procedure of this method is shown in Fig.3.2.

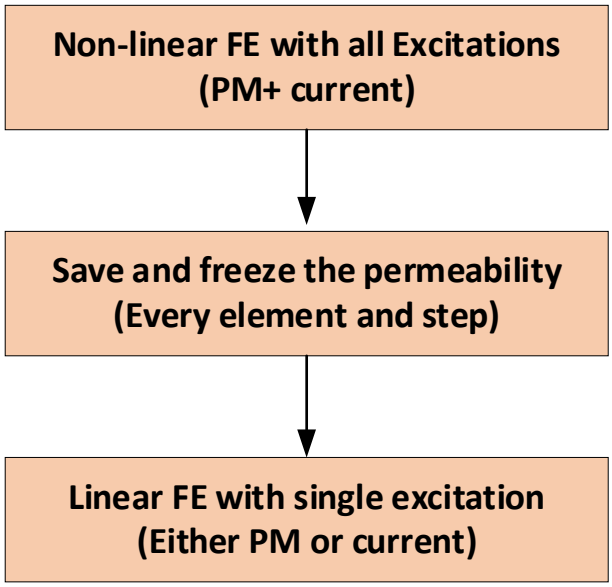

Fig.3.2. Procedure of the frozen permeability method.

The non-linear FE loss model is solved with both PM and current excitation sources. Then, the permeability of every element and step in the FE model is saved and frozen. Finally, the variable field due to PM and armature reaction can be obtained with either PM or armature reaction excitation only. The PM eddy current loss can thereby be determined in the FE model with the corresponding magnetic field.

The investigations are conducted on a 6-slot 4-pole HSPMM whose main parameters are given in Table 3.1. As shown in Fig.3.3, with the FP method, the equal potential distribution of PM field, armature reaction field and the resultant field are obtained. The profiles of the radial flux density on the magnet surface due to PM and armature reaction respectively are given in Fig.3.4. It can be seen that the on-load flux density can be strictly decomposed as the superposition of the fluxes due to PM and armature field at every rotor position.

On the other hand, it can be seen that the flux variation on the magnet surfaces results from flux fluctuations from both PM and armature reaction field. There are three drops in the value of PM field which accounts for the three slot openings in one electrical cycle. This slotting effect will be addressed in detail in the next section. The variable flux due to armature reaction field is dependent on the specific slot /pole combination and winding configuration which will also be discussed in section 3.4. Nevertheless, the slot harmonics as well as the asynchronous armature reaction harmonics with respect to the rotor lead to the production of magnet loss. Fig.3.5 illustrates the spectra of the flux density in the magnet surfaces at the rotor reference frame. Abundant triplen harmonics from both PM field and armature reaction field do exist, which are sources of magnet loss in the 6-slot 4-pole HSPMM.

For the magnet loss calculation, in [WU12], it was pointed out that the superposition of magnet loss due to PM field and armature reaction field respectively, can be applicable only when the I_d=0 control is adopted. In that case, there is no armature reaction field with same or opposite direction to the PM field. Hence, the PM eddy current loss due to different origins can be obtained in Fig.3.6. It can be seen that the total eddy current loss increases dramatically with the rise of armature current due to the increase of eddy current loss. On the other hand, the PM loss resulting from the PM field variation almost keeps constant with the increase of armature current which indicates the permeability has not be influenced much by the armature current. Fig.3.7 illustrates the eddy current loss distribution with PM and armature reaction excitation respectively, when the load current is 80A. It is obvious that a significant portion of eddy current is induced in the inner part of magnets due to armature reaction only. It indicates more asynchronous harmonics due to armature reaction penetrate deeper into the magnets compared with those from PM field. However, it remains unknown the contribution of each asynchronous armature reaction harmonic to the resultant eddy current loss. Hence, in the next section, the segregation of PM eddy current loss due to each harmonic in the armature reaction is conducted.

Table 3.1 Specifications of 6-slot 4-pole High Speed PM Machine

Parameters		Parameters	
Stator outer diameter (mm)	90	Stator yoke thickness (mm)	7
Stator bore diameter (mm)	42	Stator teeth width (mm)	10.87
Split ratio	0.46	Packing factor	0.6
Rotor outer diameter (mm)	36	Stack axial length (mm)	55
Sleeve thickness (mm)	2	Number of turns per phase	20
PM thickness (mm)	6	Pole-arc to pole pitch	1

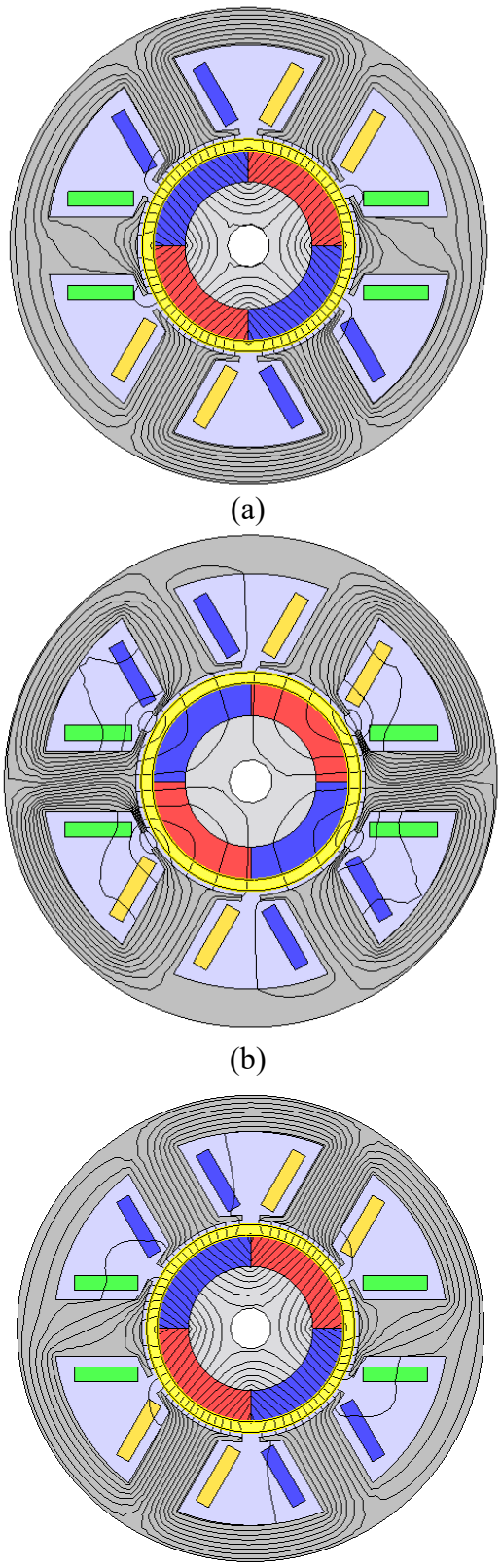

(a)

(b)

(c)

Fig.3.3. Equal potential distribution of HSPMM (*I*a=80A). (a) PM field. (b) Armature reaction field. (c) Resultant field.

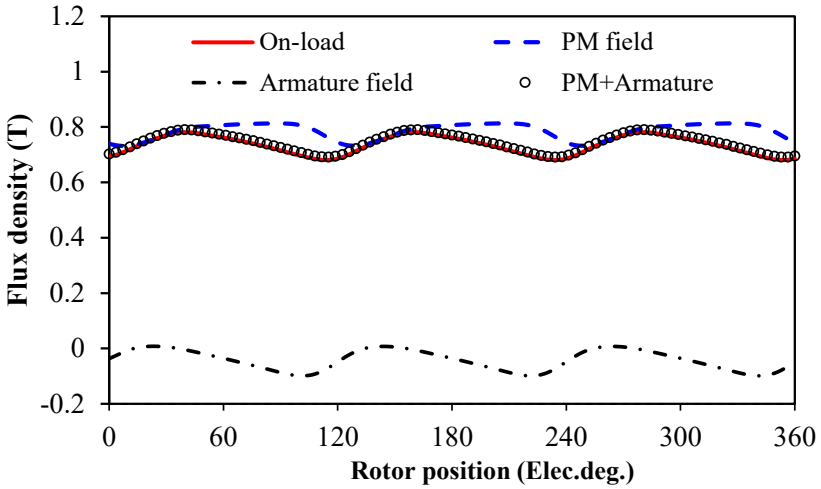

Fig.3.4. Radial flux density at magnet surfaces due to PM and armature reaction respectively (*I*a=80A).

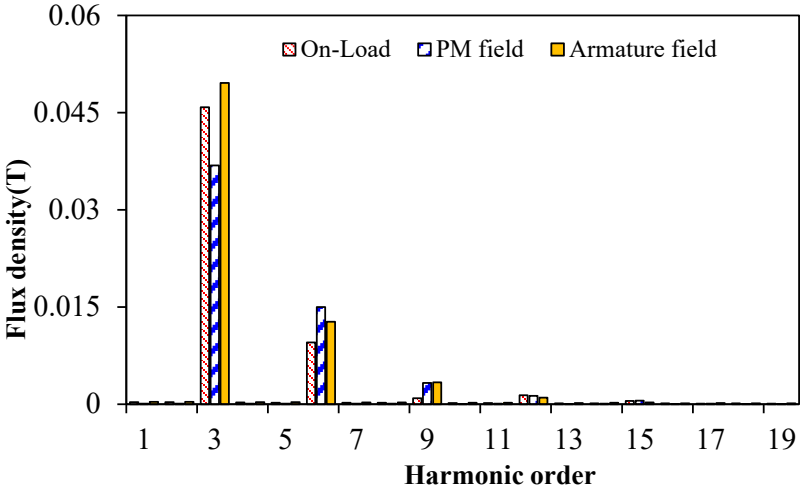

Fig.3.5. Spectra of radial flux density due to PM and armature reaction respectively (*I*a=80A).

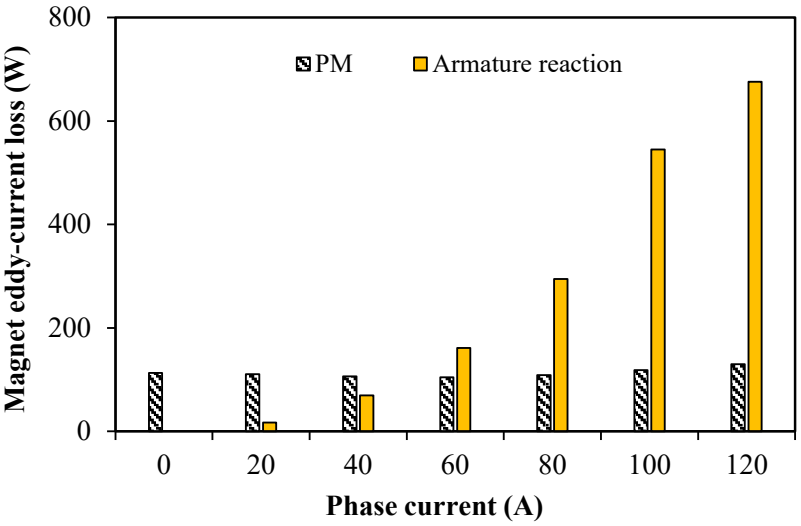

Fig.3.6. Magnet loss due to different origins.

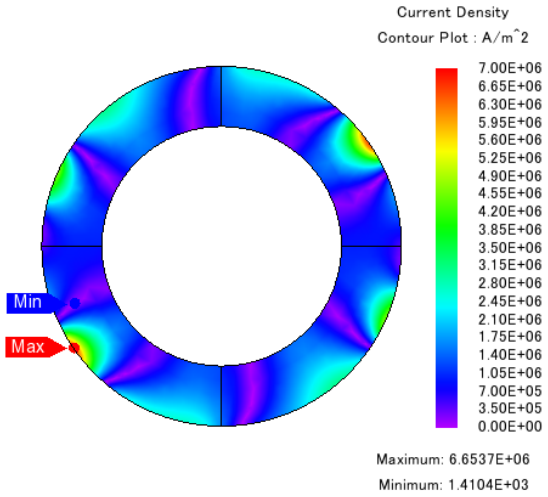

(a)

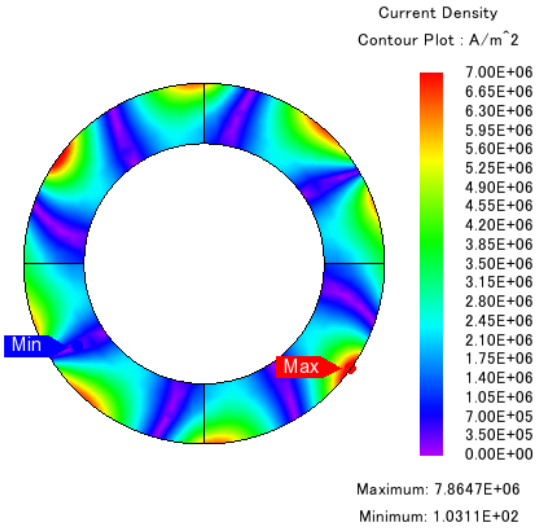

(b)

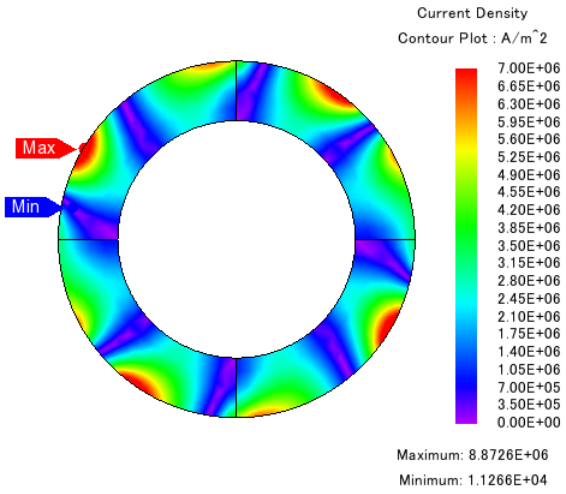

(c)

Fig.3.7. PM eddy current distribution due to different origins. (a) PM field only. (b) Armature reaction field only. (c) Resultant field. (I_a=80A).

3.2.3 Segregation of PM Eddy Current Loss Due to Each Spatial Harmonic in Armature Reaction

For a typical 6s/4p-Non-overlapping HSPMM, the stator MMF can be written as:

$$\begin{aligned} F_s(\theta,\mathrm{t}) &= \sum_{h}^{\infty} F_h \cos(k\theta_s \pm \omega_s \mathrm{t}) \\ &= F_2 \cos(2\theta_s - \omega_s \mathrm{t}) + F_4 \cos(4\theta_s + \omega_s \mathrm{t}) + F_8 \cos(8\theta_s - \omega_s \mathrm{t})... \end{aligned} \tag{3.1}$$

where F_h denotes the amplitude of hth- harmonic, w_s denotes the electrical angular frequency. In the rotor reference frame, the following can be observed:

$$\theta_s = \theta_r + \omega_r t \tag{3.2}$$

$$\omega_r = \frac{\omega_s}{p} \tag{3.3}$$

substituting into (3.1):

$$F_s(\theta,\mathrm{t}) = F_2 \cos(2\theta_r) + F_4 \cos(4\theta_r + 3\omega_s \mathrm{t}) + F_8 \cos(8\theta_r + 3\omega_s \mathrm{t}) + F_{10} \cos(10\theta_r + 6\omega_s \mathrm{t})... \tag{3.4}$$

As can be seen from (3.4), the 4th and 8th special harmonics due to armature reaction contributes significantly to the 3th spatial harmonic seen by the magnet. The 10th and 14th special harmonics lead to the presence of 6th harmonics in the magnet. Table 3.2 lists the harmonic characteristics of MMF in the 6s/4p HSPMM. Fig.3.7 illustrates the amplitudes of the MMF spatial harmonics when the load current is 80A.

Fig.3.8 shows the basic procedure for the armature reaction harmonic induced magnet loss segregation. The amplitude of each MMF harmonic should be determined in the FE model at the first stage. The permeability is saved under the load condition. Then, the specific harmonic is modelled with the method introduced in [ZHU18]. After that, the PM permanence is set to be zero and the stator and rotor iron permeability is frozen. Finally, with the specific harmonic as the only excitation modelled in step 2, the corresponding magnet loss is calculated.

The key of loss segregation is modelling of individual harmonic in MMF. As shown in Fig.3.9, an outer slotless stator consists of eight pieces of sinusoidally magnetized PMs with the speed of $0.5\omega_r$ is set up. The stator PMs are distributed evenly at the inner surface of the stator. The thickness of stator PMs should be as thin as possible so that the distribution of stator MMF can be equivalent. The remanence of stator PMs are adjusted according to the obtained amplitude of the specific MMF harmonic. Similarly, the initial position of the stator PMs is adjusted according to the obtained phase angle of the specific MMF harmonic.

Table 3.2 Harmonic characteristics of MMF in 6s/4p- HSPMM

Harmonic order		Winding factor	Rotation direction
Order	Seen by rotor	K_h	*Sgn*
2	0(DC)	0.866	+
4	3	0.866	-
8	3	0.866	+
10	6	0.866	-
14	6	0.866	+
16	9	0.866	-
20	9	0.866	+

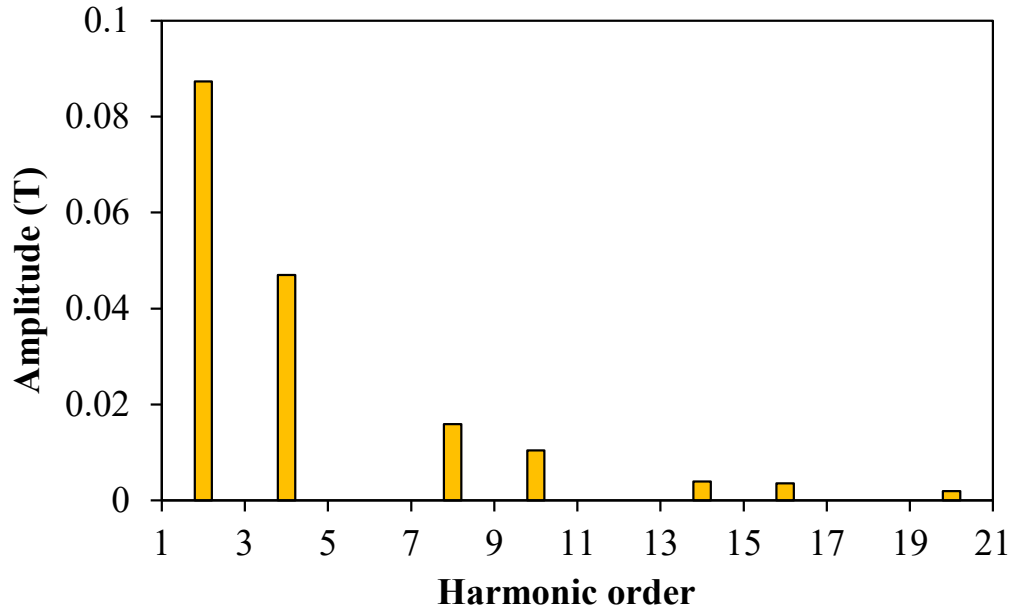

Fig.3.8. Amplitude of each spatial harmonic of MMF (*I*a=80A).

According to the amplitude and phase angle shown in Table 3.3, each corresponding slotless model is set up. The field distributions of the dominant harmonics are illustrated in Fig.3.10. It can be seen that the 2nd harmonic penetrates into the rotor magnets deeper than the other two harmonics. In addition, the value of the 2nd harmonic is larger as shown in Fig.3.7. However, the 2nd harmonic rotates at the same speed and direction from the rotor point of view. Hence, no eddy current loss would be induced from the 2nd harmonic.

On the other hand, both the 4th and 8th harmonics penetrate into the permanent magnets and rotate asynchronously with the rotor, inducing significant variation of flux density in the magnets. Fig.3.11 illustrates the flux density at the surface of rotor magnets from different origins. It can be seen that the superposition of the 2nd and 4th and 8th harmonics is almost identical to the original MMF, indicating the validity of harmonic modelling techniques.

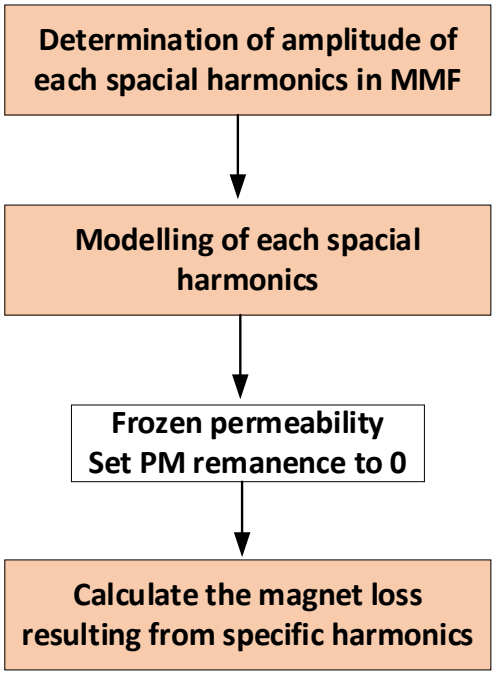

Fig.3.9. Procedure for armature reaction harmonic induced magnet loss segregation.

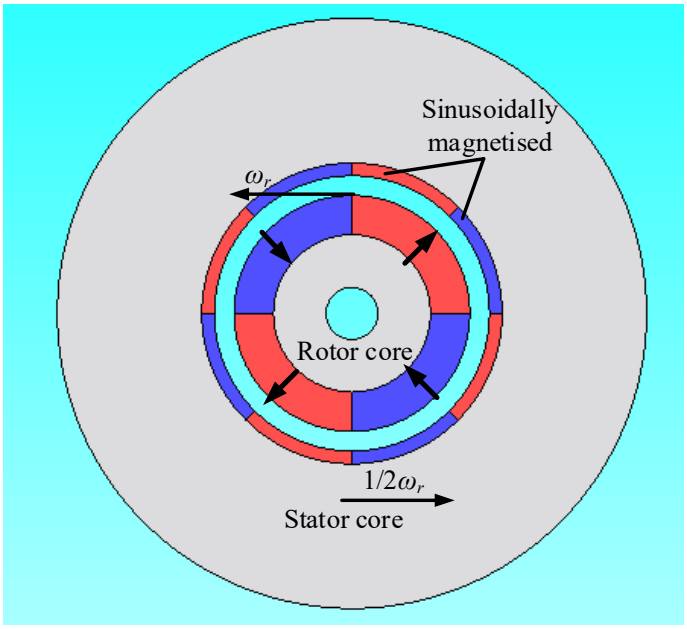

Fig.3.10. Modelling of 4th harmonic in MMF.

Table 3.3 Amplitude and phase angle of dominant MMF harmonics (*I*a=80A)

Harmonics	**Amplitude (T)**		**Phase(°)**	
	Slotted model	Slotless model	Slotted model	Slotless model
2	0.0867	0.0865	180.7	180.2
4	0.0480	0.0473	168.68	167.34
8	0.0163	0.0159	345.70	344.69

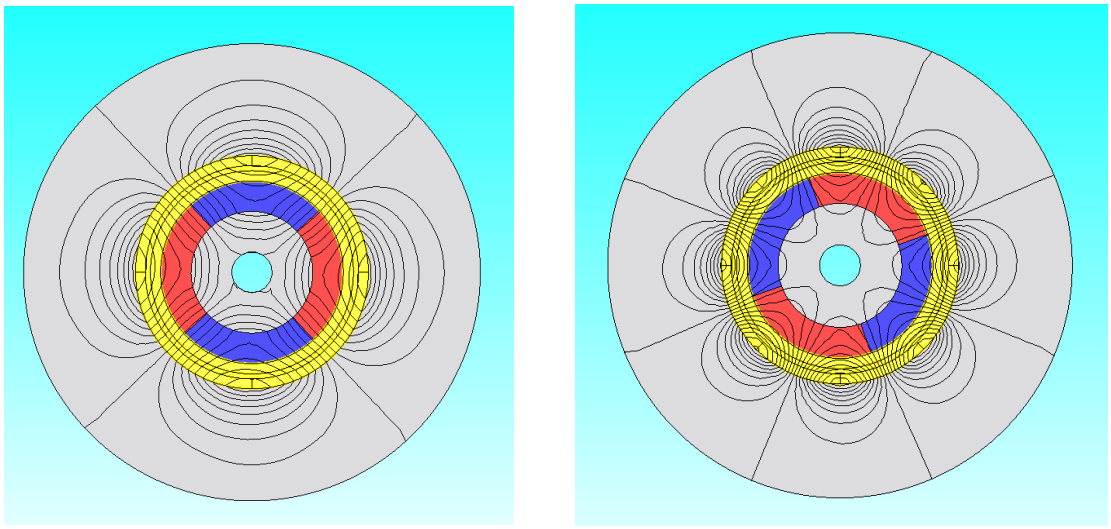

(a) (b)

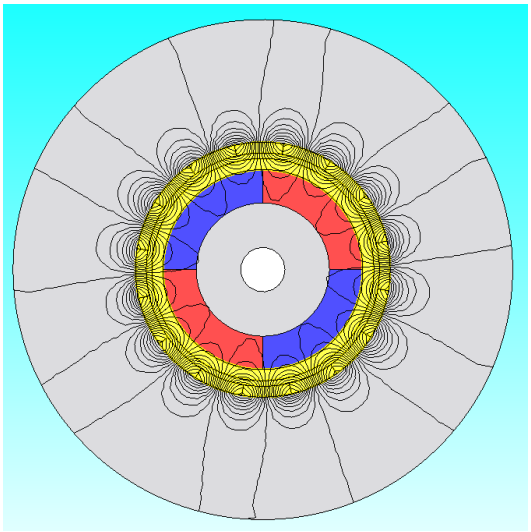

(c)

Fig.3.11 Distribution of each MMF spatial harmonic (I_a=80A). (a) 2nd spatial harmonic. (b) 4th spatial harmonic. (c) 8th spatial harmonic.

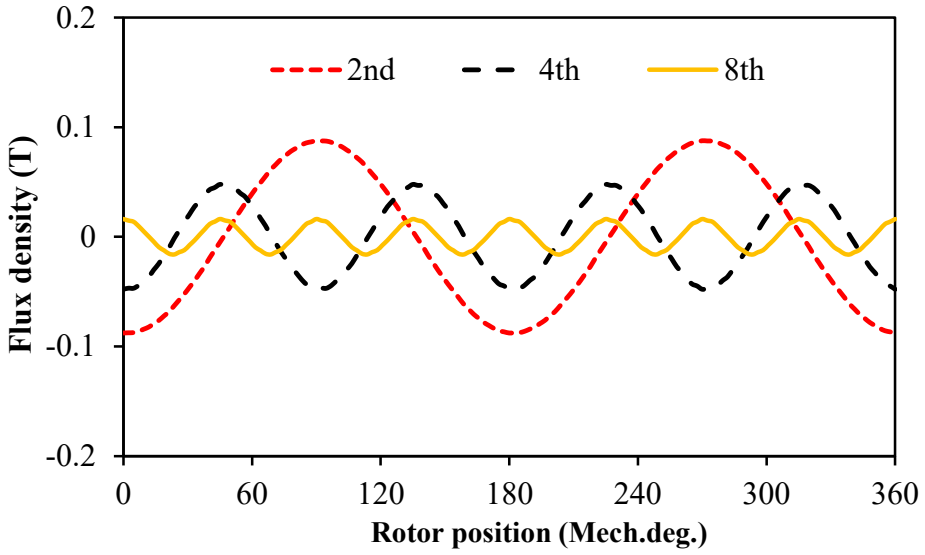

(a)

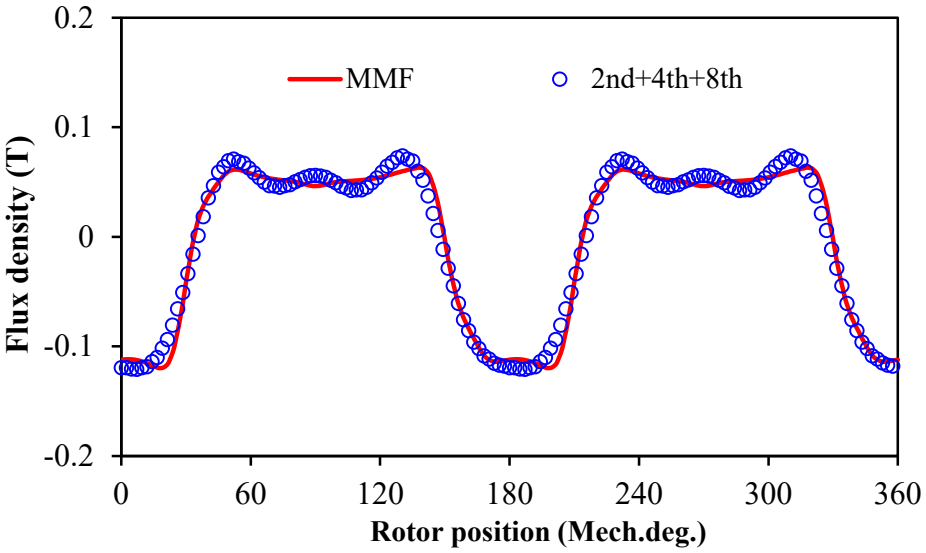

(b)

Fig.3.12. Flux density in the rotor magnet surface due to different sources. (a) Dominant harmonics. (b) Comparison of MMF and superposition of dominant harmonics.

Fig.3.13 illustrates the eddy current distributions due to different harmonic sources. Fig.3.14 compares the amplitude of eddy current loss due to different harmonic sources. The following can be observed:

1) It is obvious that the 4^{th} spatial harmonic dominates the contribution of the induced eddy current loss due to larger wavelength and amplitude. The 8^{th} spatial harmonic contributes

less than 2% of the total eddy current loss due to armature reaction.

2) The superposition of eddy current loss due to 4th harmonic and 8th harmonic (276.92W) is almost identical to the loss produced by the 4th and 8th harmonics acting together. It indicates that the interaction between the 4th and 8th harmonics is negligible in high speed PM machines.

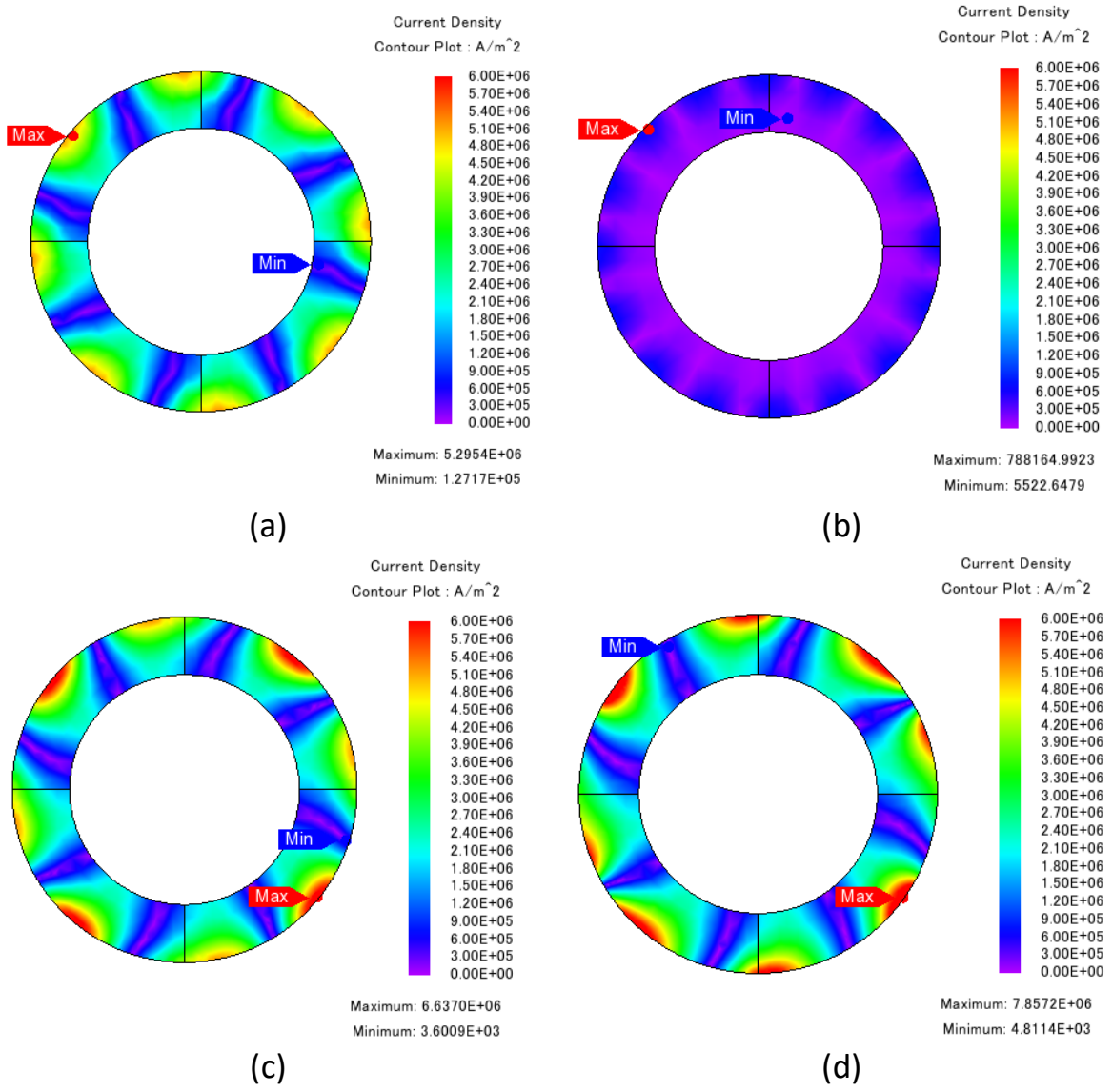

Fig.3.13. Distributions of eddy current due to different sources (I_a=80A). (a) 4th spatial harmonic. (b) 8th spatial harmonic. (c) 4th and 8th spatial harmonics. (d) MMF.

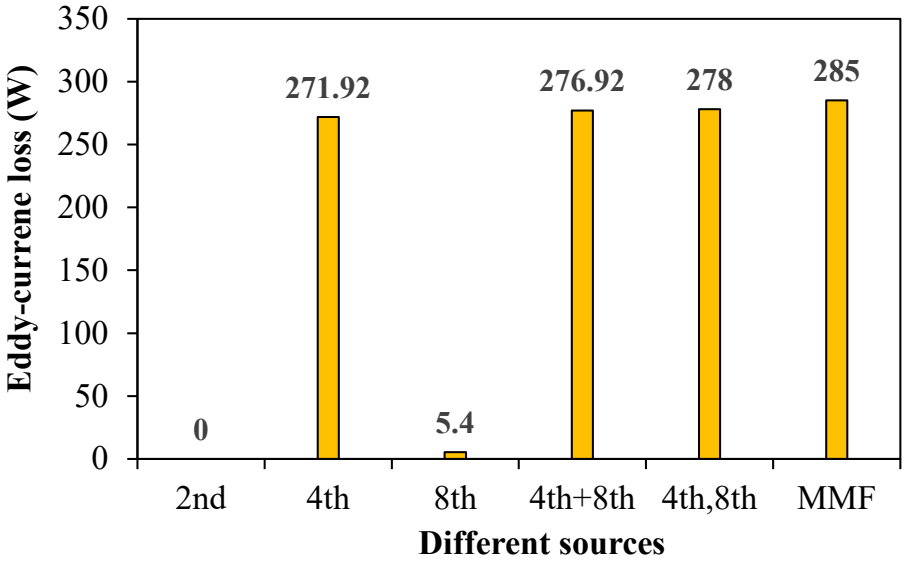

Fig.3.14. Resultant PM eddy current loss due to different sources.

3.3 Analysis of Slotting Opening Effect on the Rotor Magnet Loss

In this section, the slotting opening effect on the resultant eddy current loss of the 4-pole HSPMM with different numbers of stator slots is investigated. The analysis is firstly focused on the 6-slot/4-pole HSPMM. The slotting opening effects on the eddy current loss resulting from open-circuit and armature reaction field are comprehensively studied.

3.3.1 Slotting Effect on Magnet Loss Due to PM Harmonics

From Fig.3.5, it can be seen that significant asynchronous PM harmonics do exist in the magnet surface which induce the open-circuit magnet loss. Fig.3.15 shows the variation of flux density at the magnet surface with different slot opening angle. It is clear that the flux distortion become more serious with the enlarged slot opening angle. It can be seen from Fig.3.15 (b) that the amplitude of the 3th harmonic keeps increasing with the slot opening.

Fig.3.16 illustrates the variation of magnet loss due to PM harmonics. Hence, for the 6-slot/4-pole HSPMM. It is obvious that the eddy current loss due to PM harmonics is minimum when the slot opening angle is zero. Hence, a stator with closed slot or magnetic wedge should be adopted from the perspective of reduction of magnet loss.

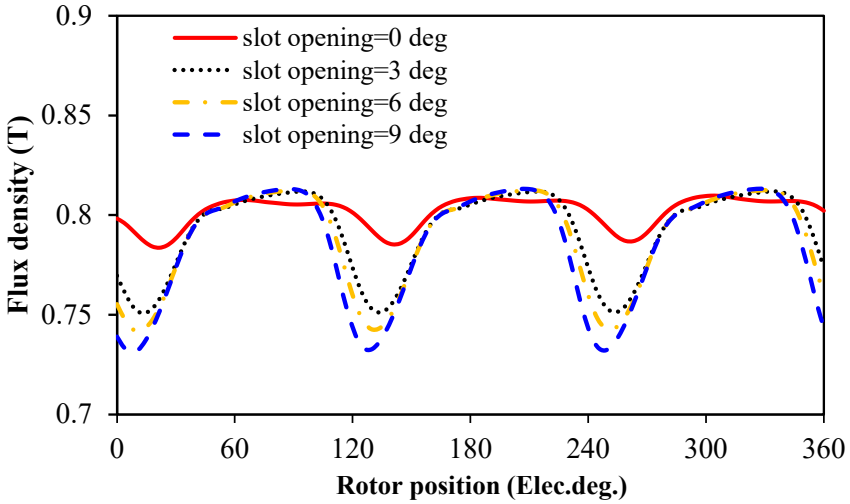

(a)

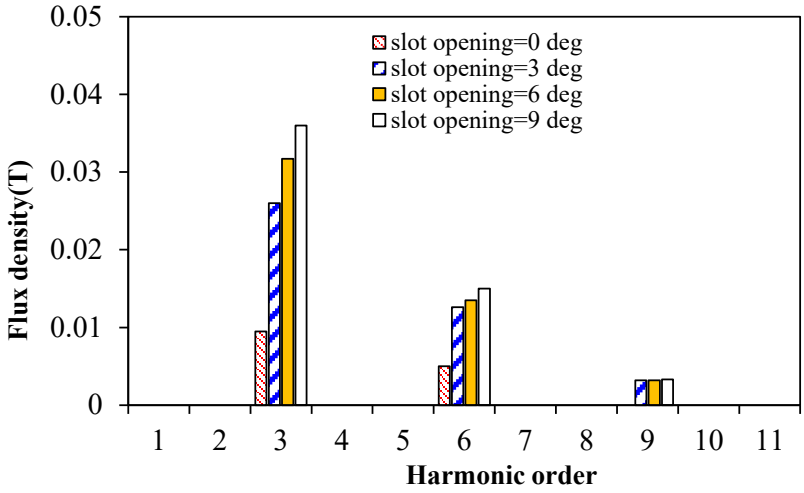

(b)

Fig.3.15. Variation of flux density in magnet surface with different slot opening angle. (a) Flux density waveforms. (b) Spectra.

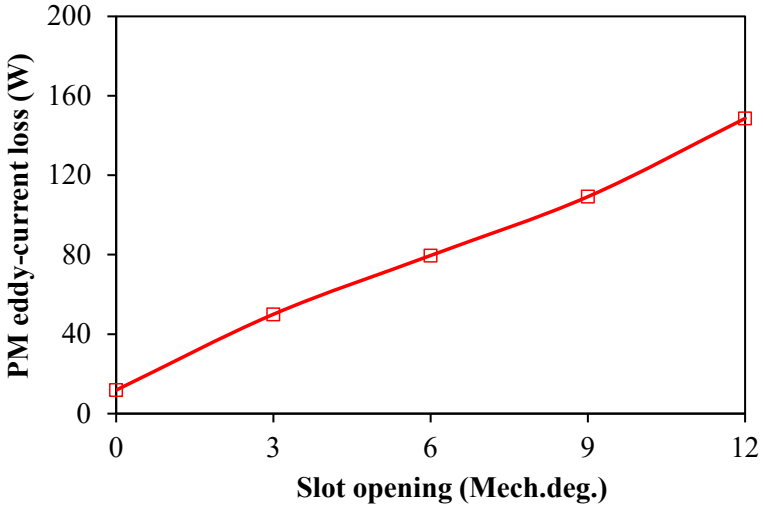

Fig.3.16. Variation of magnet loss due to PM harmonics with different slot opening angle.

3.3.2 Slot Opening Effect on Armature Reaction Field Induced Magnet Loss

As has been proved in Section 3.2.3, the 4th spatial harmonic in the armature reaction accounts for the vast majority of contributing sources to the magnet loss due to armature reaction. However, the 4th spatial harmonic consists of both the original 4th spatial harmonic as well as the modulated 4th harmonic due to slot opening effect [ZHU18]. The 2nd fundamental harmonic in the stator MMF, which is modulated by the 6th stator permanence harmonic, generates the 4th slot harmonic. Hence, in this section, the decomposition of portions of the original 4th spatial harmonic in the armature reaction and the modulated 4th slot harmonic in the contribution of magnet loss is firstly quantified.

The flowchart for the determination of magnet loss due to the original MMF harmonics is illustrated in Fig.3.17. The key procedure is to obtain the original MMF harmonics before modulation. Hence, the equivalent current sheet method (ECSM) is adopted in order to approximate an identical MMF with the slotted stator. The current sheet is placed at the slot opening as shown in Fig.3.18. FSCW denotes the conventional FE model with winding in the stator slot. It should be noted that the rotor magnet is closer to the stator MMF in the ECSM-based FE model. The amplitude of harmonics with higher order in ECSM tends to be larger with same current, as shown in Fig.3.19. It can be seen that the 4th spatial harmonic is significantly increased. The flux penetrated into the magnet will be increased as well, as shown in Fig.3.18. Hence, in order to obtain an equivalent MMF, a calibration factor k is defined as the ratio between the amplitudes of specific harmonic in the FSCW and ECSM models, respectively.

$$k = \frac{A_v^F}{A_v^E} \tag{3.5}$$

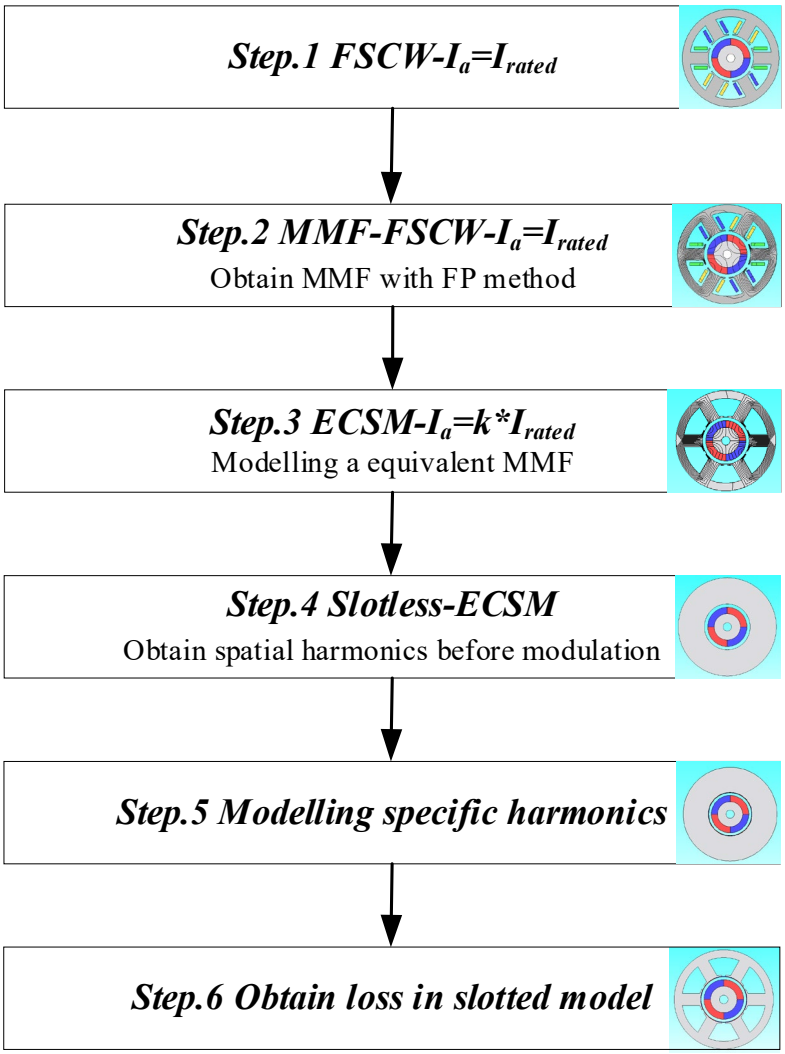

Fig.3.17. Flowchart for the determination of magnet loss due to original MMF harmonics.

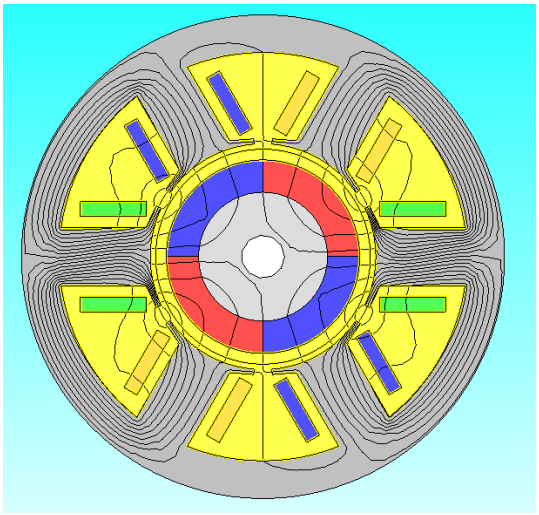

(a)

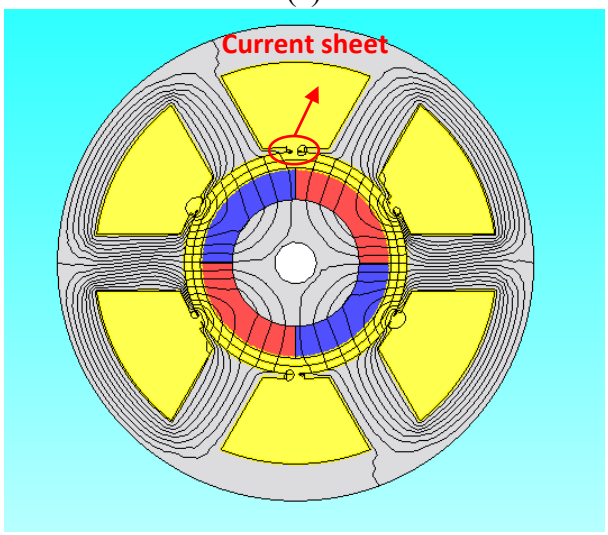

(b)

Fig.3.18. Equal potential distributions of armature reaction in different models. (a) FSCW (b) ECSM.

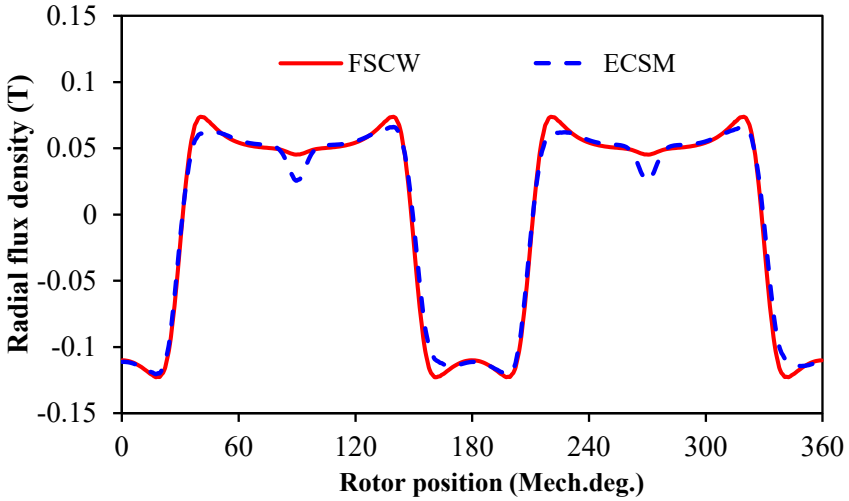

Fig.3.19. Comparison of radial air gap flux densities due to MMF by FSCW and ECSM models (I_a=80A).

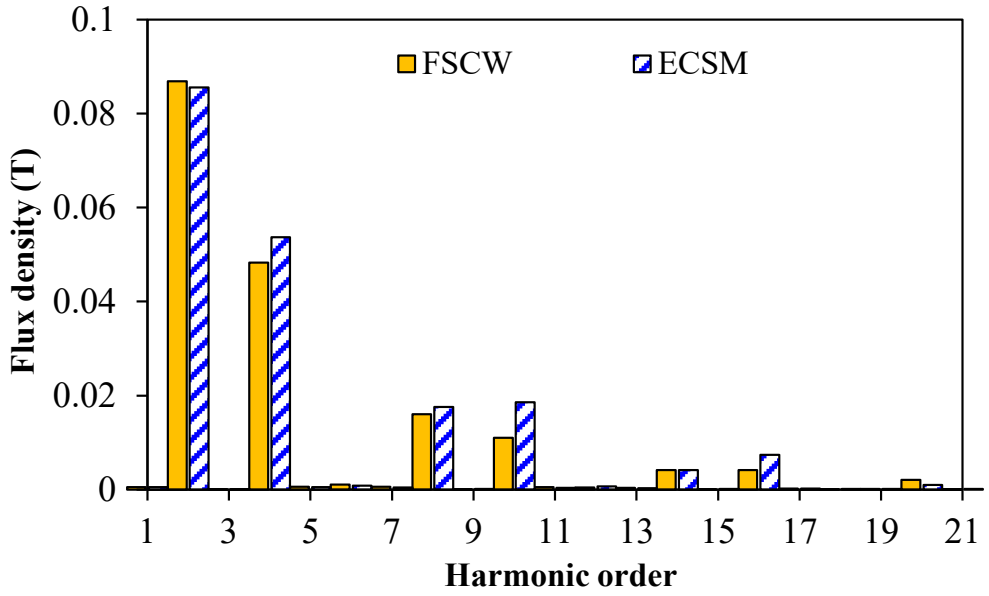

(a)

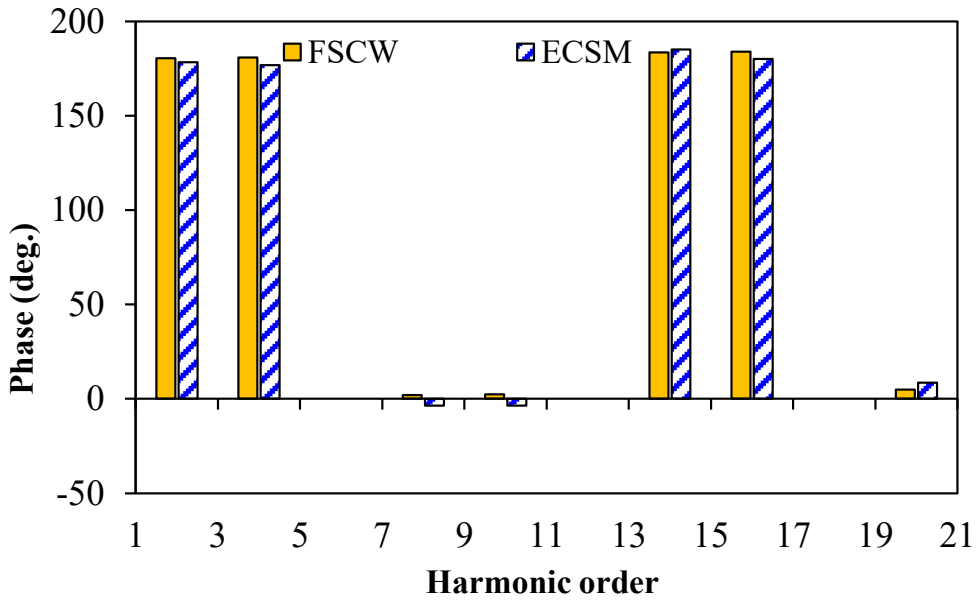

(b)

Fig.3.20. Comparison of radial air gap flux density spectra due to MMF by FSCW and ECSM models (I_a=80A). (a) Amplitude. (b) Phase angle.

Fig.3.21 shows the air gap flux densities due to MMF in two different models. It can be seen that the 4th spatial harmonic in the ECSM-based model is the same with that in FSCW model. Although the 10th spatial harmonic in the ECSM model is still larger than that in FSCW model,

the contribution of the 10^{th} harmonic to the generation of the resultant magnet loss is negligible. Thus, the magnet loss due to MMF in the FSCW model is the same with that in the ECSM model after calibration.

In order to further obtain the original MMF before slot modulation, the slotless stator is used to replace the slotted stator in ECSM-based model. Hence, the amplitude and phase of specific harmonic before modulation can be determined. Then, with the same modelling method mentioned in the previous section, the contributing spatial harmonic in the MMF without modulation can be obtained in step 5. Finally, the slotless stator is replaced by the slotted stator so that the magnet loss due to the original MMF harmonics can be obtained. Hence, the amplitude of the original 4^{th} spatial harmonic in the MMF can be obtained. On the other hand, the modulated 4^{th} harmonic from the 2^{nd} spatial harmonic can be determined with the same method.

Fig.3.22 shows the amplitude of the original 4^{th} harmonic in the MMF and the 4^{th} harmonic modulated by the 2^{nd} harmonic in the MMF. Compared with the original MMF harmonics, the amplitude of the modulated 4^{th} harmonic is very small. On the other hand, the amplitude of modulated 4^{th} harmonic will be increased with the enlarged slot opening angle due to enhanced modulation effect. However, the modulated 4^{th} harmonic does contribute to a small portion of magnet loss, as can be seen in Fig.3.22.

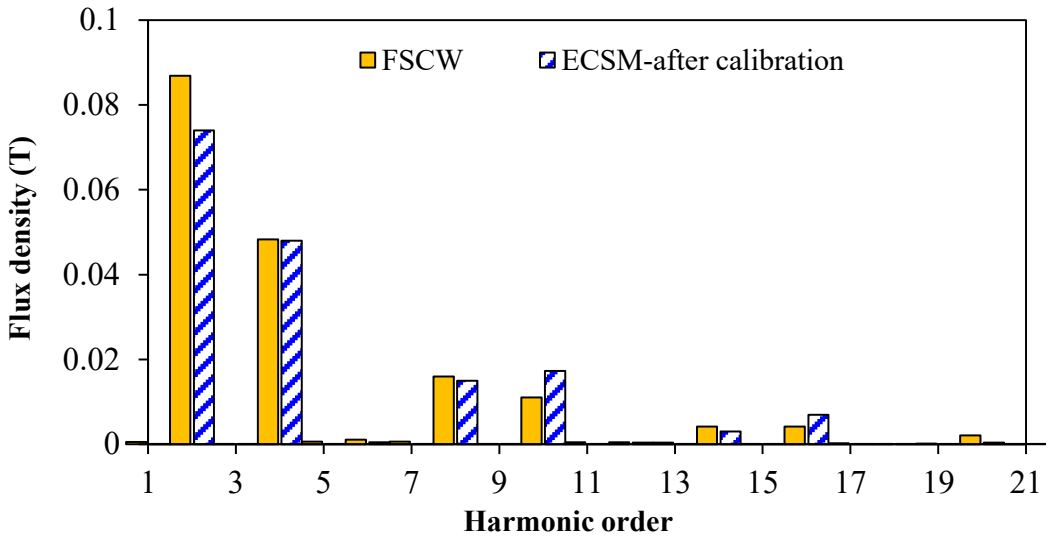

(a)

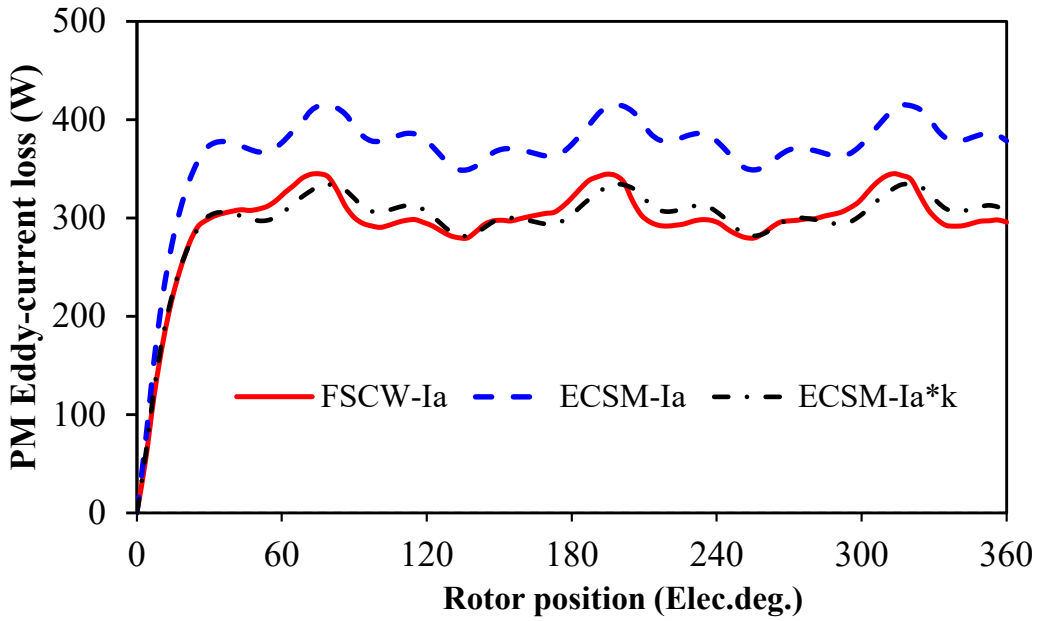

(b)

Fig.3.21. Comparison of air gap flux density spectra and magnet loss due to MMF (I_a=80A). (a) Amplitude. (b) Magnet loss.

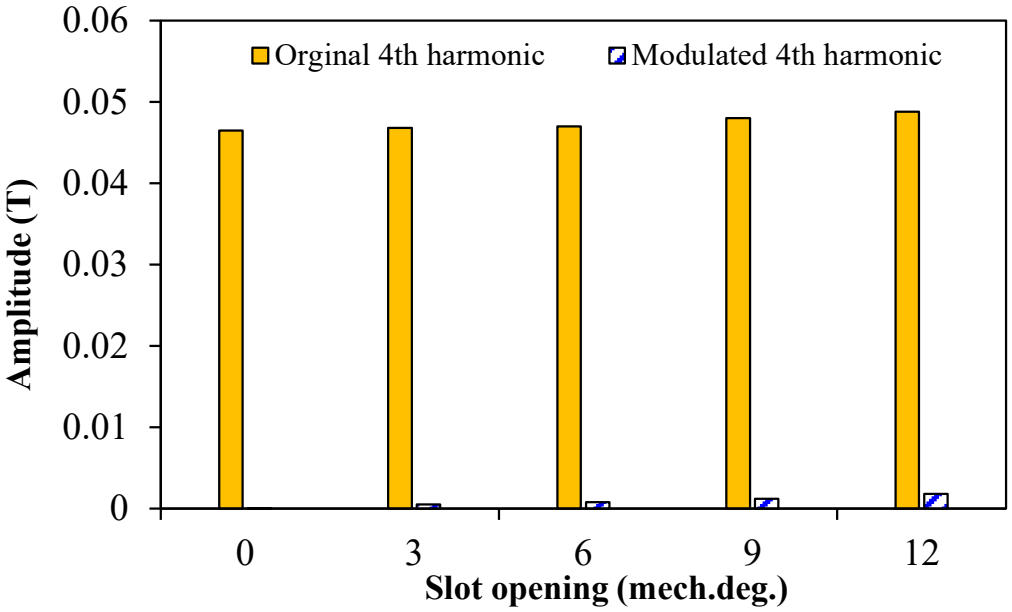

Fig.3.22. Variation of amplitude of original and modulated 4th harmonics with slot opening angle.

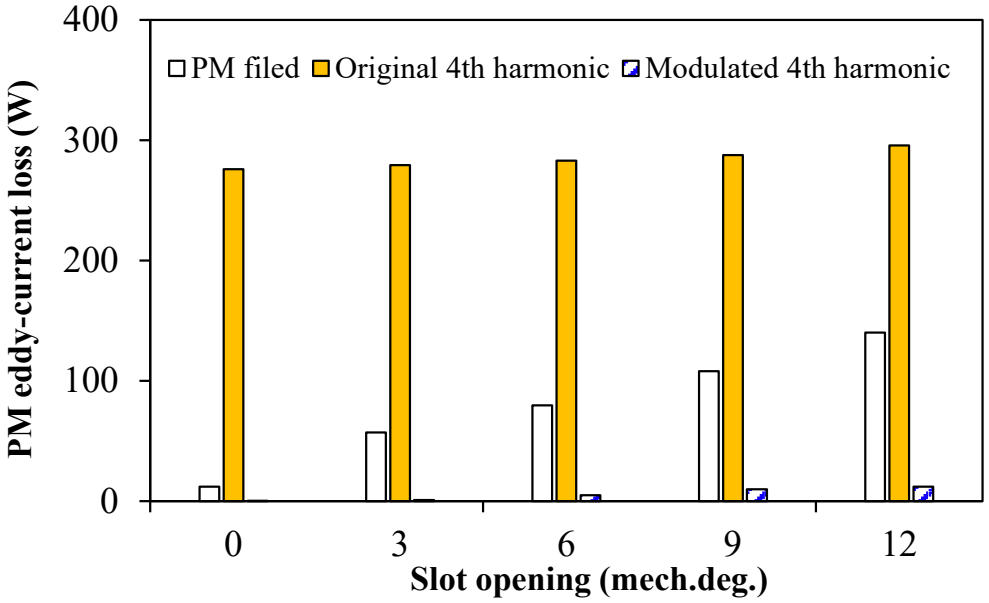

Fig.3.23. Variation of magnet loss due to different origins with slot opening angle (I_a=80A).

3.4 Comparison of Armature Reaction Induced Magnet Loss with Different Slot and Pole Number Combinations

In the previous section, the influential harmonics for the magnet loss generation in the armature reaction of the 6-slot 4-pole HSPMM are quantified. However, the spatial harmonics in MMF are significantly related with the slot and pole number combination. For the four-pole HSPMM, it remains unknown how the stator winding configuration which yields distinct spatial MMF harmonics affects the generation of magnet loss. Hence, in this section, three machines with same pole number of 4 but different slot numbers of 6, 9, 12 are compared in terms of armature reaction induced magnet loss. The selected topologies are typical machines equipped with coil pitch of 1, 2, 3, as shown in Fig.3.24. Of all the machines to be investigated, the rated torque is around 5.45Nm. The rated current is 80A. The specifications of three machines are given in Table 3.4.

Table 3.4 Parameters of Machines

Parameter	A	B	C
Pole number	4		
Slot number	6	9	12
Coil pitch	1	2	3
Stator bore diameter(mm)	42	43.4	49.8
Tooth body width(mm)	10.8	8.28	8.2
Stator yoke height(mm)	7.0	5.4	7.45
Slot opening(mm)	3.29	2.47	0.9
Stator outer diameter(mm)	90		
Stack length(mm)	55		
Sleeve thickness	2		
Number of turns per phase	20		
Magnet thickness(mm)	6		
Magnet μ_r	1.05		
Remanence(T)	1.2		
Magnetisation	Parallel		
Magnet conductivity($(\Omega \cdot m)^{-1}$)	6.67E+05		

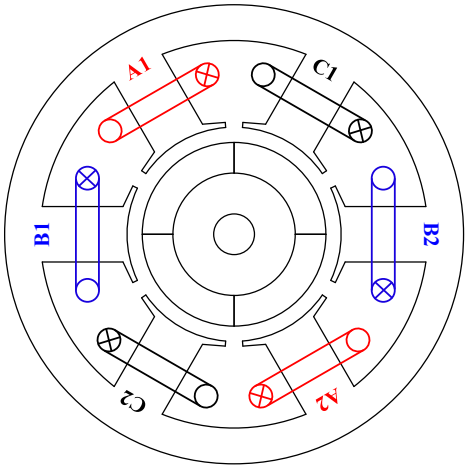

(a)

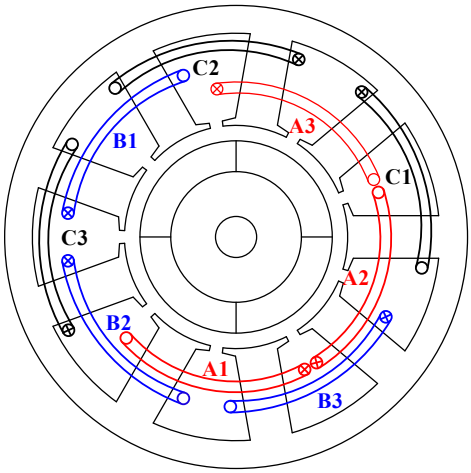

(b)

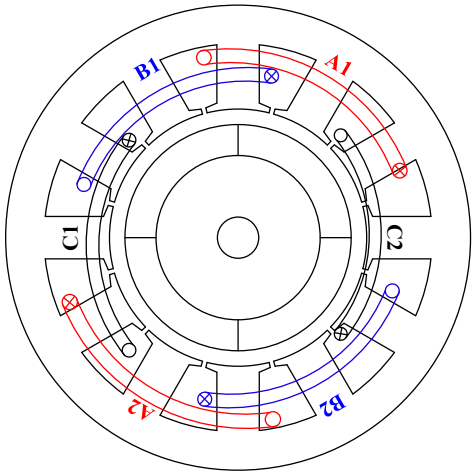

(c)

Fig.3.24. Cross-sections of investigated 4-pole HSPMMs with different coil pitch.

Fig.3.25 illustrates the variation of magnet loss due to MMF with phase current for three machines. It can be observed that the armature reaction induced magnet loss in the 6-slot 4-pole HSPMM is the maximum of all. On the other hand, the HSPMM with 12-slot/4-pole and full pitched winding shows distinct advantages in maintaining a lower magnet loss. In order to further explain this phenomenon, each contributing harmonic in the MMF of three machines should be determined with the proposed loss segregation method in Section 3.2.3. Thus, in this section, the amplitude of each spatial harmonic is firstly identified. Then, the contribution of each harmonic to the magnet loss can be further determined. For comparison of three machines, it is essential to identify the characteristics of the inherent MMF. Then, the harmonics which actually account for the generation of magnet loss can be compared. The low-order pass filter effect of air gap and magnet is therefore revealed.

In [WU12], it was pointed out that the amplitude of spatial harmonics is dependent on both the winding factor and the harmonic order. For the 6-slot/4-pole and 12-slot/4-pole HSPMMs, the winding factors for all the feasible harmonics are 0.866 and 1, respectively. For the 9-slot 4-pole HSPMM, only the fundamental spatial harmonic and slot harmonics, such as the 7^{th} harmonic and the 11^{th} harmonic, have a relatively higher winding factor of 0.945. That explains why the amplitude of sub-harmonic is smaller than the 7^{th} harmonic in the 9-slot 4-pole HSPMM.

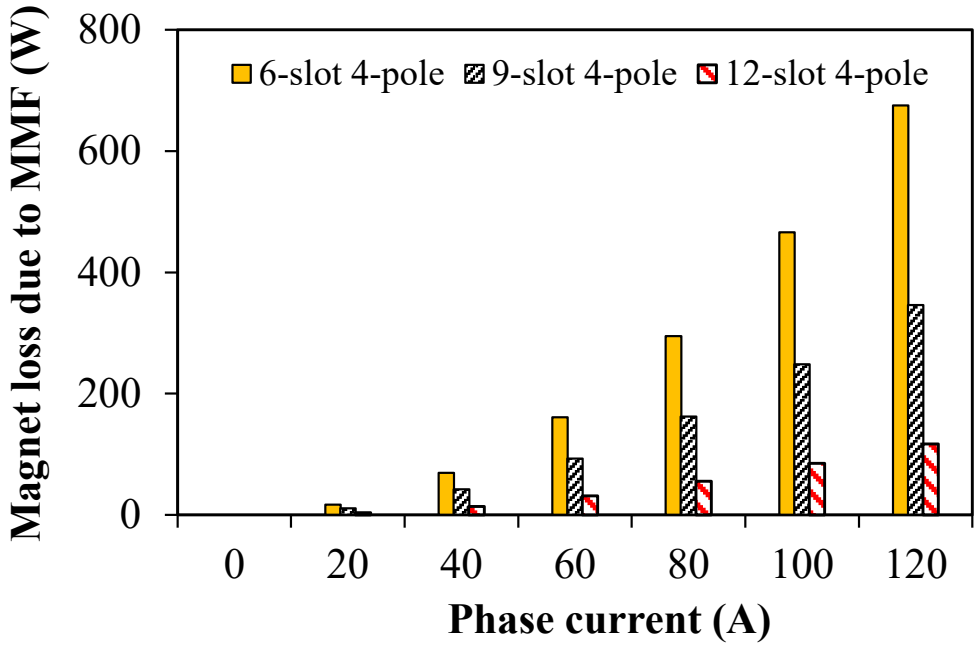

Fig.3.25. Variation of magnet loss due to MMF with phase current.

Table 3.5 Harmonic characteristics of MMF in three machines

	Harmonic order			Winding factor			Rotation direction		
Order	Frequency seen by rotor			K_w			*sgn*		
	6s/4p	9s/4p	12s/4p	6s/4p	9s/4p	12s/4p	6s/4p	9s/4p	12s/4p
1	-	1.5 *f*	-	-	0.139	-		-	
2	0(DC)			0.866	0.945	1	+		
4	3*f*	3*f*	-	0.866	0.060	-	-		
5	-	1.5 *f*	-	-	0.060	-		+	
7	-	4.5 *f*	-	-	0.945	-		-	
8	3*f*	3*f*	-	0.866	0.139	-	+		
10	6*f*	6 *f*	6 *f*	0.866	0.139	1	-		
11	-	4.5 *f*	-	-	0.945	-		+	
13	-	7.5 *f*	-	-	0.060	-		-	
14	6*f*	6 *f*	6 *f*	0.866	0.060	1	+		

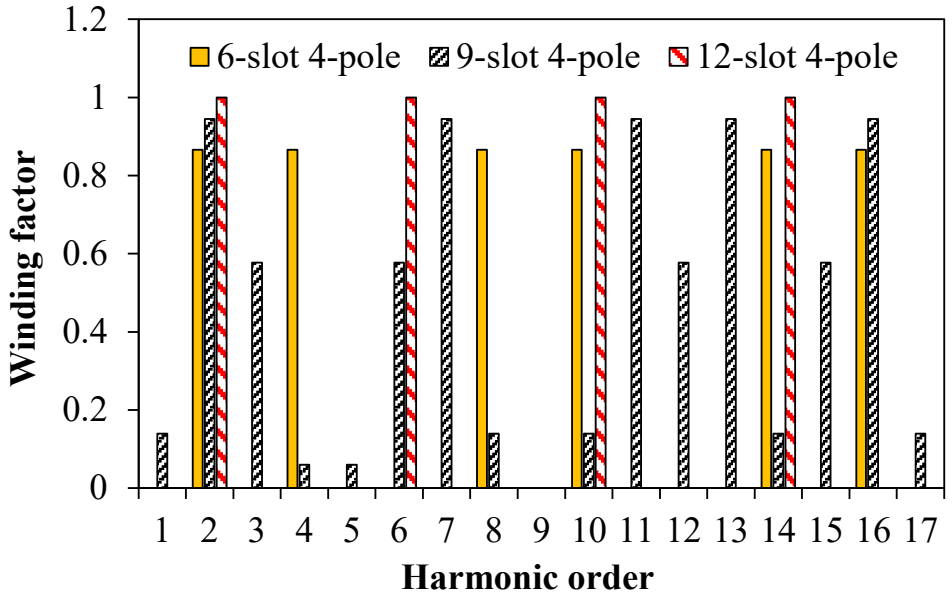

Fig.3.26. Winding factors for each MMF harmonic in three machines.

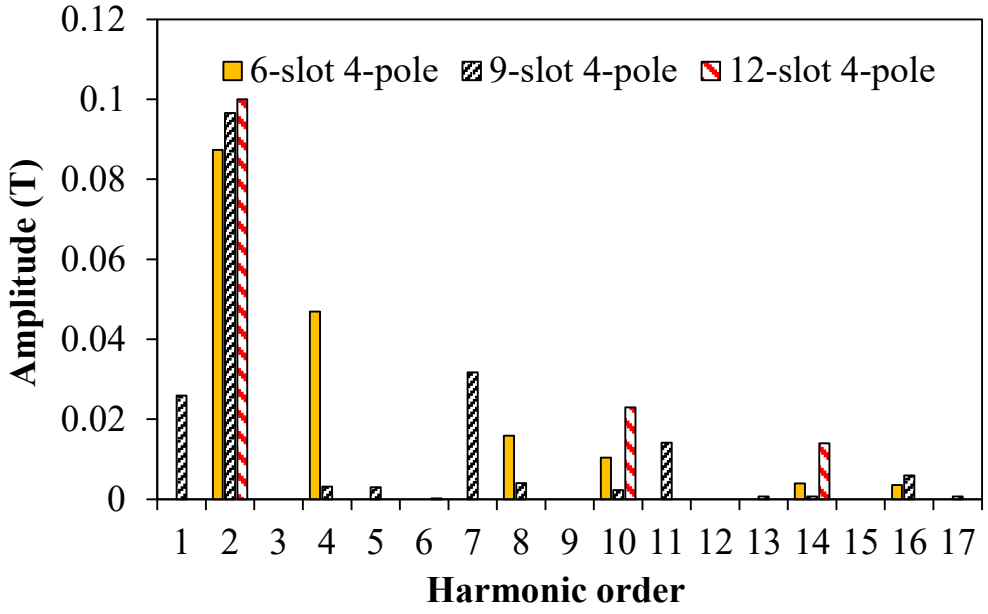

Fig.3.27. Spectra of air gap flux density due to MMF for three machines (I_a=80A).

In order to further identify the contributing harmonic sources for the three machines, the flux density inside the magnet are extracted at the selected two points shown in Fig.3.28. The two points are selected to be at the outer and inner surface of magnets, respectively. The penetration depth of harmonics can be further observed by the comparison of amplitudes in these two points. Fig.3.29 and Fig.3.30 show the flux density waveforms at this two points and the corresponding spectra. Fig.3.32 illustrates the magnet loss due to different harmonic sources. Several findings are summarized as follows:

1) It is interesting to note that only the amplitude of the sub-harmonic (Point 1) in MMF of the 9-slot/4-pole machine is increased compared with that at Point 2. All the other harmonics are significantly reduced in terms of amplitude. This can be attributed to the larger wavelength of the sub-harmonic. The penetration depth of lower order harmonic is larger than that of higher order harmonic, which is reflected in Fig.3.29. Hence, the eddy current loss at the inner side of magnets is mainly caused by the lower-order harmonics in MMF.

2) On the other hand, the relatively thicker air gap and PM in HSPMM act as the low-order harmonic filter [MA19]. The flux weakening effect becomes more obvious for the higher order harmonics than the lower order harmonics. From Fig.3.27 and Fig.3.28, it can be seen that the amplitudes of the 12th harmonics for all three machines at point 2 become negligible compared with those at point 1. In addition, the amplitude of the 9th harmonic resulting from

the 7th and 11th spatial harmonics in the 9-slot/4-pole HSPMM at point 1 is also significantly reduced. Hence, the eddy current loss at the outer side of magnet is caused by both the super-harmonics and sub-harmonics in MMF.

3) The value of armature-reaction induced eddy current loss depends both the penetration depth and the amplitude of MMF harmonics. For the 12-slot/4-pole HSPMM, only the 10th and 14th spatial harmonics are noticeable on the magnet outer surface. Those harmonics penetrate into the magnets with a smaller depth. In addition, those higher order super-harmonics normally have a lower amplitude as illustrated in Fig.3.25. Hence, these two factors yield the smallest magnet loss in three machines. On the other hand, although significant sub-harmonics do exist in the MMF of the 9-slot/4-pole HSPMM, its amplitude is relatively low due to small winding factor. The magnet loss due to sub-harmonics is comparable to that from the 7th harmonic. On the contrary, the 4th spatial harmonic with relatively larger amplitude in the 6-slot 4-pole yields significant magnet loss at both the outer and inner sides of the magnet. This accounts for its maximum value of magnet loss in three machines.

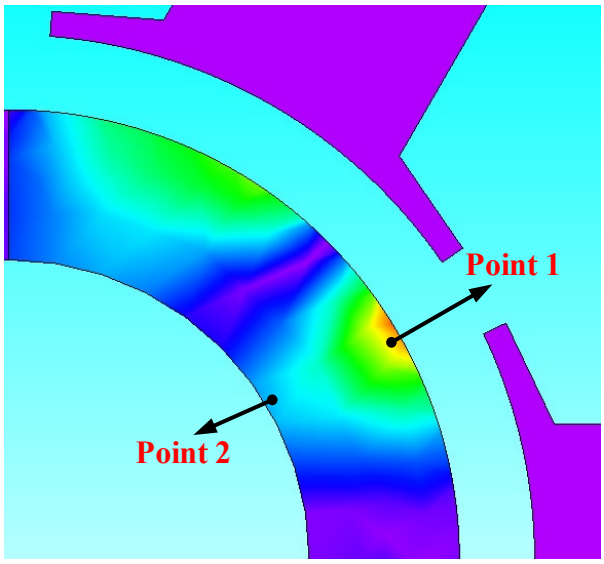

Fig.3.28. Positions of selected points inside the magnets.

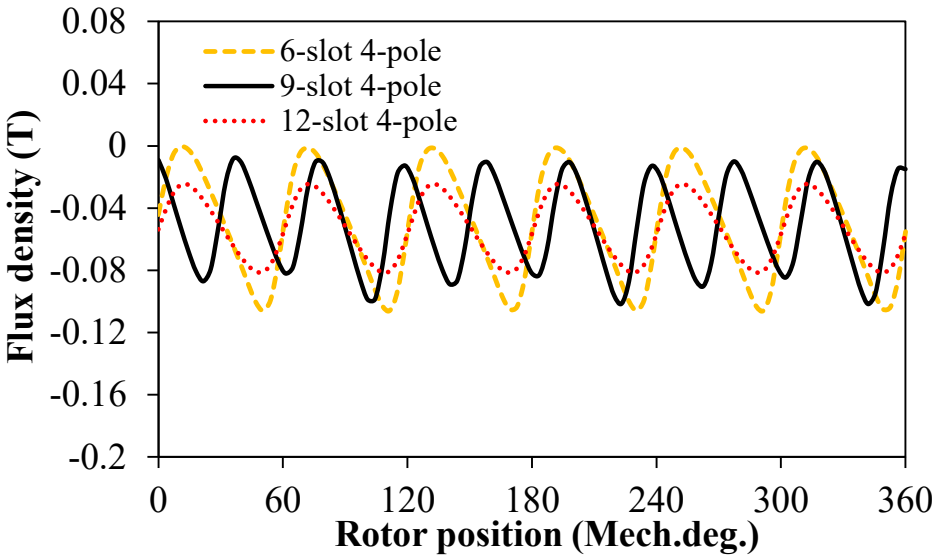

(a)

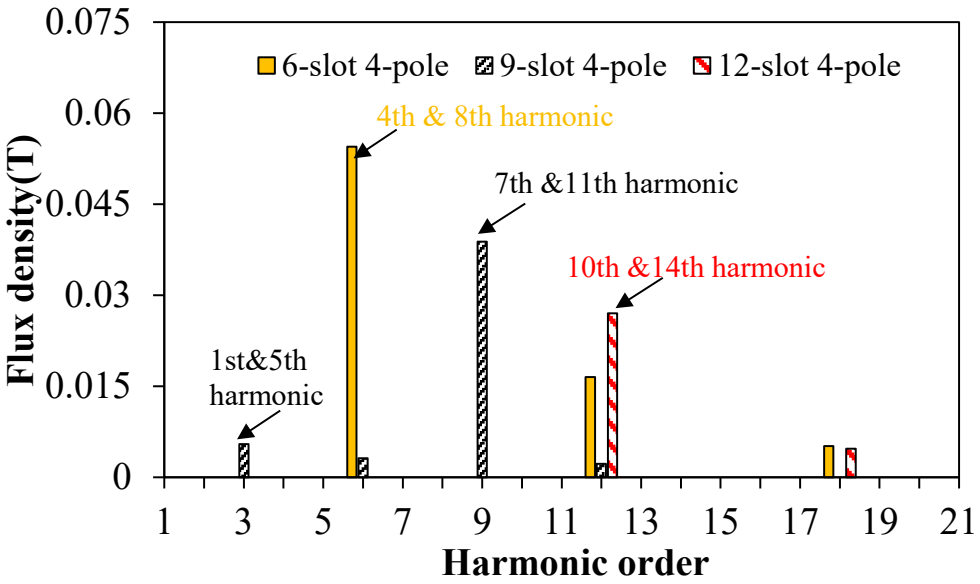

(b)

Fig.3.29. Variation of flux density at the magnet outer surface (Point 1, I_a=80A).

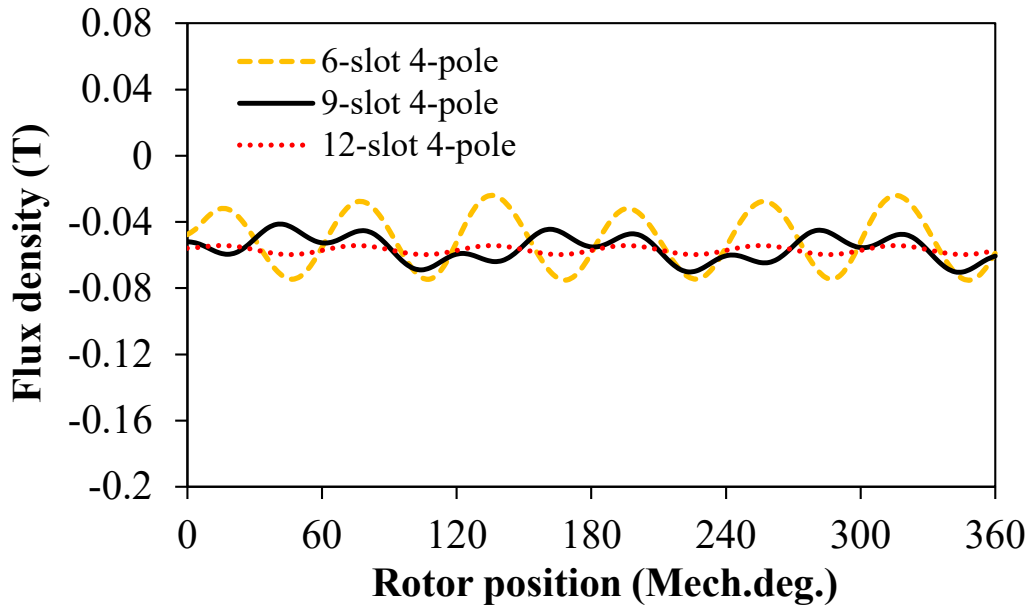

(a)

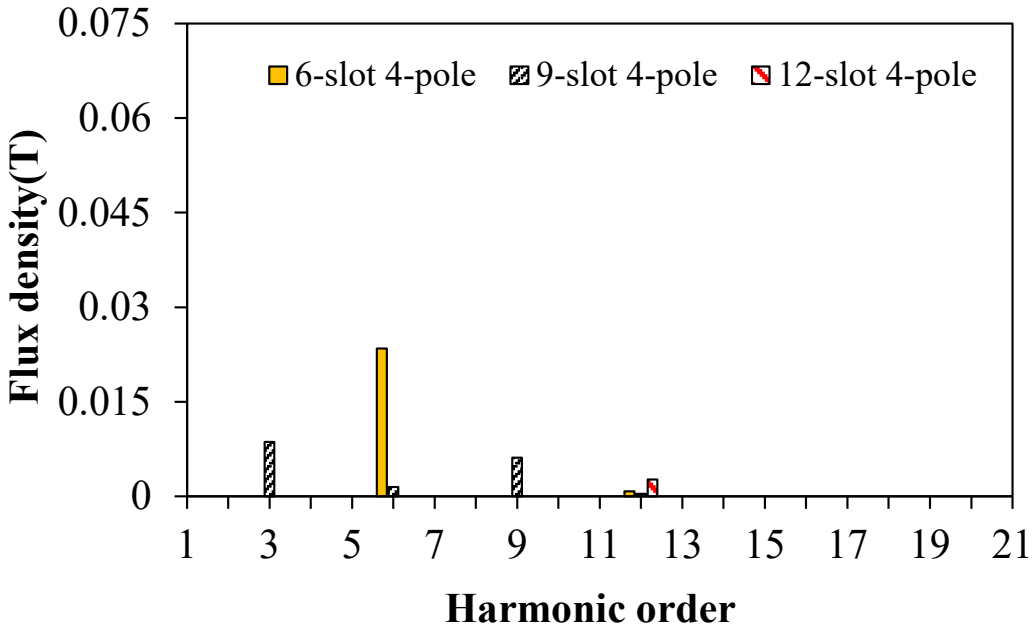

(b)

Fig.3.30. Variation of flux density at the magnet inner surface (Point 2, I_a=80A).

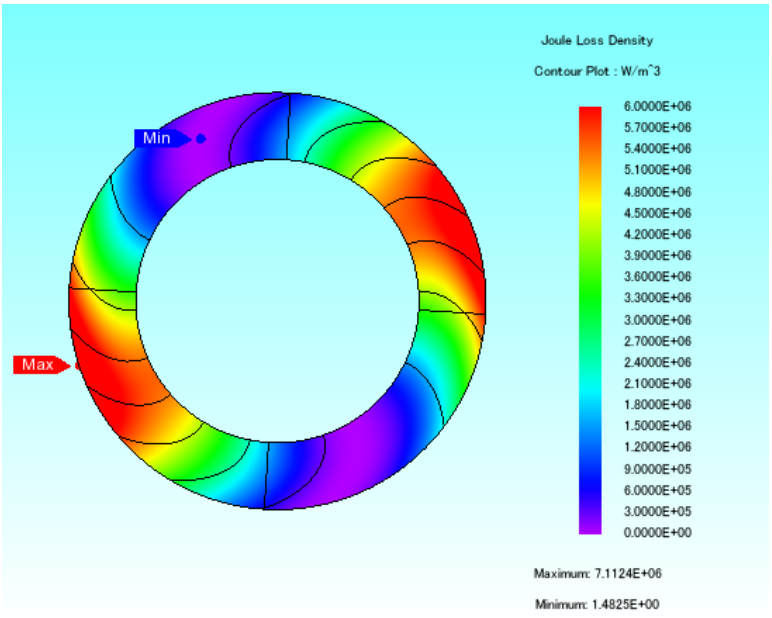

(a)

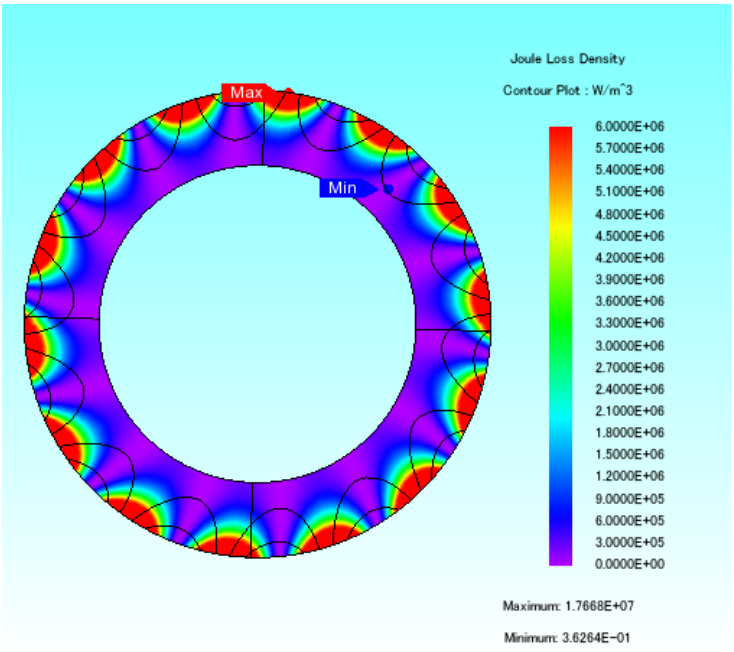

(b)

Fig.3.31. Magnet loss due to different spatial harmonics in 9-slot/4-pole HSPMM (I_a=80A). (a) Sub-harmonic. (b) 7th harmonic.

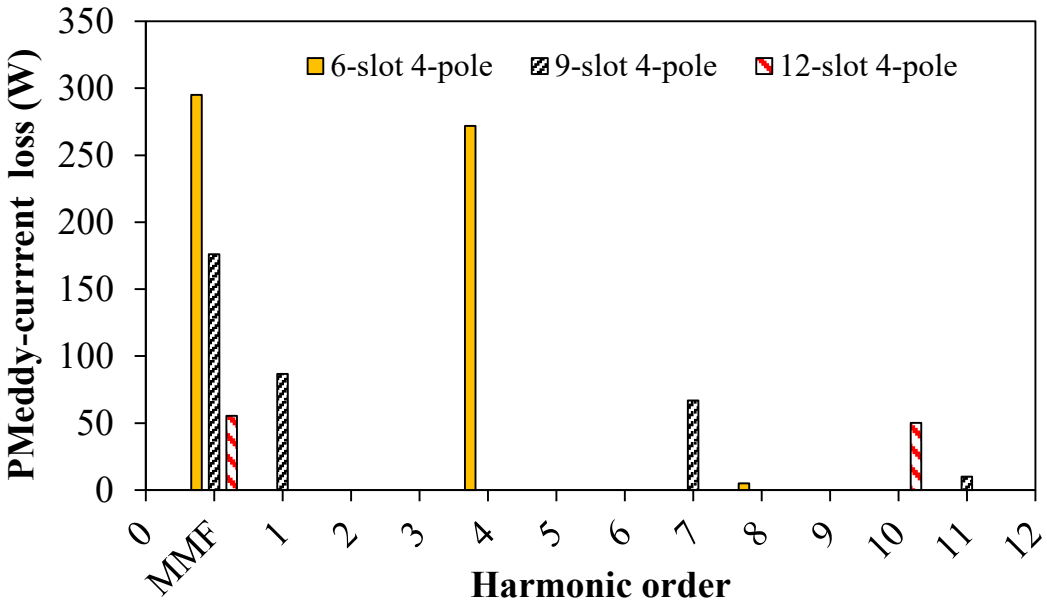

Fig.3.32. Loss segregation of three machines.

3.5 Experimental Validation

In order to verify the theoretical analysis on the rotor magnet loss of HSPMM, three machines with same pole number of 4 but different stator slot number and coil pitch are prototyped. The main parameters are given in Table 3.5. Due to the huge difficulties to measure the rotor magnet loss directly, the tests of small scaled prototype machines are only used for the validation of FE harmonic analysis in this section. The stator configurations can be seen in Fig.3.31.

Table 3.5 Parameters of Prototype Machines

Parameter	A	B	C
Pole number	4		
Slot number	6	9	12
Coil pitch	1	2	3
Stator bore diameter(mm)	34.08	35.1	38.6
Tooth body width(mm)	7.71	5.64	4.19
Stator yoke height(mm)	5.36	4.71	5.08
Slot opening(mm)	2.5	2.5	2.5
Stator outer diameter(mm)	90		
Stack length(mm)	30		
Air gap thickness(mm)	2		
Number of turns per phase	20		
Magnet thickness(mm)	6		

The test rig for the back-EMF and on-load phase current measurement is shown in Fig.3.32. The prototype machine can be driven to the required speed. The back-EMF can therefore be measured. In addition, the phase current can be measured when the machine is fed with the load shown in Fig.3.32. The measured and simulated open-circuit back-EMFs as well as the spectra are shown in Fig.3.33. The harmonics of back-EMF are extracted based on the FFT analysis, as illustrated in Fig.3.34. It can be seen that the measured results agree well with the predicted ones. The mild difference is caused by the ignorance of leakage of ending winding in FE models and manufacturing error.

On the other hand, it is interesting to find that the 5^{th} and 7^{th} time harmonics in the back-EMF of the 9-slot/4-pole HSPMM is almost negligible. This is quite advantageous from the high-speed motor control point of view. The potential current harmonics resulting from the 5^{th} and 7^{th} harmonics in the back-EMF will produce significant rotor magnet loss.

Fig.3.35 illustrates the test rig for the torque measurement. The measurement method was introduced in [ZHU09]. The measured and FE predicted cogging torque waveforms and the corresponding spectra are shown in Fig.3.36 and Fig.3.37. Fig.3.38 illustrates the measured phase current waveform of the 9-slot/4-pole machine in the generating mode. As shown in Fig.3.32, the generator driven by the dynamometer is connected to a three-phase AC resistance load. The operating speed is 20krpm. As can be seen from Fig.3.39, the measured torque matches well with the FE predicted one with a deviation less than 10%, confirming the validity of the FE models.

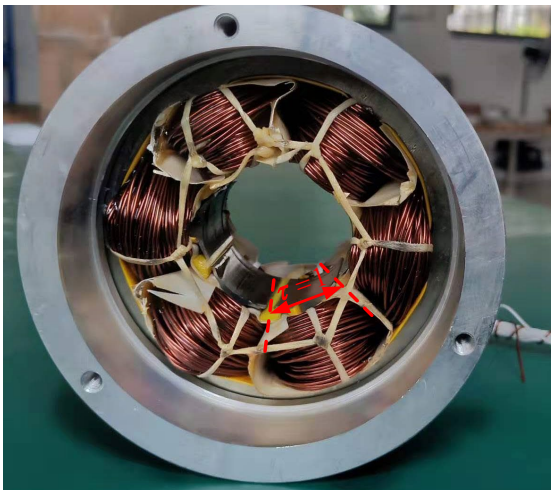

(a)

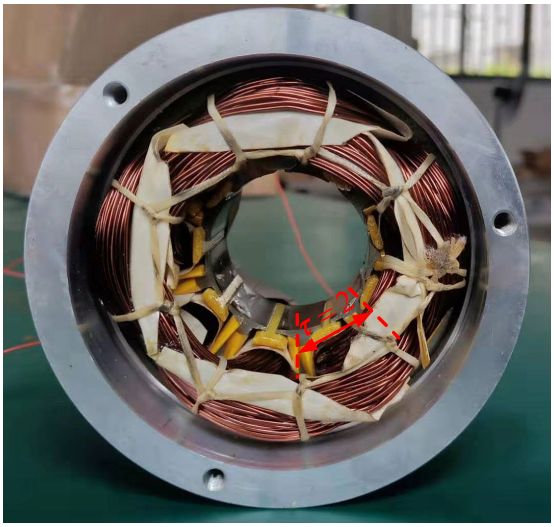

(b)

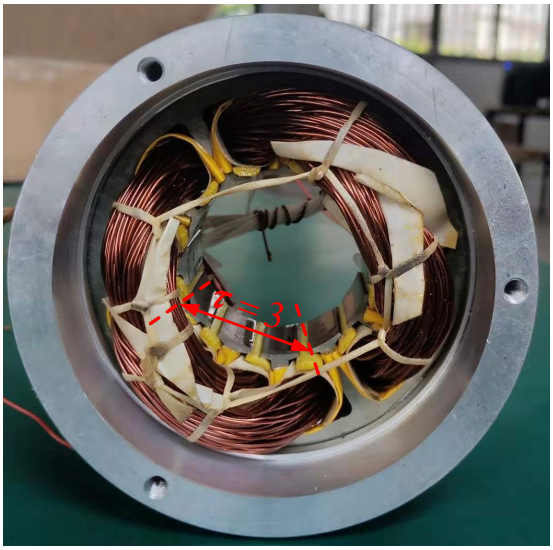

Fig.3.31. Three stators with alternate coil pitch. (a) Coil pitch=1(6-slot/4-pole). (b) Coil pitch=2 (9-slot/4-pole). (c) Coil pitch=3 (12-slot/4-pole).

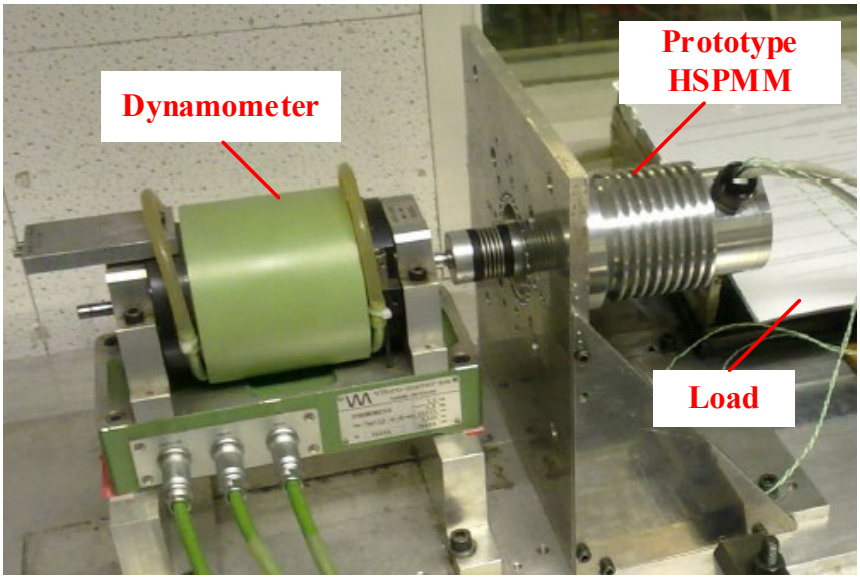

Fig.3.32. Test rig for back-EMF and on-load phase current measurement.

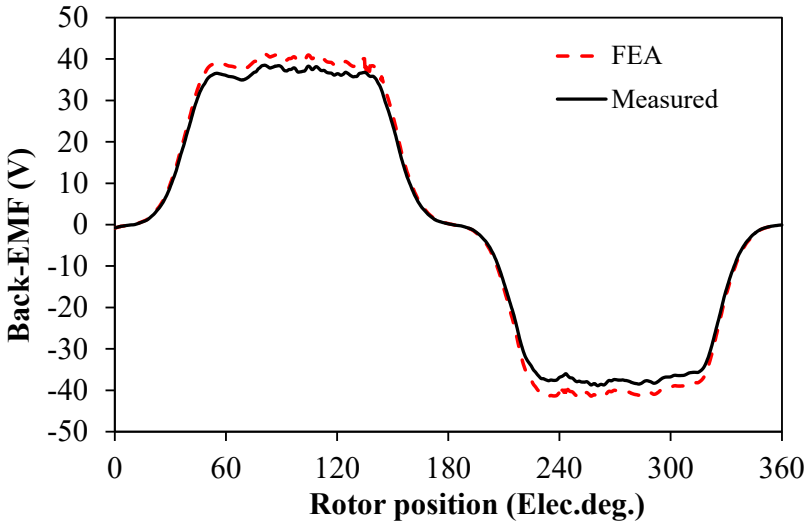

(a)

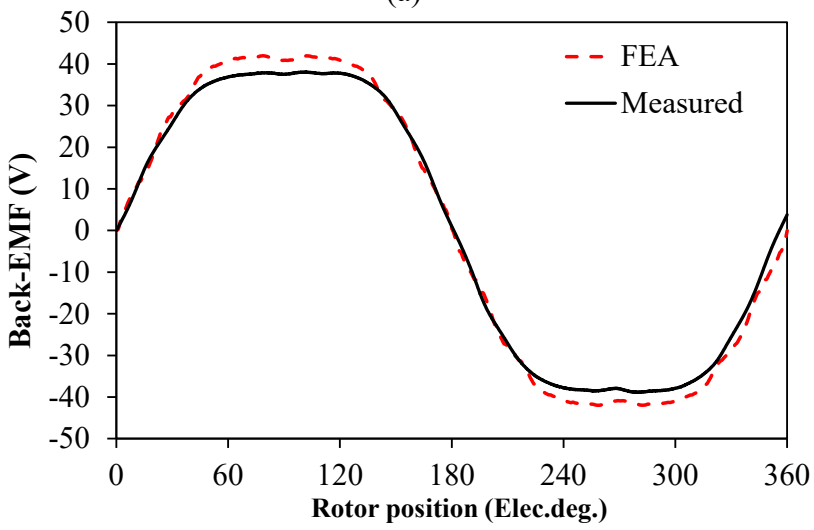

(b)

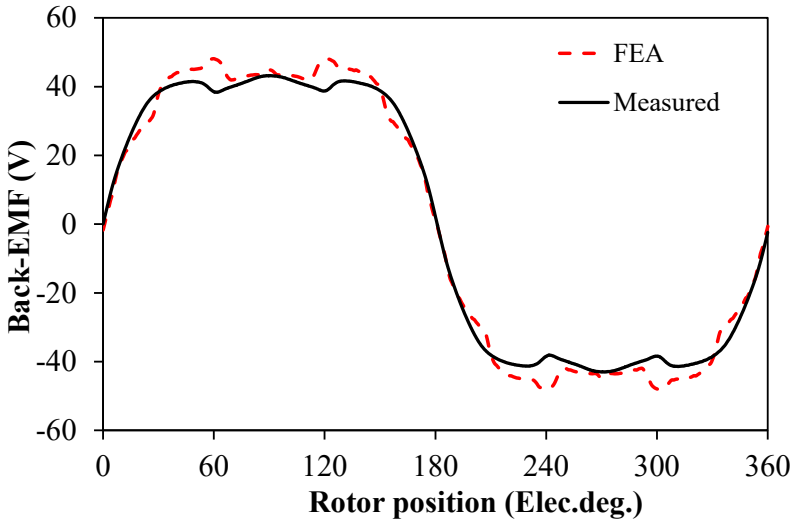

(c)

Fig.3.33. Measured and simulated back-EMF waveforms (n=20000rpm). (a) 6-slot/4-pole profile. (b) 9-slot/4-pole. (c) 12-slot/4-pole.

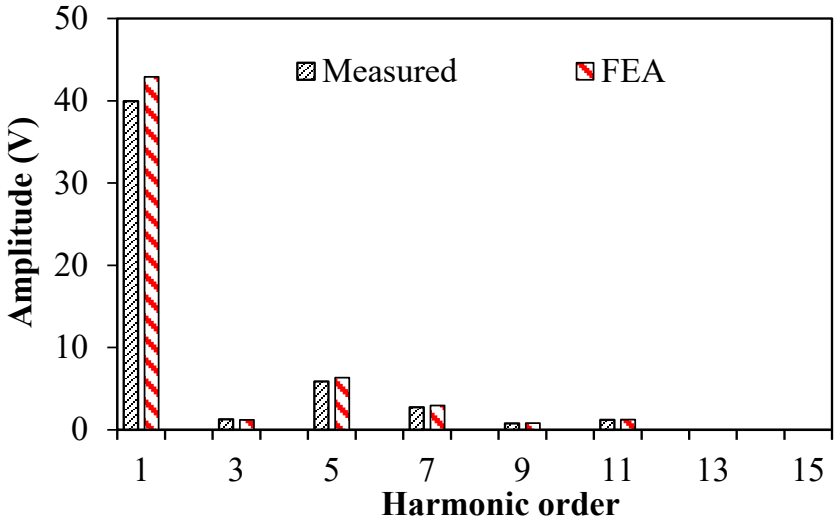

(a)

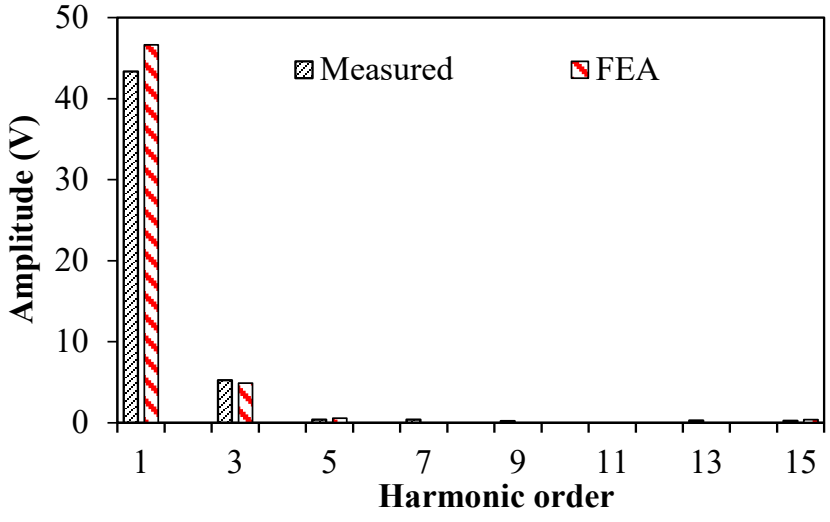

(b)

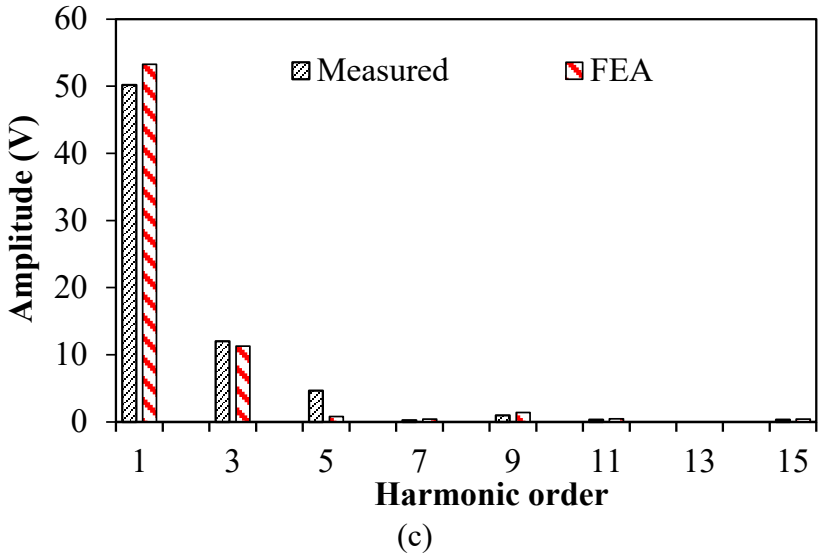

(c)

Fig.3.34. Spectra of measured and simulated back-EMF waveforms (20000rpm). (a) 6-slot/4-pole profile. (b) 9-slot/4-pole. (c) 12-slot/4-pole.

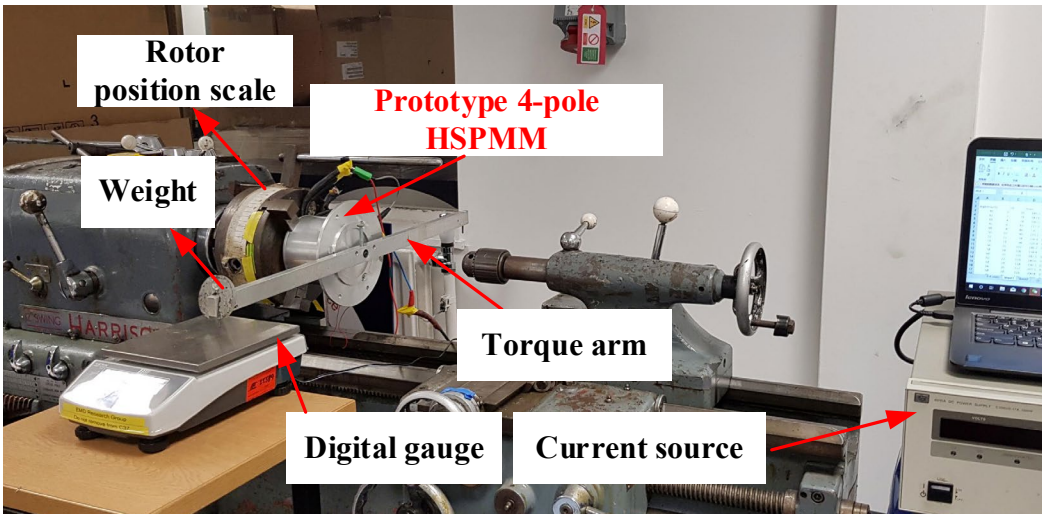

Fig.3.35. Test rig for torque measurement.

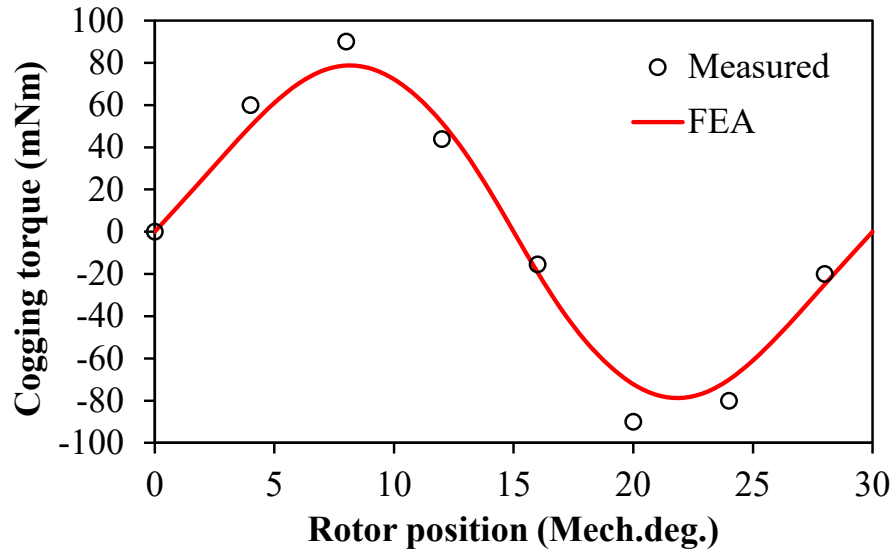

(a)

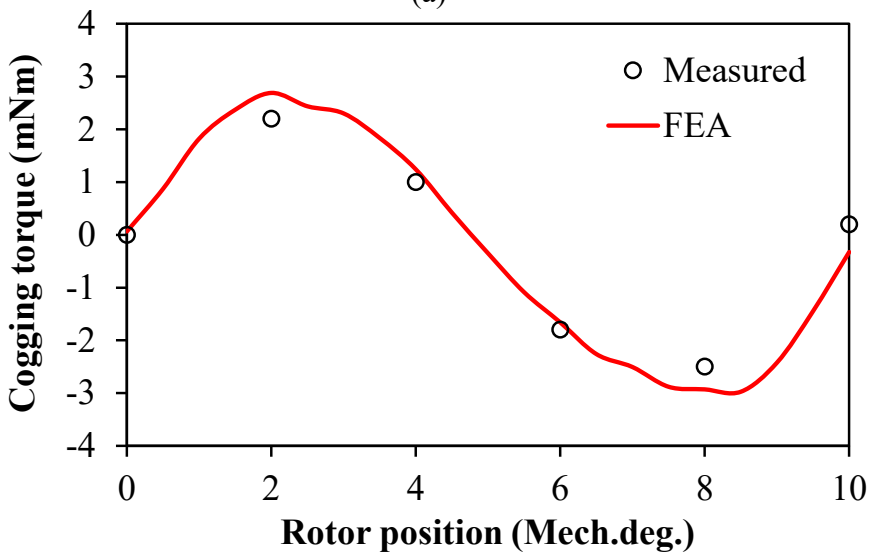

(b)

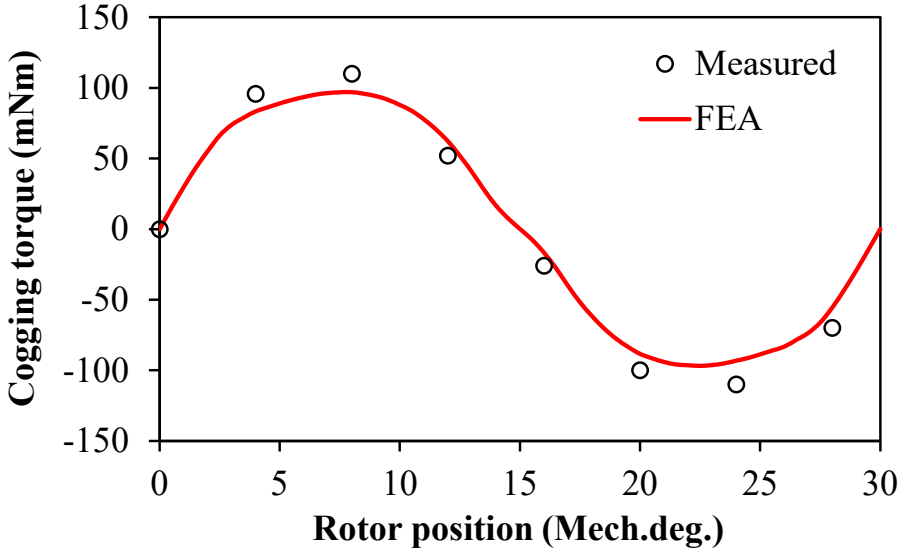

(c)

Fig.3.36. Measured and simulated cogging torque waveforms. (a) 6-slot/4-pole machine. (b) 9-slot/4-pole machine. (c) 12-slot/4-pole machine.

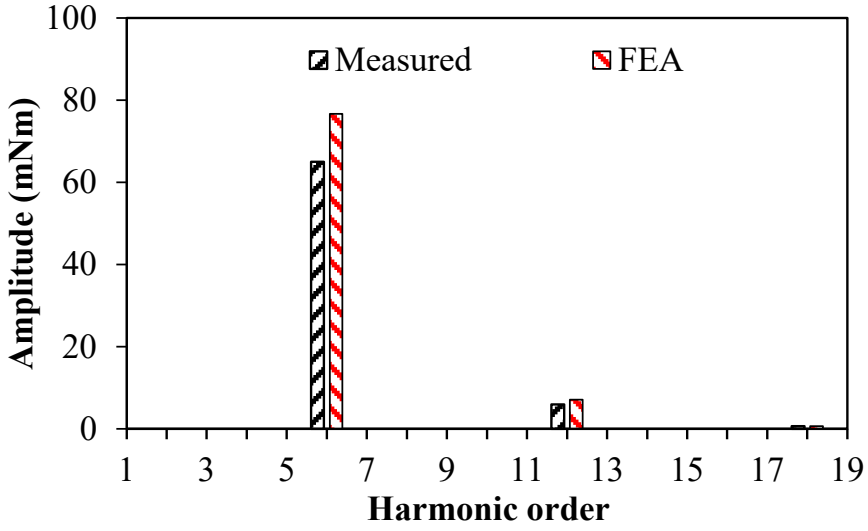

(a)

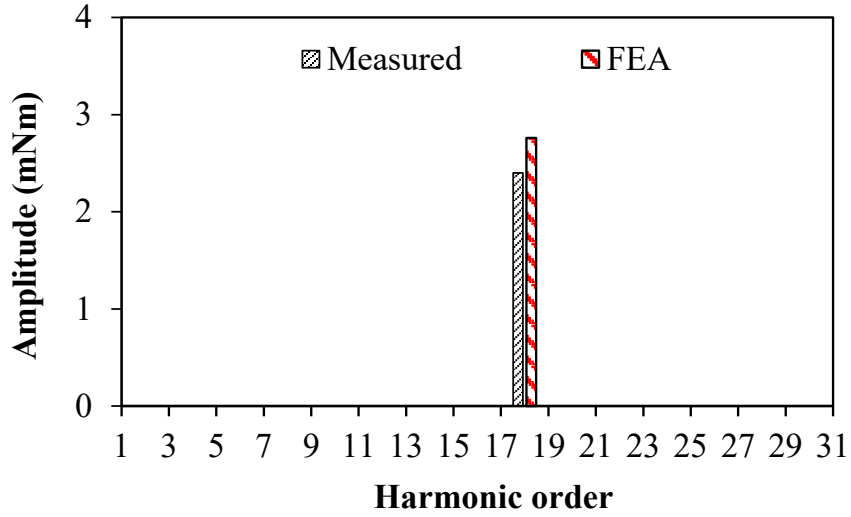

(b)

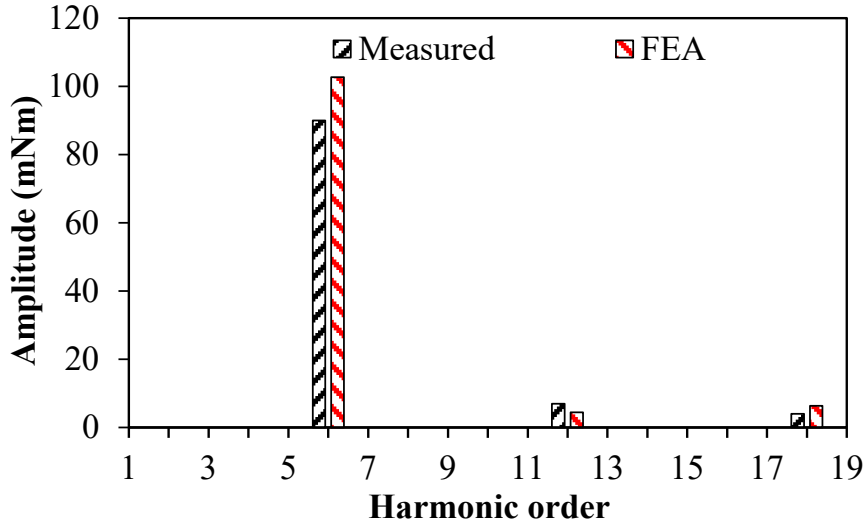

(c)

Fig.3.37. Spectra of measured and simulated cogging torque. (a) 6-slot/4-pole machine. (b) 9-slot/4-pole machine. (c) 12-slot/4-pole machine.

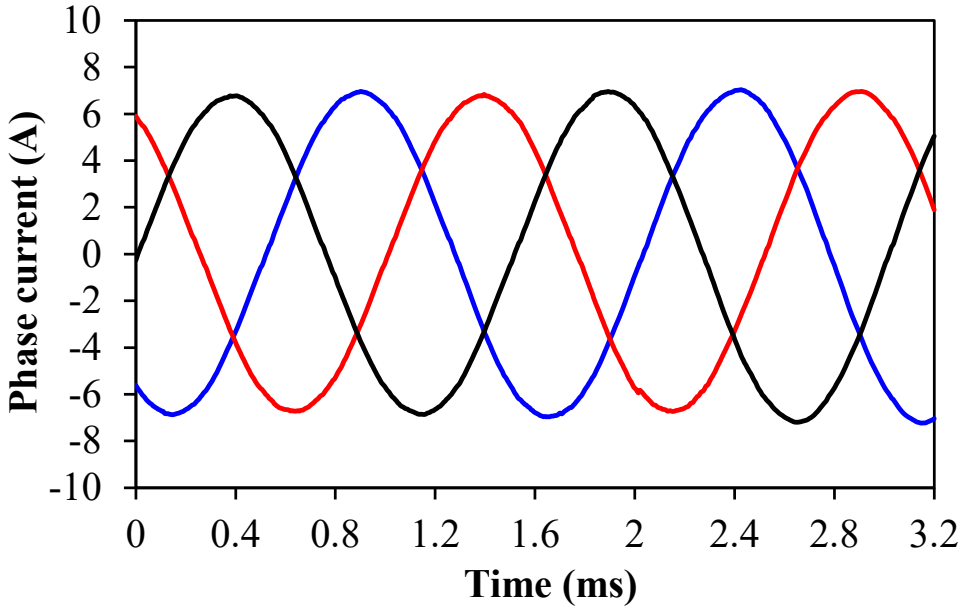

Fig.3.38. Measured 3-phase phase current waveforms for 9-slot/4-pole HSPMM (n=20000rpm).

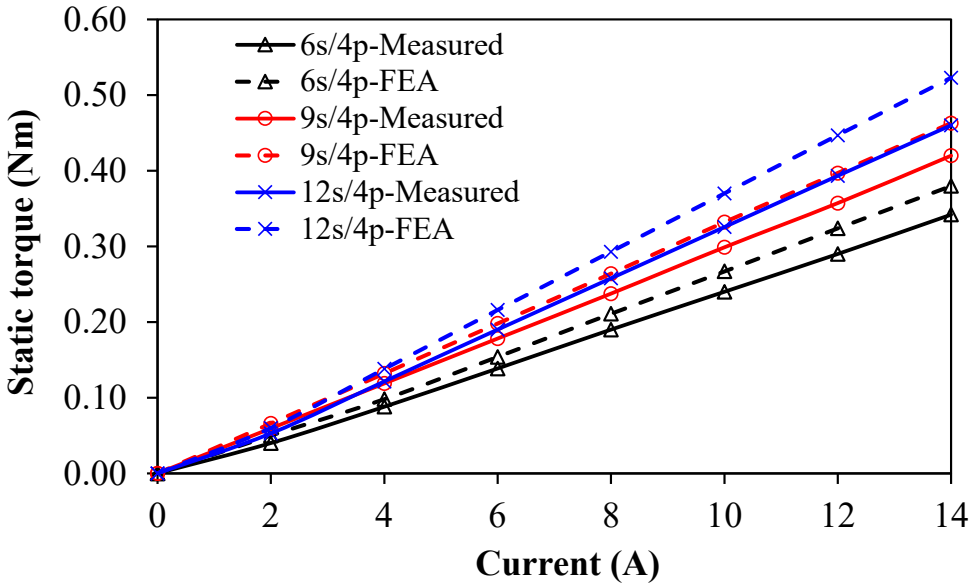

Fig.3.39. Variation of peak torque with current (I_a=-2I_b=-2I_c).

3.6 Summary

In this chapter, the rotor magnet loss analysis is conducted on the 4-pole HSPMM with the focus on the loss segregation. Firstly, the contribution of PM field and armature reaction field to the resultant rotor magnet loss of a 6-slot/4-pole HSPMM is determined. It is found that both the PM field and armature reaction field variation contribute significantly to the production of magnet loss. The portion of armature reaction-induced rotor magnet loss increases vastly with load current. Then, each individual MMF harmonics are modelled with a slotless stator equipped with Halbach magnetized magnets so that their share to generation of the magnet loss can be quantified. The validity of harmonic superposition principle is also confirmed with the FE method. It is observed that the 4^{th} spatial harmonic dominates in the production of magnet loss for the 6-slot/4-pole HSPMM. In addition, the slotting effect on both the PM field-induced and armature reaction induced magnet losses is revealed. It is found that the open-circuit magnet loss due to slot opening is significantly increased with the enlarged slot opening angle. On the other hand, the magnet loss generated by the 4^{th} spatial harmonic due to slot modulation is almost negligible. The armature reaction induced magnet loss with different stator slot (6, 9, 12) and winding coil pitch (1, 2, 3) is compared as well. It is found that the value of magnet loss is dependent on both the penetration depth and the amplitude of asynchronous spatial harmonic, which are determined by the specific slot and pole number combination. Finally, three 4-pole HSPMMs with different stator slot number and coil pitch are prototyped and tested. Due to the huge difficulties of direct measurement of magnet loss, only the back-EMF and electromagnetic torque of three machines are measured. The measured results match well with the FE predicted ones in terms of both the amplitude and harmonic order of back-EMF and electromagnetic torque.

Chapter 4 Investigation of Unbalanced Magnetic Force in Fractional-Slot PM Machines with Odd Number of Stator Slot

In Chapter 3, it is shown that the HSPMM with 9-slot 4-pole configuration exhibits significant advantages in terms of maintaining a low rotor eddy current loss as well as the short end-winding length. However, its inherent unbalanced winding configuration will finally yield potential unbalanced magnetic force (UMF) which is undesirable for the rotor stability of HSPMM. As a matter of fact, fractional-slot PM machines with odd number of stator slots such as 9-slot 8-pole machine are attractive candidates for industrial applications due to high torque density and low torque ripple. However, the existence of UMF is detrimental to the bearing and yields noise and vibration. First of all, this chapter determines the criterion for existence of UMF either on open-circuit or on-load condition by analytical analysis of air gap field and magnetic force wave. It is found that only when the machine periodicity is one, will the open-circuit UMF be generated due to the mutual interaction between the modulated PM harmonics and the original PM harmonics. In addition, the existence of on-load UMF in machines with periodicity of one is confirmed since both the self-interaction of armature reaction harmonics and the mutual interaction between the fundamental PM harmonic and the armature reaction harmonics will appear even when the slotting effect is ignored. Furthermore, among the five investigated machines with a given odd slot number of 9 but different pole numbers, the UMF in a machine with two poles is the smallest in machines with periodicity of one since the magnitude of the 2^{nd} harmonic in armature reaction is the smallest compared with other contributing harmonics. On the other hand, the UMF in a machine with pole number $2p=N_s-1$ is the largest due to relatively larger magnitude of the $(p+1)^{th}$ armature reaction harmonic as well as the additive effect between the first order radial and tangential stresses. Finally, a prototype machine with 9-slot 6-pole configuration is implemented and tested. The measured data confirm the validity of the electromagnetic performances obtained from the 2D FE model and the analytical models.

4.1 Introduction

Fractional-slot permanent magnet (PM) machines have been gaining increasing interest over last decade due to high efficiency, high torque density, and low torque ripple, as well as high flux-weakening capability [CRO02], [REF05], [BIA06b], [ZHU07a], [BIA08], [REF10]. In order to reduce the cogging torque and on-load torque ripple, odd stator slot number is a design alternative without skewing stator slots or rotor magnets in fractional-slot PM machines [HAN10], [DOR11], [YOL17].

On the other hand, unbalanced magnetic force (UMF) which jeopardizes the bearing life and yields noise and vibration may occur in fractional-slot machines with odd number of stator slots, even when there are no rotor eccentricities or other manufacture tolerances [BI97], [DOR08], [LI09], [ZHU07b]. As shown in Fig.4.1 (d), (e), machines with odd slot number N_s and pole number $2p$ differed by one are typical representatives, e.g. 9-slot 8-pole machine and 9-slot 10-pole machine. Such machines are featured with high winding factor thus high torque density and low torque ripple whilst exhibiting the UMF due to the asymmetric field distribution.

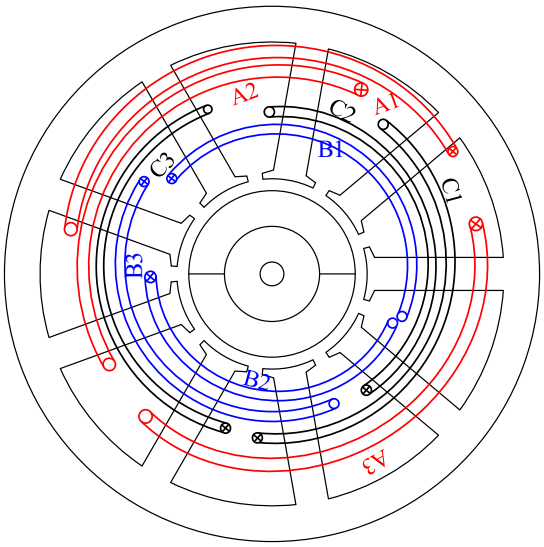

(a)

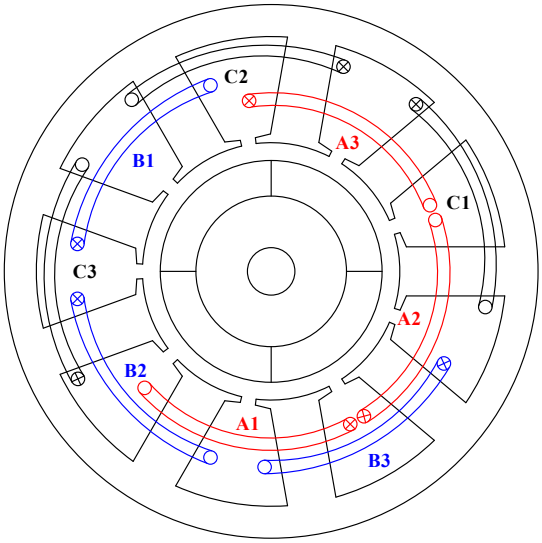
C2
A3
B1
C1
C3
A2
B2
A1
B3

(b)

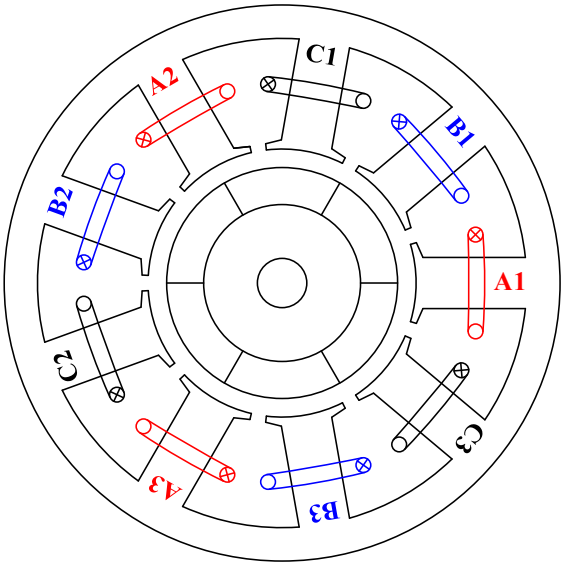
C1
A2
B1
B2
A1
C2
C3
A3
B3

(c)

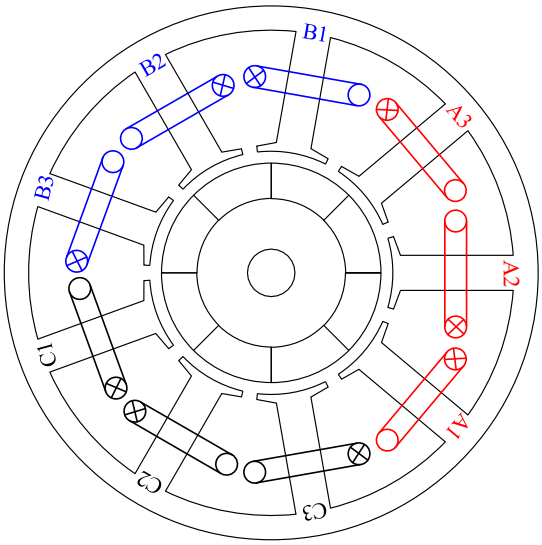
B1
B2
A3
B3
A2
C1
A1
C2
C3

(d)

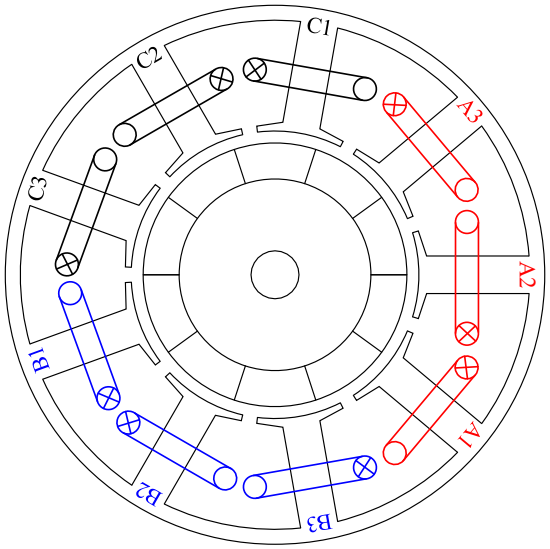

(e)

Fig.4.1. Configurations of 9-slot machines with different pole numbers (*N*s/2*p*). (a) 9s/2p. (b) 9s/4p. (c) 9s/6p. (d) 9s/8p. (e) 9s/10p.

Hence, the UMF in fractional-slot PM machines has always been one of the significant issues in the field of electrical machines over the last few years [BIN73], [DOR08], [MAH15], [KIM16]. The production and characteristics of UMF in different types PM machines with and without rotor eccentricity are comprehensively studied. In order to reveal the harmonic content and the generating mechanism of UMF, Maxwell stress tensor method is normally adopted in literature [JAN96], [JAN03], [MIC14] [MAH15], [KIM16]. In [JAN96], it was pointed out the unbalanced radial magnetic force in the 9-slot 8-pole and 9-slot 10-pole machines exhibit the UMF. In [JAN03], the preference of Halbach magnetization rather than radial magnetization for high-speed slot-less machine for reduction of UMF was highlighted. In [MIC14], an approximate analytical model was developed for the prediction of UMF due to rotor eccentricity with due account only for the radial air gap field. [KIM16] investigated the UMF due to rotor eccentricity in a toroidally wound BLDC motor. In [MAH15], an analytical model was proposed to investigate the impact of rotor eccentricity in a synchronous reluctance machine.

However, all of the aforementioned literature failed to take account of either the tangential component of air gap flux density or the tangential magnetic travelling stress in the analysis of UMF. Although compared with the radial flux density, the tangential counterpart is relatively small, it may still contribute significantly to the resultant UMF, which was verified in [BIN73], [DOR10], [WU10b], [ZHU13]. In [DOR10], UMF was analytically derived together with the

finite element (FE) analysis of fractional-slot PM machines with different slot/pole number combinations with and without rotor eccentricities, providing an excellent guideline for the design of fractional-slot PM machines. It was pointed out that the UMF in a 9-slot 6-pole machine is negligible compared with that of a 9-slot 8-pole machine due to the symmetrical winding disposition for the machine with 9-slot 6-pole. Hence, there only exists the open-circuit UMF rather than additional on-load UMF due to the absence of winding harmonics with the order varying by one for this type of machine. However, it remains unclear of the criterion for this open-circuit UMF existence in the fractional-slot PM machines with odd stator number. In [WU10b] and [ZHU13], it was demonstrated that a UMF can be divided into two sources resulting from radial magnetic stress and tangential magnetic stress respectively. It was validated that the on-load UMF in a 9-slot 8-pole machine is significantly larger than that in a 9-slot 10-pole machine due to the different effect between the radial magnetic stress and tangential stress. It was concluded that they are additive for the machines having pole number $2p=N_s-1$, e.g. 9-slot 8-pole, but are partially cancelling for the machines having pole number $2p=N_s+1$, e.g. 9-slot 10-pole. However, the majority of the findings focused on the machines having $2p= N_s\pm1$. It is still unknown how the UMF would be affected in the fractional-slot PM machines with lower pole number, e.g. 27-slot 4-pole machine, which are design candidates for high speed applications [RED11], [ZHA15], [ZHA17]. Thus, this paper focuses on the systematic investigation of UMF in fractional-slot PM machines having odd number of stator slots.

This chapter is organized as follows. In Section 4.2, the air gap field and magnetic forces are analytically analyzed in order to identify the contributing harmonic sources in the fractional-slot PM machines with odd number of stator slots. Then, in Section 4.3, the existence of the open-circuit and on-load UMF in different types of fractional-slot PM machines can be determined, together with FE validation. Afterward, in Section 4.4, five machines with a given odd slot number of 9 but different pole numbers, i.e. 2, 4, 6, 8 and 10 are compared in terms of UMF so that the influence of slot/pole combination on UMF can be determined, especially for the machines with lower pole number. Finally, the numerically predicted results are validated by the experimental measurements in Section 4.5, together with the conclusion in section 4.6.

4.2 Analytical Analysis of Air Gap Field and Magnetic Forces

In this section, the analytical analysis of air gap field harmonics in fractional-slot PM machines with odd number of stator slots is conducted so that the contributing sources of UMF can be further identified. As pointed out in [WU10b], the tangential component of air gap field should be taken into account due to its significant contribution to the tangential travelling stress thus the total unbalanced magnetic force. Meanwhile, it should be noted that the analytical model adopted here is not for accurately predicting the air gap field magnitude but the harmonic order and the corresponding rotating speed, direction and phase angle. Hence, the following assumptions are made.

1) The permanence of iron lamination is infinite which means the saturation effect is ignored.
2) The relative permeability of permanent magnet is considered to be equal to that of air.
3) Only the 2-D field is considered. The flux leakage and end-effect are neglected for simplicity.

4.2.1 Open-Circuit Air Gap Flux Density

Generally, for a fractional-slot PM machine with surface mounted magnets, the magnetic motive force generated by the PMs can be assumed as the square wave which is variable with air gap circumferential position, as shown in Fig.4.2. Its Fourier series expansion $F_r\ (\alpha, t)$ can be expressed as

$$F_r(\alpha,t) = \sum_{i=1,3,5...}^{\infty} A_i \cos[ip(\omega_r t - \alpha)] \tag{4.1}$$

where i is the harmonic index and A_{ri} denotes the amplitude the ith harmonic which has been revealed in [ZHU93]; p is the number of rotor pole-pairs; ω_r is the rotor angular mechanical speed.

On the other hand, the air gap permanence distribution can be modeled as shown in Fig.4.3, with the consideration of stator slotting effect. Its Fourier series can be written as

$$P(\alpha) = P_0 + \sum_{j=1,2,3...}^{\infty} P_j \cos[jN_s(\alpha - \alpha_0)] \tag{4.2}$$

where P_0 denotes the dc component of air gap permanence; j is the harmonics index; N_s is the stator slots number; α_0 is the initial rotor position angle.

Therefore, the radial field component of open-circuit flux density with the consideration of slotting effect can be obtained by multiplying $F_r\ (\alpha, t)$ and $P\ (\theta)$ from (1) and (2) as

$$\begin{cases} B_r = F_r(\alpha,t)P(\alpha) = \underbrace{\sum_{i=1,3,5\ldots}^{\infty} B_{ri}\cos[ip(\omega_r t-\alpha)]}_{PM-original\,harmonics} \\ \underbrace{+\frac{1}{2}\sum_{i=1,3,5\ldots}^{\infty}\sum_{j=1,2,3}^{\infty} B_{ri}[\cos(ip\omega_r t-\alpha_1)+\cos(ip\omega_r t-\alpha_2)]}_{PM-modulated\,harmonics} \\ \alpha_1 = (ip+jN_s)\alpha - jN_s\alpha_0 \\ \alpha_2 = (ip-jN_s)\alpha + jN_s\alpha_0 \end{cases} \tag{4.3}$$

It can be seen that the open-circuit radial PM harmonics consist of both the original harmonics with the order of *ip* and the modulated harmonics with the order of $|ip \pm jN_s|$ due to stator slotting effect.

As revealed in [ZHU93], the tangential PM field under open-circuit shares the same harmonic order as well as the rotation speed and direction with those of radial one. The only differences lie in the amplitude and phase angle.

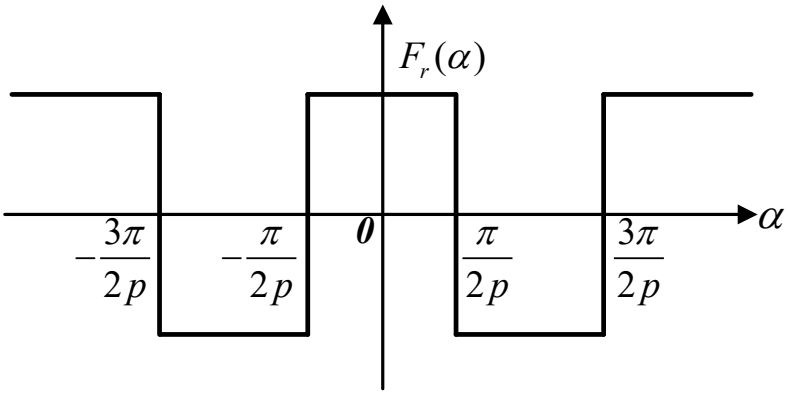

Fig.4.2. MMF distribution generated by PMs in fractional-slot PM machines.

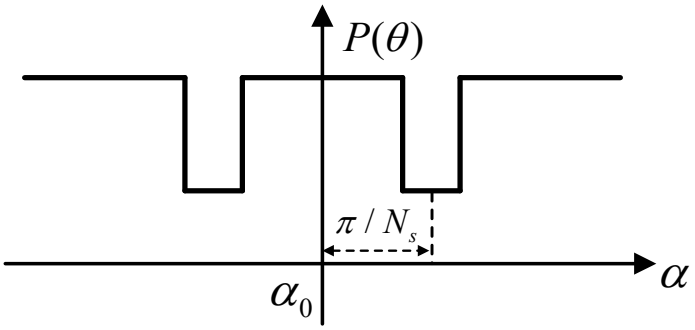

Fig.4.3. Air gap permanence distribution accounting for stator slots.

4.2.2 Armature Reaction Air Gap Flux Density

For a fractional-slot PM machine, the armature reaction MMF can be expressed as Fourier series:

$$F_{ABC}(\alpha,t)=\sum_{\nu}^{\infty}F_{\nu}\cos[p\omega_r t\pm\nu\alpha)] \tag{4.4}$$

where F_ν denotes the amplitude of the υth- order harmonic, υ represents the harmonic order index whose value will be given in the following.

Similarly, the armature reaction flux density accounting for the slotting effect can be obtained as the product of MMF and air gap permanence

$$\begin{cases} B_{arm}=F_{ABC}(\alpha,t)P(\alpha)=\underbrace{\sum_{\nu}^{\infty}F_{\nu}P_0\cos[p\omega_r t\pm\nu\alpha)]}_{MMF-original\,harmonics} \\ \underbrace{+\frac{1}{2}\sum_{\nu}^{\infty}\sum_{j=1,2,3}^{\infty}F_{\nu}P_j[\cos(p\omega_r t\pm\alpha_3)+\cos(p\omega_r t\pm\alpha_2)]}_{MMF-modulated\,harmonics} \\ \alpha_3=(\nu+jN_s)\alpha-jN_s\alpha_0 \\ \alpha_4=(\nu-jN_s)\alpha+jN_s\alpha_0 \end{cases} \tag{4.5}$$

From (5), it can be seen that apart from the original MMF harmonics with the order of υ, the modulated MMF harmonics with the order $|\upsilon \pm jN_s|$ also exist due to air gap permanence variation.

In order to further identify the harmonic order of MMF armature reaction, the machine periodicity should be clarified. For the fractional-slot PM machines with N_s slots and p pole pairs, the periodicity t is defined as the great common divisor between N_s and p [BIA09]

$$t=G.C.D.\{N_s,p\} \tag{4.6}$$

In this paper, for the machine having odd number of stator slots, the value of t is always odd (t=1, 3, 5…) which indicates that the MMF distribution contains harmonics of both even and odd orders multiplied by t. On the other hand, all triple MMF harmonics are cancelled out in the symmetrical three-phase winding. Therefore, the harmonic order of armature reaction field

can be written as $|(3n \pm 1)t \pm jN_s|$ (n=0,1,2… j=0,1,2…).

Table 4.1 Attributes of Air Gap Field in Fractional Slot PM Machines Having Odd Number of Slots

Sources	Harmonic order	Rotating speed
PM field	$\|ip \pm jN\mathrm{s}\|$	$\frac{ip\omega_r}{\|ip \pm jN_s\|}$
Armature reaction field	$\|(3n \pm 1)t \pm jN_s\|$	$\frac{\pm p\omega_r}{\|(3n \pm 1)t \pm jN_s\|}$

Hence, the modulated on-load air gap field of a fractional slot PM machine having odd number of stator slots can be obtained by adding (5) to (3). The attributes of air gap flux harmonics are given in Table 4.1.

4.2.3 Radial Stress and Tangential Stress

According to the Maxwell stress tensor, the radial and tangential magnetic stresses can be obtained by

$$\begin{cases} F_r = \dfrac{1}{2\mu_0}(B_r^2 - B_\alpha^2) \\ F_\alpha = \dfrac{B_r B_\alpha}{\mu_0} \end{cases} \tag{4.7}$$

where B_r and B_α denote the radial and tangential flux density components in air gap either on open-circuit or load condition.

As mentioned in the previous section, the harmonic orders in the radial and tangential air gap fields are the same.

4.2.4 Unbalanced Magnetic Force

It is well known that the unbalanced magnetic force results from the asymmetric air gap field distribution. Similarly, it can be obtained by the Maxwell stress tensor in the rectangular coordinate as

$$\begin{cases} F_x = F_{rx} + F_{\alpha x} \\ \quad = rl_a \int_0^{2\pi} (F_r \cos\alpha - F_\alpha \sin\alpha) d\alpha \\ F_y = F_{ry} + F_{\alpha y} \\ \quad = rl_a \int_0^{2\pi} (F_r \sin\alpha + F_\alpha \cos\alpha) d\alpha \end{cases} \tag{4.8}$$

where r refers to the position at which flux density is accumulated. l_a is the stack length.

Table 4.2 Attributes of Radial and Tangential Travelling Stress

	Source	Harmonic order
Open-circuit	PM	$\|\|i_1 p \pm j_1 N_s\| \pm \|i_2 p \pm j_2 N_s\|\|$ (i_1, i_2=1, 3, 5… j_1,j_2=0, 1, 2…)
On-load	Armature reaction	$\|(3n_1 \pm 1)t \pm j_1 N_s\| \pm \|(3n_2 \pm 1)t \pm j_2 N_s\|$ (n_1, n_2=0, 1, 2… j_1,j_2=0, 1, 2…)
	Mutual interaction	$\|i_1 p \pm j_1 N_s\| \pm \|(3n_2 \pm 1)t \pm j_2 N_s\|$ (n_1, n_2=0, 1, 2… j_1,j_2=0, 1, 2…)
Note: MI designates for mutual interaction of PM field and armature reaction field.		

4.3 Existence of Criterion for Unbalanced Magnetic Force in PM Brushless Machines Having Odd Number of Stator Slots

In this section, the existence criterion of unbalanced magnetic force in fractional slot PM machines having odd number of slots will be firstly elaborated. The canceling effect of radial stress and tangential stress in each sub-motor of one specific type of machines with odd stator slots will then be revealed.

4.3.1 Determination for UMF Existence

From (4.8), it can be concluded that due to the orthogonality of trigonometric function, only the first-order harmonic component in the radial stress as well as the tangential stress will generate UMF. On the other hand, from Table I, although abundant harmonics do exist in the air gap, only when the harmonic orders of any two flux harmonics differ by one, will the first-order harmonic of the stress be produced. On the other hand, the existence of UMF in fractional slot PM machines is closely related with the slot/pole number combination (Ns/2p) either on open-circuit or load condition.

For slot/pole combinations of odd slot number as investigated in this paper, the following relations can be given

A. Open-circuit

As discussed in the previous section, the air gap harmonics under the open-circuit condition can be classified into two types: original PM harmonics and corresponding modulated one. The features of the open-circuit air gap field are summarized in Table 4.3.

Table 4.3 Attributes of Open-Circuit Air Gap Field

Sources	Harmonic order
Original PM harmonics	$it(3m\pm1)$
Modulated PM harmonics	$\lvert it(3m\pm1) \pm jt(6k+3) \rvert$

Hence, the difference between any two field harmonic orders can be summarized as follows:

1) Harmonic order difference between the original PM harmonics: $t(3m \pm 1)(i_1 - i_2)$;
2) Harmonic order difference between the modulated PM harmonics and the original one: $t[(3m \pm 1)i_1 - |i_2(3m \pm 1) \pm j_1(6k + 3)|]$;
3) Harmonic order difference between the modulated PM harmonics: $t[|i_1(3m \pm 1) \pm j_1(6k + 3)| - |i_2(3m \pm 1) \pm j_2(6k + 3)|]$;

From the forgoing equations for the existence criterion of UMF under the open-circuit condition, it can be seen that whatever the machine periodicity t is, no UMF exists under the open-circuit if the stator slotting effect is ignored since the harmonic order difference between any two original PM harmonics is not smaller than two. On the other hand, only when the machine periodicity t equals to one, will the open-circuit UMF be generated since the harmonic order difference between either modulated PM harmonics or original PM harmonics must be

the multiple of *t*.

To conclude, for the fractional slot PM machine having odd number of stator slots, the open-circuit UMF will only exist when the great common divisor between the number of stator slots and rotor pole pairs is one. This UMF is caused by the stator slotting effect.

B. On-load

When the machine is under on-load condition, it is essential to investigate whether the adjacent armature reaction harmonics differed by one exist. In addition, the mutual interaction between PM harmonics and armature reaction harmonics should also be accounted for. Actually, it is the most significant source contributing to the production of UMF, if any, due to the relatively larger amplitude of PM field.

Hence, the harmonic order difference can be written as:

1) Self-interaction in armature reaction harmonics: $t[|(3n_1 \pm 1) \pm j_1(6k+3)| - |(3n_2 \pm 1) \pm j_2(6k+3)|]$;
2) Mutual-interaction between PM harmonics and armature reaction harmonics: $t[|(3n_1 \pm 1) \pm j_1(6k+3)| - |i_1(3m \pm 1) \pm j_2(6k+3)|]$;

It can be found that the harmonic order difference in either self-interaction or mutual interaction is always the multiple of t, even when the slotting effect is considered for the armature reaction. When the machine periodicity is larger than one, no UMF will be produced under the on-load condition.

On the other hand, when the machine periodicity *t* is one, the UMF due to self-interaction of armature reaction harmonics and mutual interaction with PM harmonics will be produced even when the slotting effect is ignored. This is because the armature reaction always consists of the 1th and 2nd harmonics when *t*=1, hence the self-interaction will appear.

As for the mutual interaction, there always exist the corresponding armature reaction harmonics which differ by one with the PM fundamental harmonics, as shown in Table 4.4.

In summary, only when the machine periodicity is one, will the UMF be produced in fractional slot PM machines having odd number of stator slots both on open-circuit and on-load condition.

Table 4.4 Harmonic Sources of UMF Due to Mutual Interaction

Pole pairs number	Sources	
	PM fundamental harmonic order	Armature reaction harmonic order
$p = 3m + 1$	$3m + 1$	$3n - 1 = 3m + 2$ $(n = m + 1)$
$p = 3m - 1$	$3m - 1$	$3n + 1 = 3m - 2$ $(n = m - 1)$

4.3.2 FE Validation

In order to verify the forgoing theoretical analyses, in this section, two 9-slot surface-mounted PM brushless machines with different rotor pole numbers, as shown in Fig.4.1, corresponding to different machine periodicity are compared by FE method. The design parameters are listed in Table 4.5.

Fig.4.4 illustrates the open-circuit air gap field spectra of two machines. For the machines with periodicity of 1, it can be seen that the modulated PM harmonics interacting with adjacent original PM harmonics leads to the open-circuit UMF. On the other hand, for the machines with periodicity of three, it is obvious that the harmonic order difference between existing harmonics must be triplen. Thus, no UMF will be produced under this circumstance, as shown in Fig.4.5. It can be seen that there still exists a negligible amount of UMF in the machine with periodicity >1. This is introduced by the local saturation in the stator which yields certain adjacent PM harmonics interacting with the existing one.

Under on-load condition, it is important to determine whether there exists mutual interaction between adjacent PM harmonics and armature reaction harmonics. As shown in Fig.4.6 (a), in the machine with periodicity of 1, the sub-harmonic in the MMF interacts with the PM fundamental harmonic, which contributes most to the production of UMF. Meanwhile, for the machine with periodicity of three, the harmonic order difference between the armature reaction and PM harmonics must be multiples of three. Hence, there will be no additional UMF compared with open-circuit condition. Fig.4.7 shows the profile of on-load UMF in the rectangular coordinate. It can be seen that the additional UMF resulting from armature reaction only exists in machines with periodicity of 1. The on-load UMF of machine with periodicity >1 is negligible.

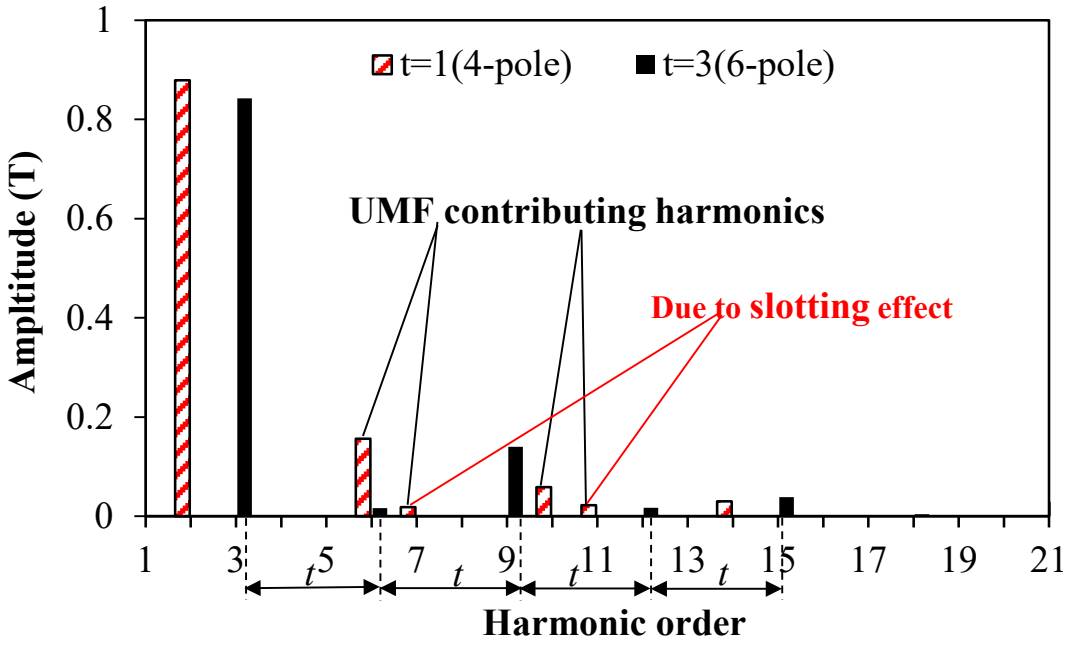

Fig.4.4. FE predicted open-circuit radial air gap field spectra for two 9-slot machines.

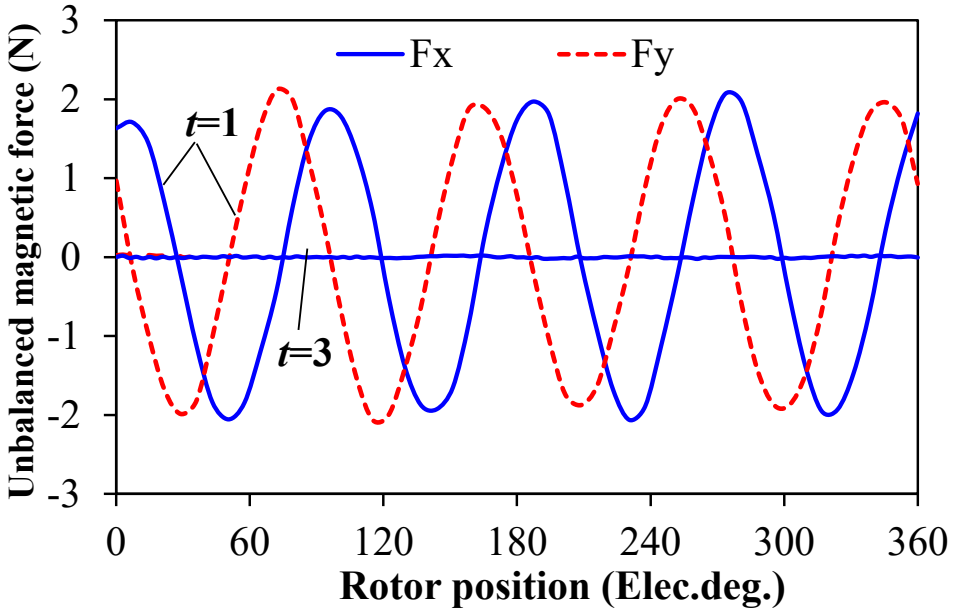

Fig.4.5. Open-circuit UMFs for two 9-slot machines.

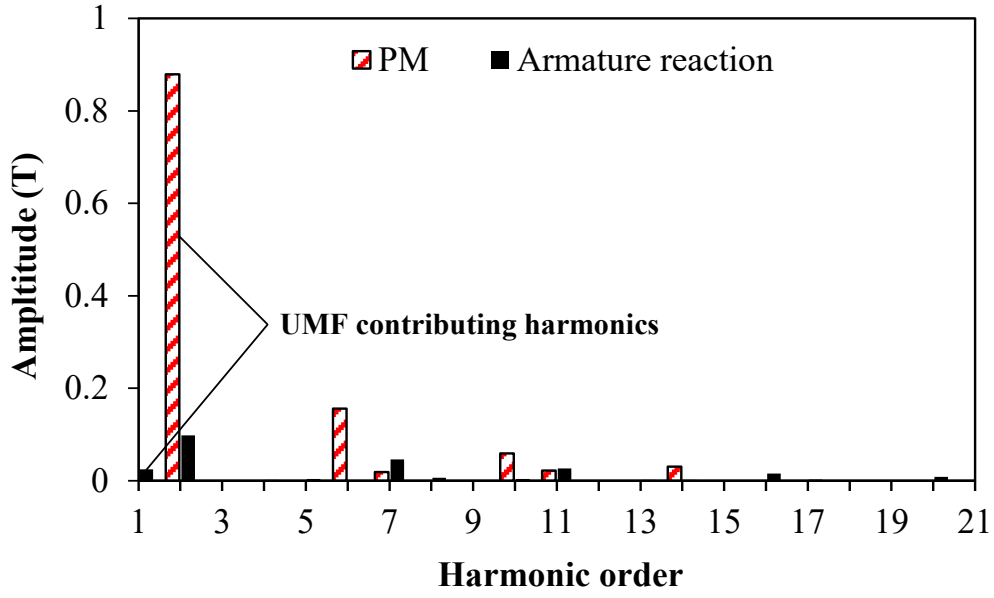

(a)

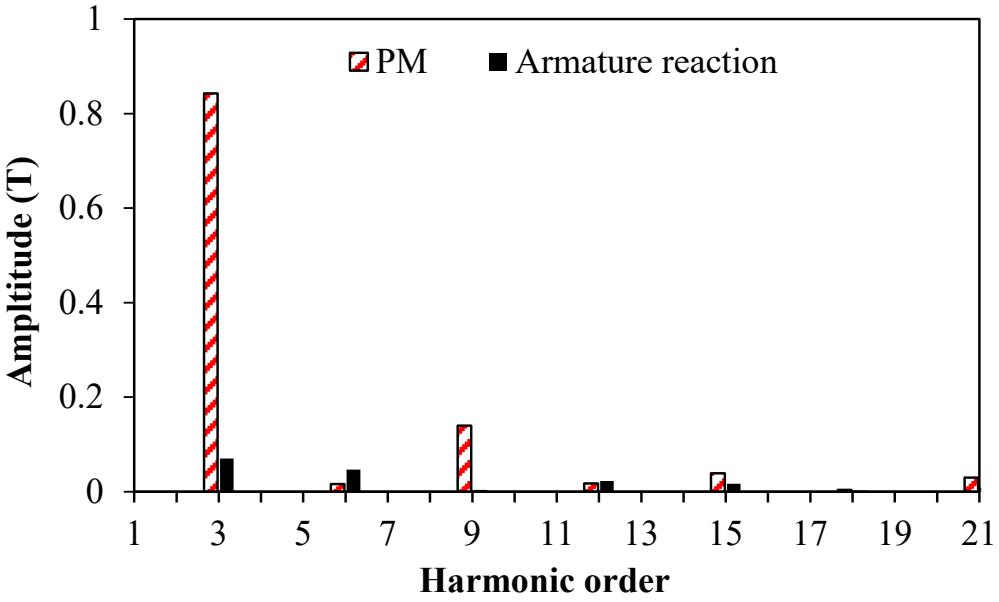

(b)

Fig.4.6. FE predicted on-load radial air gap field spectra for two 9-slot machines (I_a=80A). (a) t=1(4-pole). (b) t=3 (6-pole).

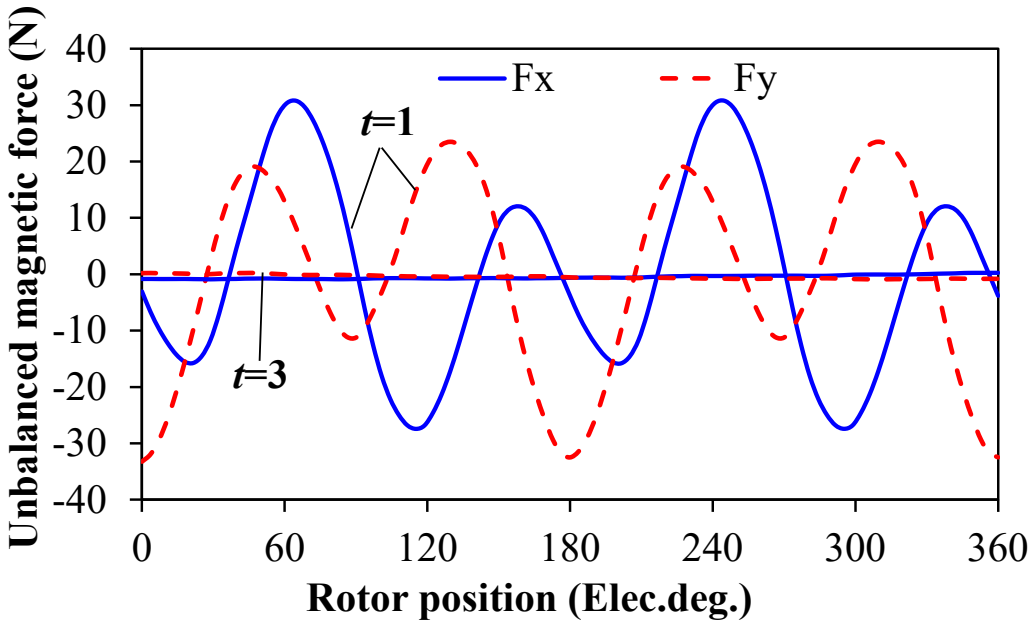

Fig.4.7. On-load UMFs for two 9-slot machines (I_a=80A).

4.4 Influence of Slot and Pole Number Combinations on Unbalanced Magnetic Force

In the previous section, the existence criterion of UMF in fractional slot PM machine with odd number of stator slots is clarified. However, it remains unknown how the slot and pole number combination influence the magnitude of UMF in machines with periodicity of one. In this section, five machines with same odd stator slot number of 9 but different rotor pole numbers of 2, 4, 6, 8, 10 are compared in terms of UMF. Two machines are featured with a low pole number (9-slot 2-pole and 9-slot 4-pole) and the other two machines have the slot and pole number differing by one (9-slot 8-pole and 9-slot 10-pole). Of all the machines to be investigated, the rated torque is around 2.6Nm. The rated current is 80A. It should be noted that the current advance angle is zero which indicates that the current is in phase with the phase back-EMF. The initial rotor position is defined as the rotor position at which the magnitude of Phase A back-EMF is zero.

The cross-sections of five machines are shown in Fig.4.1. The detailed design parameters are listed in Table 4.5. The variations of UMF with the phase current for four different machines are illustrated in Fig.4.8. Obviously, the magnitudes of UMF in fractional-slot PM machines

with odd number of stator slots are closely related to the slot and pole number combinations which determine the adjacent field harmonics thus the magnetic stress and force. It can be seen that the 9-slot 8-pole machine has a significantly larger UMF compared with that of others. On the contrary, the UMF of the 9-slot 2-pole machine is the smallest among all the five machines, except for the 9-slot 6-pole machine with periodicity of 1. Meanwhile, the UMF in the 9-slot 4-pole machine is slightly larger than that in the 9-slot 10-pole machine. In order to further explain this phenomenon, both the radial travelling stress and tangential travelling stress which are significant sources contributing to UMF are calculated analytically by the Maxwell stress tensor method given in (4.7). It should be noted that the air gap flux density is based on FE method. The radial and tangential components of flux density are acquired in the Maxwell 2D so that magnetic stresses are thereby obtained as shown in Fig.4.9.

Table 4.5 Parameters of Machines

Parameter	A	B	C	D	E
Slot number	9				
Pole number	2	4	6	8	10
Stator bore diameter(mm)	28	39	40	38	40
Tooth body width(mm)	5.6	5.6	5.7	5.9	6.3
Stator yoke height(mm)	6	4.7	4.3	4.1	3
Stator outer diameter(mm)	90				
Stack length(mm)	30				
Air gap length(mm)	2				
Slot opening(mm)	2.5				
Number of turns per phase	24				
Magnet thickness(mm)	6				

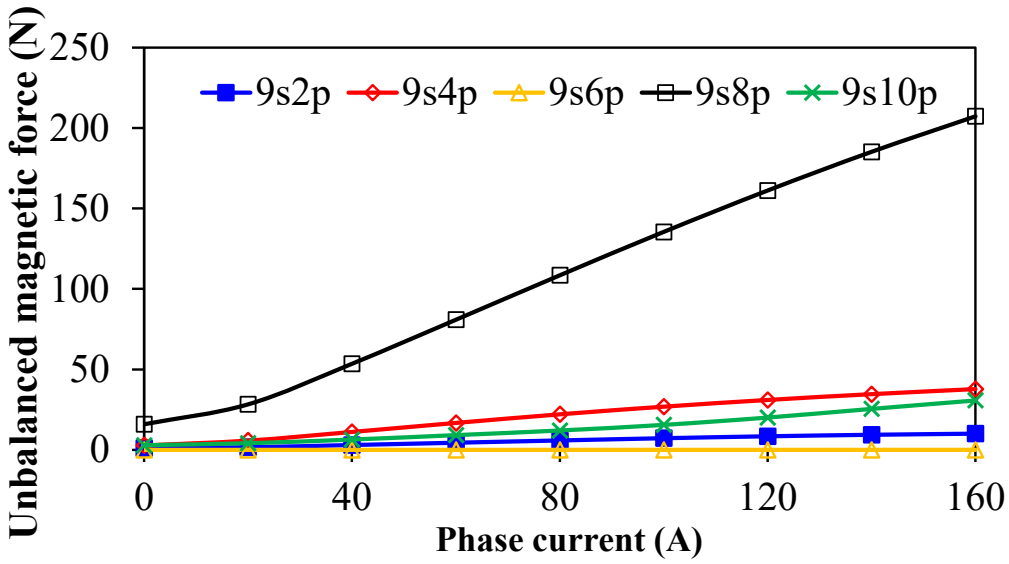

Fig.4.8. Variation of UMF with phase current.

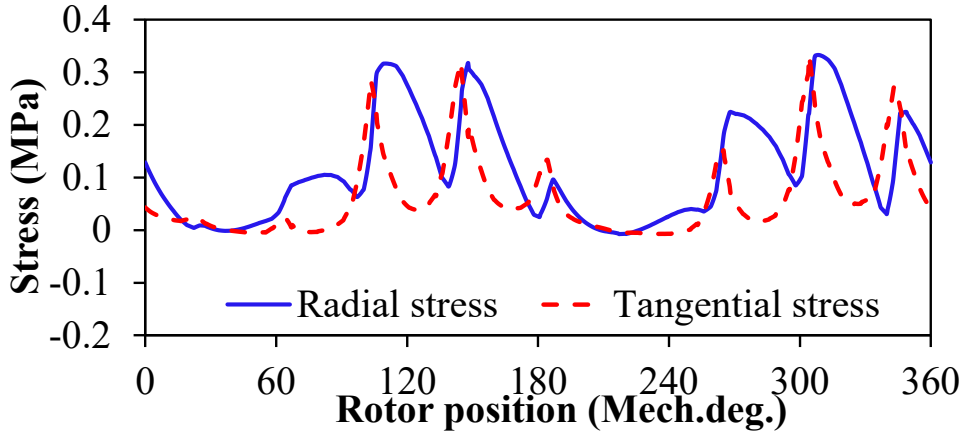

(a)

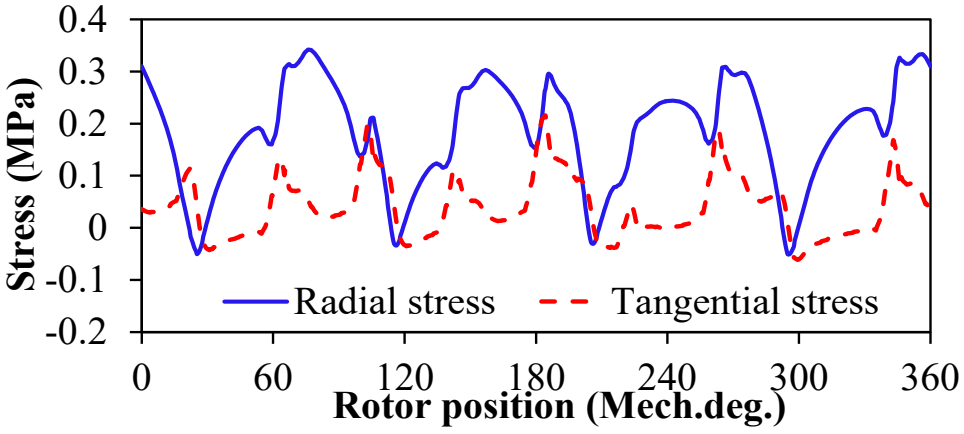

(b)

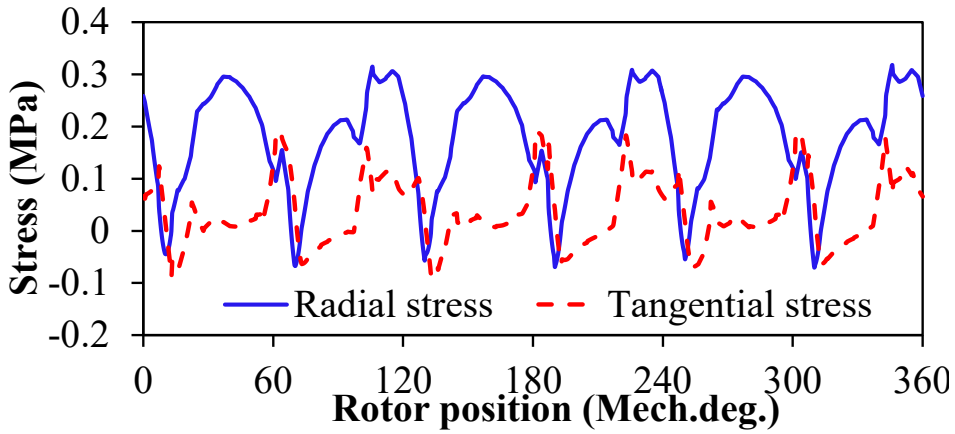

(c)

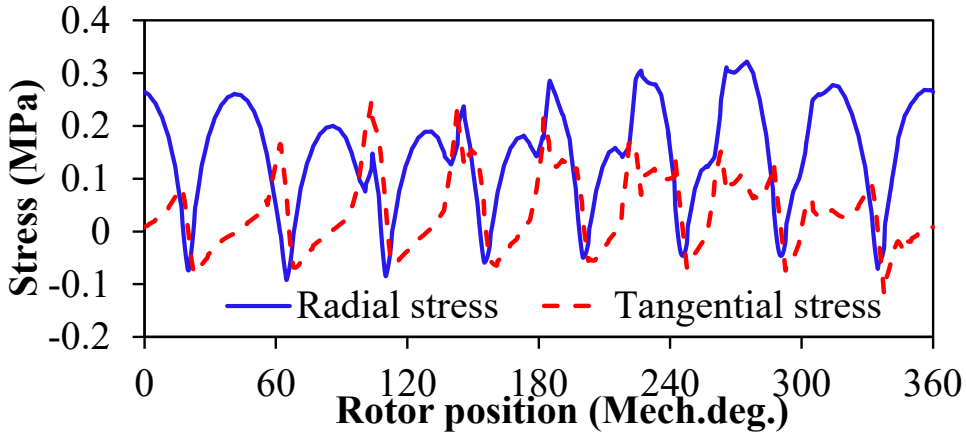

(d)

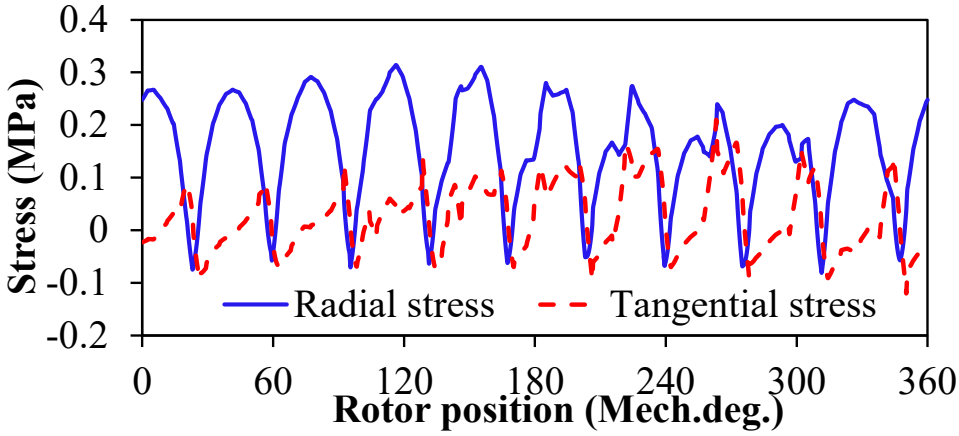

(e)

Fig.4.9. Variation of stress in 9-slot machines with rotor position. (a) 9-slot/2-pole machine. (b) 9-slot/4-pole machine. (c) 9-slot/6-pole machine. (d) 9-slot 8-pole machine. (e) 9-slot/10-pole machine.

For all five machines, the number of fluctuations in one mechanical cycle corresponds to the pole number. Similarly, with the air gap flux density variation, there also exist the drops in the stress profile which are caused by the stator slotting effect. As discussed in Section II, there are abundant harmonics in the radial and tangential magnetic stresses. However, only the first order component will contribute to the UMF. Hence, the first spatial order components are illustrated in Fig.4.10 by fast Fourier transform. It can be seen that the radial and tangential magnetic stresses in the 9-slot 8-pole and the 9-slot 10-pole are much larger than those in the 9-slot 2-pole and the 9-slot 4-pole. In addition, the value for the 9-slot 6-pole machine is negligible.

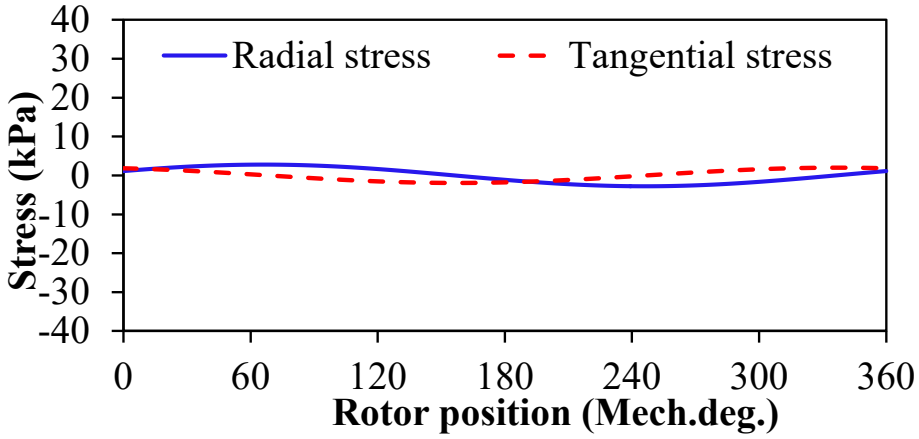

(a)

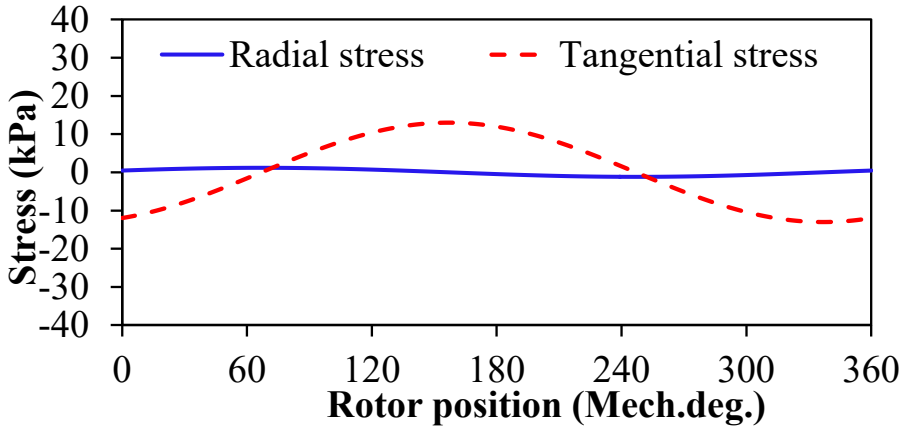

(b)

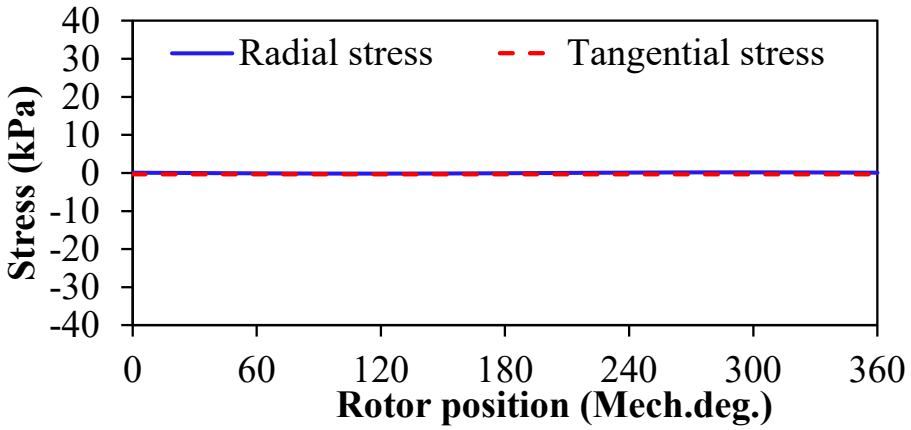

(c)

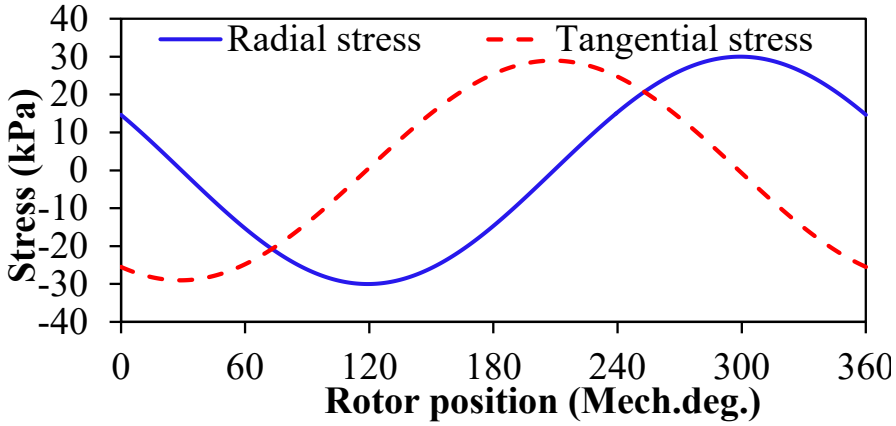

(d)

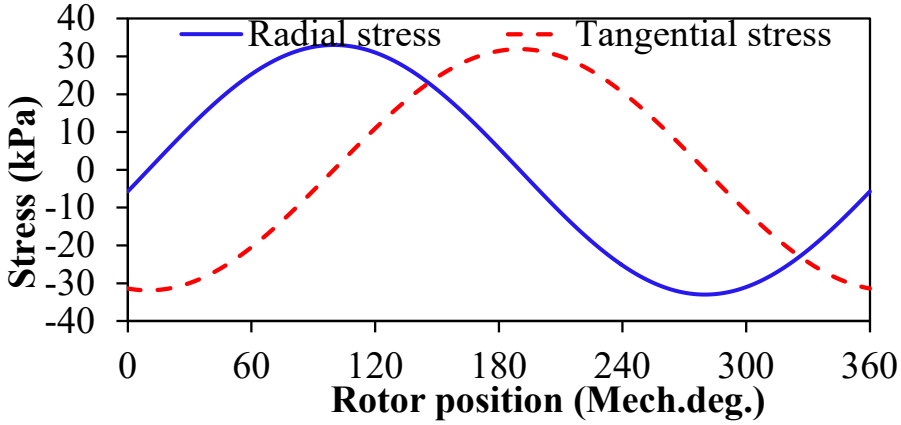

(e)

Fig.4.10. First order of stress of 9-slot machines. (a) 9-slot/2-pole machine. (b) 9-slot/4-pole machine. (c) 9-slot/6-pole machine. (d) 9-slot 8-pole machine. (e) 9-slot/10-pole machine.

This can be explained by the comparison of air gap flux density harmonics of these four machines as shown in Fig.4.11. As has been proven in Section II, the first order component of magnetic stress is mainly generated by the mutual interaction of fundamental PM harmonics and adjacent armature harmonics due to armature reaction. It can be found that magnitudes of the 5th spatial harmonic in the 9-slot 8-pole machine and the 4th spatial harmonic in the 9-slot 10-pole machine are significantly larger than those of the 1st spatial harmonic in the 9-slot 4-pole machine and the 2nd spatial harmonic in the 9-slot 2-pole machine. Hence, this will result in difference of magnitude of magnetic stress. Generally, the magnitudes of the 1st and 2nd spatial harmonics due to armature reaction are always smaller than those of the (p-1) th and (p+1) th spatial harmonics, thus leading to a smaller first order magnetic stress for the fractional-slot PM machines with a lower pole number.

Meanwhile, the value of UMF is also influenced by the phase of first order component of radial and tangential magnetic stresses which will determine whether cancelling or additive effect presents. As can be seen from Fig.4.10, in the 9-slot 2-pole machine and the 9-slot 8-pole machine, the tangential magnetic stresses are 90 degrees in advance compared with the radial magnetic stress. On the contrary, in the 9-slot 4-pole machine and the 9-slot 10-pole machine, the radial magnetic stresses are 90 degrees in advance of the tangential stress. The spatial phase differences in four machines eventually determine whether the radial magnetic stress and tangential magnetic stress are superimposed or canceled, as shown in Fig.4.12. It can be seen that the additive effect exists in the 9-slot 2-pole and 9-slot 8-pole machine whilst in the 9-slot 4-pole and 9-slot 10-pole machines the radial magnetic stresses are partially cancelled. Fig.4.13 shows the average UMF resulting from the radial and tangential magnetic stresses as well as the resultant UMF. Although the radial magnetic stress and tangential stress are additive in the 9-slot 2-pole machine, the amplitude of stress is the relatively small which overall leads to the smallest resultant UMF. On the other hand, due to the same additive effect as well as relatively larger magnetic stress in the 9-slot 8-pole machine, the resultant UMF is the largest among four machines. For the 9-slot 4-pole machine and the 9-slot 10-pole machine, the resultant UMFs are comparable and depend on the difference of radial and tangential magnetic stresses.

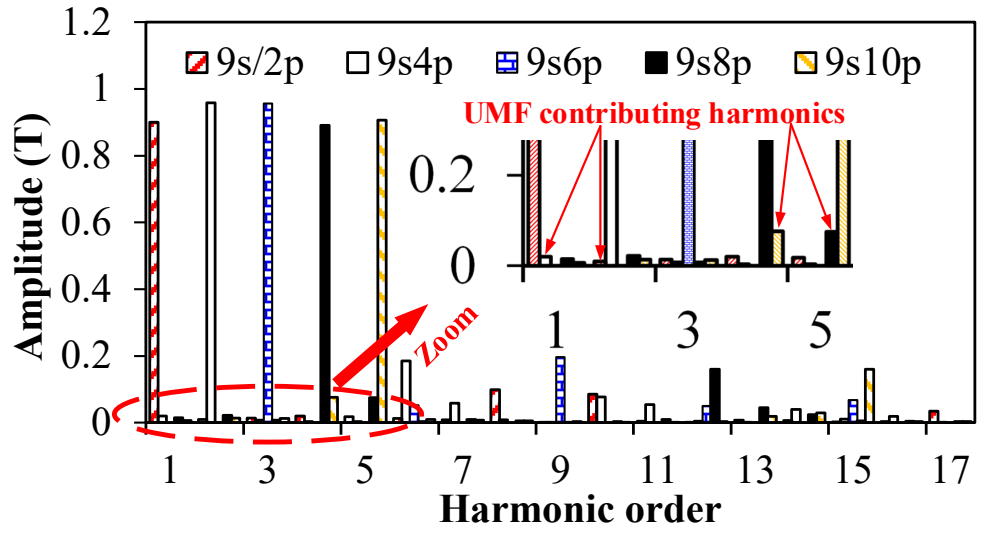

(a)

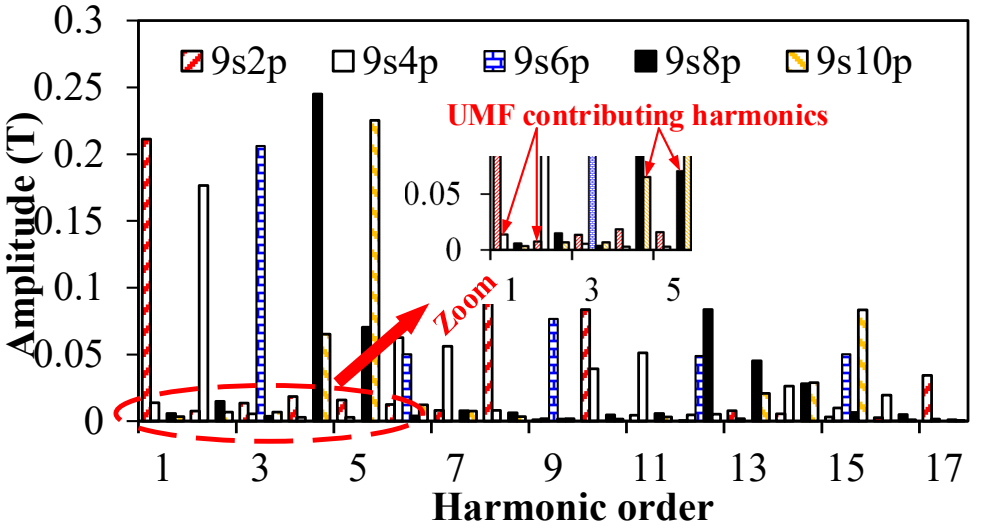

(b)

Fig.4.11. On-load air gap flux density harmonics of four machines. (a) Radial flux density harmonics. (b) Tangential flux density harmonics.

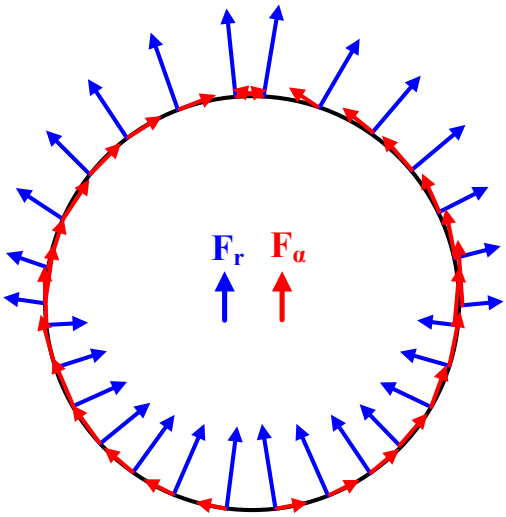

(a)

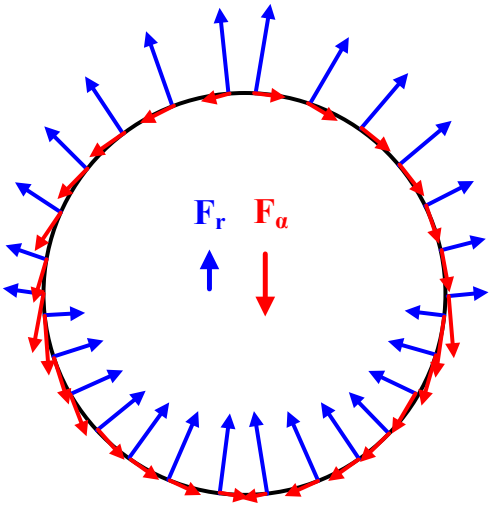

(b)

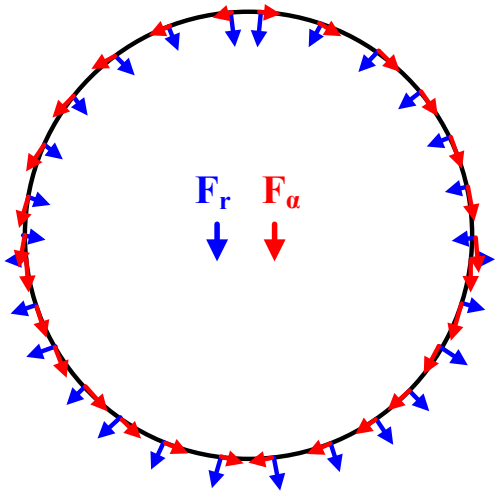

(c)

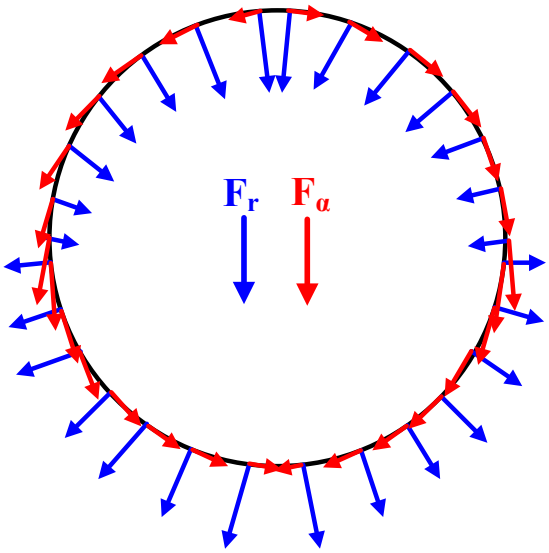

(d)

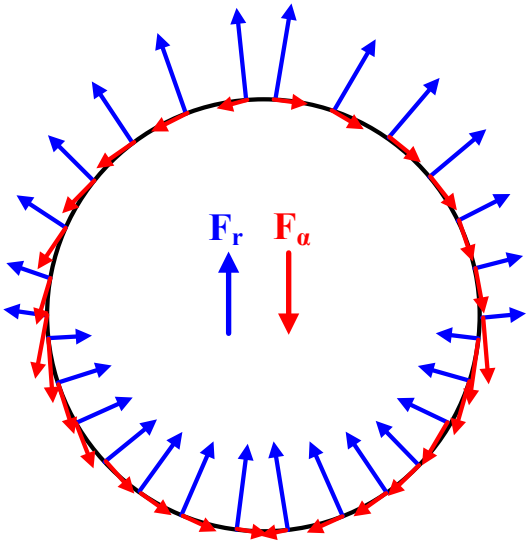

(e)

Fig.4.12. Cancelling and additive effects of magnetic stresses in 9-slot machines. (a) 9-slot 2-pole. (b) 9-slot 4-pole. (c) 9-slot 6-pole. (d) 9-slot 8-pole. (e) 9-slot 10-pole.

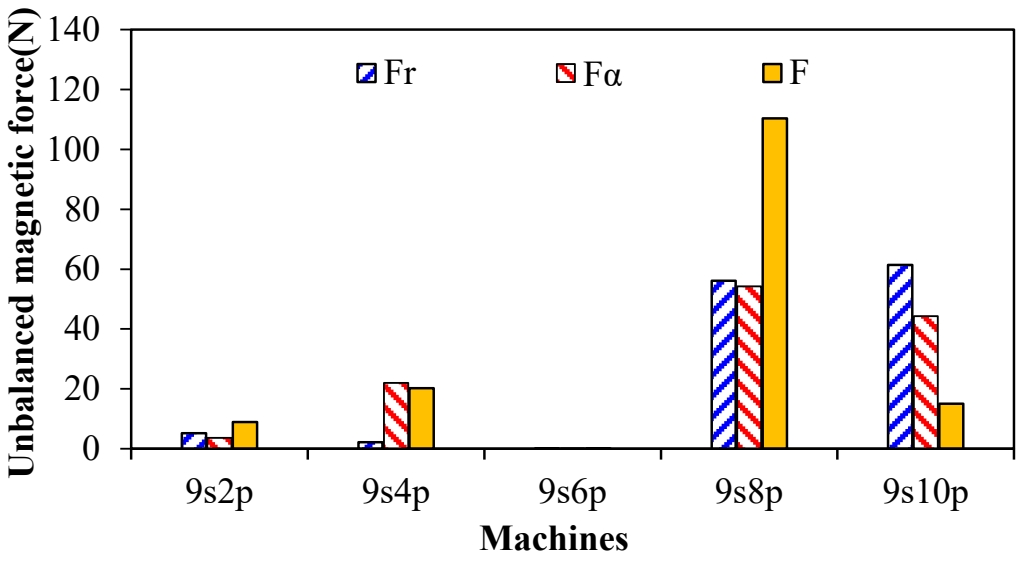

Fig.4.13. Comparison of average UMF resulting from radial magnetic stress and tangential magnetic stress.

4.5 Experimental Validation

Due to negligible UMF, a fractional-slot PM machine with 9-slot and 6-pole configuration is prototyped. As shown in Fig.4.14, the stator is equipped with nine non-overlapping coils. The rotor magnets are axially segmented in order to reduce the rotor eddy current loss. Due to the difficulties in the direct measurement of UMF, the electromagnetic performances of the prototype are tested so that the validity of the 2D FE model and the analytical models can be confirmed. The conclusion for the UMF based on the harmonic analysis can be further verified.

The measured and simulated open-circuit back-EMFs as well as the spectra are shown in Fig.4.15. The harmonics of back-EMF are extracted based on the FFT analysis, as illustrated in Table 4.6. It can be seen that the measured results agree well with the predicted ones.

Fig.4.16 illustrates the cogging torque and static torque profile as well as the variation of peak torque with current. The measured torque matches well with the FE predicted one with a deviation less than 10%, confirming the validity of the 2D FE models.

Table 4.6 Harmonics in the Back-EMF of 9-slor 6-pole Prototype Machine

	9-slot 6-pole phase back-EMF (%)	
Harmonic order	FEA	Measured
1	100 (0.93V)	100 (0.88V)
3	1.79	1.21
5	16.40	12.37
7	0.86	0.72
9	0.66	0.39
11	1.80	1.13
13	0.88	0.47

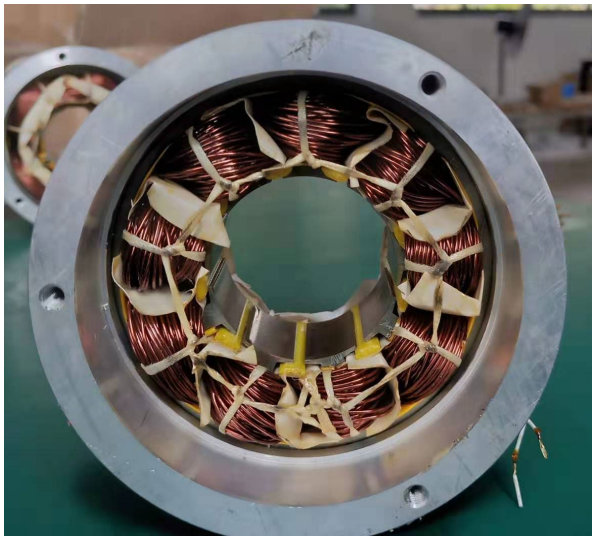

(a)

(b)

Fig.4.14. 9-slot 6-pole prototype machine. (a) Stator assembly. (b) Rotor assembly.

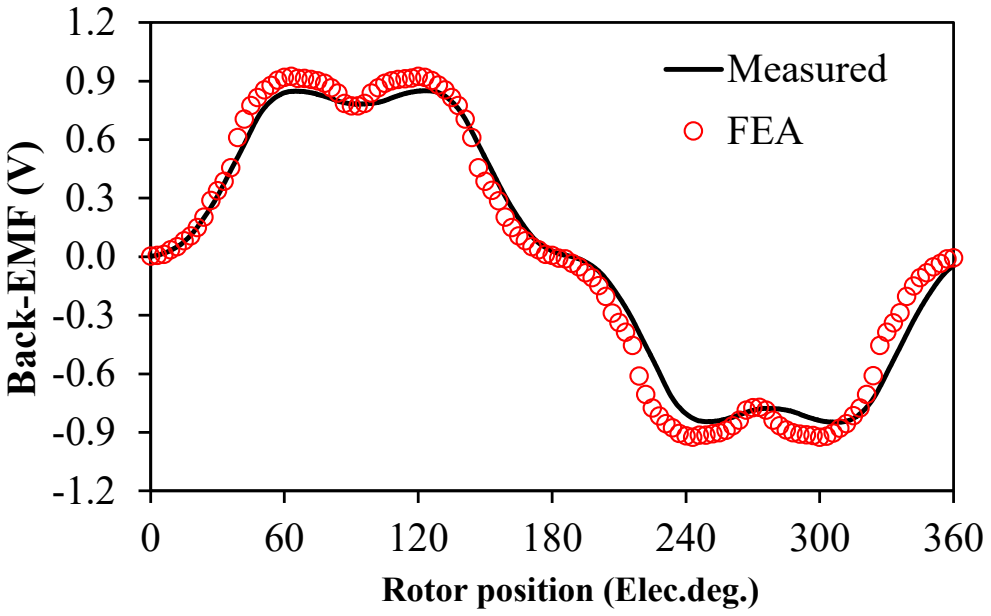

(a)

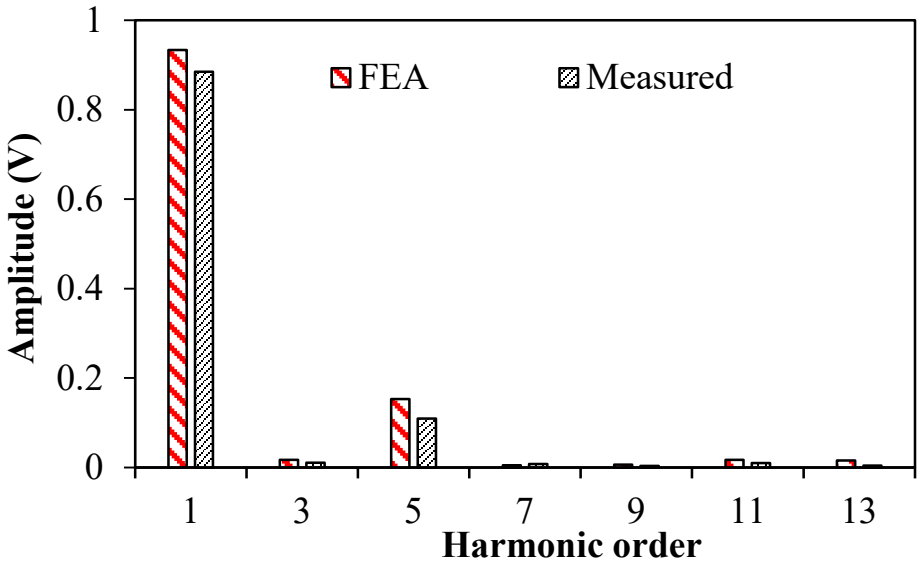

(b)

Fig.4.15. Measured and simulated back-EMF waveforms (*n*=400rpm). (a) Back-EMF profile. (b) Spectra.

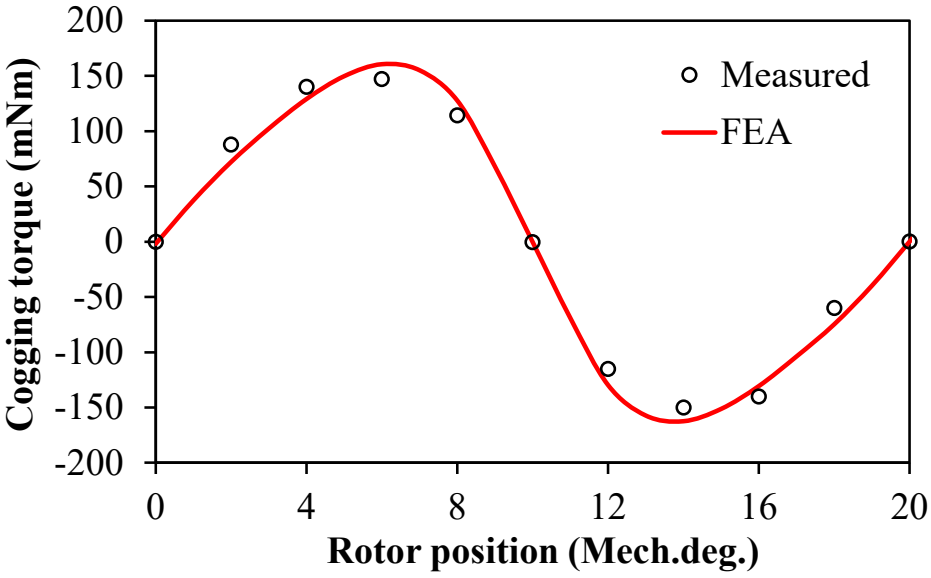
Cogging torque (mNm)
200
150
100
50
0
-50
-100
-150
-200
0
4
8
12
16
20
Rotor position (Mech.deg.)
Measured
FEA

(a)

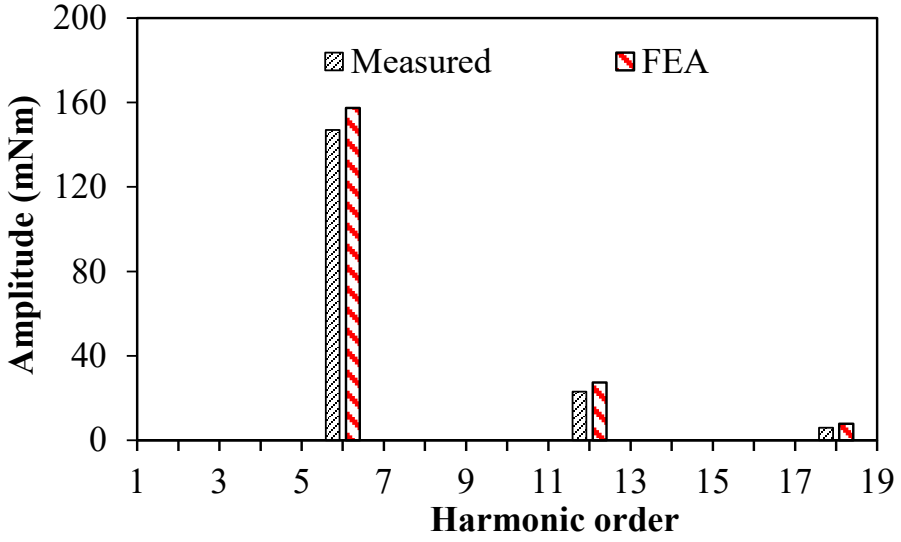
Amplitude (mNm)
200
160
120
80
40
0
1
3
5
7
9
11
13
15
17
19
Harmonic order
Measured
FEA

(b)

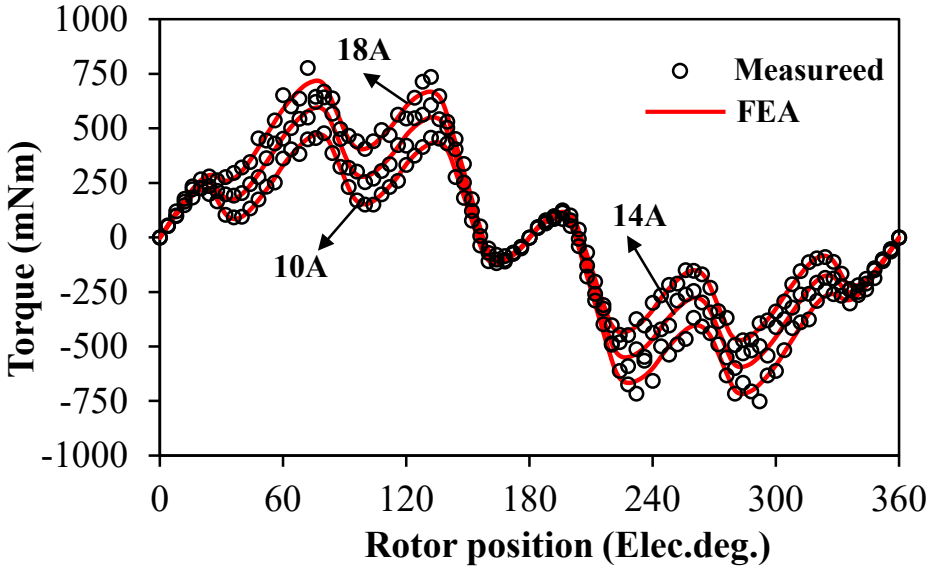
Torque (mNm)
1000
750
500
250
0
-250
-500
-750
-1000
0
60
120
180
240
300
360
Rotor position (Elec.deg.)
18A
10A
14A
Measureed
FEA

(c)

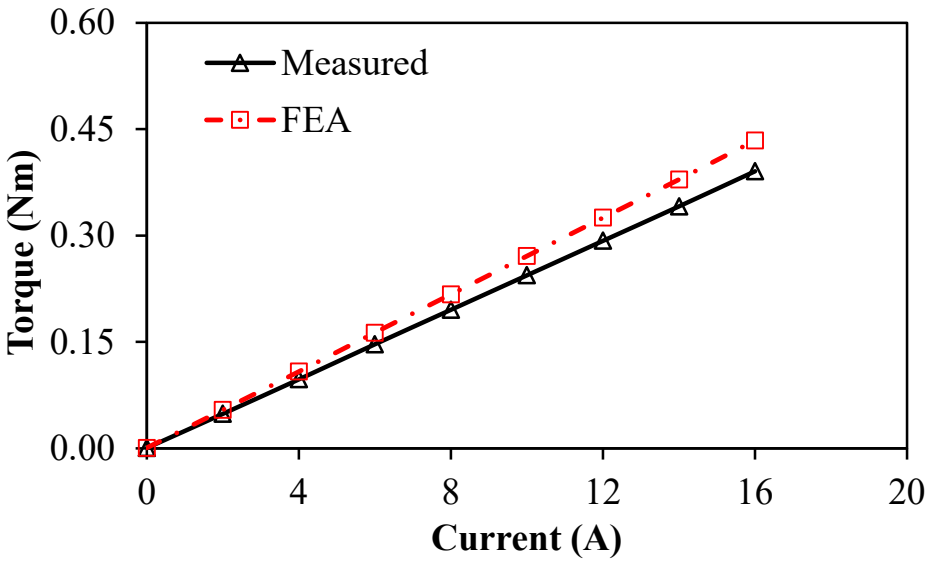

(d)

Fig.4.16. Measured and simulated static torque. (a) Cogging torque waveform. (b) Cogging torque spectra. (c) Static torque waveform (I_a=-2I_b=-2I_c). (d) Variation of peak torque with current.

4.6 Summary

In this chapter, the criterion for existence of UMF both on open-circuit and on-load condition in fractional-slot PM machines with odd stator slot number is investigated. It is concluded that only when the machine periodicity is one and the stator slotting effect is considered, will the open-circuit UMF be generated due to the mutual interaction between the modulated PM and original PM harmonics. On the other hand, the existence criterion of on-load UMF in the machines with periodicity of one is confirmed since both the self-interaction of armature reaction harmonics and the mutual interaction between the fundamental PM harmonic and the armature reaction harmonics will appear even when the slotting effect is ignored. For the fractional-slot PM machines with periodicity >1, e.g. 9-slot 6-pole machine, the first order of radial magnetic forces and tangential magnetic forces are quite small due to the absence of adjacent field harmonics thus the resultant UMF is negligible. Furthermore, the fractional-slot PM machines with a lower pole number, e.g. 2-pole and 4-pole, are compared with machines with a pole number $2p=N_s\pm1$. The UMF in machine with two poles is the smallest due to the smallest magnitude of the 2nd harmonic in armature reaction compared with counterparts in other machines. Instead, the UMF in the machines having pole number $2p=N_s$-1 is the largest due to the relatively larger magnitude of the $(p+1)^{th}$ armature reaction harmonics as well as the

additive effect between the first order radial and tangential stresses. Overall, in fractional-slot PM machines with a given odd number of stator slots of 9, the machines with periodicity >1, e.g. 9-slot 6-pole, 9-slot 12-pole as well as the machines with two-pole, e.g. 9-slot 2-pole are more preferred in terms of UMF. Finally, a prototype 9-slot 6-pole PM machine is manufactured and tested. The measured data confirm the validity of the electromagnetic performances obtained from the 2D FE model and the analytical models, which indirectly verify the conclusions on the UMF.

Chapter 5 Design and Analysis of High-Speed PM Machines Considering Electromagnetic and Mechanical Issues

In this chapter, the rotor stress analysis is conducted on a high-speed PM machine with segmented magnets retained by carbon-fibre sleeve. The rotor permanent magnet segmentation is first considered in the stress analysis of HSPMM. An explicit analytical model is firstly established whose results are then compared with that from 2D and 3D finite element methods (FEM). The worst operating scenario for HSPMM rotor mechanical robustness considering the PM segmentation is identified Afterwards, the geometric constraints considering the mechanical issue can be determined. Based on the transformation of mechanical issue into geometric constraints, a novel multi-physics design methodology for HSPMM considering both the electromagnetic and mechanical issue is proposed.

5.1 Introduction

High-speed PM machine (HSPMM) is very promising for high-speed application due to higher efficiency, power factor, and utilization factor in comparison with other types of high-speed electrical machines. However, there are still many obstacles and challenges for the HSPMM design, especially on the rotor side. Significant rotor eddy current loss and rotor mechanical stress will be produced under high-speed operation. Fig.1 illustrates a typical rotor cross-section of high-speed PM machine. Normally, the rotor pole numbers of high-speed PM machines are selected to be 2 or 4 depending on specific requirements and constraints.

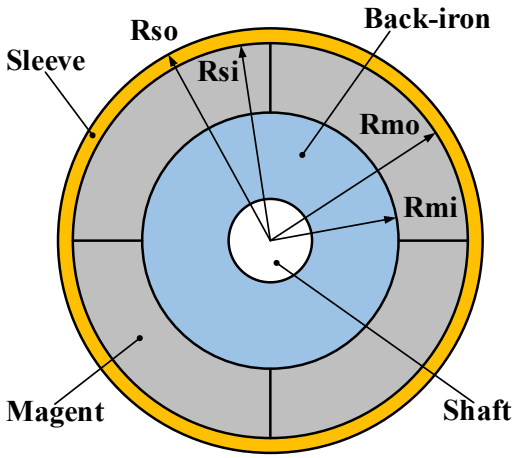

Fig.5.1. Cross-section of a typical 4-pole high-speed PM machine rotor.

The 4-pole rotor is more inclined to be adopted for high-power high-speed applications due to reduced end-winding length and stator copper loss, which are quite advantageous for stator thermal equilibrium in high power application [JAN04], [BIN06], [LUI14], [ZHA15]. However, the relatively high fundamental frequency introduced by the higher pole number will inevitably lead to higher rotor PM eddy current loss. Hence, for the 4-pole high-speed PM machine, the rotor magnets are usually segmented to reduce the eddy current loss.

In addition, as shown in Fig.5.1, the rotor magnets are retained by the sleeve to withstand the extremely high tangential stress resulting from high speed. Generally, the retaining sleeves can be classified into two types: Non-metallic ones and metallic ones. Glass-fiber and carbon-fiber are typical non-metallic sleeves which are featured with high yield strength and low mass density [BIN06]. This is quite desirable for the protection of PMs. In addition, the sleeve thickness can be maintained minimum for a given operating speed so that its influence on the air gap flux density can be minimized. The problem for this type of sleeve mainly lies in the thermal aspect. The thermal conductivity of carbon-fiber is quite low which means the heat generated from the rotor magnets cannot be dissipated easily [LI14]. Hence, the rotor magnets are normally segmented to reduce the eddy current loss. Alternatively, the copper shield may be placed at the inner side of carbon-fiber sleeve [SHA09]. On the other hand, the metallic sleeve such as titanium and Inconel are equipped with a relatively lower strength to density ratio compared to that of carbon-fiber. The advantages of metallic sleeve are high thermal conductivity and electrical conductivity as well as cost. The eddy current will be induced in the metallic sleeve instead of magnets. The metallic sleeve acts as the shield for the harmonic penetration into the magnets. Nevertheless, the selection of retaining sleeve should not only consider the mechanical aspects such as the magnet protection but also the electromagnetic and thermal aspects including the rotor eddy current loss reduction and rotor thermal issue.

In this chapter, the retaining sleeve is selected to be the carbon-fibre due to its large tensile strength. At high-speed operation, the rotor components will suffer huge centrifugal force and certain amount of thermal stress. The permanent magnet material ideally has a high compressive strength (800MPa) and a medium flexural strength (120MPa), but it is rather brittle [HUA16]. Hence, stress analysis is key issue for the mechanical robustness of HSPMMs. There are generally two sub-issues involved in the stress analysis of HSPMMs. Firstly, the exact value of stress in each rotor parts should be obtained. Then, the maximum stress induced in each components of the rotor should be ensured within the material strength under all

operating speed and temperature, especially for PMs which are quite vulnerable to tangential tensile stress. In addition, the contact pressure pointing to the inner side should always exist so that the electromagnetic torque can be transferred to the shaft.

The methods for stress calculation can be classified into analytical and numerical ones. Several papers on the analytical calculation of rotor stress can be found [BIN06], [WAN07], [BOR10], [BUR17]. [BIN06] proposed a simplified analytical model for stress calculation based on the assumption that the rotor is strictly rotational symmetry. In [WAN07] and [BOR10], the displacement technique was adopted for the stress calculation of the HSPMM with the nonmagnetic alloy sleeve. The PM rotors are normally modelled as the multi-layered cylinders. However, all the aforementioned analytical models are based on the assumption of planar stress which is valid for rotors with short axial length. Hence, in [BUR17], a 3D analytical model considering the axial stress was established for both solid and hollow magnet rotors in the plane strain condition. Although all these analytical solutions can provide a fundamental insight from the stress generation to reduction, as pointed out in [BIN06], the non-linear factor such as geometry discontinuity and edging effect cannot be considered in the analytical model. A derivation can still be generated in the analytical models. Hence, in order to obtain the exact value of rotor stress, 2D or 3D Finite-Element Methods (FEM) are more widely adopted in the calculation of rotor stress with complicated structure or other aforementioned non-linear factors. In this chapter, the limitation of analytical calculation will also be highlighted in Section 5.2.

Another important design consideration is to ensure all the obtained stress within the material limit in the whole operating speed and temperature range, so does the contact pressure. Whenever the speed and temperature change, there is always the contact pressure pushing magnets into the rotor back-iron. Hence, it is essential to find the worst operating scenarios with respect to operating speed and temperature for each components of the rotor. The rotor stress is therefore checked only under the worst operating scenario instead of the whole working range. In fact, quite a few papers discussed about this issue. [BIN06] did point out the thermal expansion must be considered due to its significant portion in the sleeve tangential stress. However, how the rotor stress is affected by the temperature is not further studied. [FAN17] did investigate the worst operating points for the rotor with carbon-fiber sleeve. However, the PM tangential stress was ignored in the analysis. [ZHA15] comprehensively investigated the influence of operating speed and temperature on the sleeve and magnet

tangential and radial stresses.

However, all the mentioned findings are only valid for the PMs in an integral ring. The potential influence of PM segmentation on the worst operating scenarios is ignored in the literature. On the other hand, the influence of PM segmentation on the amplitude of rotor stress also remains to be investigated. It will be demonstrated in this chapter that certain sleeve stress concentration will occur while the segmented magnets are under tensile tangential stress. As a matter of fact, the stress concentration issue in the HSPMM with inter-pole gap has been reported in several papers. In [BIN06], the inter-pole gap was cancelled in order to avoid the sleeve stress concentration. In [ZHA15], it was concluded that the inter-pole filler can significantly reduce the stress concentration. In addition, the influence of material properties on the stress concentration cancelling effect was also revealed. In this chapter, three types of pole filler with different shapes are compared in terms of sleeve and PM stress reduction.

As can be concluded from the previous analysis, the rotor mechanical design is closely related with the electromagnetic design. As a matter of fact, the design of HSPMM has never been about one single aspect only. Several issues should be addressed including the loss reduction, rotor integrity and so on. Hence, several multi-physics design methodologies for HSPMM are proposed.

The most traditional design method is conducting the optimization in each of sub-models (electromagnetic, mechanical, thermal, etc.) separately and iteratively [ZWY05], [GER09], [HUA16], [DU19]. The optimization is conducted individually in each domain which is called fragmented conception [PFI10]. This methodology ensures that all the physical constraints can be considered. However, the problem lies in the ignorance of mutual influence between those different design aspects. The electromagnetic optimum may not be the real optimum when the mechanical constraints are considered. [FEN19] gives a good example of how the optimal electromagnetic design is influenced by the mechanical constraints by showing the determination of optimal split ratio of HSPMM. Thus, it is necessary to establish a design methodology which considers the multi-physics mutual interactions.

Generally, there are two different ways for the multi-physics design considering the mutual influence. One way is to establish a simplified analytical model so that a mathematical optimization can be conducted [PFI10], [JAN11], [BER16]. The advantage of this method is that it is super fast and very convenient. It also provides significant insights into the principles

of the machine. However, some non-linear factors are ignored in the analytical models such as local saturation in the electromagnetic model or local concentrated stress in mechanical model. Thus, another multi-physics optimization is based on the FE method. A typical example of rotor shape optimization for IPM is introduced in [YAM13]. In [YAM13], a shaping technique considering the stress and electromagnetic field is proposed for the high speed machine. The permeability and the core-loss coefficients used in the electromagnetic field analysis are modified due to the results of the stress analysis. This method has the advantages in that it can be applied to complicated structures. However, the cost is enormous computation time due to the two-way coupling between the electromagnetic aspect and the mechanical aspect.

In order to combine the merits of accuracy of FE-based multi-physics design and convenience of analytical-based mathematical optimization, in this chapter, a novel design methodology which considers the electromagnetic and mechanical stress constraints simultaneously is proposed. The mechanical stress limitations are transformed into the geometric constraints which are incorporated in the electromagnetic design. The influence of mechanical constraints on the electromagnetic design can be clearly identified.

This chapter will be organized as follows. In Section 5.2, the explicit analytical models considering the material anisotropy and thermal effects are established. The analytical results are then compared with the ones from 2D and 3D FEM respectively. The phenomenon of sleeve stress concentration due to PM segmentation is therefore revealed in this section. The conditions of the stress concentration are also clarified. Then, the influence of PM segmentation on the worst operating scenario is studied. Meantime, the influence of sleeve thickness and interference fit on the rotor stress while the PMs are segmented is investigated, providing a guideline to avoid the presence of stress concentration by adjusting these two parameters. Furthermore, the stress concentration due to geometry discontinuity is systematically investigated. Pole-fillers with different shape are compared in terms of reduction of sleeve tangential stress and PM tangential stress. Based on the transformation of mechanical stress constraint into the geometric constraints, a novel multi-physics design methodology for HSPMM considering mechanical and electromagnetic issue simultaneously is proposed in Section 5.3. Finally, in Section 5.4, a prototype 6-slot 4-pole machine is made based on the previous guidelines. The electromagnetic performance is validated by the experiments together with the summary given in Section 5.5.

5.2 Rotor Mechanical Stress Analysis of High-Speed PM Machines Considering PM Segmentation

Although the general expressions of rotor stress in HSPMM with carbon-fibre sleeve were given in [BOR10] and [ZHA15], the detailed expression of coefficients were missing. In order to obtain the exact value of rotor stress in the HSPMM with carbon-fibre sleeve, in this section, the explicit 2D analytical analysis of the rotor stress is conducted on a 4-pole high-power high-speed PM machine with the highest power and speed of 25kW and 100krpm, respectively. The rotor thermal expansion and material anisotropy are considered. Then, the analytically predicted results are compared with 2D and 3D FEM predicted data to verify the validity and constraints of those stress-predicting methods. In addition, the impact factors for the rotor stress are obtained by the analytical analysis so that the worst-case scenario can be further determined with and without consideration of magnet segmentation. The following paragraphs are from [J4].

5.2.1 Theoretical Analysis of Rotor Stress with Carbon-Fibre Sleeve

The analytical model assumes planar stress which is normally correct for the rotor with short axial length. The planar strain model should be accounted for only in very long cylindrical rotors in which the axial stress will occur. It should be noted the magnet segmentation is not considered in the analytical model for simplicity. However, in the following section, the analytical data will be compared with 2D and 3D FEM predicted results considering the magnet segmentation which verifies the validity and limitation of 2D planar stress model shown in Fig.5.1.

5.2.1.1 Analytical analysis

The basic strategy for obtaining the stress analytically is to establish of the correlations between stress and displacement. Then the general solution of stress can be further determined by solving the non-homogeneous differential equation. The coefficients can be obtained through the boundaries condition.

A. Sleeve stress

According to Hooke's law for linear-elastic material, the relationship between stress and strain considering material anisotropy and temperature rise can be written as [YON13]

$$\begin{bmatrix} \varepsilon_r \\ \varepsilon_\theta \end{bmatrix} = \begin{bmatrix} \frac{1}{E_r} & -\frac{v_{\theta r}}{E_\theta} \\ -\frac{v_{r\theta}}{E_r} & \frac{1}{E_\theta} \end{bmatrix} \begin{bmatrix} \sigma_r \\ \sigma_\theta \end{bmatrix} + \begin{bmatrix} \alpha_r \\ \alpha_\theta \end{bmatrix} \Delta T \tag{5.1}$$

Hence, the stress can be expressed as

$$\begin{bmatrix} \sigma_r \\ \sigma_\theta \end{bmatrix} = \begin{bmatrix} \frac{1}{E_r} & -\frac{v_{\theta r}}{E_\theta} \\ -\frac{v_{r\theta}}{E_r} & \frac{1}{E_\theta} \end{bmatrix}^{-1} \begin{bmatrix} \varepsilon_r - \alpha_r \Delta T \\ \varepsilon_\theta - \alpha_\theta \Delta T \end{bmatrix} \tag{5.2}$$

where ε_r and ε_θ denote the radial strain and tangential strain of sleeve material with anisotropy such as carbon-fibre. E_r and E_θ represent the radial and tangential Young's modulus, respectively. $\nu_{\theta r}$ and $\nu_{r\theta}$ are radial and tangential Poisson's ratios, respectively. The following relations can be given:

$$\frac{v_{\theta r}}{E_r} = \frac{v_{r\theta}}{E_\theta} \tag{5.3}$$

α_r and α_θ denote the radial and tangential coefficients of thermal expansion (CTE). ΔT is the temperature rise of the sleeve material. It should be noted that the rotor temperature rise in this analytical model is considered to be constant for each cylinder parts in the radial direction for simplicity. Thus, the following relations can be obtained:

$$\frac{\partial \Delta T}{\partial r} = 0 \tag{5.4}$$

In order to establish the differential equation for displacement, the relations between the strain and the radial displacement u are given as

$$\begin{cases} \varepsilon_r = \dfrac{\partial u}{\partial r} \\ \varepsilon_\theta = \dfrac{u}{r} \end{cases} \tag{5.5}$$

Substituting (5.3) and (5.5) into (5.2), the radial and tangential sleeve stresses can be written

as

$$\begin{cases} \sigma_r = \dfrac{E_r}{1-v_{\theta r}v_{r\theta}}\left[\dfrac{\partial u}{\partial r}+\dfrac{v_{\theta r}}{r}u-\left(\alpha_r+v_{\theta r}\alpha_t\right)\Delta T\right] \\ \sigma_\theta = \dfrac{E_\theta}{1-v_{\theta r}v_{r\theta}}\left[v_{r\theta}\dfrac{\partial u}{\partial r}+\dfrac{1}{r}u-\left(\alpha_t+v_{r\theta}\alpha_r\right)\Delta T\right] \end{cases} \tag{5.6}$$

On the other hand, according to the material mechanics theory, the balance differential equation can be given by [YON13]

$$r\frac{\partial \sigma_r}{\partial r} = \sigma_\theta - \sigma_r - \rho r^2\Omega^2 \tag{5.7}$$

where ρ denotes the material density and Ω is the rotating speed of the material. Substituting (5.6) and (5.4) into (5.7), the differential equation of displacement can be obtained

$$\frac{\partial^2 u}{\partial r}+\frac{1}{r}\frac{\partial u}{\partial r}-A\frac{u}{r^2}+B\frac{\Delta T}{r}+C\rho\Omega^2 r=0 \tag{5.8}$$

where

$$\begin{cases} A = \dfrac{E_\theta}{E_r} \\ B = (v_{\theta r}-1)\alpha_r+(\dfrac{E_\theta}{E_r}-v_{\theta r})\alpha_\theta \\ C = \dfrac{1-v_{\theta r}v_{r\theta}}{E_r} \end{cases} \tag{5.9}$$

The general solution of the non-homogeneous differential equation (5.8) is

$$u_{sr} = C_{s1}r^{\sqrt{A}}+C_{s2}r^{-\sqrt{A}}+\frac{B}{A-1}\Delta T+\frac{C}{A-9}\rho_s\Omega^2 r^3 \tag{5.10}$$

Where C_{s1} and C_{s2} are integration constants depending on the boundaries which will be given later. Substituting (5.10) and (5.4) into (5.6), the sleeve radial and tangential stresses can be finally obtained as

$$\sigma_{sr}=\frac{E_r}{1-v_{\theta r}v_{r\theta}}\left\{\begin{array}{l}(1+v_{\theta r})(C_{s1}r^{\sqrt{A}-1}+C_{s2}r^{-\sqrt{A}-1})+\\(3+v_{\theta r})\dfrac{C\rho_s}{A-9}\Omega^2r^2+(\dfrac{B}{A-1}v_{\theta r}r^{-1}-\alpha_r-v_{\theta r}\alpha_t)\Delta T\end{array}\right\}$$
$$\sigma_{s\theta}=\frac{E_\theta}{1-v_{\theta r}v_{r\theta}}\left\{\begin{array}{l}(1+v_{r\theta})(C_{s1}r^{\sqrt{A}-1}+C_{s2}r^{-\sqrt{A}-1})+\\(1+3v_{r\theta})\dfrac{C\rho_s}{A-9}\Omega^2r^2+(\dfrac{B}{A-1}r^{-1}-\alpha_t-v_{r\theta}\alpha_r)\Delta T\end{array}\right\} \tag{5.11}$$

B. PM stress

For the PM stress calculation, the general procedure is the same as that of sleeve stress. Due to the isotropic characteristic for PM material, the following can be given:

$$\begin{cases}E_r=E_\theta=E_m\\v_{\theta r}=v_{r\theta}=v_m\end{cases} \tag{5.12}$$

Similarly, substituting (5.12) into (5.8), the differential equation for the radial displacement of PM can be written as

$$r^2\frac{\partial^2u}{\partial r}+r\frac{\partial u}{\partial r}-u+\frac{1-v_m^2}{E_m}\rho_m\Omega^2r^3=0 \tag{5.13}$$

The general solution for this differential equation can be given as

$$u_{mr}=C_{m1}r+\frac{C_{m2}}{r}-\frac{1-v_m^2}{8E_m}\rho_m\Omega^2r^3 \tag{5.14}$$

Where C_{m1} and C_{m2} are integration constants depending on the boundaries which will be given later. The PM radial stress and tangential stress can be obtained as

$$\begin{aligned}\sigma_{mr}&=-\left[\frac{C_{m2}E_m}{1+v_m}\frac{1}{r^2}+\frac{(3+v_m)\rho_m\Omega^2r^2}{8}\right]+\left(\frac{C_{m1}E_m}{1-v_m}-\frac{\rho_mE_m\Delta T}{1+v_m}\right)\\\sigma_{m\theta}&=\left[\frac{C_{m2}E_m}{1+v_m}\frac{1}{r^2}-\frac{(3v_m+1)\rho_m\Omega^2r^2}{8}\right]+\left(\frac{C_{m1}E_m}{1-v_m}-\frac{\rho_mE_m\Delta T}{1+v_m}\right)\end{aligned} \tag{5.15}$$

C. Rotor back-iron stress

The radial displacement for the rotor back-iron can be similarly written as

$$u_{br} = C_{b1} r + \frac{C_{b2}}{r} - \frac{1-v_b^2}{8E_b} \rho_b \Omega^2 r^3 \tag{5.16}$$

The radial and tangential stresses in the rotor back-iron can be given as

$$\begin{aligned} \sigma_{br} &= -\frac{(3+v_b)\rho_b \Omega^2 r^2}{8} + \left(\frac{C_{b1} E_b}{1-v_b} - \frac{\rho_b E_b \Delta T}{1+v_b} \right) \\ \sigma_{b\theta} &= -\frac{(3v_b+1)\rho_b \Omega^2 r^2}{8} + \left(\frac{C_{b1} E_b}{1-v_b} - \frac{\rho_b E_b \Delta T}{1+v_b} \right) \end{aligned} \tag{5.17}$$

where E_b and ν_b are Young's modulus and Poisson's ratio, respectively. C_{b1} and C_{b2} are integration constants depending on the boundaries.

For the geometric constraints, there is always an interference fit between the retaining sleeve and the rotor magnets so that the pre-stress generated by the sleeve can be imposed on the magnets to withstand both the centrifugal and tensile forces at high speed. In addition, due to the existence of pre-pressure on the magnets, there is no fit requirement for the interface between the rotor back-iron and the magnet inner face. Thus, the following can be given:

$$\begin{cases} R_{mo} - R_{si} = \delta \\ R_{bo} - R_{mi} = 0 \end{cases} \tag{5.18}$$

On the other hand, the boundary conditions should be given to determine the six integration constants in (5.11), (5.15) and (5.17). Hence, the six boundary equations are given as

$$\begin{cases} \sigma_r(0) \neq \infty \\ \sigma_{sr}(R_{so}) = 0 \\ \sigma_{sr}(R_{si}) - \sigma_{mr}(R_{mo}) = 0 \\ \sigma_{mr}(R_{mi}) - \sigma_{br}(R_{bo}) = 0 \\ u_{mr}(R_{mo}) - u_{sr}(R_{si}) = \delta \\ u_{br}(R_{bo}) - u_{mr}(R_{mi}) = 0 \end{cases} \tag{5.19}$$

The detailed expressions of those six constants are quite lengthy and complicated which are given as follows.

$$C_{s1}=\frac{\left\{hR_{si}^{1+\sqrt{A}}-P\Omega^2(R_{so}^{3+\sqrt{A}}-R_{si}^{3+\sqrt{A}})+[Q(R_{so}^{\sqrt{A}}-R_{si}^{\sqrt{A}})+K(R_{so}^{1+\sqrt{A}}-R_{si}^{1+\sqrt{A}})]\Delta T\right\}}{R_{so}^{2\sqrt{A}}-R_{si}^{2\sqrt{A}}}$$
$$C_{s2}=\frac{\left\{hR_{si}^{1-\sqrt{A}}-P\Omega^2(R_{so}^{3-\sqrt{A}}-R_{si}^{3-\sqrt{A}})+[Q(R_{so}^{-\sqrt{A}}-R_{si}^{-\sqrt{A}})+K(R_{so}^{1-\sqrt{A}}-R_{si}^{1-\sqrt{A}})]\Delta T\right\}}{R_{so}^{-2\sqrt{A}}-R_{si}^{-2\sqrt{A}}} \tag{5.20}$$

$$h=\frac{(1-v_{\theta r}v_{r\theta})}{(1+v_{\theta r})E_r}p_2$$
$$P=\frac{C\rho_s(3+v_{\theta r})}{(A-9)(1+v_{\theta r})}$$
$$Q=\frac{Bv_{\theta r}}{A-1} \tag{5.21}$$
$$K=\frac{\alpha_r+v_{\theta r}\alpha_t}{1+v_{\theta r}}$$

$$C_{m1}=\frac{1-v_m}{E_m}[\frac{R_{mi}^2(p_2-p_1)}{R_{mi}^2-R_{mo}^2}-p_2]+\frac{(1+v_m)(3+v_m)(R_{mi}^2+R_{mo}^2)}{8E_m}\rho_m\Omega^2+\frac{1-v_m}{1+v_m}\rho_m\Delta T$$
$$C_{m2}=\frac{(1+v_m)(p_2-p_1)}{E_m}\frac{R_{mi}^2R_{mo}^2}{R_{mi}^2-R_{mo}^2}+\frac{(1+v_m)(3+v_m)}{8E_m}\rho_m\Omega^2R_{mi}^2R_{mo}^2 \tag{5.22}$$

$$C_{b1}=-\frac{(1-v_b)p_1}{E_b}+\frac{(1-v_b)(3+v_b)\rho_b\Omega^2{R_{bo}}^2}{8E_b}+\frac{1-v_b}{1+v_b}\rho_b\Delta T$$
$$C_{b2}=0 \tag{5.23}$$

$$p_1=\frac{q_1\delta_1-q_2\delta_2}{q_3q_1}$$
$$p_2=\frac{\delta_2-q_4p_1}{q_1} \tag{5.24}$$

$$q_1=\frac{v_{\theta r}v_{r\theta}-1}{E_r[(\frac{R_{si}}{R_{so}})^{\sqrt{A}-1}-(\frac{R_{si}}{R_{so}})^{-\sqrt{A}-1}]}\times[\frac{{R_{si}}^{\sqrt{A}}}{(\sqrt{A}+v_{\theta r}){R_{so}}^{\sqrt{A}-1}}+\frac{{R_{si}}^{-\sqrt{A}}}{(\sqrt{A}-v_{\theta r}){R_{so}}^{-\sqrt{A}-1}}]-$$
$$(\frac{1-v_m}{E_m}\frac{{R_{mo}}^3}{R_{mo}^2-R_{mi}^2}+\frac{1+v_m}{E_m}\frac{R_{mo}R_{mi}^2}{R_{mo}^2-R_{mi}^2})$$
$$q_2=\frac{2R_{mi}R_{mo}^2}{E_m(R_{mi}^2-R_{mo}^2)} \tag{5.25}$$
$$q_3=\frac{1-v_m}{E_m}\frac{{R_{mi}}^3}{R_{mo}^2-R_{mi}^2}+\frac{1+v_m}{E_m}\frac{R_{mi}{R_{mo}}^2}{R_{mo}^2-R_{mi}^2}+\frac{1-v_b}{E_b}R_{bo}$$
$$q_4=\frac{2R_{mo}{R_{mi}}^2}{E_m(R_{mi}^2-R_{mo}^2)}$$

$$\delta_1 = \left\{ \begin{array}{l} \dfrac{(1-v_b)\rho_b \Omega^2 R_{bo}^3}{4E_b} + (\alpha_b R_{bo} + \alpha_m R_{mi})\Delta T + \dfrac{\rho_m \Omega^2 (1-v_m{}^2)}{8E_m} \times \{(3+v_m) \\ [\dfrac{R_{mi} R_{mo}{}^2}{1-v_m} + \dfrac{(R_{mi}^2 + R_{mo}^2) R_{mi}}{1+v_m}] + R_{mi}{}^3 \} \end{array} \right\}$$

$$\delta_2 = \left\{ \begin{array}{l} \delta + \dfrac{\rho_m \Omega^2 (1-v_m{}^2)}{8E_m} \{(3+v_m) \\ [\dfrac{R_{mo} R_{mi}{}^2}{1-v_m} + \dfrac{(R_{mi}^2 + R_{mo}^2) R_{mo}}{1+v_m}] - R_{mo}{}^3 \} + \alpha_m R_{mo} \Delta T - \dfrac{\rho_s \Omega^2 R_{si}{}^3 (1-v_{\theta r} v_{r\theta})}{E_r (A-9)} - \\ \dfrac{\rho_s \Omega^2 R_{si}{}^2 (1-v_{\theta r} v_{r\theta})(3+v_{\theta r})}{E_r (A-9)[(\dfrac{R_{si}}{R_{so}})^{\sqrt{A}-1} - (\dfrac{R_{si}}{R_{so}})^{-\sqrt{A}-1}]} \times \\ \{ \dfrac{R_{si}{}^{\sqrt{A}} [(\dfrac{R_{si}}{R_{so}})^{\sqrt{A}-1} - (\dfrac{R_{si}}{R_{so}})^2]}{R_{so}{}^{\sqrt{A}-1}(v_{\theta r} + \sqrt{A})} - \dfrac{R_{si}{}^{-\sqrt{A}} [(\dfrac{R_{si}}{R_{so}})^{-\sqrt{A}-1} - (\dfrac{R_{si}}{R_{so}})^2]}{R_{so}{}^{-\sqrt{A}-1}(v_{\theta r} - \sqrt{A})} \} \end{array} \right\} \tag{5.26}$$

5.2.1.2 FE validation

In order to verify the validity of analytical models for the rotor stress calculations, in this section, the 2D FE and 3D FE rotor models are established. The analytically predicted data are compared with those obtained in 2D and 3D FE models with and without consideration of magnet segmentation. The rotor structural parameters and the material properties are given in Table 5.1 and Table 5.2.

Table 5.1 Main Parameters of Rotor Geometry

Parameter	Symbol	Value
Pole pair number	p	2
Sleeve outer radius(mm)	R_{so}	25
Sleeve inner radius(mm)	R_{si}	22.5
Sleeve interference fit(mm)	δ	0.25
PM outer radius(mm)	R_{mo}	22.625
PM inner radius(mm)	R_{mi}	15.125
Back-iron outer radius(mm)	R_{bo}	15.125
Shaft radius(mm)	R_{bi}	5
Stack length(mm)	l	60

Table 5.2 Material Properties

Material	PM (NdFeB)	Carbon-fibre		Structural steel
		⊥	//	
Density(kg/m^3)	7500	1790		7850
Young's Modulus (GPa)	160	9.5	186	210
Poisson's ratio	0.24	0.018	0.31	0.3
CTE(μm/m/°C)	8	35	0.02	10
Maximum allowable strength(MPa)	Tensile 80	Tensile 1400		500
	Compressive 800	Compressive -120		

A. Rotor stress validation without PM segmentation

In the following, the rotor stress is calculated with a whole magnet ring or cylinder established in the FE models. Fig.5.2 shows the distribution of sleeve stress in the 2D and 3D FE models, respectively. It can be seen that the maximum sleeve stress occurs at the contact surface between the sleeve and the magnets due to the pre-stress induced by the inference fit. On the other hand, as shown in Table 5.3, the analytical data are compared with the FE predicted ones under both the cold and hot states, respectively. The analytical results agree well with the FE prediction one, indicating the validity of analytical model under this linear circumstance. In addition, the 2D FE predicted results match well with 3D FE predicted one,

which indicates a quite small stress in the axial direction and therefore justifies the planar stress assumption in the analytical models. Hence, the analytical models and 2D FE model are more suitable for the stress calculation due to shorter computation time as well as acceptable accuracy.

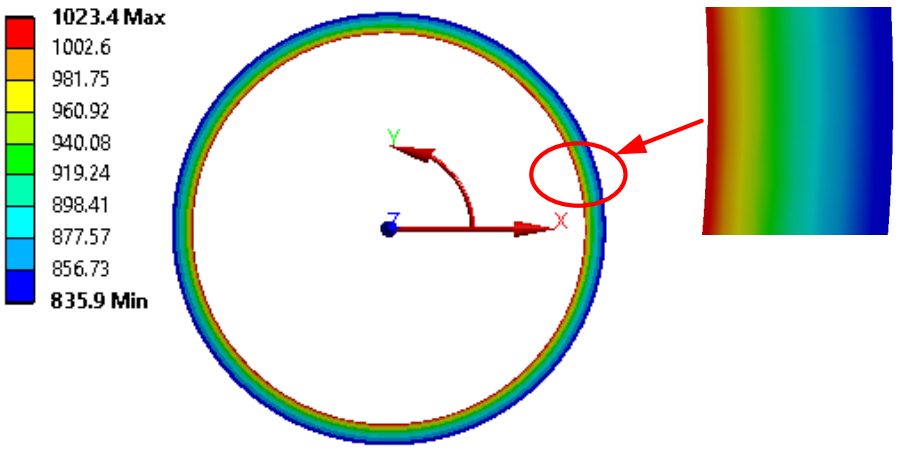

(a)

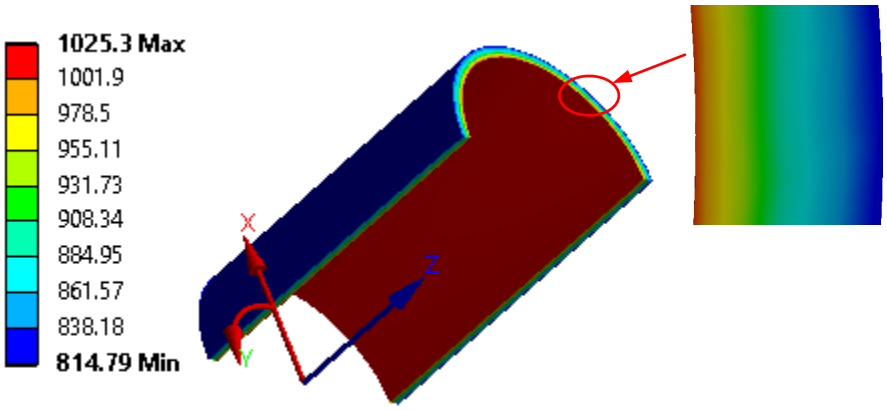

(b)

Fig.5.2. Sleeve tangential stress without magnet segmentation (T=20°C *n*= 100krpm). (a) 2D. (b) 3D.

Table 5.3 Comparison of Different Stress Models

Rotor stress (MPa)		Calculation models		
		Analytical	2D-FEA	3D-FEA
Sleeve Tangential (Inner side)	T=20°C	1018.5	1023.4	1025.3
	T=150°C	1201.6	1214.5	1178
Sleeve Radial (Inner side)	T=20°C	-85.3	-88.4	-88.0
	T=150°C	-120.9	-112.3	-125.9
PM Tangential (Inner side)	T=20°C	65.7	66.3	69.0
	T=150°C	-21.5	-23.2	-20.3
PM Radial (Inner side)	T=20°C	0.18	0.15	0.20
	T=150°C	0.05	0.04	0.07

B. Rotor stress validation considering PM segmentation

For high-speed PM machines, the metallic sleeve or the permanent magnets are always segmented to reduce the rotor eddy current loss [SHE13], [YAM09]. As has been mentioned, the rotor stress is mainly in the form of planar stress. Thus, in this section, the edging effect resulting from the circumferential segmentation is considered in the 2D FE model. It should be noted that except otherwise stated, the PM segmentation in this paper all refers to the circumferential segmentation.

The permanent magnet is established as a whole ring and eight individual segments in the 2D FE model which corresponds to the different scenarios. The influence of segment number will be studied in Section IV. Fig.5.3 illustrates the variation of rotor tangential stress with operating speed with and without consideration of PM segmentation, respectively. The following observations can be concluded:

When the magnets are under the compressive tangential stress at a relatively lower operating speed (<90krpm), both the sleeve stress and PM stress remain stable while the magnets are segmented. The magnet segmentation will not cause a significant difference in terms of rotor stress under this condition.

While the operating speed is relatively higher (>90krpm), the PM tangential stress due to rotation exceeds the pre-stress imposed by the retaining sleeve. The overall PM tangential stress tends to be tensile instead of compressive. As shown in Fig.5.3, the sleeve tangential

stress will rise sharply with the increase of operating speed. Fig.5.4 shows the sleeve tangential stresses with and without magnet segmentation at the speed of 100krpm. The stress concentration does occur at the position aligned with edges of the magnets. When the magnets are under the tensile stress which increases significantly with the operating speed, the tangential displacement will become larger as well, as shown in Fig.5.6. Hence, the geometry discontinuity will be more serious. This in turn deteriorates sleeve stress concentration which will be investigated individually in Section V.

Although the sleeve stress will increase significantly when the magnets are segmented and under the tensile strength, the PM tangential stress is reduced compared to that of an integral PM ring, as shown in Fig.5.3. This is because the gaps between the magnets provide a leak way for the travelling of tangential stress. Fig.5.5 shows the PM tangential stress with and without PM segmentation at the speed of 100krpm. The hottest spot transfers from the inner side of PMs to the outer middle part. The maximum PM tangential stress is reduced from 66.3MPa to 21.9MPa.

To conclude, the analytical models established in this paper can predict the stress of rotor with satisfying accuracy while the PMs are not segmented. For the rotors with segmented magnets, the edging effect must be considered in the FE models, especially when the PMs are under the tensile strength. Significant stress concentration will occur at the inner side of sleeve. On the contrary, the PMs itself will benefit from the segmentation due to the presence of leak way.

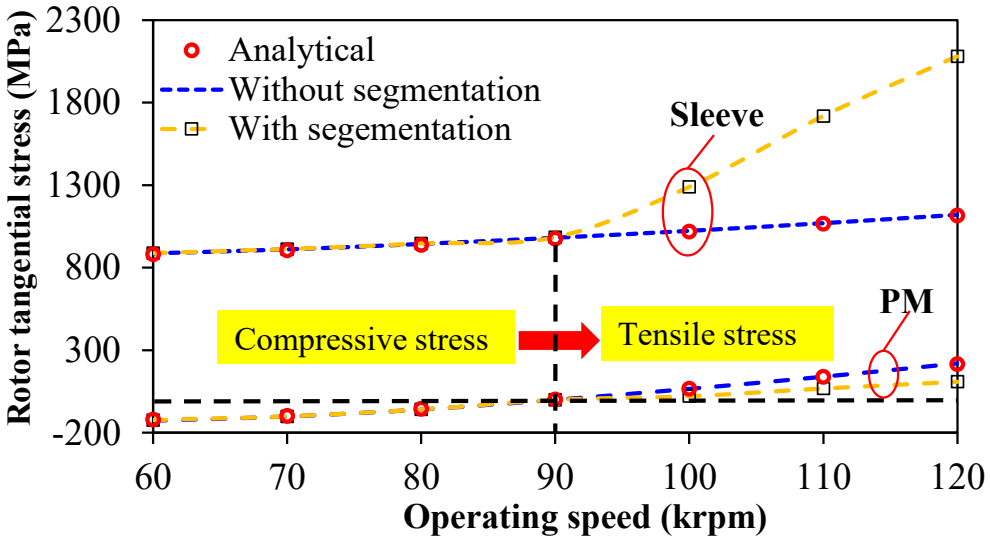

Fig.5.3. Variation of rotor tangential stresses with operating speed with and without magnet segmentation. (T=20°C)

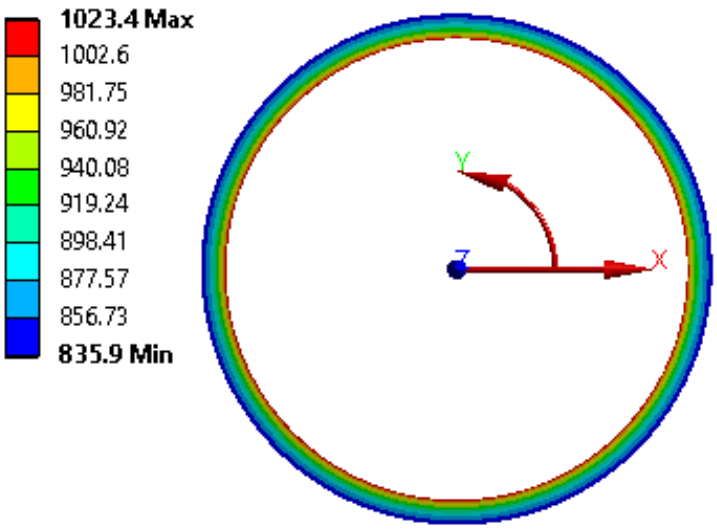

(a)

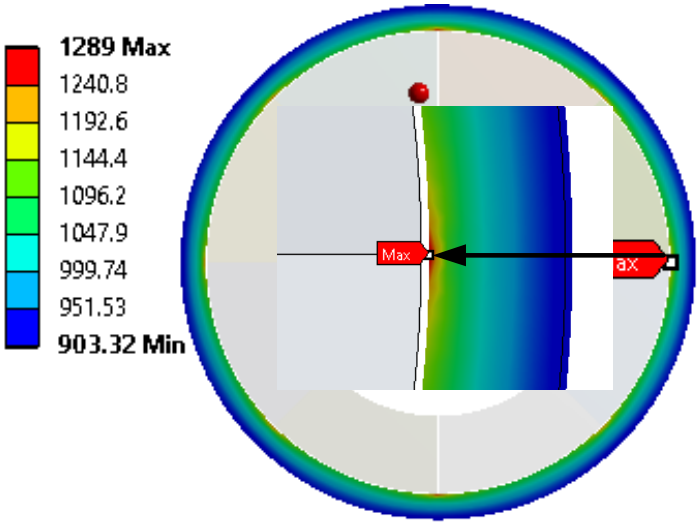

(b)

Fig.5.4. Sleeve tangential stresses with and without magnet segmentation (T=20°C *n*=100krpm). (a) Without segmentation. (b) With segmentation.

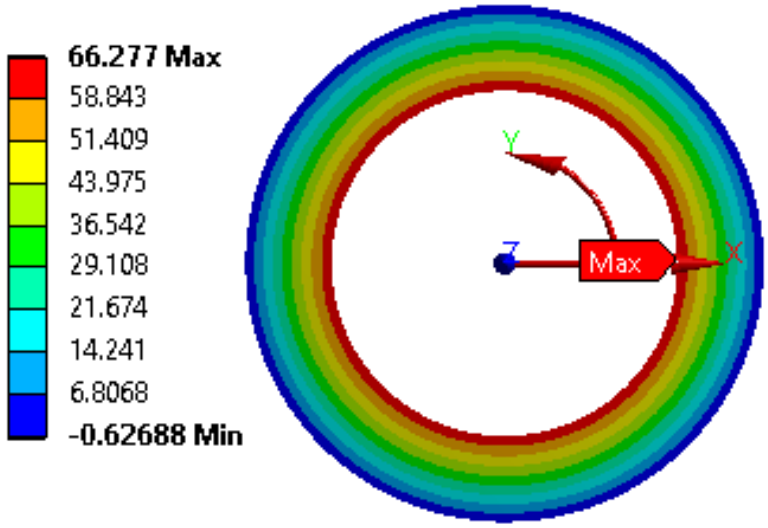

(a)

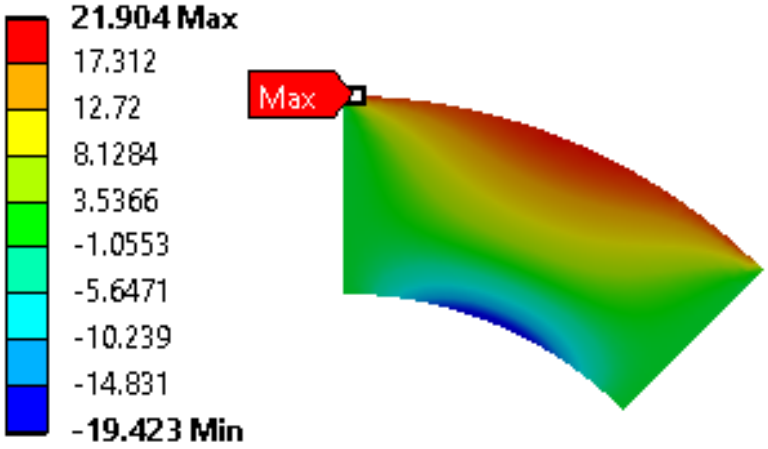

(b)

Fig.5.5. PM tangential stresses with and without magnet segmentation (T=20°C *n*=100krpm). (a) Without segmentation. (b) With segmentation.

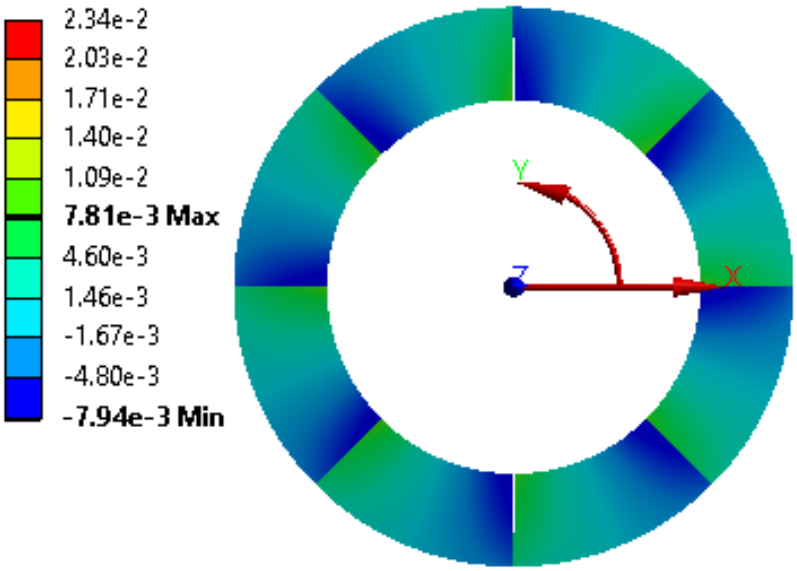

(a)

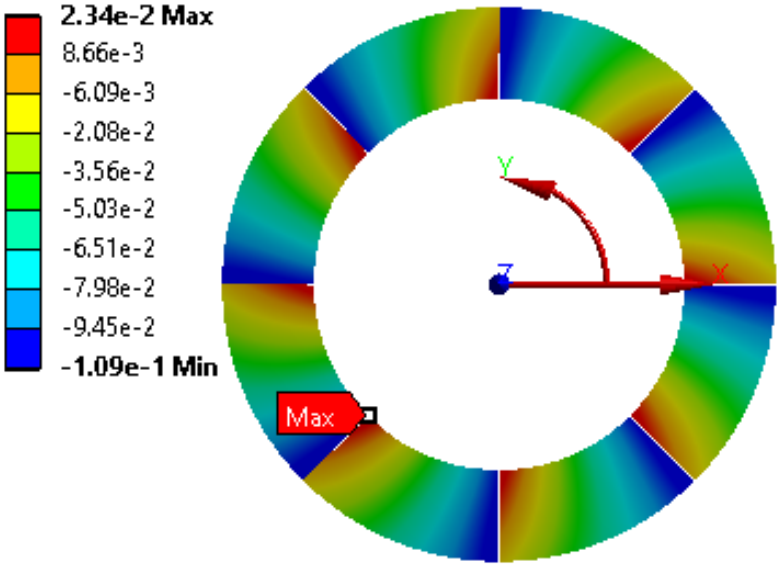

(b)

Fig.5.6. Variation of segmented PM tangential displacements with different operating speed (T=20°C). (a) *n*=90krpm. (b) *n*=120krpm.

5.2.2 Determination of Worst Operating Scenarios Considering PM Segmentation

In the previous section, the influence of PM segmentation on the amplitude of rotor tangential stress has been determined. However, this is only applicable within a narrow speed range at a single rotor temperature. It remains unclear how the rotor stress will be affected in the whole operating speed and rotor temperature range. Moreover, the rotor stress is also significantly influenced by the mechanical design parameters such as sleeve thickness and interference fit which can be seen from the established analytical equations.

Fig.5.7 shows the stress-impact factors which are grouped into three groups, namely operating parameters, mechanical design parameters and geometry parameters. In real cases, the geometry parameters are firstly determined in the initial electrical design process. With the geometric parameters obtained from the initial electrical design, the mechanical design can thereby conducted. The rotor stability check is normally conducted for different choices of mechanical design parameters such as interference fit and sleeve thickness. Fundamentally, the rotor mechanical stability conditions for a high-speed surface-mounted PM machine can be written as

$$\begin{cases} \mathrm{Ref}[\sigma_{s,m}(r)] < \sigma_{\mathrm{lim}it}, \sigma_c < 0 \\ R_{bi} \le r \le R_{si}, 0 \le \Omega \le \Omega_{\max}, T_{\min} \le T \le T_{\max} \end{cases} \tag{5.27}$$

As can be seen from (5.27), each rotating parts in the rotor must be smaller than the yield strength or the tensile strength depending on the type of materials. For the carbon-fibre sleeve and permanent magnet investigated in this paper, the Tresca's criterion should be adopted. The tangential stresses of sleeve and magnet must be smaller than the material tensile strength. In addition, the contact pressure between the magnets and the rotor back-iron must be negative in the cylindrical coordinate system, indicating that there is always a pressure pushing the PMs into the back-iron so that the torque can be transferred. It should be noted that the aforementioned conditions should be fulfilled in the whole speed and rotor temperature range. Hence it is necessary to figure out the influence of operating speed and temperature on the rotor stress so that maximum rotor stress can be quickly obtained and the post-check of mechanical solutions can be more efficient. In other words, the worst operating scenarios concerning with the speed and temperature should be determined, especially when the magnets are segmented.

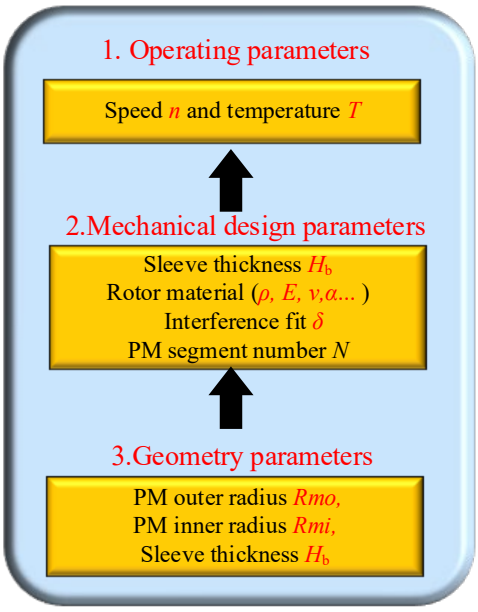

Fig.5.7. Influential parameters for rotor stress.

A. Sleeve tangential stress

Fig.5.8 illustrates the variation of maximum sleeve tangential stress at the inner side of sleeve with operating speed and rotor temperature with and without consideration of PM segmentation. The observations can be found in the following paragraphs.

When the magnets are under the compressive tangential stress, the maximum sleeve tangential stress increases significantly with the rise of operating speed and temperature, regardless of the magnet segmentation. The sleeve tangential stress consists of pre-tangential stress, rotating tangential stress and thermal tangential stress. The latter two parts will increase with the rise of speed and rotor temperature. The increase of speed and temperature will yield the different level of displacements for the magnets and sleeve due to the different material properties. The actual interference fit will be significantly enlarged with the increase of speed and temperature compared to static one. This can be validated by the increase of sleeve inner side radial stress as shown in Fig.5.9. It can be seen that when the temperature rises from 20°C to 150 °C, the sleeve radial stress at the inner side increases from 78.9MPa to 104MPa.

As has been proven in the previous section, the sleeve stress concentration will occur when the PM tangential stress turns to be tensile. Fig.5.8 (b) shows the variation of the concentrated sleeve tangential stress with speed and temperature. There is no doubt that the stress will be increased with the rising speed. However, it is also interesting to see the concentrated sleeve

tangential stress will reduce with the increase of rotor temperature. This can be explained by the smaller gaps between PM segments when the temperature is higher. The PM tensile tangential stress will be reduced with the increase of rotor speed as shown in Fig.5.11. Hence, the deformation of magnet edges will be correspondingly reduced. Fig.5.10 illustrates the tangential displacements of PMs under different rotor speed. The tangential displacement is significantly reduced by 78.11%.

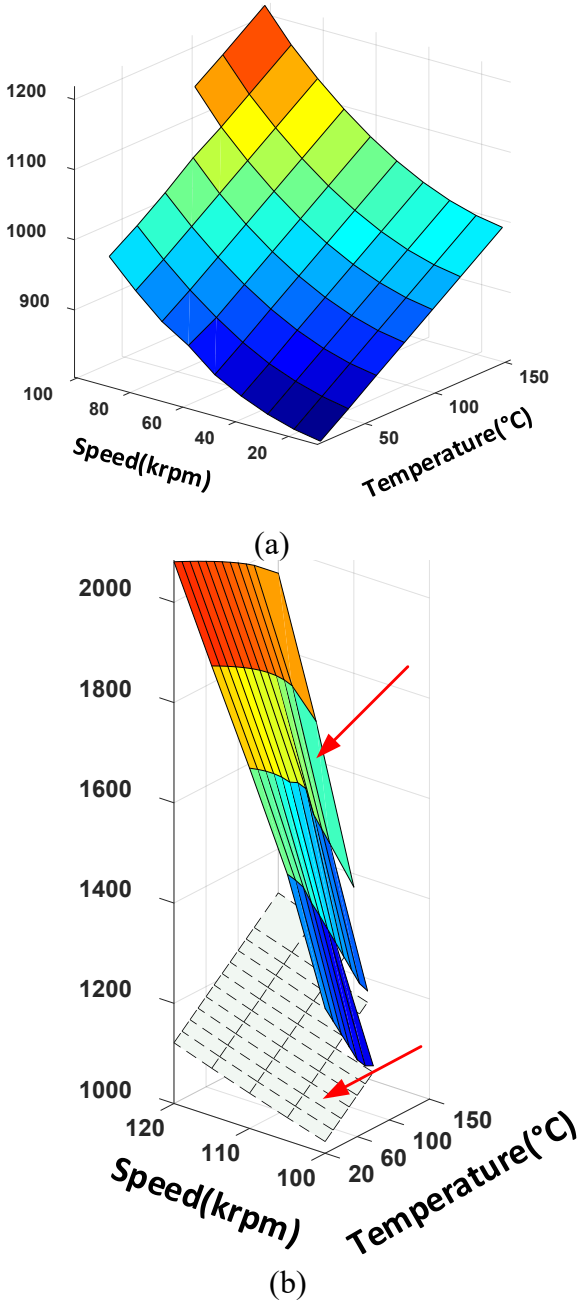

Fig.5.8. Variation of maximum sleeve tangential stress with operating speed and rotor temperature with and without PM segmentation. (a) PMs under compressive tangential stress. (b) PMs under tensile tangential stress.

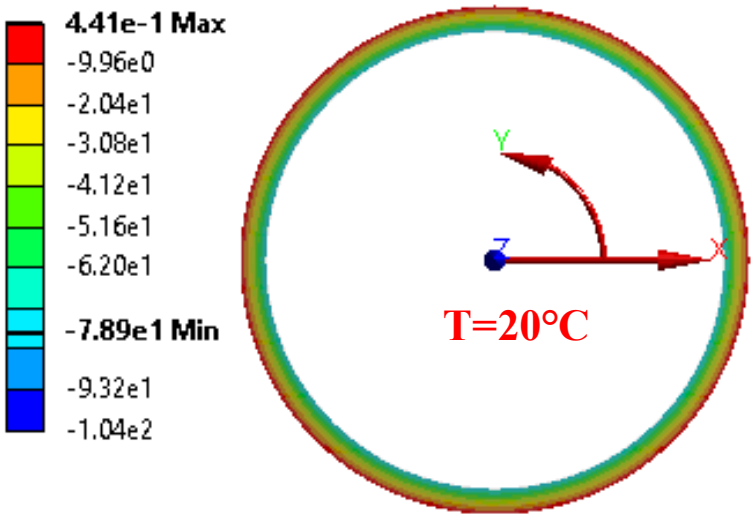

(a)

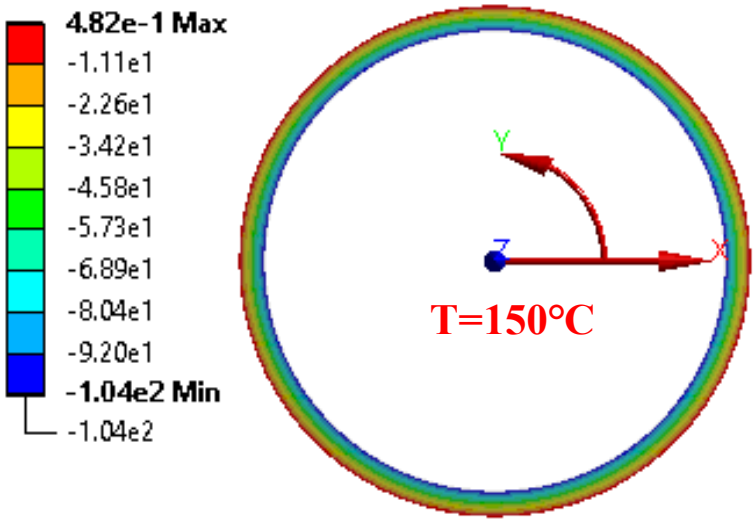

(b)

Fig.5.9. Distribution of sleeve radial stress with PMs withstanding compressive tangential stress (*n*=30krpm). (a) T=20°C. (b) T=150°C.

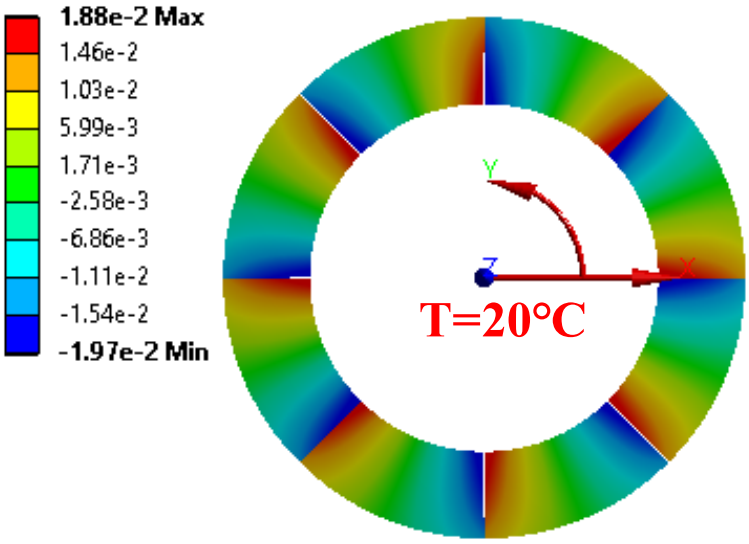

(a)

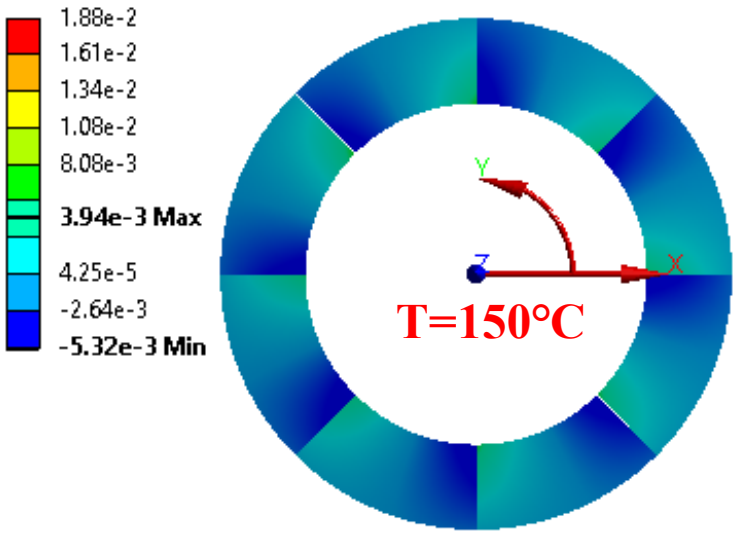

(b)

Fig.5.10. Tangential displacements of PMs withstanding tensile tangential stress (n=100krpm). (a) T=20°C. (b) T=150°C.

B. PM tangential stress

Fig.5.11 illustrates the variation of maximum PM tangential stress with operating speed and rotor temperature. Similarly, the value will be maximum at the maximum operating speed no matter whether the PMs are segmented or not. However, the maximum PM tangential stress will be significantly reduced with the increasing temperature. The maximum PM tangential stress is reached at the maximum operating speed and lowest rotor temperature. As mentioned in the previous section, the interference fit will be increased when the rotor temperature becomes higher thus resulting a larger radial stress and compressive tangential stress on the rotor magnets. Hence, the tensile PM tangential stress resulting from high speed rotating is partially cancelled by the compressive PM tangential stress imposed by the retaining sleeve.

On the other hand, while the PMs are segmented, the maximum tensile PM tangential stress will be significantly reduced due to the presence of leak way between the segmented magnets, which is beneficial to the rotor mechanical stability.

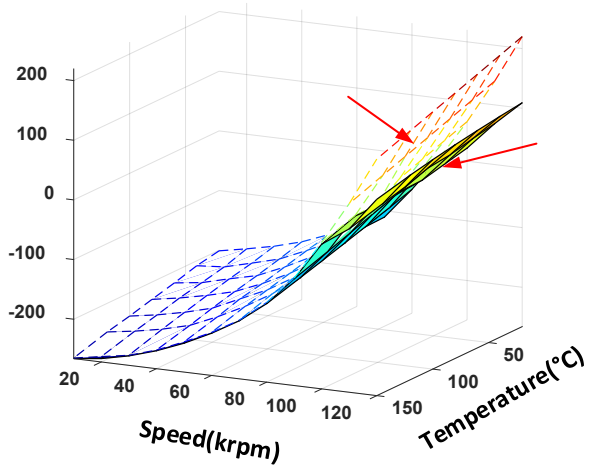

Fig.5.11. Variation of maximum PM tangential stress with operating speed and rotor temperature with and without PM segmentation.

C. Contact pressure between magnets and rotor back-iron

As shown in Fig.5.12, the variation of contact pressure with operating speed and rotor temperature. It can be seen that the maximum contact pressure occurs at maximum operating speed and minimum rotor temperature. It shares the same trend with the PM tangential stress. In addition, the PM segmentation will yield a larger contact pressure while the PMs are under tensile strength.

Table 5.4 summarizes the worst operating scenarios with and without consideration of PM segmentation. It is obvious that the worst case always occurs at the maximum speed even when the magnets are segmented. While the magnets are not segmented, the worst case for the sleeve tangential stress occurs at the highest rotor temperature. In contrast, the worst cases for PM tangential stress and contact pressure occur at the lowest rotor temperature. When the magnets are segmented, the worst cases for the PM tangential stress and contact pressure keeps the same. The worst case for sleeve tangential stress remains stable only when the PMs are under compressive stress. When the PMs are under tensile stress, the worst case for sleeve tangential stress occurs at the lowest rotor temperature which is opposite to that of unsegmented condition.

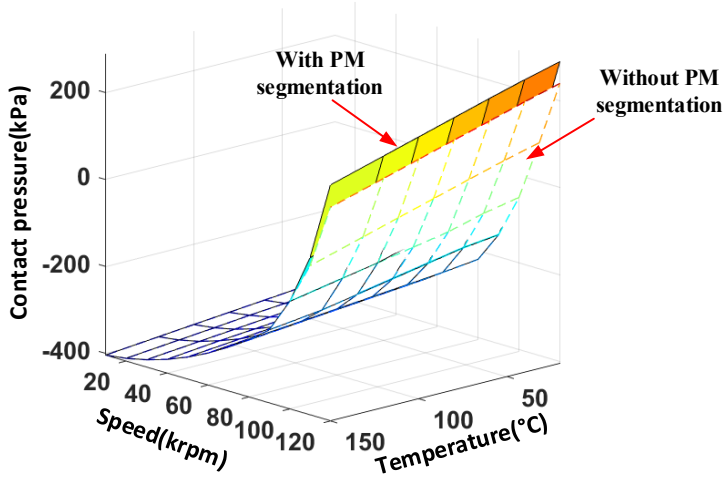

Fig.5.12. Variation of maximum PM tangential stress with operating speed and rotor temperature with and without PM segmentation.

On the other hand, although the PM tangential stress can be reduced significantly when it is under the tensile stress. However, simultaneously, it also causes the stress concentration in the retaining sleeve, Moreover, the risk of loose of contact is increasing. Hence, the machine designers should keep the segmented PMs under the compressive state as much as possible to avoid sleeve stress concentration. Even when the magnets must be under the tensile state, special attention should be made to ensure the maximum concentrated sleeve tangential stress smaller than the tensile strength of sleeve at the maximum speed and lowest rotor temperature.

Table 5.4 Worst Operating Scenarios With and Without PM Segmentation

Rotor stress		Speed n		Temperature T	
		W/O SEG	W/ SEG	W/O SEG	W/ SEG
Sleeve Tangential Stress	PM CS	Max.	Max.	Max.	Max.
	PM TS	Max.	Max.	Max.	Min.
PM Tangential Stress		Max.	Max.	Min.	Min.
Contact Pressure		Max.	Max.	Min.	Min.

Note: W/SEG and W/O SEG designate for with and without PM segmentation. PM CS and PMTS designates for PM compressive stress and tensile stress.

5.2.3 Influence of Mechanical Design Parameters on Rotor Stress

The worst operating case of high-speed PM machine considering the magnet segmentation has been determined in the previous section. However, as shown in Fg.5.7, the rotor stress is also significantly influenced by the mechanical design parameters such as sleeve thickness and interference fit. In addition, the geometry parameters such as PM thickness and rotor split ratio also have a great impact on the exact value of rotor stress which has been discussed in [FEN19]. In this section, the influence of sleeve thickness and interference fit on the rotor stress considering the PM segmentation is investigated. Another factor should be taken into account is the number of PM segment. Although the influence of PM segment number has been discussed in a variety of papers. All the investigations focus on the PM eddy current loss reduction only. Hence, the influence of PM segment number on the rotor stress will be addressed in this section.

5.2.3.1 Number of PM segment

Fig.5.13 illustrates the variation of rotor stress with the number of PM segment in two different scenarios. While the segmented PMs are under compressive stress (PMCS), the rotor stress almost keeps stable despite of changes of PM segment number. However, while the PMs are under tensile stress, the number of PM segments has a great impact on the rotor stress.

For the sleeve tangential stress, although a significant increase of amplitude can be observed due to the presence of stress concentration in all the inner side of sleeve with different PM segment number, it is decreased with increase of PM segment number. The increase of PM segment number weakens the edging effect of segmentation. Fig.5.14 shows the tangential

displacements of segmented PMs under tensile tangential stress. It is obvious when the segment number increases from 2 to 8, the maximum tangential displacement decreases by 42.3%.

On the other hand, the PM tangential stress and contact pressure also benefit from the increase of PM segment number. Both the PM tangential stress and contact pressure decrease significantly with the rise of number of PM segment.

In real cases, the increase of PM segment number will increase the manufacturing difficulties. A trade-off should be made between reducing the rotor stress and loss and increasing the manufacturing difficulties.

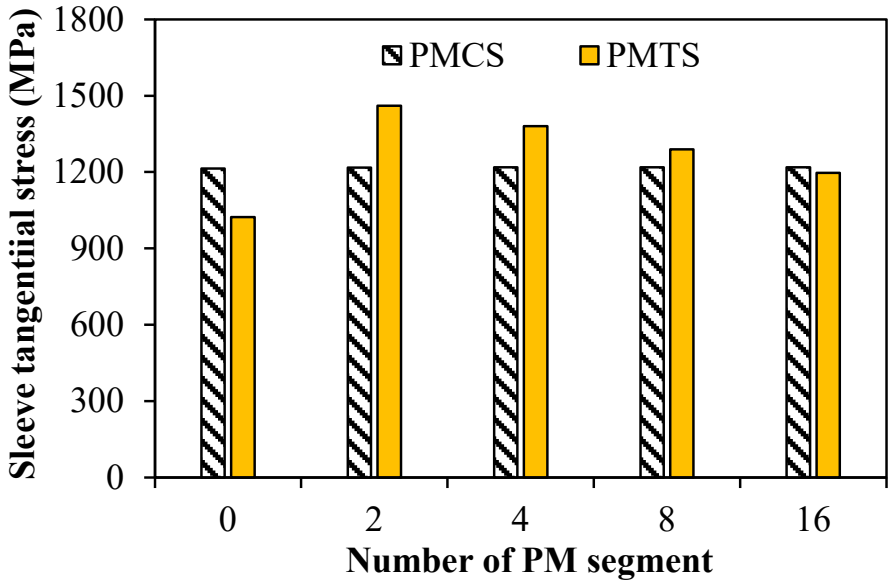

(a)

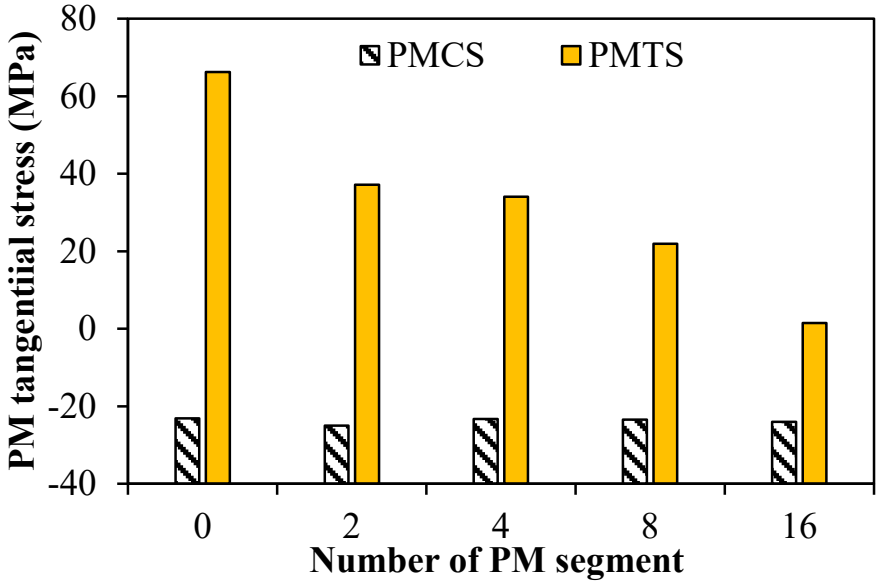

(b)

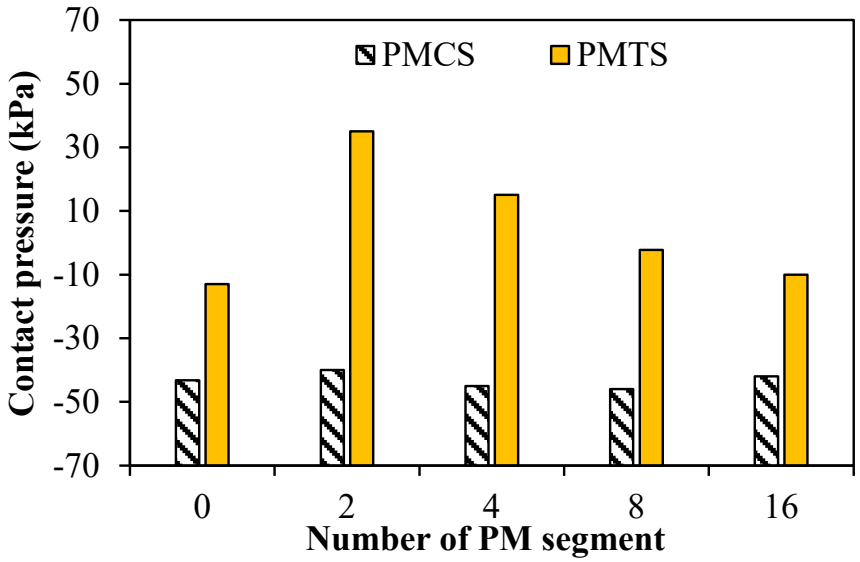

(c)

Fig.5.13. Influence of PM segment number on the rotor stress. (a) Sleeve tangential stress. (b) PM tangential stress. (c) Contact pressure between PM and rotor back-iron.

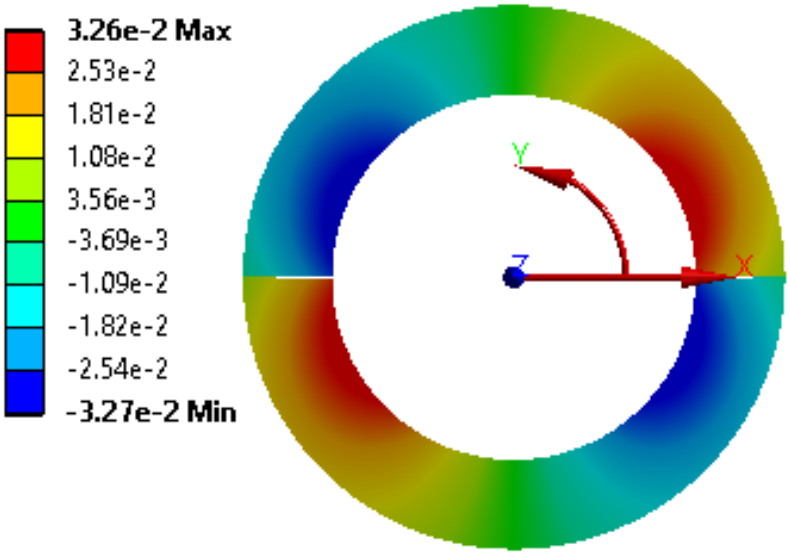

(a)

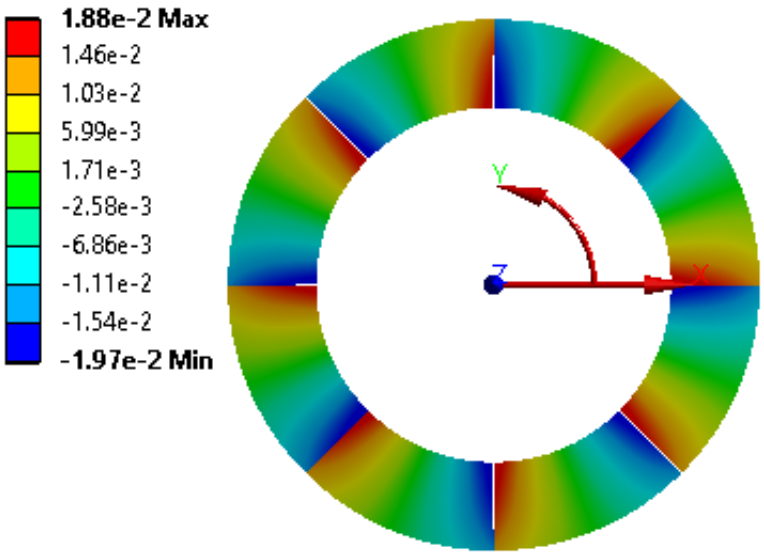

(b)

Fig.5.14. Tangential displacements of segmented PMs withstanding tensile tangential stress. (a) N=2. (b) N=8.

5.2.3.2 Sleeve thickness and interference fit

As can be seen from (5.20)-(5.26), the sleeve thickness and interference fit determine the pre-stress imposed on the rotor magnets. In this section, the influence of sleeve thickness and interference fit on the rotor stress considering the PM segmentation is investigated.

Fig.5.15 illustrates the variation of rotor stress with sleeve thickness and interference fit. It

can be seen that the increasing sleeve thickness will significantly reduce the sleeve tangential stress, PM tangential stress and the contact pressure in the whole interference fit range. More importantly, the increase of sleeve thickness reduces the minimum interference fit beyond which the PM tangential stress tends to be compressive (less than zero). In other words, the maximum operating speed at which the PM tangential stress is compressive can be increased within given interference fit.

However, from the electromagnetic point of view, the equivalent air gap thickness will be increased simultaneously, yielding a lower air gap flux density which may decrease the torque density. Hence, a trade-off should be made between the reduction of rotor stress and torque density by increasing the sleeve thickness.

On the other hand, within given sleeve thickness, both the PM tangential stress and contact pressure are significantly reduced with the increase of interference fit. This should be attributed to the increase of pre-stress imposed on the PMs. However, for the sleeve tangential stress, it keeps decreasing before reaching the minimum value at a certain interference fit. Then, it starts to rise with the increase of interference fit. When the inference fit is relatively small, the PMs are under tensile stress as shown in Fig.5.15 (b). The stress concentration occurs at the inner side of sleeve due to the magnet edging effect. This effect is eased when the interference fit gets larger due to the reduction of segmented PM tangential tensile stress. Hence, the sleeve stress concentration effect is weakened. While the segmented PMs are under the tangential compressive stress, the sleeve stress concentration disappears. The main component of sleeve tangential stress is the pre-stress due to the interference fit. Hence, it increases significantly with the enlarged interference fit.

To conclude, for the mechanical design of rotor sleeve, on the one hand, the sleeve stress concentration due to segmented magnets edging effect can be avoided by choosing a relatively larger interference fit whose minimum value can be reduced by increasing the sleeve thickness. What is more, the PMs are under compressive stress and the contact pressure is maintained for the torque transfer under this circumstance. On the other hand, it should also bear in mind the sleeve tangential stress may exceed the material tensile strength if the interference fit becomes too high. In addition, the maximum value of interference fit is also limited by the sleeve outer diameter and CTE when the retaining sleeve are cold-shrunk into the segmented PMs.

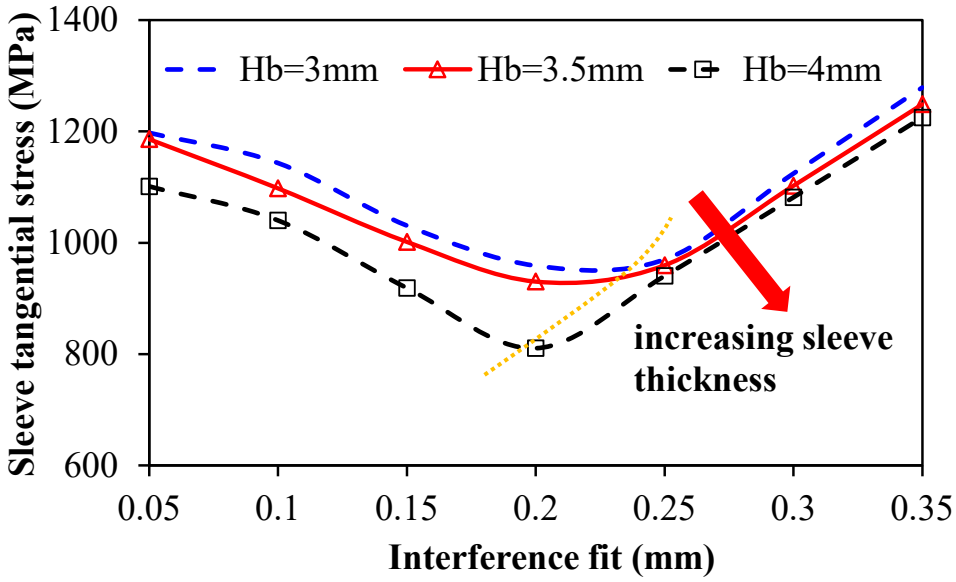
Hb=3mm
Hb=3.5mm
Hb=4mm
Sleeve tangential stress (MPa)
1400
1200
1000
800
600
0.05
0.1
0.15
0.2
0.25
0.3
0.35
Interference fit (mm)
increasing sleeve thickness

(a)

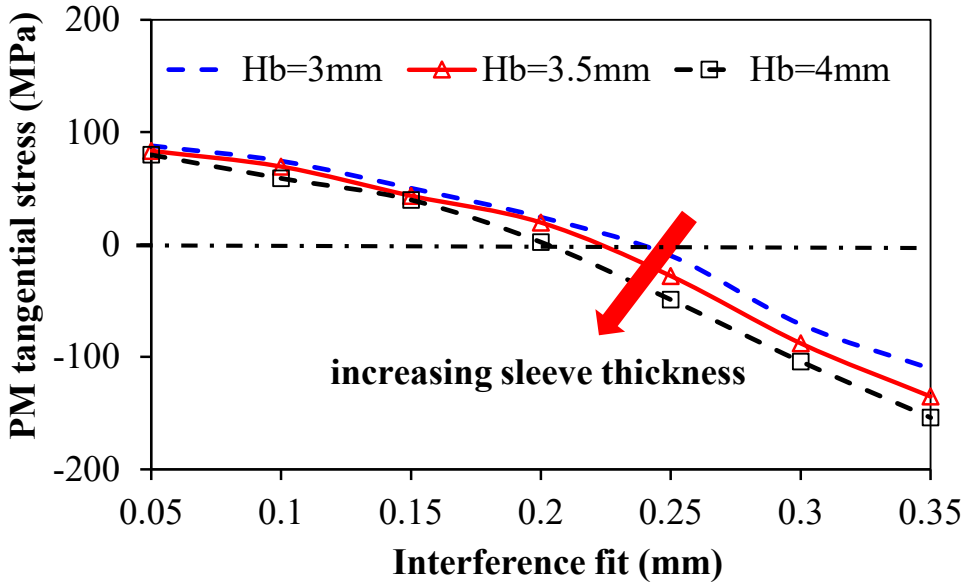
Hb=3mm
Hb=3.5mm
Hb=4mm
PM tangential stress (MPa)
200
100
0
-100
-200
0.05
0.1
0.15
0.2
0.25
0.3
0.35
Interference fit (mm)
increasing sleeve thickness

(b)

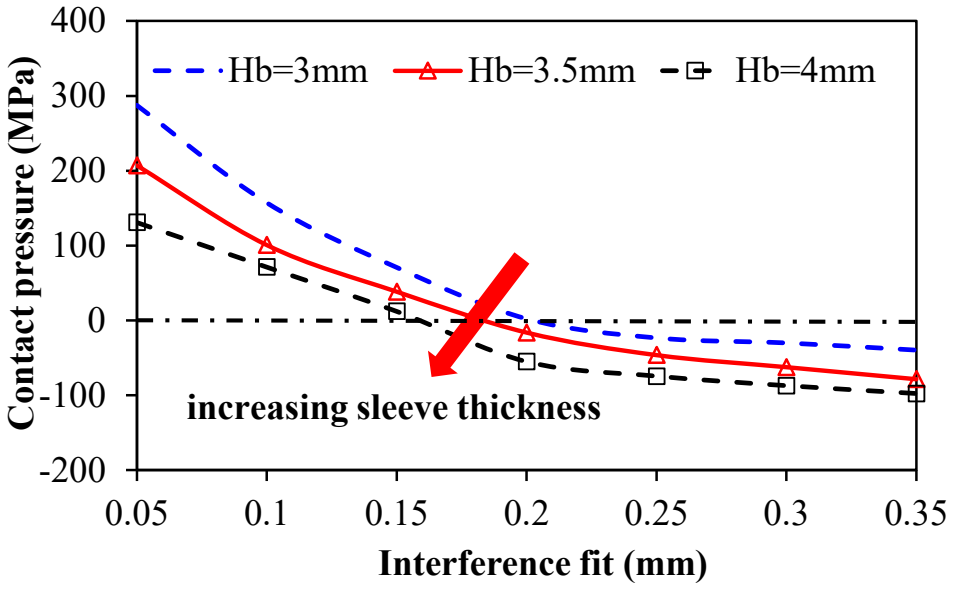

(c)

Fig.5.15. Influence of sleeve thickness and interference fit on the rotor stress. (a) Sleeve tangential stress. (b) PM tangential stress. (c) Contact pressure between PM and rotor yoke.

5.2.4 Rotor Stress Concentration and Reduction

In the previous sections, it is proven that the sleeve stress concentration will occur due to the edging effect of segmented magnets. Generally, the stress concentration occurs in a small, localized area of a structure. For low-to-medium-speed PM machines, the inter-pole gap is usually adopted in order to obtain a more sinusoidal air gap flux density. However, the stress concentration usually occurs where geometry discontinuousness exists. The inter-pole gap will lead to an extra bending stress on the retaining sleeve in high-speed PM machines as shown in Fig.5.16. Hence, in this section, the stress concentration in high-speed PM machines is systematically studied. The relationship between the maximum concentrated stress and the inter-pole gap size is revealed. The pole-fillers with different shape are compared in terms of reduction of concentrated stress.

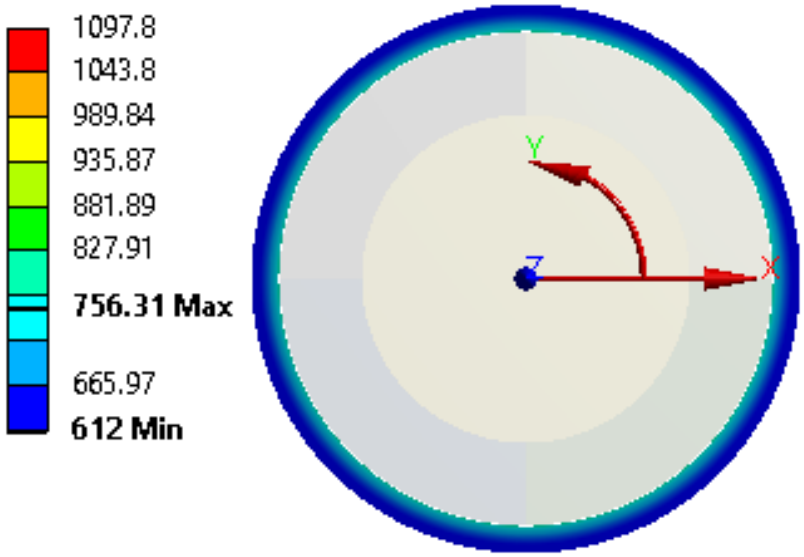

(a)

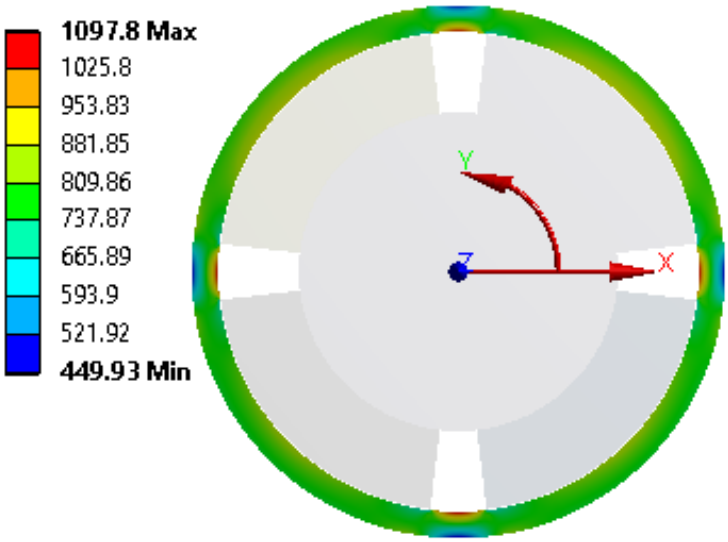

(b)

Fig.5.16. Comparison of sleeve tangential stress with different pole arc ratio (n=20krpm T=20°C). (a) pole arc ratio=1. (b) pole arc ratio=0.85.

5.2.4.1 Influence of pole-arc ratio

In order to evaluate the stress concentration, the stress concentration factor (SCF) is defined as the ratio of the maximum stress and the nominal stress.

$$SCF = \frac{\sigma_{\max}}{\sigma_{nom}} \tag{5.28}$$

Fig.5.17 shows the variation of sleeve and PM tangential SCF with pole arc ratio. When the

pole arc ratio is relatively small, the sleeve tangential stress keeps rising before reaching the maximum at a certain pole arc ratio. Then it starts to drop mildly until the pole arc ratio reaches one. For the PM tangential stress, the tensile tangential stress keeps increasing before reaching the maximum. Then, the tensile tangential stress keeps decreasing with the increase of pole arc ratio and finally tends to be compressive.

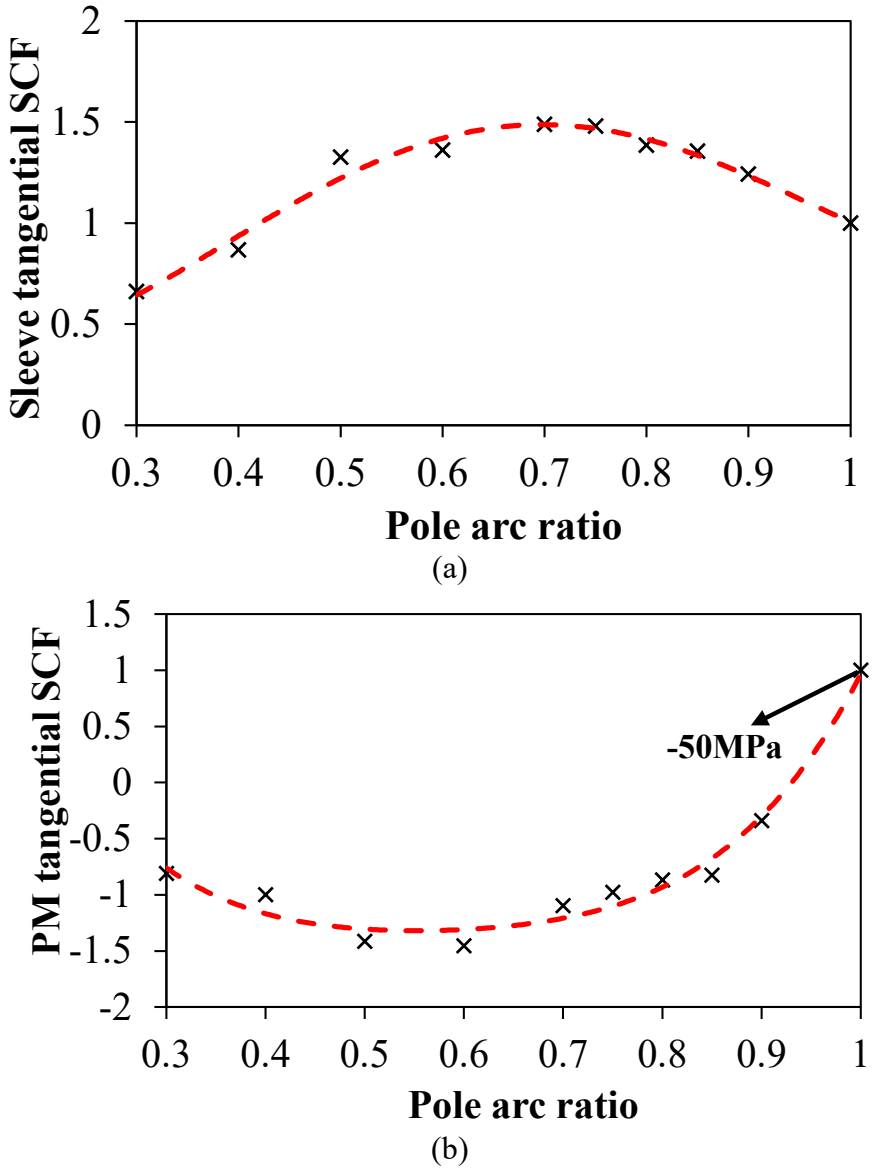

Fig.5.17. Variation of sleeve and PM tangential SCF with pole arc ratio (n=20krpm T=20°C δ=0.2mm). (a) Sleeve tangential SCF. (b) PM tangential SCF.

5.2.4.2 Stress concentration reduction

In order to mitigate the sleeve stress concentration resulting from the geometry discontinuity, the pole fillers are normally adopted [ZHA15]. The pole-filler material is usually selected to

be the one like the adjacent magnets in terms of Young’ s modulus and CTE. In addition, the selected pole filler should be non-magnetic.

Fig.5.18 shows the sleeve tangential stress without pole gap and with conventional pole-fillers. The sleeve tangential stress in the machine with conventional pole filler in the inter-pole gap is significantly reduced. The maximum sleeve tangential stress only increases by 0.6% compared to that in the machine without inter-pole gap. However, the maximum PM tangential stress in the machines with conventional pole filler increase by 15% compared to that in the machine without inter-pole gap.

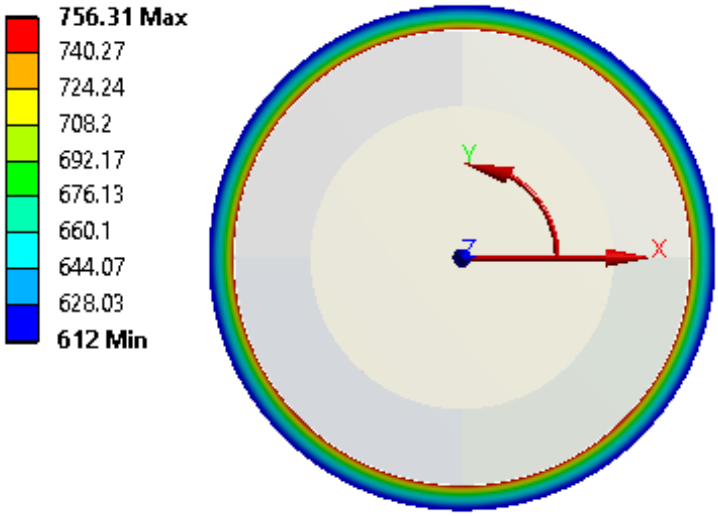

(a)

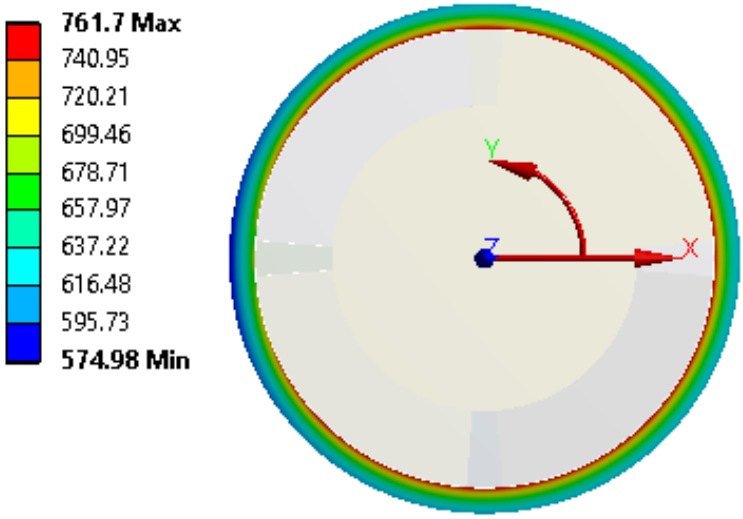

(b)

Fig.5.18. Sleeve tangential stress with and without inter-pole filler (*n*=20krpm T=20°C). (a) pole-arc ratio=1. (b) Conventional pole filler.

Hence, in this paper, three types of pole filler with different shape are compared in terms of reduction of concentrated sleeve and PM tangential stress. Fig.20 shows the rotor tangential stress with different pole fillers in a wide speed range. It is obvious that all of three pole fillers can reduce the concentrated sleeve tangential stress effectively. However, the PM tangential stress can be only significantly reduced with pole filler3. The PMs edges are curved into the concave shape for better release the energy.

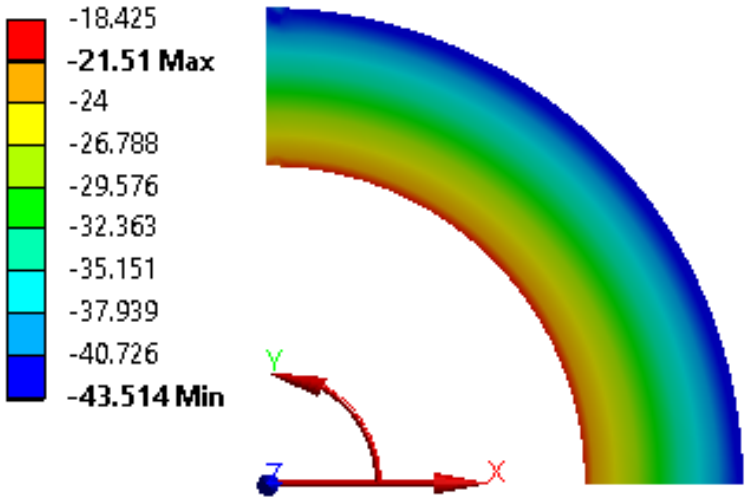

(a)

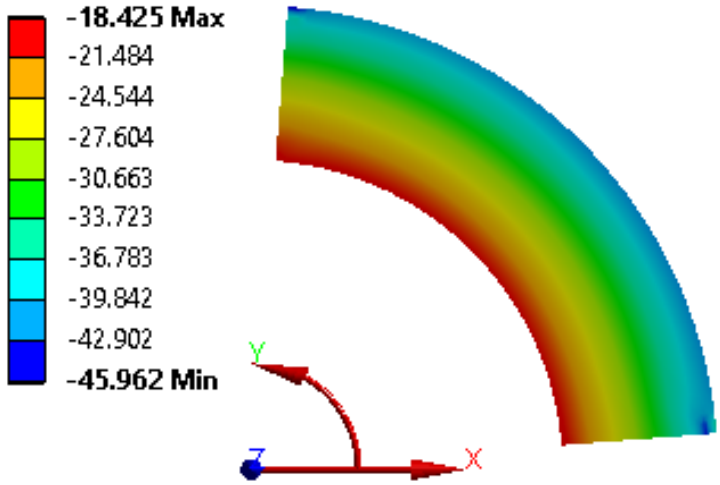

(b)

Fig.5.19. PM tangential stress with and without inter-pole filler (*n*=20krpm T=20°C). (a) pole-arc ratio=1. (b) Conventional pole filler.

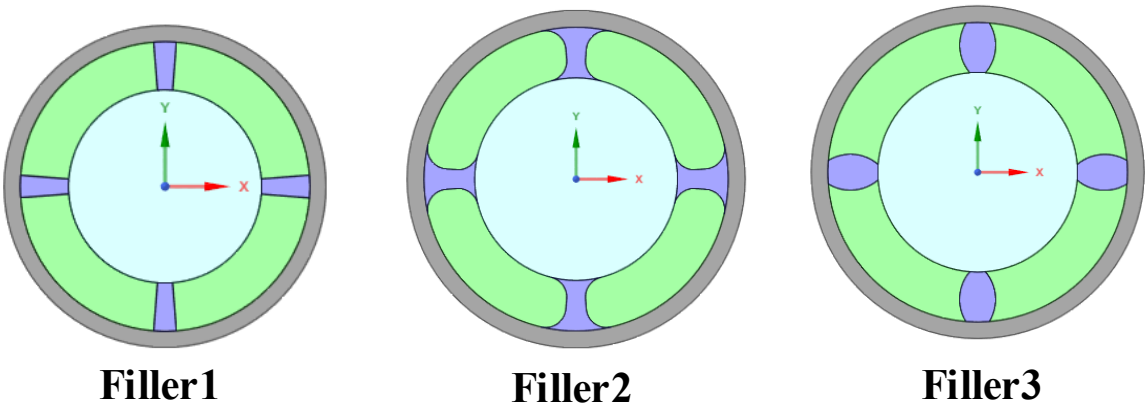

Fig.5.20. Pole fillers with different shape.

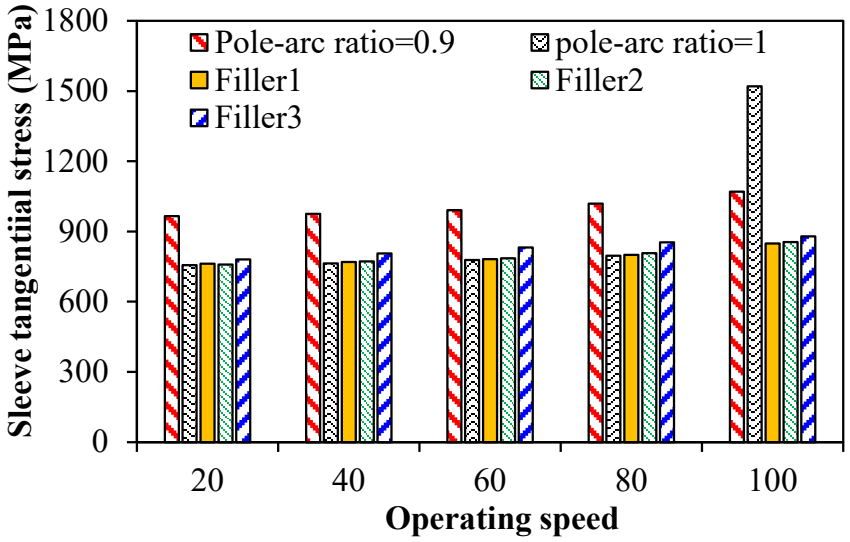

(a)

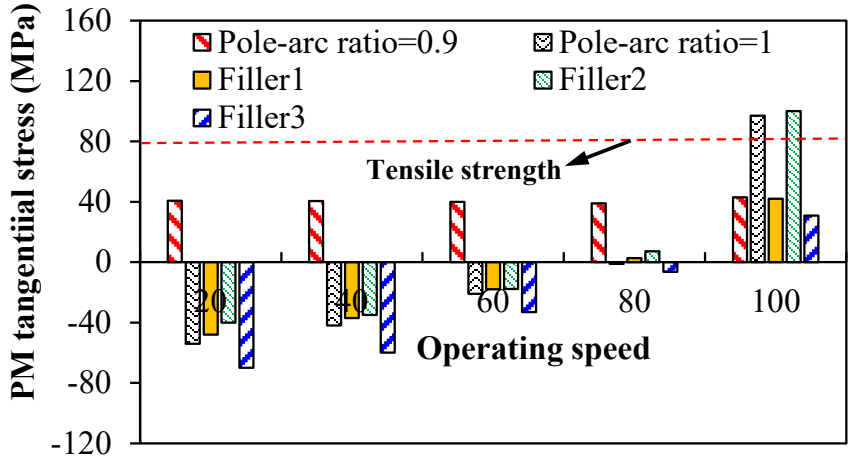

(b)

Fig.5.21. Rotor tangential stress with different pole fillers (*n*=20krpm T=20°C). (a) Sleeve. (b) PM.

5.3 Design Methodology for High Speed PM Machines Considering both Electromagnetic and Mechanical Issue

In this section, a novel design methodology is proposed which considers both the electromagnetic and mechanical issues simultaneously. The mechanical design constraints are firstly transformed into the rotor geometric constraints based on the previous stress analysis. Then, those geometric constraints are incorporated into the electromagnetic as one of the design constraints. In this way, the influence of mechanical issue on the electromagnetic design is successfully considered. The iterative post-check of mechanical integrity in the previous design method can be avoided [UZH16]. Finally, based on the proposed design methodology, a prototype 6-slot 4-pole high speed PM machine with carbon-fiber sleeve is implemented and tested. The electromagnetic performance is validated through experimental results.

5.3.1 Constraints of Rotor Geometric Parameters Considering Mechanical Stress Limitation

As has been determined in Fig.5.7, the rotor stress is significantly influenced by the geometric parameters such as rotor outer diameter and sleeve thickness. It was pointed that the feasible selection of sleeve thickness is inter-dependent on the value of rotor diameter in [FEN19]. However, the thermal stress was ignored in the stress analysis. Hence, in this section, the feasible variation of rotor diameter with sleeve thickness is determined through 2D FE parametric analysis in ANSYS Workbench. The mechanical stress constraints for the HSPMM rotor design are thereby transformed into the constraints on the rotor geometric parameters (rotor diameter and sleeve thickness).

Fig.5.22 illustrates the variation of rotor stress including sleeve and PM tangential stress as well as contact pressure with rotor outer diameter and sleeve thickness under the obtained worst working scenarios. On one hand, there is no doubt that the smallest sleeve thickness will yield the maximum rotor stress within given rotor diameter. On the other hand, it can be seen that both the maximum PM tangential stress and the minimum contact pressure occur at the geometry with maximum rotor outer diameter and smallest sleeve thickness. However, for the sleeve tangential stress, there exists a unique rotor outer diameter at which the value of stress reaches the minimum within given sleeve thickness. This phenomenon is also confirmed in [FEN19]. This can be explained by the different trend of sleeve tangential stress components with the enlarged rotor diameter. In [BIN06], it was pointed that sleeve tangential stress

consists of pre-stress due to the shrink-fit between sleeve and rotor magnets and the rotation stress. The pre-stress is reduced with the increase of rotor diameter in the hyperbolic trend due to the decreasing strain. On the other hand, as can be seen from (5.11) the rotation tangential stress is proportional to the square of rotor diameter. Hence, the sleeve tangential stress starts to decrease with the increase of rotor diameter due to the dominating pre-stress reduction effect. When the rotor diameter become larger, the pre-stress tends to be stable. However, the sleeve tangential stress due to rotation increase significantly with the rotor outer diameter. Hence, the resultant sleeve tangential stress becomes larger.

On the other hand, according to the aforementioned conditions for rotor non-failure of HSPMM, the stress limitation surfaces are placed in Fig.5.22. It can be seen from Fig.5.22 (a) that the lower part of surface is valid. There are three intersections created by the six surfaces. When those intersection are projected into the 2D plane (X-Y plane), the valid selection of rotor diameter and sleeve thickness can thereby be obtained as shown in Fig.5.23. It should be noted that although the PM tensile stress limit is 80MPa, the limitation surface is set to be 0MPa to ensure the PMs are under compressive tangential stress so that the stress concentration can be avoided when the PM segmentation is adopted.

With the help of curve-fitting tool in MATLAB, the analytical expression of rotor geometric constraints considering the rotor mechanical integrity can be written as:

$$H_b \geq k_1 R_{mo}{}^3 + k_2 R_{mo}{}^2 + k_3 R_{mo} + k_4 \tag{5.28}$$

where k_1, k_2, k_3, k_4 are the coefficients which highly depend on the permanent magnet thickness, interference fit, retaining sleeve and permanent magnet material as well as maximum operating speed and rotor temperature.

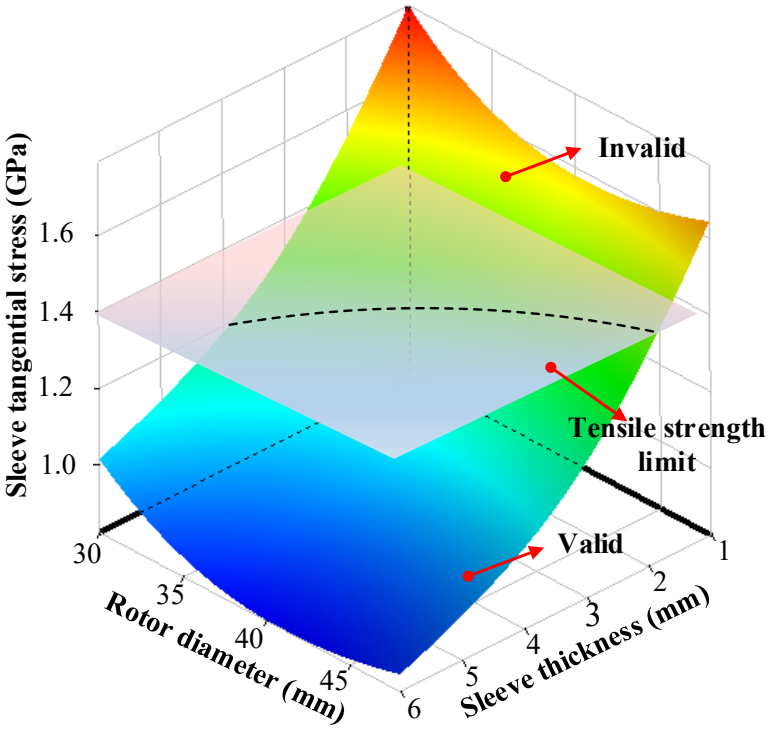
Sleeve tangential stress (GPa)
1.6
1.4
1.2
1.0
Invalid
Tensile strength limit
Valid
30
35
40
45
Rotor diameter (mm)
6
5
4
3
2
1
Sleeve thickness (mm)

(a)

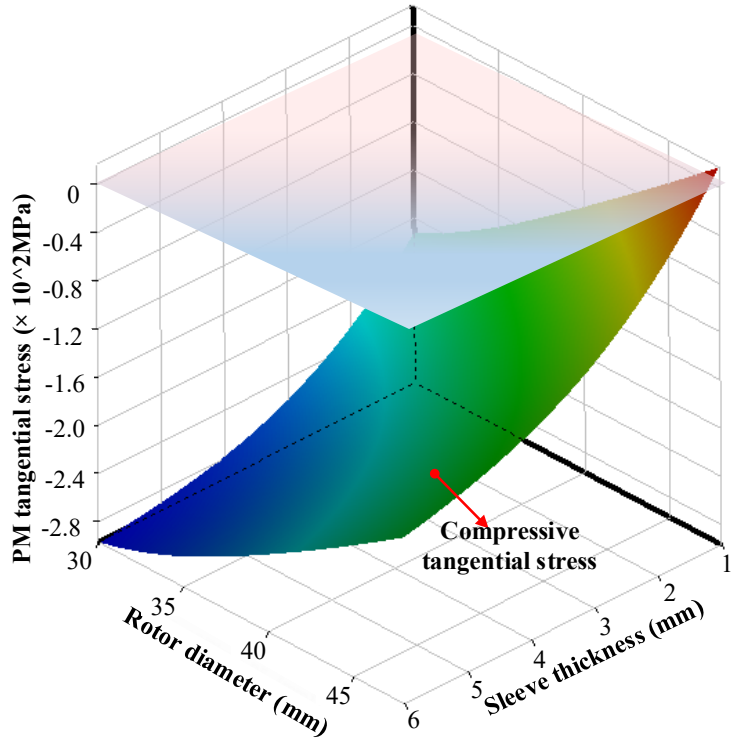
PM tangential stress (× 10^2MPa)
0
-0.4
-0.8
-1.2
-1.6
-2.0
-2.4
-2.8
Compressive tangential stress
30
35
40
45
Rotor diameter (mm)
6
5
4
3
2
1
Sleeve thickness (mm)

(b)

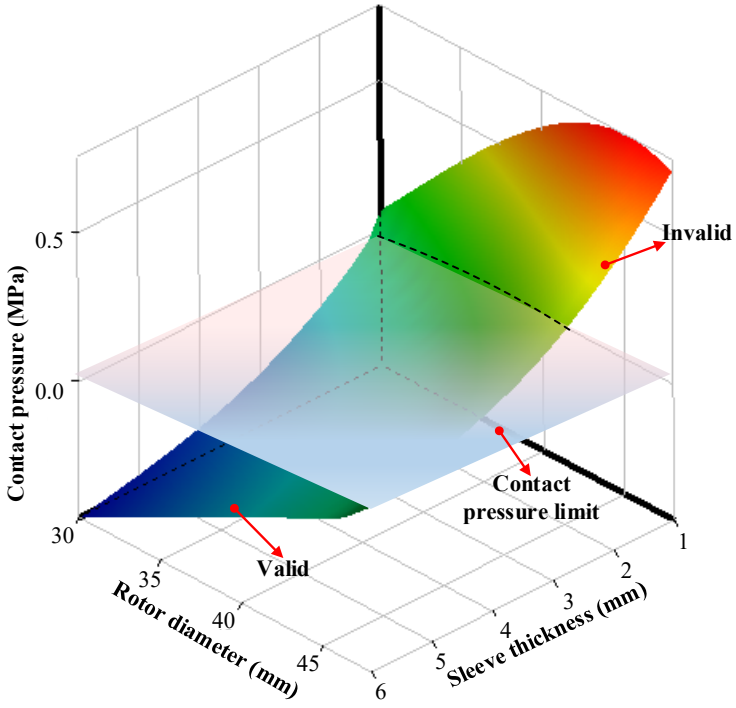

(c)

Fig.5.22. Variation of rotor stress with rotor diameter and sleeve thickness at worst-operating scenario (n=120krpm). (a) Maximum sleeve tangential stress. (b) Maximum PM tangential stress. (c) Contact pressure between PM and rotor back-iron.

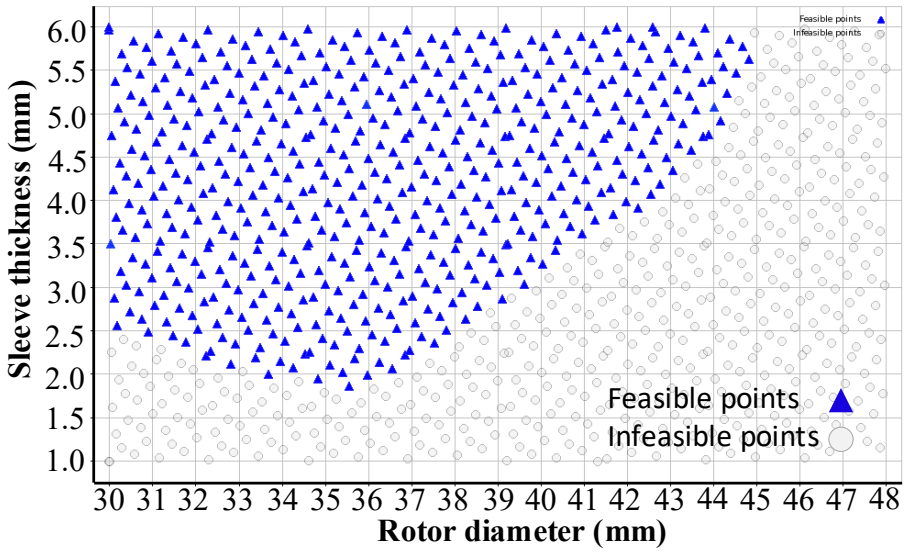

(a)

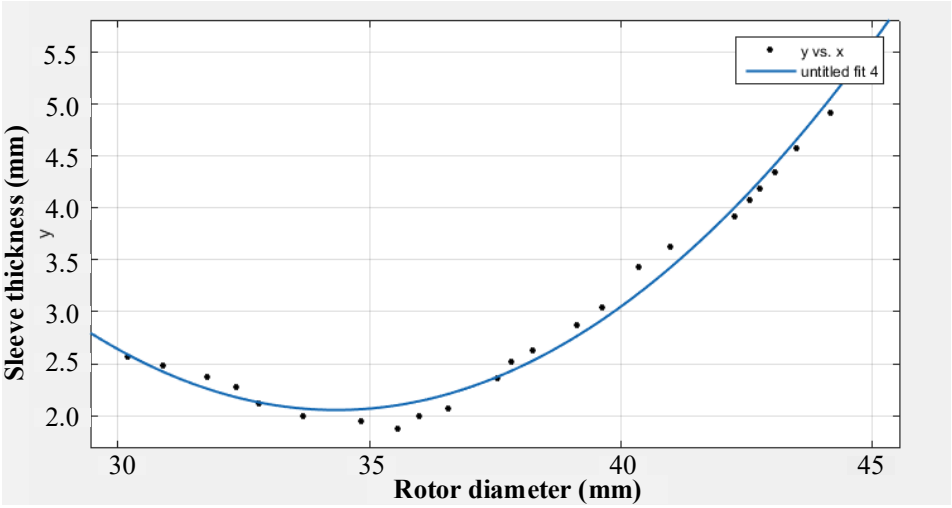

(b)

Fig.5.23. Feasible variation of sleeve thickness with rotor diameter considering mechanical stress constraints. (a) Pareto fronts. (b) Curve-fitted constraints for rotor diameter and sleeve thickness.

5.3.2 Multi-physics Design of HSPMM Considering Electromagnetic and Mechanical Constraints Simultaneously

As discussed in the introduction, in the most traditional multi-physics design methodology, the mechanical issue such as rotor stress constraint is normally treated as the post-check. A typical multi-physics design methodology is introduced in [UZH16]. The rotor stress limits are checked after the active part of the machine is determined in the electromagnetic design. There are at least two issues concerned with this design methodology. The first one is the air gap thickness cannot be reasonably selected in the electromagnetic design due to the required sleeve thickness is dependent on the rotor outer diameter which is variable in the electromagnetic design. The second one is that the post-check of geometric parameter can be time-consuming due to iterations. The electromagnetic optimum may be not valid from the mechanical point of view [FEN19]. Hence, in this section, a novel design methodology is proposed which transforms the mechanical constraints into the geometric constraints so that the mechanical issue can be considered in the electromagnetic design. The influence of mechanical stress constraints on the electromagnetic design can be considered. The optimization cost can be significantly reduced.

Fig.5.24 shows the proposed multi-physics design methodology for the electromagnetic and mechanical aspects. It can be seen that the feasible variation ranges of sleeve thickness and rotor diameter are determined before the electromagnetic design. Then the mechanical stress

limitation are transferred into the electromagnetic geometry design as the geometry constraints. The electromagnetic design is based on the GA global optimization. After the determination of stack length in the electromagnetic design, the rotor dynamics issue can be checked.

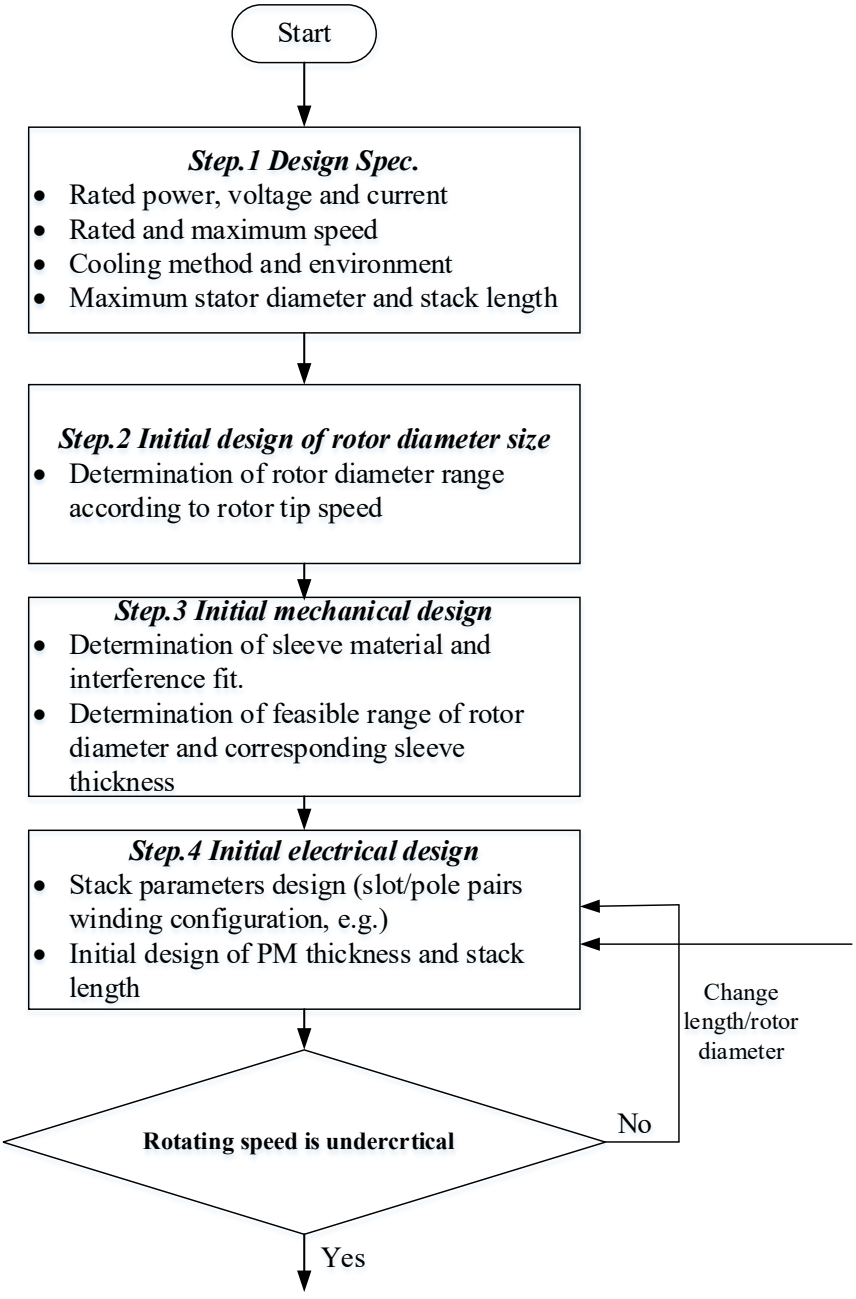

Fig.5.24. Proposed multi-physics design methodology for HSPMM considering mechanical and electromagnetic constraints simultaneously.

Based on the proposed design methodology, a high-speed PM machine of 25kW and 65krpm is design and optimized. It should be noted that there is a supply voltage limitation on the electromagnetic design. In the following, the influence of mechanical stress constraints on the electromagnetic design will be shown through the observations on the typical electromagnetic

performance such as torque and power factor.

Fig.5.25 illustrates the variation of supply voltage with electromagnetic torque. It is obvious that a significant portion of design points turn into invalid due to the mechanical constraints. The maximum torque within a given supply voltage limit is reduced by 10%. As is shown in Fig.5.26, the minimum number of turns for HSPMM with the variation of supply voltage becomes larger when the mechanical constraints is taken into account. In addition, as shown in Fig.5.23, while the stress constraints is considered, the maximum permissible rotor diameter is limited as well. On the other hand, the minimum air gap would be increased. Hence, the air gap flux density would be significantly reduced while the stress constraints are considered. Hence, as shown in Fig.5.23, the serial number of turns of per phase would increase in order to compensate for the reduction of rotor diameter and flux density so that the supply voltage can be constant.

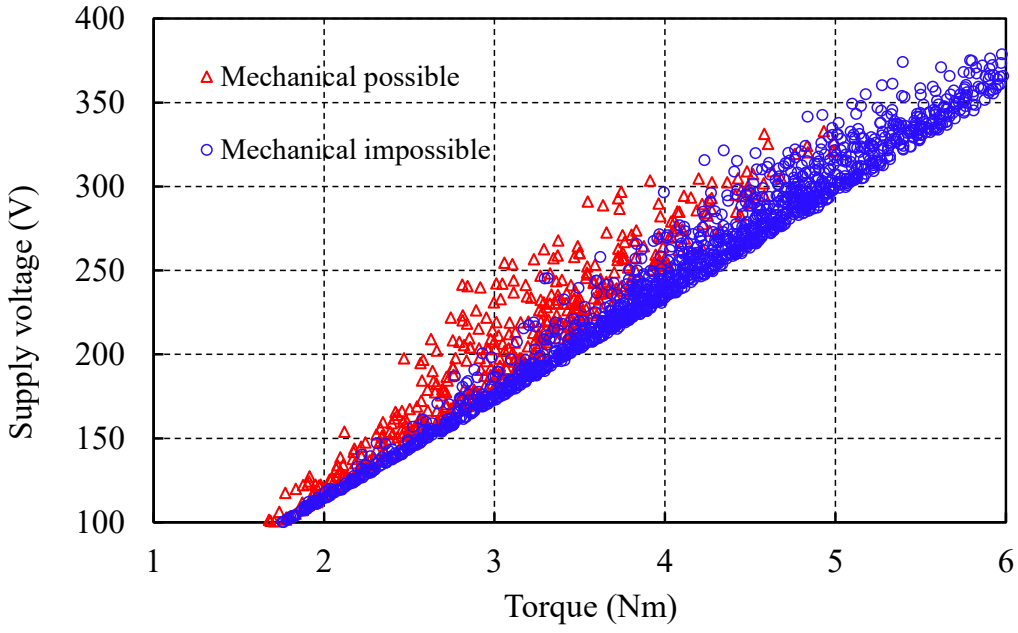

(a)

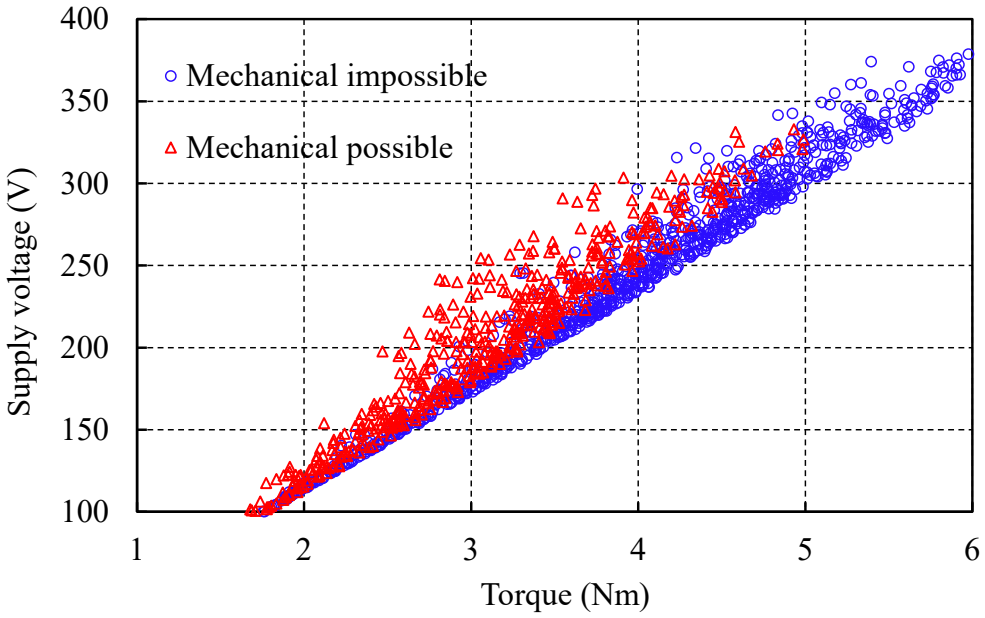

(b)

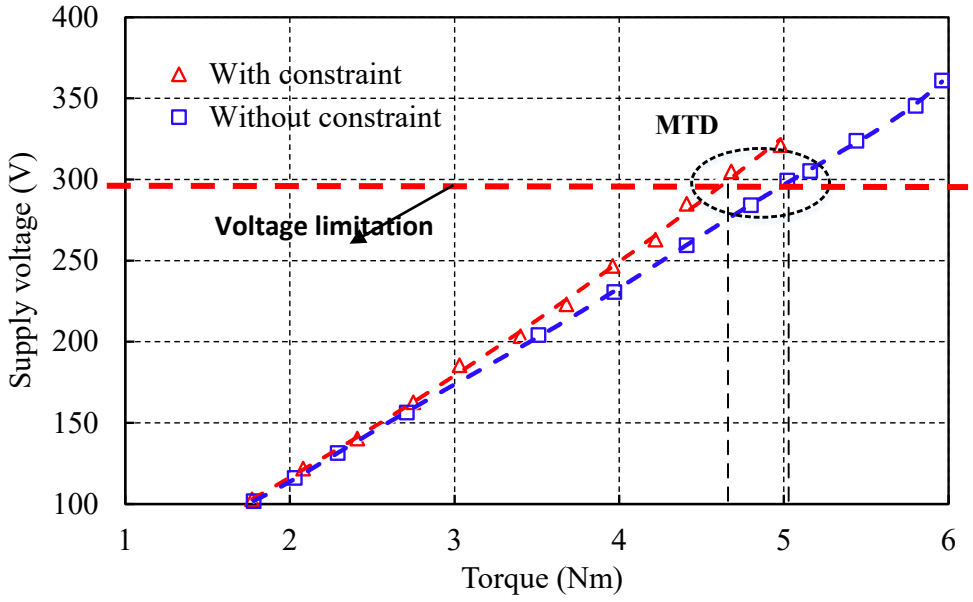

(c)

Fig.5.25. Variation of supply voltage with electromagnetic torque considering the mechanical stress constraints (I_a=100A, n_{rated}=65kr/min, n_{max}=120kr/min). (a) Invalid design points. (b) Valid design points. (c) Pareto fronts.

However, the increase of number of turns will lead to an enlarged inductance. Fig.5.27 shows the phasor diagram of MTDs with and without the mechanical constraints. It can be seen that U_d would be significantly increased due to the increase of L_d as a result of the increase of number of turns and the reduction of saturation. Hence, the power factor is accordingly reduced within the same supply voltage, as shown in Fig.5.28. Therefore, the maximum torque would

be reduced within the same input current and voltage while the mechanical stress constraints are considered.

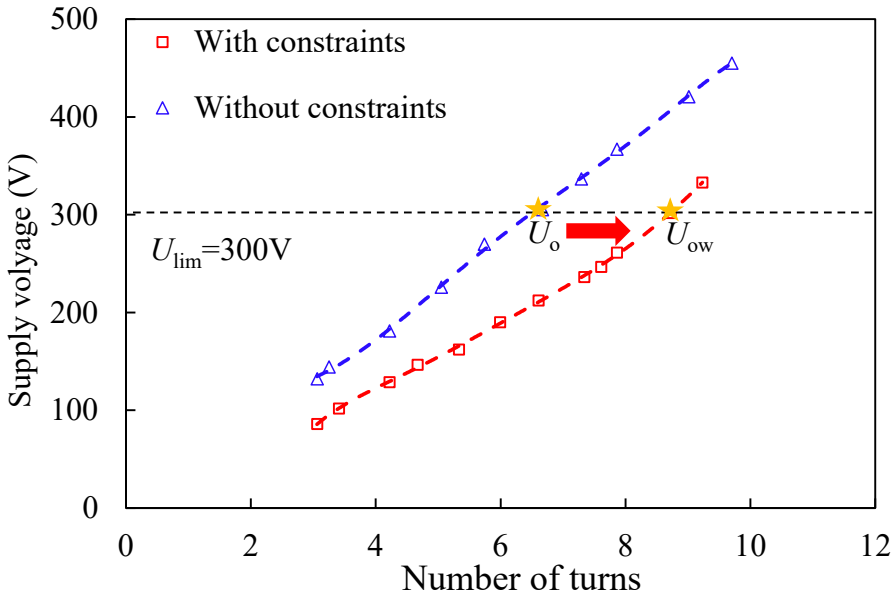

Fig.5.26. Variation of minimum number of turns with supply voltage.

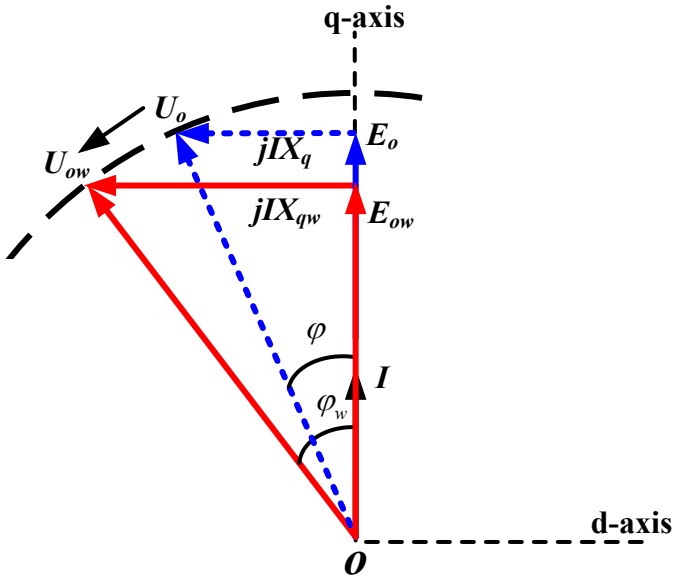

Fig.5.27. Phasor diagram of MTDs with and without consideration of mechanical stress constraints (I_a=100A, n_{rated}=65kr/min, n_{max}=120kr/min).

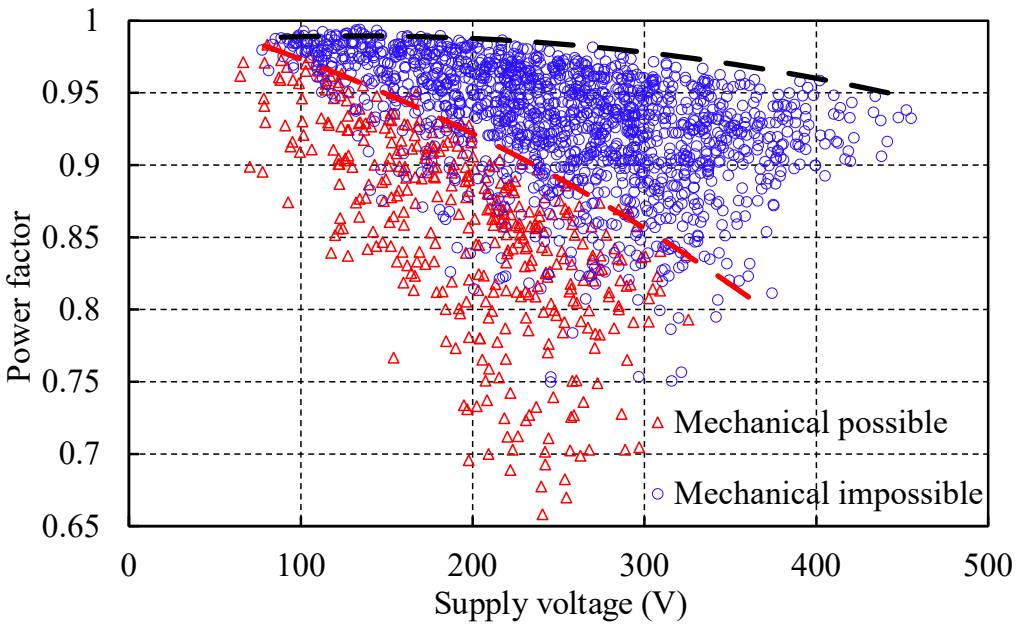

Fig.5.28. Variation of power factor with supply voltage (I_a=100A, n_{rated}=65kr/min, n_{max}=120kr/min).

5.4 Summary

In this paper, the rotor stress is analyzed for a high-speed PM machine with segmented magnets retained by carbon-fiber sleeve. The rotor permanent magnet segmentation is firstly considered in the stress analysis of high-speed PM machines. An explicit analytical model is established for the stress calculation with and without consideration of PM segmentation. Then, the analytical predicted results are compared with those from 2D and 3D FE analyses. It is shown that significant sleeve tangential stress concentration will occur when the segmented magnets are under tensile tangential stress. On the other hand, the PM tensile tangential stress will be reduced when the segmentation is adopted. In addition, with the increase of segment number, the sleeve stress concentration effect is weakened whilst the PM tangential stress reduction effect is enhanced. Increasing sleeve thickness and interference fit can be adopted to avoid the stress concentration effectively. Meanwhile, the influence of PM segmentation on the worst operating scenario is determined. It is shown that the maximum concentrated sleeve stress occurs at the minimum operating temperature instead of the maximum temperature for the one without PM segmentation. Furthermore, the relationship between the rotor pole arc ratio and the maximum concentrated stress is given. There exists a unique pole-arc ratio where the stress concentration factor reaches the maximum. Then, three pole-fillers with different shapes are compared in terms of stress concentration reduction. The pole-filler with concave

shaped edge is proved to be better in the reduction of PM tangential stress. With the obtained geometric constraints from the mechanical stress limitation, a novel multi-physics design methodology considering the electromagnetic and mechanical issue simultaneously is proposed. The influence of mechanical constraints on the electromagnetic design is analyzed.

Chapter 6 General Conclusion and Future Work

6.1 General Conclusion

In this thesis, both electromagnetic and mechanical issues of HSPMM including rotor split ratio optimization, rotor stress analysis, and parasitic effects such as rotor eddy current loss and UMF are investigated elaborately by means of analytical and finite element analyses, together with experimental validation. As shown in Fig.6.1, the main content structure of the thesis can be divided as three parts, i.e. electromagnetic issue, mechanical issue and coupling issue.

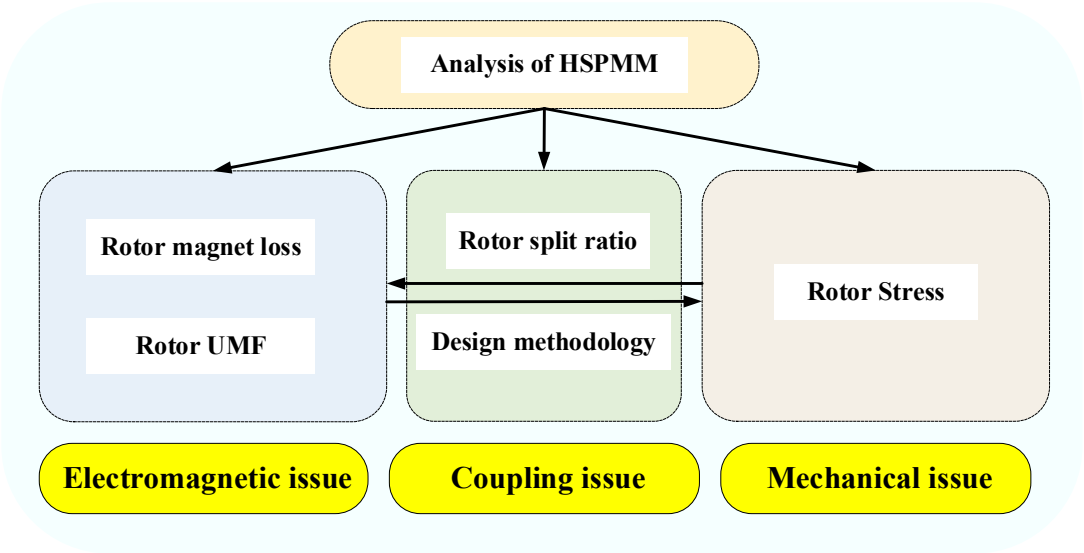

Fig.6.1. Content structure of thesis.

6.2 Optimal Split Ratio

The optimal split ratio for HSPMM has been analyzed with different electromagnetic and mechanical considerations including the stator iron loss and the mechanical stress limitation. It has been shown that the optimal split ratio is significantly reduced when the mechanical constraints and the stator iron loss are taken into account. Furthermore, the achievable torque has also been decreased sharply due to the limitation on the maximum air gap flux density. Furthermore, it is also found that the optimal split ratio is reduced significantly with the increase of flux density ratio and maximum operating speed. The carbon fibre exhibits distinctive advantages among the commonly used sleeve materials with the highest torque density, making it extremely suitable for ultra-high-speed applications.

6.3 Rotor Eddy Current Loss

The rotor eddy current losses of the four-pole HSPMM with various stator winding configurations are investigated. The contribution of each harmonic in the production of magnet loss, either from PM field or armature field, is determined with the proposed method. It is observed that the 4^{th} spatial harmonic dominates in the production of magnet loss for the 6-slot/4-pole HSPMM. In addition, the slotting effect on both the PM field-induced and armature reaction induced magnet losses is revealed. It is found that the open-circuit magnet loss due to slot opening is significantly increased with the enlarged slot opening angle. On the other hand, the magnet loss generated by the 4^{th} spatial harmonic due to slot modulation is almost negligible. The armature reaction induced magnet losses with various stator winding configurations are compared as well. It is observed that the value of magnet loss is dependent on both the penetration depth and the amplitude of asynchronous spatial harmonic, which are determined by the specific slot and pole number combination.

6.4 Rotor Mechanical Stress and Design Methodology

The rotor stress is analyzed for a high-speed PM machine with segmented magnets retained by carbon-fiber sleeve with an explicit analytical model. The rotor permanent magnet segmentation is firstly considered in the stress analysis. It is shown that significant sleeve tangential stress concentration will occur when the segmented magnets are under tensile tangential stress. On the other hand, the PM tensile tangential stress will be reduced when the segmentation is adopted. In addition, with the increase of segment number, the sleeve stress concentration effect is weakened whilst the PM tangential stress reduction effect is enhanced. It is shown that the maximum concentrated sleeve stress occurs at the minimum operating temperature instead of the maximum temperature for the one without PM segmentation. Then, three pole-fillers with different shapes are compared in terms of stress concentration reduction. The pole-filler with concave shaped edge is proved to be better in the reduction of PM tangential stress. With the obtained geometric constraints from the mechanical stress limitation, a novel multi-physics design methodology considering the electromagnetic and mechanical issues simultaneously is proposed.

6.5 Unbalanced Magnetic Force

The existence criterion of UMF both on open-circuit and on-load conditions in fractional-

slot PM machines with odd stator slot number is investigated. It is concluded that only when the machine periodicity is one and the stator slotting effect is considered, will the open-circuit UMF be generated due to the mutual interaction between the modulated PM harmonics and the original PM harmonics. On the other hand, the existence criterion of on-load UMF in the machines with periodicity of one is confirmed since both the self-interaction of armature reaction harmonics and the mutual interaction between the fundamental PM harmonic and the armature reaction harmonics will appear even when the slotting effect is ignored. Furthermore, the influence of slot and pole number combination on the resultant UMF is investigated in depth. The fractional-slot PM machines with a lower pole number, e.g. 2-pole and 4-pole, are compared with machines with a pole number $2p=N_s\pm1$. The UMF in the machine with two poles is the smallest due to the smallest magnitude of the 2^{nd} harmonic in armature reaction field compared with counterparts in other machines. Instead, the UMF in the machines having pole number $2p=N_s-1$ is the largest due to the relatively larger magnitude of the $(p+1)^{th}$ armature reaction harmonics as well as the additive effect between the first order radial and tangential stresses.

6.6 Future work

Based on the investigations of the HSPMM, the future research can be listed as follows:

1) In this thesis, the optimal split ratio is investigated with the consideration of rotor mechanical stress limitation and the stator electromagnetic loss. However, for ultra-high-speed applications, both aerodynamics loss and rotor dynamics issue impose the significant constraints on the feasible variation range of rotor split ratio and aspect ratio. Hence, the optimal split ratio and aspect ratio of HSPMM can be further investigated with considerations of rotor dynamic/aerodynamic issues.

2) As mentioned in Chapter 1, the winding configuration is one of the most promising techniques for the higher efficiency of HSPMM. In this thesis, the 9-slot 4-pole is found to be the topology equipped with fewer rotor loss thus good rotor thermal endurance and with short end-winding length thus good rotor dynamic performance. However, the sub-harmonics in this topology still produce significant rotor loss and UMF. Hence, alternate winding techniques such as multi-layered winding can be further investigated for the cancelation of sub-harmonic in the 9-slot 4-pole HSPMM

References

[AHO07] T. Aho, “Electromagnetic design of a solid steel rotor motor for demanding operation environments,” Ph.D. dissertation, Lappeenranta Univ. Technol., Lappeenranta, Finland, 2007.

[ALB13] L. Alberti and N. Bianchi, “Theory and design of fractional-slot multilayer windings,” *IEEE Trans. Ind. Appl*., vol. 49, no. 2, pp. 841–849, Mar./Apr. 2013.

[ANB96] R. Anbarasu, R. K. Gupta, N. D. Sharma, G. Gauthaman, A. K. Wankhede, P. H. Chavda, J. Nataraj, and B. Bhattacharjee, “Design and experimental investigation of high speed squirrel cage induction motor,” in *Proc. Int. Conf. Power Electron., Drives Energy Syst. Ind. Growth*, Jan. 1996, vol. 2, pp. 920–926.

[ANC10] R. Ancuti, I. Boldea, and G.-D. Andreescu, “Sensorless V/f control of high-speed surface permanent magnet synchronous motor drives with two novel stabilising loops for fast dynamics and robustness,” *IET Elect. Power Appl*., vol. 4, no. 3, pp. 149–157, Mar. 2010.

[ARU16] P. Arumugam, Z. Xu, A. La Rocca, G. Vakil, M. Dickinson, E. Amankwah, “High-speed solid rotor permanent magnet machines: Concept and design,” *IEEE Trans. Transp. Electrif.*, vol. 2, no. 3, pp. 391-400, Sep.2016.

[ATA00] K. Atallah, D. Howe, P. H. Mellor, and D. A. Stone, “Rotor loss in permanent-magnet brushless AC machines,” *IEEE Trans. Ind. Appl*., vol. 36, no. 6, pp. 1612–1618, Nov./Dec. 2000.

[ATA92] K. Atallah, Z. Q. Zhu, and D. Howe, “An improved method for predicting iron losses in brushless permanent magnet DC drives,” *IEEE Trans. Magn*., vol. 28, no. 5, pp. 2997-2999, Sep. 1992.

[BAI07] C. Bailey, D. M. Saban, and P. Guedes-Pinto, “Design of high speed direct-connected permanent-magnet motors and generators for the petrochemical industry,” *IEEE Trans. Ind. Appl*., vol. 45, no. 3, pp. 1159–1165, May/Jun. 2009.

[BEN11] K. Bennion, “Electric motor thermal management,” Nat. Renew. Energy Lab., U.S. Dept. Energy, Golden, CO, USA, Project ID: APE030, 2011.

[BER16] N. Bernard, R. Missoum, L. Dang, N. Bekka, H. Ben Ahmed, and M. E.-H. Zaim, “Design methodology for high-speed permanent magnet synchronous machines,” *IEEE Trans. Energ Convers.*, vol. 31, no. 2, pp. 477-485, Jun. 2016.

[BER88] G. Bertotti, ‘‘General properties of power losses in soft ferromagnetic materials,’’ *IEEE Trans. Magn*., vol. 24, no. 1, pp. 621-630, Jan. 1988.

[BI97] C. Bi, Z. J. Liu, and T. S. Low, “Effects of unbalanced magnetic pull in spindle motors,” *IEEE Trans. Magn.*, vol. 33, no. 5, pp. 4080–4082, Sep. 1997.

[BIA04] N. Bianchi, S. Bolognani, and F. Luise: 'Potentials and limits of high-speed PM motors', *IEEE Trans. Ind. App*., vol. 40, pp. 1570-1578, Nov./Dec.2004.

[BIA05] N. Bianchi, S. Bolognani, and F. Luise, “Analysis and Design of a PM Brushless Motor for High-Speed Operations,” *IEEE Trans. Energy Convers.*, vol. 20, no. 3, pp. 629-637, Sep.2005.

[BIA06a] N. Bianchi, S. Bolognani, and F. Luise, “High speed drive using a slotless PM motor,” *IEEE Trans. Power Electron*., vol. 21, no. 4, pp. 1083–1090, Jul. 2006.

[BIA06b] N. Bianchi, S. Bolognani, and G. Grezzani, “Design considerations for fractional-slot winding configurations of synchronous machines,” *IEEE Trans. Ind. Appl*., vol. 42, no. 4, pp. 997–1006, Jul./Aug. 2006.

[BIA08] N. Bianchi, S. Bolognani, and M. Dai Pre, “Magnetic loading of fractional-slot three-phase PM motors with non-overlapped coils,” *IEEE Trans. Ind. Appl*., vol. 44, no. 5, pp. 1513–1521, Sep./Oct. 2008.

[BIA09] N. Bianchi and E. Fornasiero, “Impact of MMF space harmonic on rotor losses in fractional-slot permanent-magnet machines,” *IEEE Trans. Energy Convers*., vol. 24, no. 2, pp. 323–328, Jun. 2009.

[BIA13] N. Bianchi, D. Durello, and A. Fasolo, “Relationship between rotor losses and size of permanent-magnet machines,” *IEEE Trans. Ind. Appl*., vol. 49, no. 5, pp. 2015–2023, Sep./Oct. 2013.

[BIA15] Mahmoud and N. Bianchi, “Eccentricity in synchronous reluctance motors—Part I: Analytical and Finite-Element Models,” *IEEE Trans. Energy Convers.*, vol. 30, no. 2, pp. 745–753, Jan. 2015.

[BIN06] A. Binder, T. Schneider, and M. Klohr, “Fixation of buried and surface-mounted magnets in high-speed permanent-magnet synchronous machines,” *IEEE Trans. Ind. Appl*., vol. 42, no. 4, pp. 1031-1037, Jul./Aug. 2006.

[BIN07] A. Binder and T. Schneider, “High-speed inverter-fed AC drives,” in Proc. *Int. Aegean Conf. Elect. Mach. Power Electron., Electromotion*, Bodrum, Turkey, Sep. 10–12, 2007, pp. 9–16.

[BIN73] K. J. Binns and M. Dye, “Identification of principal factors causing unbalanced magnetic pull in cage induction motors,” *Proc. Inst. Electr.Eng.*, vol. 120, pp. 349–354, 1973.

[BOG03] A. Boglietti, A. Cavagnino, M. Lazzari, and M. Pastorelli, “Predicting iron losses in soft magnetic materials with arbitrary voltage supply: An engineering approach,” *IEEE Trans. Magn*., vol. 39, no. 2, pp. 981–989, Mar. 2003.

[BOG09] A. Boglietti, A. Cavagnino, D. Staton, M. Shanel, M. Mueller, and C. Mejuto: 'Evolution and modern approaches for thermal analysis of electrical machines', *IEEE Trans. Ind. Electron*., vol. 56, pp. 871–88, Mar.2009.

[BOG92] A. Boglietti, P. Ferraris, M. Lazzari, and F. Profumo, “About the design of very high frequency induction motors for spindle applications,” in *Conf. Rec. IEEE IAS Annu. Meeting*, Oct. 1992, vol. 1, pp. 25–32.

[BOR09] Borisavljevic et al., “Motor drive for a novel high-speed micro-milling spindle,” in *Proc. IEEE/ASME Int. Conf. Adv. Intell. Mechatronics*, Jul. 2009, pp. 1492–1497.

[BOR10] A. Borisavljevic, H. Polinder, and J. A. Ferreira, "On the speed limits of permanent-magnet machines," *IEEE Trans. Ind. Electron.*, vol. 57, no. 1, pp. 220-227, Jan.2010.

[BOR10] A. Borisavljevic, H. Polinder, and J. A. Ferreira, "Enclosure design for a high-speed permanent magnet rotor," in *Proc. 5th IET Conf. PEMD*, Apr. 2010, pp. 1–5.

[BRA11] H. J. Brauer and R. W. deDoncker, "Thermal modeling of a high speed SRM for vacuum cleaners," in *Proc. EPE*, Sep. 2011, pp. 1–10.

[BUM06] J. R. Bumby, E. Spooner, and M. Jagiela, "Equivalent circuit analysis of solid-rotor induction machines with reference to turbocharger accelerator applications," *Proc. IEE Elect. Power Appl.*, vol. 153, no. 3, pp. 31–39, Jan. 2006.

[BUR17] G. Burnand, D. M. Araujo, and Y. Perriard, "Very-high-speed permanent magnet motors: Mechanical rotor stresses analytical model," in *2017 IEEE International Electric Machines and Drives Conference (IEMDC)*, 2017, pp. 1–7.

[CAP05] M. Caprio, V. Lelos, J. Herbst, and J. Upshaw, "Advanced induction motor endring design features for high speed applications," in *Proc. IEMDC*, May 2005, vol. 1, pp. 993–998.

[CHA94] F. B. Chabban, "Determination of the optimum rotor/stator diameter ratio of permanent magnet machines," *Elect. Mach. Power Syst*., vol. 22, pp. 521–531, 1994.

[CHE09] A. Chebak, P. Viarouge, and J. Cros, "Analytical computation of the full load magnetic losses in the soft magnetic composite stator of high-speed slotless permanent magnet machines," *IEEE Trans. Magn.,* vol. 45, no. 3, pp. 952-955, Mar.2009.

[CHE14] X. Chen, J. Wang, and V. I. Patel, "A generic approach to reduction of magnetomotive force harmonics in permanent-magnet machines with concentrated multiple three-phase windings," *IEEE Trans. Magn.*, vol. 50, no. 11, pp. 1–4, Nov. 2014.

[CHE15] A. Chebak, P. Viarouge, and J. Cros, "Improved analytical model for predicting the magnetic field distribution in high-speed slotless permanent-magnet machines," *IEEE Trans. Magn.*, vol. 51, no. 3, pp. 1-4, Mar.2015.

[CHI11] A. Chiba, Y. Takano, and M. Takeno, "Torque density and efficiency improvements of a switched reluctance motor without rare-earth material for hybrid vehicles," *IEEE Trans. Ind. Appl*., vol. 47, no. 3, pp. 1240– 1246, May/Jun. 2011.

[CHO16] G. Choi and T. M. Jahns, "Reduction of eddy-current losses in fractional slot concentrated-winding synchronous PM machines," *IEEE Trans. Magn*., vol. 52, no. 7, Jul. 2016, Art. no. 8105904.

[CHU13] W. Q. Chu and Z. Q. Zhu, "Average torque separation in permanent magnet synchronous machines using frozen permeability," *IEEE Trans. Magn*., vol. 49, no. 3, pp. 1202–1210, Mar. 2013.

[CRE12] F. Crescimbini, A. Lidozzi, and L. Solero, "High-speed generator and multilevel converter for energy recovery in automotive systems," *IEEE Trans. Ind. Electron.,* vol. 59, no. 6, pp. 2678-2688, Jun.2012.

[CRO02] J. Cros and P. Viarouge, “Synthesis of high performance PM motors with concentrated windings,” *IEEE Trans. Energy Convers*., vol. 17, no. 2, pp. 248–253, Jun. 2002.

[DAJ14] G. Dajaku, W. Xie, and D. Gerling, “Reduction of low space harmonics for the fractional slot concentrated windings using a novel stator design,” *IEEE Trans. Magn.*, vol. 50, no. 5, pp. 1–12, May 2014.

[DAN15] J. Dang, J. R. Mayor, S. A. Semidey, and R. Harley, “Practical considerations for the design and construction of a high speed SRM with a flux bridge rotor,” in *Proc. IEEE Energy Convers. Congr. Expo*., Pittsburgh, PA, USA, Sep. 14–18, 2014, pp. 3842–3849

[DEG96] M. W. Degner, R. van Maaren, A. Fahim, D. W. Novotny, R. D. Lorenz, and C. D. Syverson, “A rotor lamination design for surface magnet retention at high speeds,” *IEEE Trans. Ind. Appl*., vol. 32, no. 2, pp. 380–385, Mar./Apr. 1996.

[DON14] J. N. Dong, Y. K. Huang, L. Jin, H. Y. Lin, and H. Yang, “Thermal optimization of a high-speed permanent magnet motor,” *IEEE Trans. Magn*., vol. 50, no. 2, pp. 749–752, Feb. 2014.

[DOR08] D. G. Dorrell, M. Popescu, C. Cossar, and D. Ionel, “Unbalanced magnetic pull in fractional-slot brushless PM motors,” in *Proc. IEEE IAS Annual Meeting*, Edmonton, Canada, Oct. 2008, pp. 1–8.

[DOR10] D. G. Dorrell, M. Popescu, and D. M. Ionel, “Unbalanced magnetic pull due to asymmetry and low-level static rotor eccentricity in fractional-slot brushless permanent-magnet motors with surface magnet and consequent-pole rotors,” *IEEE Trans. Magn*., vol. 46, no. 7, pp. 2675–2685, Jul. 2010.

[DOR11] D. G. Dorrell and M. Popescu, “Odd stator slot numbers in brushless DC machines—An aid to cogging torque reduction,” *IEEE Trans. Magn*., vol. 47, no. 10, pp. 3012–3015, Oct. 2011.

[DU19] G. H. Du, W. Xu, J. G. Zhu, and N. Huang “Multiphysics design and optimization of high-speed permanent-magnet electrical machines for air blower applications,” *IEEE Trans. Ind. Electron*., Early access.

[DUB14] F. Dubas and A. Rahideh, “Two-dimensional analytical permanent-magnet eddy-current loss calculations in slotless PMSM equipped with surfaceinset magnets,” *IEEE Trans. Magn*., vol. 50, no. 3, pp. 54–73, Mar. 2014.

[DUT13] R. Dutta, L. Chong, F.M. Rahman, “Analysis and Experimental Verification of Losses in a concentrated wound interior permanent magnet machine”, Progress in electromagnetics Research B, vol. 48, pp. 221- 248, 2013.

[EDE01] J. D. Ede, Z. Q. Zhu, and D. Howe: 'Optimal split ratio for high-speed permanent magnet brushless DC motors', *Proc. 5th Int. Conf. Electrical Machines and Systems*, vol. 2, pp. 909–912, Aug. 2001.

[ETE12] M. Etemadrezaei, J. J. Wolmarans, H. Polinder, and J. A. Ferreira, “Precise calculation and optimization of rotor eddy current losses in high speed permanent magnet machine,” in *Proc. 20th Int. Conf. Elect. Mach. (ICEM)*, Sep. 2012, pp. 1399–1404.

[FAN15] H. Fang, R. Qu, J. Li, P. Zheng, and X. Fan “Rotor design for a high-speed high-power permanent-magnet synchronous machine,” in *Proc. IEEE ECCE*, Sep.2015, pp. 4405–4412.

[FAN16] X. Fan, R. Qu, B. Zhang, J. Li and D. Li: 'Split ratio optimization of high-speed permanent magnet synchronous machines based on thermal resistance network', *2016 XXII International Conference on Electrical Machines (ICEM),* Lausanne, pp. 4-7, Sep. 2016

[FAN17] H. Fang, R. Qu, J. Li, P. Zheng, and X. Fan, "Rotor design for high-speed high-power permanent-magnet synchronous machines," *IEEE Trans. Ind. Appl*., vol. 53, no. 4, pp. 3411–3419, Aug. 2017.

[FEI10] W. Fei, P. C. K. Luk, and K. Jinupun, "Design and analysis of high-speed coreless axial flux permanent magnet generator with circular magnets and coils," *IET Elect. Power Appl.*, vol. 4, pp. 739-747, 2010.

[FEN19] Jianghua Feng, Yu Wang, Shuying Guo, Zhichu Chen, Yu Wang, Zi-Qiang Zhu, "Split ratio optimisation of high-speed permanent magnet brushless machines considering mechanical constraints," *IET Electric Power Applications*, vol. 13, no. 1, pp. 81-90, 2019.

[FER14] W. U. N. Fernando and C. Gerada, "High speed permanent magnet machine design with minimized stack-length under electromagnetic and mechanical constraints," *Int J Appl Electrom*., vol. 46, no. 1, pp. 95–109, Jan 2014.

[FER95] C. A. Ferreira, S. R. Jones, W. S. Heglund, and W. D. Jones, "Detailed design of a 30kW switched reluctance S/G system for a gas turbine application," *IEEE Trans. Ind. Appl.*, vol. 31, no. 3, pp. 553–561, May 1995.

[GEE13] M. van der Geest, H. Polinder, J. A. Ferreira, and D. Zeilstra, "Stator winding proximity loss reduction techniques in high speed electrical machines," in *Proc. Int. Elect. Mach. Drives Conf*., 2013, pp. 340–346.

[GER09] D. Gerada, A. Mebarki, R. P. Mokhadkar, N. L. Brown, and C. Gerada, "Design issues of high-speed permanent magnet machines for high-temperature applications," in *Proc. IEEE Int. Elect. Mach. Drives Conf.*, May 3–6, 2009, pp. 1036–1042.

[GER11] D. Gerada and A. Mebarki, "Design aspects of high-speed high-power density laminated-rotor induction machines," *IEEE Trans. Ind. Electron.*, vol. 58, no. 9, pp. 4039–4047, Sep. 2011.

[GER12] D. Gerada, A. Mebarki, N. L. Brown, H. Zhang, and C. Gerada, "Design, modelling and testing of a high speed induction machine drive," in *Proc. ECCE*, Sep. 2012, pp. 4649–4655.

[GER14] D. Gerada, A. Mebarki, N. L. Brown, C. Gerada, A. Cavagnino, and A. Boglietti, "High-Speed Electrical Machines: Technologies, Trends, and Developments," *IEEE Trans. Ind. Electron.*, vol. 61, no. 6, pp. 2946-2959, Jun. 2014.

[GIE12] J. F. Gieras and J. Saari, "Performance calculation for a high-speed solid-rotor induction motor," *IEEE Trans. Ind. Electron.*, vol. 59, no. 6, pp. 2689–2700, Jun. 2012.

[GIL16] Gilson, A., Dubas, F., Depernet, D., et al.: 'Comparison of high-speed PM machine topologies for electrically-assisted turbocharger applications. *2016 19th Int. Conf. on Electrical Machines and Systems*, pp. 1–5, 2016.

[GOL03] L. Goldstein, B. Hedman, D. Knowles, S. I. Freedman, R. Woods, and T. Schweizer, "Gas-Fired Distributed Energy Resource Technology Characterizations," Nat. Renewable Energy Lab., Golden, CO, USA, Tech.

Rep. NREL/TP-620-34783, Nov. 2003.

[GON14] D. A. Gonzalez and D. M. Saban, "Study of the copper losses in a high-speed permanent-magnet machine with form-wound windings," *IEEE Trans. Ind. Electron.*, vol. 61, no. 6, pp. 3038-3045, Jun.2014.

[GOO70] J. N. Goodier and S. P. Imoskenko, *Theroy of Elasticity*. New York, NY, USA: McGraw Hill, 1970.

[GUR13] S. R. Gurumurthy, V. Agarwal, and A. Sharma, "Optimal energy harvesting from a high-speed brushless DC generator-based flywheel energy storage system," *IET Elect. Power Appl*., vol. 7, no. 9, pp. 693–700, Nov. 2013.

[HAN10] S.-H. Han, T. M. Jahns, W. L. Soong, M. K. Guven, and M. S. Illindala, "Torque ripple reduction in interior permanent magnet synchronous machines using stators with odd number of slots per pole pair," *IEEE Trans. Energy Convers.*, vol. 25, no. 1, pp. 118–127, Mar. 2010.

[HAS00] T. S. El-Hasan, P. C. K. Luk, F. S. Bhinder, and M. S. Ebaid, "Modular design of high-speed permanent-magnet axial-flux generators," *IEEE Trans. Magn.,* vol. 36, no. 5, pp. 3558-3561, Sep.2000.

[HAY09] H. Hayashi, K. Nakamura, A. Chiba, T. Fukao, K. Tungpimolrut, and D. G. Dorell, "Efficiency improvements of switched reluctance motors with high-quality steel and enhanced conductor slot fill," *IEEE Trans. Energy Convers*., vol. 24, no. 4, pp. 819–825, Dec. 2009.

[HON09] D.-K. Hong, B.-C. Woo, and D.-H. Koo, "Rotor dynamics of 120 000 r/min 15 kW ultra high speed motor," *IEEE Trans. Magn*., vol. 45, no. 6, pp. 2831–2834, Jun. 2009.

[HON12] D. K. Hong, B. C. Woo, J. Y. Lee, and D. H. Koo, "Ultra high speed motor supported by air foil bearings for air blower cooling fuel cells," *IEEE Trans. Magn*., vol. 48, no. 2, pp. 871–874, Feb. 2012.

[HON97] Y. Honda, S. Yokote, T. Higaki, and Y. Takeda, "Using the halbach magnet array to develop an ultrahigh-speed spindle motor for machine tools," in *Conf. Rec. IEEE IAS Annu. Meeting*, Oct. 1997, vol. 1, pp. 56–60.

[HSU08] J. S. Hsu, T. A. Burress, S. T. Lee, R. H. Wiles, C. L. Coomer,J. W. McKeever, and D. J. Adams, "16,000-rpm interior permanent magnet reluctance machine with brushless field excitation," in *Proc. IEEE IAS Annu. Meet*., 2008, pp. 1–6.

[HUA10] W.-Y. Huang, A. Bettayeb, R. Kaczmarek, and J.-C. Vannier, "Optimization of magnet segmentation for reduction of eddy-current losses in permanent magnet synchronous machine," *IEEE Trans. Energy Convers*., vol. 25, no. 2, pp. 381–387, Jun. 2010.

[HUA16] Z. Huang and J. Fang, "Multiphysics design and optimization of high-speed permanent-magnet electrical machines for air blower applications," *IEEE Trans. Ind. Electron.*, vol. 63, no. 5, pp. 2766-2774, May.2016.

[HUA18] L. Huang, J. Feng, S. Guo, Y. F. Li, J. Shi, and Z. Q. Zhu, "Rotor shaping method for torque ripple mitigation in variable flux reluctance machines," *IEEE Trans. Energy Conv*., vol. 33, no. 3, pp. 1579–1589, Apr. 2018.

[HUP04] J. Huppunen, "High-Speed solid-rotor induction machine—Electromagnetic calculation and design," Ph.D. dissertation, Lappeenranta Univ. Technol., Lappeenranta, Finland, 2004.

[HWA14] C.-C. Hwang, S.-S. Hung, C.-T. Liu, and S.-P. Cheng, "Optimal design of a high speed SPM motor for machine tool applications," *IEEE Trans. Mag.*, vol. 50, no. 1, pp. 1-4, Jan.2014.

[IKE90] M. Ikeda, S. Sakabe, and K. Higashi, "Experimental study of high speed induction motor varying rotor core construction," *IEEE Trans. Energy Convers.*, vol. 5, no. 1, pp. 98–103, Mar. 1990.

[ION06] D. M. Ionel, M. Popescu, S. J. Dellinger, T. J. E. Miller, R. J. Heideman, and M. I. McGlip, "On the variation with flux and frequency of the core loss coefficients in electrical machines," *IEEE Trans. Ind. Appl.*, vol. 42, no. 3, pp. 658–667, May 2006.

[ION07] D. M. Ionel, M. Popescu, and S. J. Dellinger, "Computation of core losses in electrical machines using improved models for laminated steel," *IEEE Trans. Ind. Appl*., vol. 43, no. 6, pp. 1554–1564, Nov./Dec. 2007.

[ISH05] D. Ishak, Z. Q. Zhu, and D. Howe, "Eddy-current loss in the rotor magnets of permanent-magnet brushless machines having a fractional number of slots per pole," *IEEE Trans. Magn.*, vol. 41, no. 9, pp.2462–2469, Sep. 2005.

[IWA09] S. Iwasaki, R. P. Deodhar, L. Yong, A. Pride, Z. Q. Zhu, and J. J. Bremner, "Influence of PWM on the proximity loss in permanent-magnet brushless ac machines," *IEEE Trans. Ind. Appl.*, vol. 45, no. 4, pp. 1359-1367, Jul./Aug.2009.

[JAN01] S. M. Jang and S.-S. Jeong, "Comparison of three types of PM brushless machines for an electro-mechanical battery," *IEEE Trans. Magn*., vol. 36, no. 5, pp. 3540–3543, Sep. 2001.

[JAN03] S. M. Jang, L. Sung-Ho, C. Han-Wook, and C. Sung-Kook, "Analysis of unbalanced force for high-speed slotless permanent magnet machine with Halbach array," *IEEE Trans. Magn.*, vol. 39, no. 5, pp. 3265–3267, Sep. 2003.

[JAN04] S. M. Jang, H. W. Cho, S. H. Lee, H. S. Yang, and Y. H. Jeong, "The influence of magnetization pattern on the rotor losses of permanent magnet high-speed machines," *IEEE Trans. Magn*., vol. 40, no. 4, pp. 2062-2064, Jul. 2004.

[JAN07] S.-M. Jang, H.-W. Cho, and S.-K. Choi, "Design and analysis of a high-speed brushless dc motor for centrifugal compressor," *IEEE Trans. Magn.*, vol. 43, no. 6, pp. 2573-2575, Jun.2007.

[JAN11] X. Jannot, J.-C. Vannier, C. Marchand, M. Gabsi, J. Saint-Michel, and D. Sadarnac, "Multi-physic modeling of a high-speed interior permanent-magnet synchronous machine for a multi-objective optimal design," *IEEE Trans. Energy Convers.*, vol. 26, no. 2, pp. 457-467, Jun.2011.

[JAN96] G. H. Jang, J. W. Yoon, N. Y. Park, and S. M. Jang, "Torque and unbalanced magnetic force in a rotational unsymmetric brushless dc motors," *IEEE Trans. Magn.*, vol. 32, no. 5, pp. 5157–5159, Sep. 1996.

[JIA15] Z. Jiancheng, C. Wei, H. Xiaoyan, F. Youtong, Z. Jian, M. Jien, "Evaluation of applying retaining shield rotor for high-speed interior permanent magnet motors," *IEEE Trans. Magn.*, vol. 51, no. 3, pp. 1-4, Mar.2015.

[JUM15] S. Jumayev, M. Merdzan, K. O. Boynov, J. J. H. Paulides, J. Pyrhonen, and E. A. Lomonova, “The effect of pwm on rotor eddy-current losses in high-speed permanent magnet machines,” *IEEE Trans. Magn.,* vol. 51, no. 11, pp. 1-4, Nov.2015.

[JUN12] J. W. Jung, B. H. Lee, D. J. Kim, J. P. Hong, J. Y. Kim, and S. M. Jeon, “Mechanical stress reduction of rotor core of interior permanent magnet synchronous motor,” *IEEE Trans. Magn*., vol. 48, no. 2, pp. 911–914, Feb. 2012.

[KIM01] Y. K. Kim, M. C. Choi, K. H. Suh, Y. C. Ji, and D. S. Wang, “High-speed induction motor development for small centrifugal compressor,” in *Proc. ICEMS*, Aug. 2001, vol. 2, pp. 891–894.

[KIM08] J. Kim and R. Krishnan, “High efficiency single pulse controlled SRM drive for high speed application,” in *Conf. Rec. IEEE IAS Annu. Meeting*, Oct. 2008, vol. 1, pp. 1–8.

[KIM12] S.-I. Kim, Y.-K. Kim, G.-H. Lee, and J.-P. Hong, “A novel rotor configuration and experimental verification of interior pm synchronous motor for high-speed applications,” *IEEE Trans. Magn.*, vol. 48, no. 2, pp. 843-846, Feb.2012.

[KIM16] D. Kim, M. Noh, and Y. Park, “Unbalanced magnetic forces due to rotor eccentricity in a toroidally wound BLDC motor,” *IEEE Trans. Magn.*, vol. 52, no. 7, Feb. 2016, Art no. 8203204.

[KOL09] Z. Kolondzovski, A. Belahcen, and A. Arkkio, “Comparative thermal analysis of different rotor types for high-speed permanent-magnet electrical machine,” *IET Electr. Power Appl*., vol. 3, no. 4, pp. 279–288, Jul. 2009.

[KOL10] Z. Kolondzovski, P. Sallinen, A. Belahcen, and A. Arkkio, “Rotor dynamic analysis of different rotor structures for high-speed permanent-magnet electrical machines,” *IET Elect. Power Appl*., vol. 4, no. 7, pp. 516–524, Aug. 2010.

[KOL11] Z. Kolondzovski, A. Arkkio, J. Larjola, and P. Sallinen, “Power limits of high-speed permanent-magnet electrical machines for compressor applications,” *IEEE Trans. Energy Convers.*, vol. 26, no.1, pp. 73-82, Mar.2011.

[KRA10] D. Krähenbühl, C. Zwyssig, H. Weser, and J. W. Kolar, “A miniature 500 000-r/min electrically driven turbocompressor,” *IEEE Trans. Ind. Appl*., vol. 46, no. 6, pp. 2459–2466, Nov./Dec. 2010.

[LAH02] J. Lahteenmaki, “Design and voltage supply of high-speed induction machines,” Ph.D. dissertation, Helsinki Univ. Technol., Espoo, Finland, 2002.

[LAR03] M. Larsson, M. Johansson, L. Naslund, and J. Hylander, “Design and evalution of high-speed induction machine,” in *Proc. IEMDC*, Jun. 2003, vol. 1, pp. 77–82.

[LAT09] R. Lateb, J. Enon, and L. Durantay, “High speed, high power electrical induction motor technologies for integrated compressors,” in *Proc. ICEMS*, Nov. 2009, pp. 1438–1442.

[LAZ10] M. Lazzari, A. Miotto, A. Tenconi, and S. Vaschetto, “Analytical prediction of eddy current losses in retaining sleeves for surface mounted PM synchronous machines,” in *Conf. Rec. 19th IEEE ICEM*, 2010, pp. 1–6.

[LEE13] D. H. Lee, T. H. Pham, and J.W. Ahn, “Design and operation characteristics of four-two pole high speed SRM for torque ripple reduction,” *IEEE Trans. Ind. Electron.*, vol. 60, no. 9, pp. 3637–3643, Sep. 2013.

[LI09] Y. B. Li, S. L. Ho, W. N. Fu, and B. F. Xue, “Analysis and solution on squeak noise of small permanent-magnet dc brush motors in variable speed applications,” *IEEE Trans. Magn.*, vol. 45, no. 10, pp. 4752–4755, Oct. 2009.

[LI14] W. Li, H. Qiu, X. Zhang, J. Cao, S. Zhang, and R. Yi, “Influence of rotor-sleeve electromagnetic characteristics on high-speed permanent-magnet generator,” *IEEE Trans. Ind. Electron.*, vol. 61, no. 6, pp. 3030-3037, Jun.2014.

[LI18] J. Li, K. Wang, F. Li: 'Analytical prediction of optimal split ratio of consequent-pole permanent magnet machines', *IET Electric Power Applications*, vol. 12, pp. 365-372, 2018

[LIM17] M. S. Lim, J. M. Kim, Y. S. Hwang, and J. P. Hong, “Design of an ultrahigh-speed permanent-magnet motor for an electric turbocharger considering speed response characteristics,” *IEEE/ASME Trans. Mechatron*., vol. 22, no. 2, pp. 774–784, Apr. 2017.

[LIN04] D. Lin, P. Zhou, W. N. Fu, Z. Badics, and Z. J. Cendes, “A dynamic core loss model for soft ferromagnetic and power ferrite materials in transient finite element analysis,” *IEEE Trans. Magn.*, vol. 40, no. 2, pp. 1318–1321, Mar. 2004.

[LIN08] S. Lin, T. X. Wu, L. Zhou, F. Moslehy, J. Kapat, and L. Chow, “Modeling and design of super high speed permanent magnet synchronous motor (pmsm),” in *Aerospace and Electronics Conference, 2008. NAECON 2008. IEEE National*, Jul. 2008, pp. 41–44.

[LIP11] T. A. Lipo: 'Introduction to AC machine design', Wisconsin Power Electron. Res. Center, Univ. Wisconsin, Madison, WI, USA, 2011.

[LON98] L. Xu and C. Wang, “Implementation and experimental investigation of sensorless control schemes for PMSM in super-high variable speed operation,” in *Conf. Rec. IEEE-IAS Annu. Meeting*, 1998, pp. 483–489.

[LUI14] F. Luise, A. Tessarolo, F. Agnolet, S. Pieri, M. Scalabrin, and P. Raffin, “A high-performance 640-kW 10000-rpm Halbach-array PM slotless motor with active magnetic bearings. Part II: Manufacturing and testing,” in *Proc. Int. Symp. Power Electron., Elect. Drives, Autom. Motion (SPEEDAM)*, Jun. 2014, pp. 1245–1250.

[LUO09] J. Luomi, C. Zwyssig, A. Looser, and J. W. Kolar, “Efficiency optimization of a 100-W 500 000-r/min permanent-magnet machine including air friction losses,” *IEEE Trans. Ind. Appl.*, vol. 45, no. 4, pp. 1368–1377, Jul./Aug. 2009.

[MA18] J. Ma, and Z. Q. Zhu, “Mitigation of unbalanced magnetic force in a PM machine with asymmetric winding by inserting auxiliary slots,” *IEEE Trans. Ind. Appl*., vol. 54, no. 5, pp. 4133–4146, Sept./Oct. 2018.

[MA19] J. Ma, and Z. Q. Zhu, “Magnet eddy current loss reduction in permanent magnet machines,” *IEEE Trans. Ind. Appl*., vol. 55, no. 2, pp. 1309–1320, Mar./Apr. 2019.

[MEL06] P. H. Mellor and R. Wrobel, “Investigation of proximity losses in a high speed brushless permanent magnet motor,” in *Conf. Rec. 41st IEEE IAS Annu. Meeting*, Oct. 8–12, 2006, pp. 1514–1518.

[MER15] M. Merdzan, J. J. H. Paulides, and E. a Lomonova, “Comparative analysis of rotor losses in high-speed permanent magnet machines with different winding configurations considering the influence of the inverter PWM,” in *Proc. Xth Int. Conf. Eco. Veh. Renew. Energ*., Mar./Apr. 2015, pp. 1–8.

[MIC14] M. Michon, R. C. Holehouse, K. Atallah, and J. Wang, “Unbalanced magnetic pull in permanent magnet machines,” in *Proc. 7th IET Int. Conf. Power Electron., Mach. Drives*, 2014, pp. 1–6.

[MIL91] R. D. van Millingen and J. D. van Millingen, “Phase shift torquemeters for gas turbine development and monitoring,” in *Proc. Int. Gas Turbine Aeroengine Congr. Expo.*, Jun. 1991, pp. 1–10.

[MIR12] M. Mirzaei, A. Binder, B. Funieru, and M. Susic, “Analytical calculations of induced eddy currents losses in the magnets of surface mounted PM machines with consideration of circumferential and axial segmentation effects,” *IEEE Trans. Magn*., vol. 48, no. 12, pp. 4831–4841, Dec. 2012.

[MOG14] R. R. Moghaddam, “High speed operation of electrical machines, a review on technology, benefits and challenges,” in *Proc. IEEE ECCE*, 2014, pp. 5539–5546.

[MTH06] T. L. Mthombeni and P. Pillay, “Physical basis for the variation of lamination core loss coefficients as a function of frequency and flux density,” in *Proc. IEEE Conf. Ind. Electron.*, 2006, pp. 1381–1387.

[NAK06] M. Nakano, H. Kometani, and M. Kawamura, “A study on eddy-current losses in rotors of surface permanent-magnet synchronous machines,” *IEEE Trans. Ind. Appl*., vol. 42, no. 2, pp. 429–435, Mar./Apr. 2006.

[NIU12] S. Niu, S. L. Ho, W. N. Fu, and J. Zhu, “Eddy current reduction in high-speed machines and eddy current loss analysis with multislice time-stepping finite-element method,” *IEEE Trans. Magn.*, vol. 48, no. 2, pp. 1007-1010, Feb. 2012.

[NOG07] Noguchi T, Takata Y, Yamashita Y. “220000r/min 2kW PM motor drive for turbocharger,” *Electrical Engineering in Japan*, vol. 16, no.3, pp.31-40, 2007.

[PAN06] Y. Pang, Z. Q. Zhu, and D. Howe, “Analytical determination of optimal split ratio for permanent magnet brushless motors,” *IEE Proc. Elect. Power Appl.*, vol. 153, pp. 7–13, Jan. 2006.

[PAT14] V. I. Patel, J.Wang, W.Wang, and X. Chen, “Six-phase fractional-slot-per pole- per-phase permanent-magnet machines with low space harmonics for electric vehicle application,” *IEEE Trans. Ind. Appl.*, vol. 50, no. 4, pp.2554–2563, Jan. 2014.

[PAU04] J. J. H. Paulides, G. W. Jewell, and D. Howe, “An evaluation of alternative stator lamination materials for a high-speed, 1.5 MW, permanent magnet generator," *IEEE Trans. Mag.*, vol. 40, no. 4, pp. 2041-2043, Aug.2004.

[PFI10] P.-D.Pfister and Y. Perriard, “Very-high-speed slotless permanent magnet motors: Analytical modeling, optimization, design, and torque measurement methods,” *IEEE Trans. Ind. Electron*., vol. 57, no. 1, pp. 296–303, Jan. 2010.

[POP07] M. Popescu and D. Ionel, “A best-fit model of power losses in cold rolled-motor lamination steel operating in a wide range of frequency and magnetization,” *IEEE Trans. Magn.*, vol. 43, no. 4, pp. 1753–1756, Apr. 2007.

[POP13] M. Popescu and D. G. Dorrell, “Proximity losses in the windings of high speed brushless permanent magnet ac motors with single tooth windings and parallel paths,” *IEEE Trans. Magn.,* vol. 49, no. 7, pp. 3913-3916, Jul.2013.

[PRA12] R. P. Praveen, M. H. Ravichandran, V. T. Sadasivan Achari, V. P. Jagathy Raj, G. Madhu, and G. R. Bindu, “A novel slotless Halbach array permanent-magnet brushless dc motor for spacecraft applications,” *IEEE Trans. Ind. Electron*., vol. 59, no. 9, pp. 3553–3560, Sep. 2012.

[PYR08] J. Pyrhonen, T. Jokinen, and V. Hrabovcova, Design of Rotating Electrical Machines. Hoboken, NJ: Wiley, 2008.

[PYR10] J. Pyrhonen, J. Nerg, P. Kurronen, and U. Lauber, “High-speed, high output, solid-rotor induction motor technology for gas compression,” *IEEE Trans. Ind. Electron.*, vol. 57, no. 1, pp. 272–280, Jan. 2010.

[PYR96] J. Pyrhonen and J. Huppunen, “A new medium speed solid rotor induction motor for a high speed milling machine,” in *Proc. SPEEDAM*, 1996, pp. B5-1–B5-8.

[RAH04] M. A. Rahman, A. Chiba, and T. Fukao, “Super high speed electrical machines-summary,” in *IEEE Power Engineering Society General Meeting*, Jun. 6–10, 2004, vol. 2, pp. 1272–1275.

[RED09] P. B. Reddy, T. M. Jahns, and T. P. Bohn, “Transposition effects on bundle proximity losses in high-speed PM machines,” in *Proc. IEEE Energy Convers. Congr. Expo. (ECCE’09)*, 2009, no. 1, pp. 1919–1926.

[RED10] P. B. Reddy, T. M. Jahns, and T. P. Bohn, “Modeling and analysis of proximity losses in high-speed surface permanent magnet machines with concentrated windings,” in *Proc. IEEE Energy Convers. Congr. Expo. (ECCE’10)*, 2010, pp. 996–1003.

[RED11] P. Reddy and T. Jahns, “Scalability investigation of proximity losses in fractional-slot concentrated winding surface PM machines during high-speed operation,” in *Proc. IEEE Energy Convers. Congr. Expo*., Sep. 2011, pp. 1670–1675.

[REF05] A. M. EL-Refaie and T. M. Jahns, “Optimal flux weakening in surface PM machines using concentrated windings,” *IEEE Trans. Ind. Appl*., vol. 41, no. 3, pp. 790–800, May/Jun. 2005.

[REF08] A. M. El-Refaie, M. R. Shah, Q. Ronghai, and J. M. Kern, “Effect of number of phases on losses in conducting sleeves of surface PM machine rotors equipped with fractional-slot concentrated windings,” *IEEE Trans. Ind. Appl.,* vol. 44, no. 4, pp. 1522-1532, Sep./Oct.2008.

[REF10] A. M. El-Refaie, “Fractional-slot concentrated-windings synchronous permanent magnet machines: Opportunities and challenges,” *IEEE Trans. Ind. Electron*., vol. 57, no. 1, pp. 107–121, Jan. 2010

[REI13] T. Reichert, T. Nussbaumer, and J. W. Kolar: 'Split ratio optimization for high-torque PM motors considering global and local thermal limitations', *IEEE Trans. Energy Convers*., vol. 28, pp. 493–501, Sept. 2013.

[REI95] K. Reichert and G. Pasquarella, “High speed electric machines, status, trends, and problems,” in *Proc. IEEE/KTH Stockholm Tech. Conf.*, Stockholm, Sweden, Jun. 1995, pp. 41–49.

[RIC97] E. Richter and C. Ferreira, “Performance evaluation of a 250 kW switched reluctance starter generator,” in *Conf. Rec. IEEE IAS Annu. Meeting*, Oct. 1997, vol. 1, pp. 434–440.

[SAA94] J. Saari and A. Arkkio, “Losses in high speed asynchronous motors,” in *Proc. ICEM*, Sep. 1994, vol. 3, pp. 704–708.

[SHA06] M. R. Shah and S. B. Lee, “Rapid analytical optimization of eddy current shield thickness for associated loss minimization in electrical machines,” *IEEE Trans. Ind. Appl*., vol. 42, no. 3, pp. 642–649, May/Jun. 2006.

[SHA09] M. R. Shah and A. M. EL-Refaie, “Eddy current loss minimization in conducting sleeves of high speed machine rotors by optimal axial segmentation and copper cladding,” *IEEE Trans. Ind. Appl*., vol. 45, no. 2, pp. 720–728, Mar./Apr. 2009.

[SHE06] J. X. Shen and S. Iwasaki, “Sensorless control of ultrahigh-speed PM brushless motor using PLL and third harmonic back EMF,” *IEEE Trans. Ind. Electron*., vol. 53, no. 2, pp. 421–428, Apr. 2006.

[SHE13] J.-X. Shen, H. Hao, M.-J. Jin, and C. Yuan, “Reduction of rotor eddy current loss in high speed PM brushless machines by grooving retaining sleeve,” *IEEE Trans. Mag.*, vol. 49, no. 7, pp. 3973-3976, Jul.2013.

[SHI04] K. Shigematsu, J. Oyama, T. Higuchi, T. Abe, and Y. Ueno, “The study of eddy current in rotor and circuit coupling analysis for small size and ultra high speed motor,” in *Proc. IPEMC*, Aug. 2004, pp. 275–279.

[SIE90] R. Siegwart, R. Larsonneur, and A. Traxler, “Design and performance of high speed milling spindle in digitally controlled AMB’s,” in *Proc. Int. Symp. Magn. Bearings*, Aug. 1990, vol. 1, pp. 197–204.

[SIL14] S. Silber, J. Sloupensky, P. Dirnberger, M. Moravec, W. Amrhein, and M. Reisinger, “High-Speed drive for textile rotor spinning applications,” *IEEE Trans. Ind. Electron.,* vol. 61, no. 6, pp. 2990-2997, Jun. 2014.

[SKF12] SKF Group, “Rolling Bearings Catalog”, October 2012.

[SMI10] D. Smith, B. Mecrow, G. Atkinson, A. Jack, and A. Mehna, “Shear stress concentrations in permanent magnet rotor sleeves,” in *Proc. XIX Int. Conf. Electr. Mach*., Sep. 2010, pp. 1–6.

[SOO00] W. L. Soong, G. B. Kliman, R. N. Johnson, R. A. White, and J. E. Miller, “Novel high-speed induction motor for a commercial centrifugal compressor,” *IEEE Trans. Ind. App.*, vol. 36, no. 3, pp. 706–713, May 2000.

[SUL99] C. R. Sullivan, “Optimal choice for number of strands in a litz-wire transformer winding,” *IEEE Trans. Power Electron*., vol. 14, pp. 283–291, Mar. 1999.

[SUN14] A. Sun, J. Li, R. Qu, and D. Li, “Effect of multilayer windings on rotor losses of interior permanent magnet generator with fractional-slot concentrated-windings,” *IEEE Trans. Magn*., vol. 50, no. 11, Nov. 2014, Art. ID 8105404.

[TAK93] I. Takahashi, T. Koganezawa, G. Su, and K. Oyama, “A super high speed PM motor drive system by a quasi-current source inverter,” in *Conf. Rec. IEEE IAS Annu. Meeting*, Oct. 1993, vol. 1, pp. 657–662.

[TAK94] I. Takahashi, T. Koganezawa, G. Su, and K. Ohyama, “A super high speed PM motor drive system by a quasi-current source inverter,” *IEEE Trans. Ind. Appl*., vol. 30, no. 3, pp. 683–690, May/Jun.1994.

[TEN14] A. Tenconi, S. Vaschetto, and A. Vigliani, “Electrical machines for high-speed applications: Design considerations and tradeoffs,” *IEEE Trans. Ind. Electron.*, vol. 61, no. 6, pp. 3022-3029, Jun.2014.

[TES11] A. Tessarolo, G. Zocco, and C. Tonello, “Design and testing of a 45-MW100-Hz quadruple-star synchronous motor for a liquefied natural gas turbo-compressor drive,” *IEEE Trans. Ind. Appl.*, vol. 47, no. 3, pp. 1210–1219, May 2011.

[THO09] A. S. Thomas, Z. Q. Zhu, and G. W. Jewell, “Proximity loss study in high speed flux-switching permanent magnet machine,” *IEEE Trans. Magn.,* vol. 45, no. 10, pp. 4748-4751, Oct.2009.

[TOD04] H. Toda, Z. P. Xia, J. Wang, K. Atallah, and D. Howe, “Rotor eddy current loss in permanent magnet brushless machines,” *IEEE Trans. Magn*., vol. 40, no. 4, pp. 2104–2106, Jul. 2004.

[TSA03] P. I. Tsao, “An integrated flywheel energy storage system with a homopolar inductor motor/generator and high-frequency drive,” Ph.D. dissertation, Univ. California, Berkeley, CA, USA, 2003.

[TUY17] A. Tuysuz, F. Meyer, M. Steichen, C. Zwyssig, and J. W. Kolar, “Advanced cooling methods for high-speed electrical machines,” *IEEE Trans. Ind. Appl*., vol. 53, no. 3, pp. 2077–2087, May/Jun. 2017.

[UZH16] N. Uzhegov, E. Kurvinen, J. Nerg, J. Pyrhonen, J. T. Sopanen, and S. Shirinskii, “Multidisciplinary design process of a 6-slot 2-pole high-speed permanent-magnet synchronous machine,” *IEEE Trans. Ind. Electron.,* vol. 63, no. 2, pp. 784-795, Feb.2016.

[VAN97] J. L. F. van der Veen, L. J. J. Offringa, and A. J. A. Vanderput, “Minimizing rotor losses in high-speed high-power permanent magnet synchronous generators with rectifier load,” *Inst. Elect. Eng. Proc.—Electr. Power Applicat*., vol. 144, no. 5, pp. 331–337, Sept. 1997.

[VIG92] F. Viggiano and G. Schweitzer, “Active magnetic support and design of high speed rotors for powerful electric drives,” in *Proc. Int. Symp. Magn. Bearings*, Jul. 1992, vol. 1, pp. 549–558.

[VRA68] J. Vrancik, “Prediction of windage power loss in alternators,” NASA Technical Note, 1968.

[WAN07] T. Wang, F. Wang, H. Bai, and J. Xing, “Optimization design of rotor

structure for high-speed permanent-magnet machines," in *Proc. Int. Conf. Elect. Mach. Syst*., 2007, pp. 1438–1442.

[WAN10b] J. Wang, K. Atallah, R. Chin, W. M. Arshad, and H. Lendenmann, "Rotor eddy current loss in permanent magnet brushless AC machines," *IEEE Trans. Magn*., vol. 46, no. 7, pp. 2701–2707, Jul. 2010.

[WAN10a] K. Wang, M. J. Jin, J. X. Shen, and H. Hao, "Study on rotor structure with different magnet assembly in high-speed sensorless brushless DC motors," *Electric Power Applications, IET*, vol. 4, no. 4, pp. 241–248, Mar. 2010.

[WAN15] Y. Wang, R. Qu, and J. Li, "Multilayer windings effect on interior PM machines for EV applications," *IEEE Trans. Ind. Appl*., vol. 51, no. 3, pp. 2208–2215, May/Jun. 2015.

[WAN18] Y. Wang, J. H. Feng, S. Y. Guo, Y. F. Li, Z. C. Chen, Y. Wang, and Z. Q. Zhu, "Investigation of optimal split ratio for high-speed permanent-magnet brushless machines," *IEEE Trans. Magn*., vol. 54, no.11, Nov. 2018, Art no. 8105605.

[WOO97] B.M.Wood, C. L. Olsen, G. D. Hartzo, J. C. Rama, and F. R. Szenasi, "Development of an 11000-r/min 3500-HP induction motor and adjustablespeed drive for refinery service," *IEEE Trans. Ind. Appl.*, vol. 33, no. 3, pp. 815–825, May 1997.

[WU10a] L. J. Wu, Z. Q. Zhu, J. T. Chen, Z. P. Xia, and G. W. Jewell, "Optimal split ratio in fractional-slot interior permanent-magnet machines with non-overlapping windings," *IEEE Trans. Magn*., vol. 46, no. 5, pp. 1235–1242, May 2010.

[WU10b] L. J. Wu, Z. Q. Zhu, J. T. Chen, and Z. P. Xia, "An analytical model of unbalanced magnetic forces in fractional-slot surface-mounted permanent magnet machines," *IEEE Trans. Magn.*, vol. 46, no. 7, pp. 2686–2700, Jul. 2010.

[WU12] L. J. Wu, Z. Q. Zhu, D. Staton, M. Popescu, and D. Hawkins, "Analytical model for predicting magnet loss of surface-mounted permanent magnet machines accounting for slotting effect and load," *IEEE Trans. Magn.*,vol. 48, no. 1, pp. 107–117, Jan. 2012.

[XIA15] M. Xiaohe, S. Rong, T. K. Jet, W. Shuai, Z. Xiaolong, V. Vaiyapuri, "Review of high speed electrical machines in gas turbine electrical power generation," in *2015 IEEE Region 10 Conference*, Macau, 2015, pp.1-9

[XIN10] J. Xing, F. Wang, T. Wang, and Y. Zhang, "Study on anti-demagnetization of magnet for high speed permanent magnet machine," *IEEE Trans. Appl. Supercondu*., vol. 20, no. 3, pp. 856–860, Jun.2010.

[XUE18a] S. Xue, J. Feng, S. Guo, J. Peng, W. Q. Chu, and Z. Q. Zhu, "A new iron loss model for temperature dependencies of hysteresis and eddy current losses in electrical machines," *IEEE Trans. Magn*., vol. 54, no. 1, pp. 1–10, Jan. 2018

[XUE18b] S. S. Xue, Z. Q. Zhu, Y. Wang, J. H. Feng, S. Y. Guo, Y .F. Li, Z. C. Chen, and J. Peng, "Thermal-loss coupling analysis of an electrical machine using the improved temperature-dependent iron loss model," *IEEE Trans. Magn*., vol. 54, no.11, Nov. 2018, Art no. 8105005.

[YAM09] K. Yamazaki, M. Shina, Y. Kanou, M. Miwa, and J. Hagiwara, "Effect of eddy current loss reduction by segmentation of magnets in synchronous motors: Difference between interior and surface types," *IEEE Trans. Magn.*, vol. 45, pp. 4756–4759, Oct. 2009.

[YAM10a] K. Yamazaki and N. Fukushima, "Iron-loss modeling for rotating machines: comparison between Bertotti's three-term expression and 3-D eddy-current analysis," *IEEE Trans. Magn.*, vol. 46, no. 8, pp. 3121–3124, Aug. 2010.

[YAM10b] K. Yamazaki, Y. Kanou, F. Yu, S. Ohki, A. Nezu, T. Ikemi, and R. Mizokami, "Reduction of magnet eddy-current loss in interior permanent-magnet motors with concentrated windings," *IEEE Trans. Ind. Appl*., vol. 46, no. 6, pp. 2434–2441, Nov./Dec. 2010.

[YAM13] K. Yamazaki and Y. Kato, "Optimization of high-speed motors considering centrifugal force and core loss using combination of stress and electromagnetic field analyses," *IEEE Trans. Magn.*, vol. 49, no. 5, pp. 2181-2184, May.2013.

[YOL17] Yolacan, E., Guven, M.K., Aydin, M.: 'A novel torque quality improvement of an asymmetric windings permanent-magnet synchronous motor', *IEEE Trans. Magn*., 2017, 53, (11), Art. 8111906, pp. 1–6.

[YON12] J. M. Yon, P. H. Mellor, R. Wrobel, J. D. Booker, and S. G. Burrow, "Analysis of semipermeable containment sleeve technology for high-speed permanent magnet machines," *IEEE Trans. Energy Convers.*, vol. 27, no. 3, pp. 646-653, 2012.

[YON13] W. Young and R. Budynas, Roark's Formulas for Stress and Strain, 7th ed. Bellingham, WA, USA: SPIE, 2013.

[ZHA15] F. Zhang, G. Du, T. Wang, G. Liu, and W. Cao, "Rotor retaining sleeve design for a 1.12 MW high-speed PM machine," *IEEE Trans. Ind. Appl*., vol. 51, no. 5, pp. 3675–3685, Sep./Oct. 2015.

[ZHA16] F. Zhang, G. Du, T. Wang, F. Wang, W. Cao, and J. L. Kirtley, "Electromagnetic design and loss calculations of a 1.12-mw high-speed permanent-magnet motor for compressor applications," *IEEE Trans. Energy Converse*., vol. 31, no. 1, pp. 132-140, Mar.2016.

[ZHA17] Y. Zhang, S. McLoone, W. Cao, F. Qiu, and C. Gerada, "Power loss and thermal analysis of a MW high speed permanent magnet synchronous machine," *IEEE Trans. Energy Convers*., vol. 32, no. 4, pp. 1468–1478, Dec. 2017.

[ZHO06] F. Zhou, J. Shen, W. Fei, and R. Lin, "Study of retaining sleeve and conductive shield and their influence on rotor loss in high-speed PM BLDC motors," *IEEE Trans. Magn*., vol. 42, no. 10, pp. 3398–3400, Oct. 2006.

[ZHO06] F. Zhou, J. Shen, W. Fei, and R. Lin, "Study of retaining sleeve and conductive shield and their influence on rotor loss in high speed PMBLDC motors," *IEEE Trans. Magn*., vol. 42, no. 10, pp. 3398–3400, Oct. 2006.

[ZHO18] W. Zhao, J. Zheng, J. Ji, S. Zhu, and M. Kang, "Star and delta hybrid connection of a FSCW PM machine for low space harmonics," *IEEE Trans. Ind. Appl*., vol. 65, no. 12, pp. 9266–9279, Dec. 2018.

[ZHU02] J. Ede, Z. Zhu, and D. Howe, "Rotor resonances of high-speed permanent-magnet brushless machines," *IEEE Trans. Ind. Appl.*, vol. 38, no. 6, pp.

1542–1548, Nov. 2002.

[ZHU04] Z. Q. Zhu, K. Ng, N. Schofield, and D. Howe, "Improved analytical modelling of rotor eddy current loss in brushless machines equipped with surface-mounted permanent magnets," *IEE Proc.-Electr. Power Appl*., vol. 151, no. 6, pp. 641–650, Nov. 2004.

[ZHU07a] Z. Q. Zhu and D. Howe, "Electrical machines and drives for electric, hybrid, and fuel cell vehicles," *Proc. IEE*E, vol. 95, no. 4, pp. 746–765, Apr. 2007.

[ZHU07b] Z. Q. Zhu, D. Ishak, D. Howe, and J. Chen, "Unbalanced magnetic forces in permanent-magnet brushless machines with diametrically asymmetric phase windings," *IEEE Trans. Ind. Appl.*, vol. 43, no. 6,pp. 1544–1553, Nov./Dec.2007.

[ZHU09] Zhu, Z.Q.: 'A simple method for measuring cogging torque in permanent magnet machines'. *Proc. of IEEE Power Energy Society General Meeting*, pp. 1–4, 2009.

[ZHU13] Z. Q. Zhu, M. Jamil, and L. Wu "Influence of slot and pole number combinations on unbalanced magnetic force in PM machines with diametrically asymmetric windings," *IEEE Trans. Ind. Appl*., vol. 49, no. 1, pp. 19–30, Jan./Feb. 2013.

[ZHU18] Z. Q. Zhu and Y. Liu, "Analysis of air-gap field modulation and magnetic gearing effect in fractional-slot concentrated-winding permanent-magnet synchronous machines," *IEEE Trans. Ind. Electron*., vol. 65, no. 5, pp. 3688–3698, May 2018.

[ZHU93] Z. Q. Zhu, D. Howe, E. Bolte, and B. Ackermann, "Instantaneous magnetic field distribution in brushless permanent magnet DC motors. I. Open-circuit field," *IEEE Trans. Magn*., vol. 29, no. 1, pp. 124–135, Jan. 1993.

[ZHU97] Z. Q. Zhu, K. Ng, and D. Howe, "Design and analysis of high-speed brushless permanent magnet motors," in *Proc. Inst. Elect. Eng. Int. Conf. Elect. Mach. Drives*, Cambridge, U.K., 1997, pp. 358–381.

[ZWY05] C. Zwyssig, J. W. Kolar, W. Thaler, and M. Vohrer, "Design of a 100W, 500 000 rpm permanent-magnet generator for mesoscale gas turbines," in *Proc. IEEE IAS Ind. Appl. Soc. 40th Annu. Meeting*, CD, Oct. 2005.

[ZWY09] C. Zwyssig, J. W. Kolar, and S. D. Round, "Megaspeed drive systems: Pushing beyond 1 million r/min," *IEEE/ASME Trans. Mechatronics*,vol. 14, no. 5, pp. 564–574, Oct. 2009.

Appendix A: AutoCAD drawings for all machines

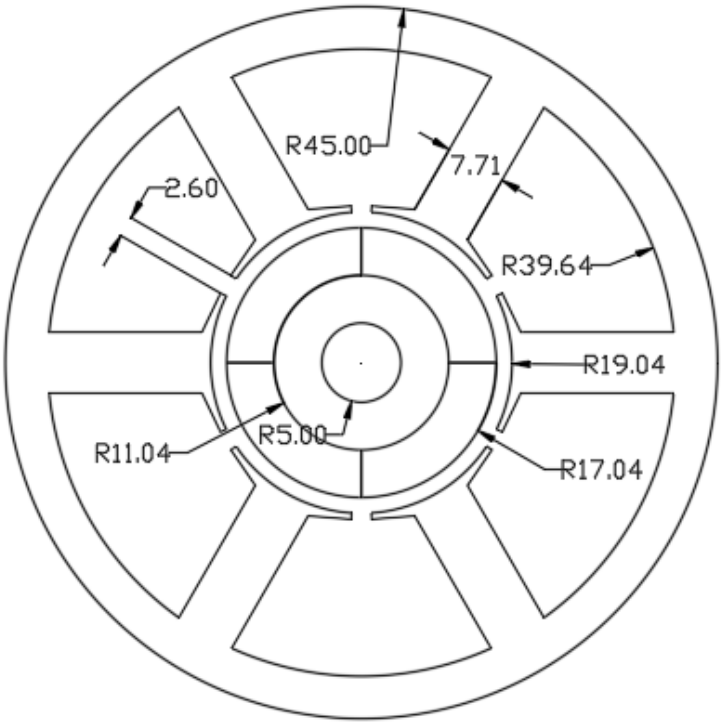

Fig.A.1. 6-slot/4-pole HSPMM laminations.

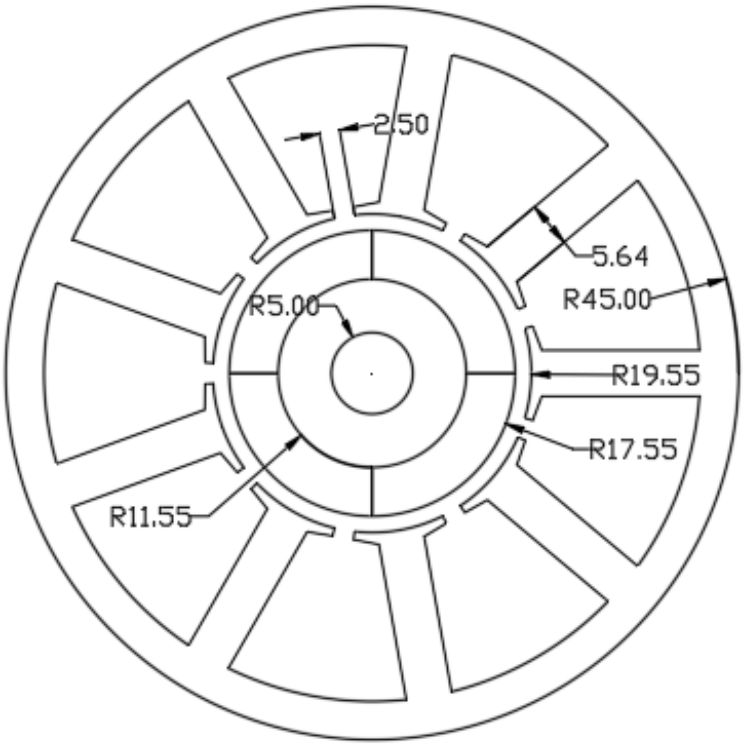

Fig.A.2. 9-slot/4-pole HSPMM laminations.

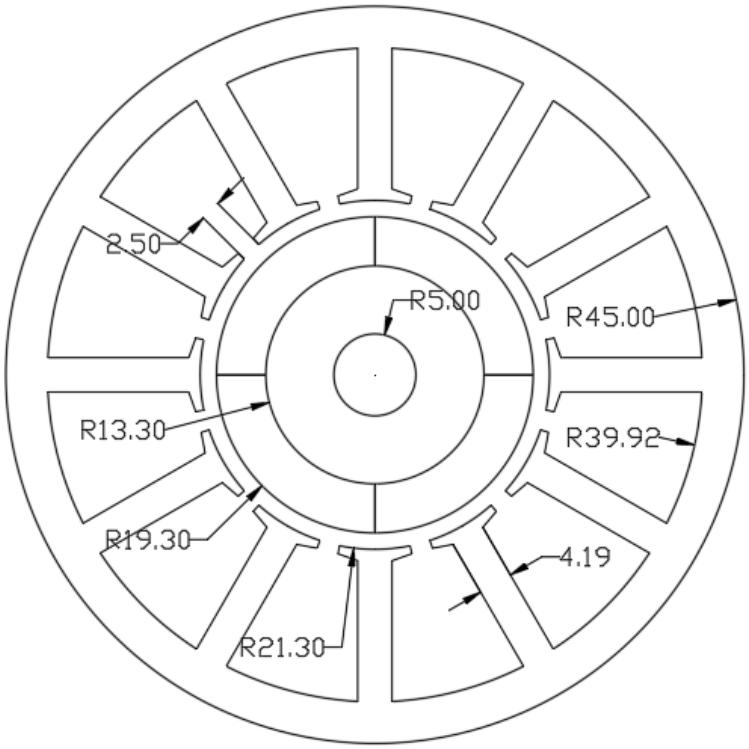

Fig.A.3. 12-slot/4-pole HSPMM laminations.

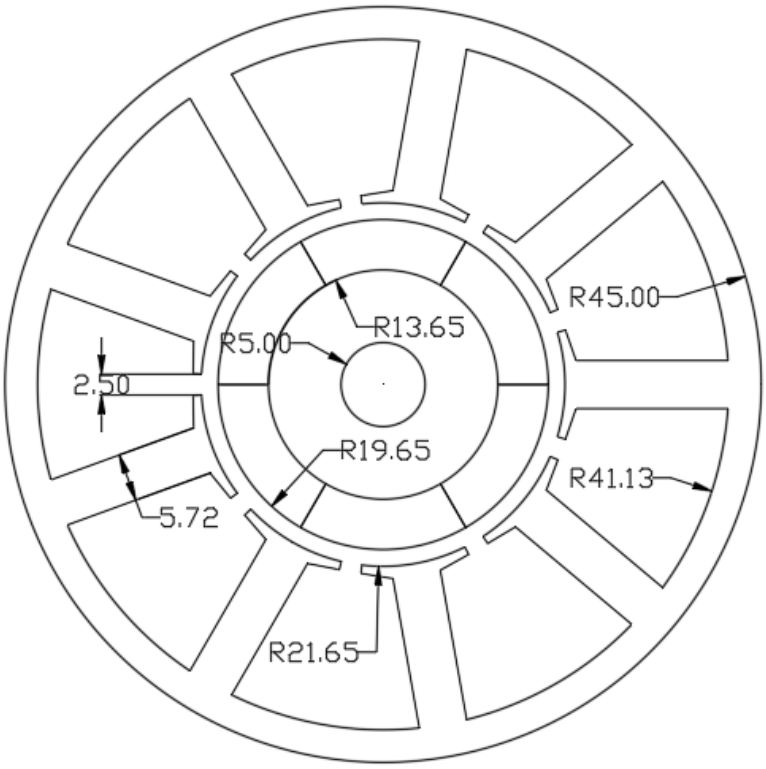

Fig.A.4. 9-slot/6-pole HSPMM laminations.

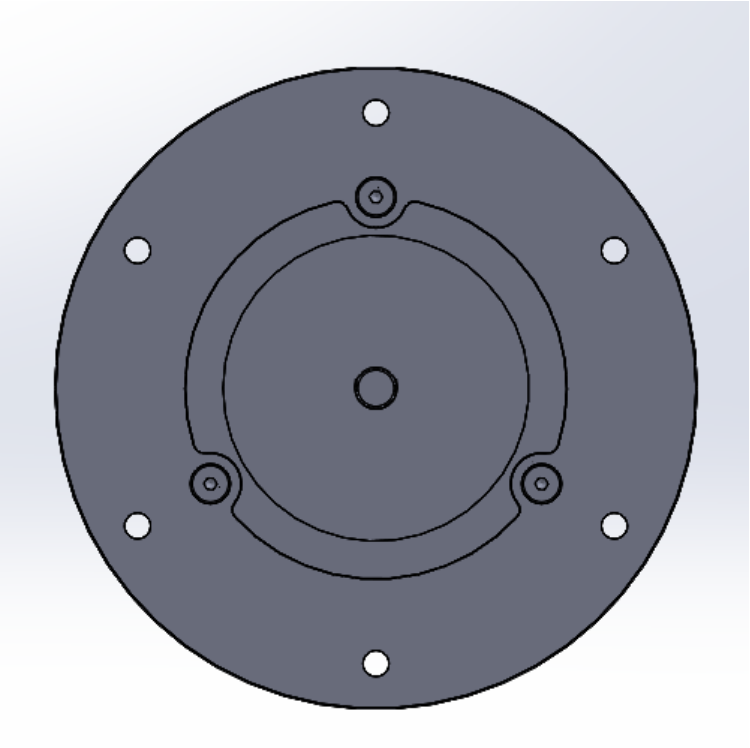

Fig.A.5. Front cup.

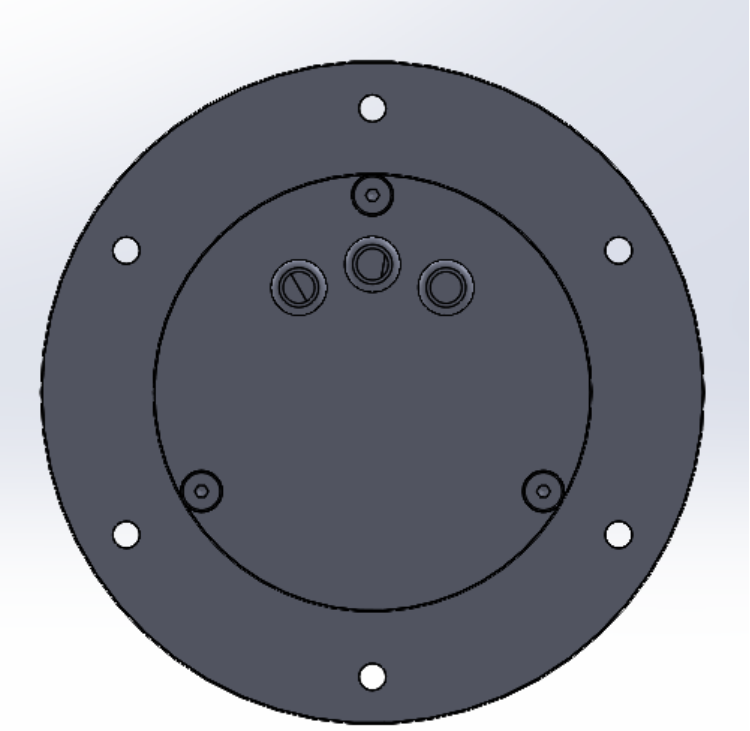

Fig.A.6. End plate.

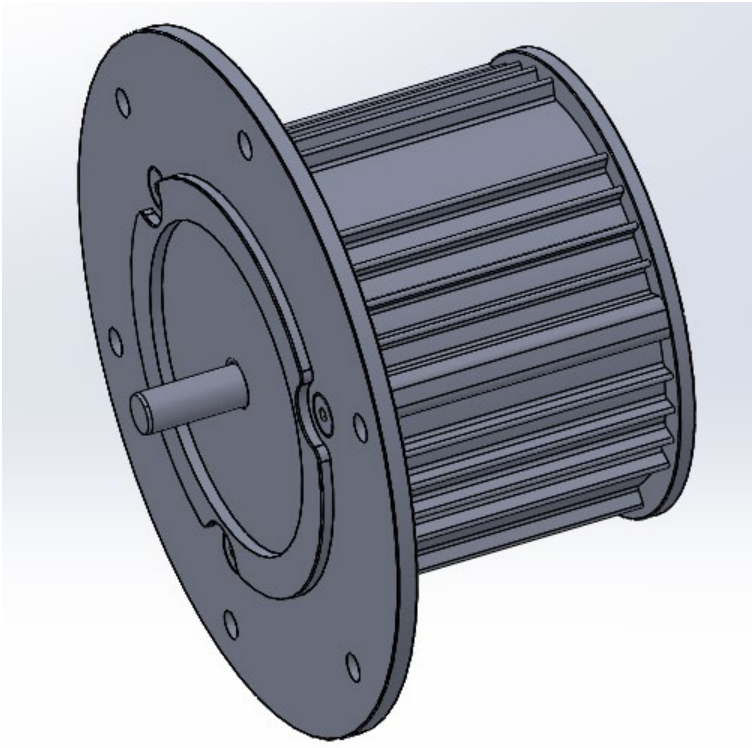

Fig.A.7. Assembled HSPMM.

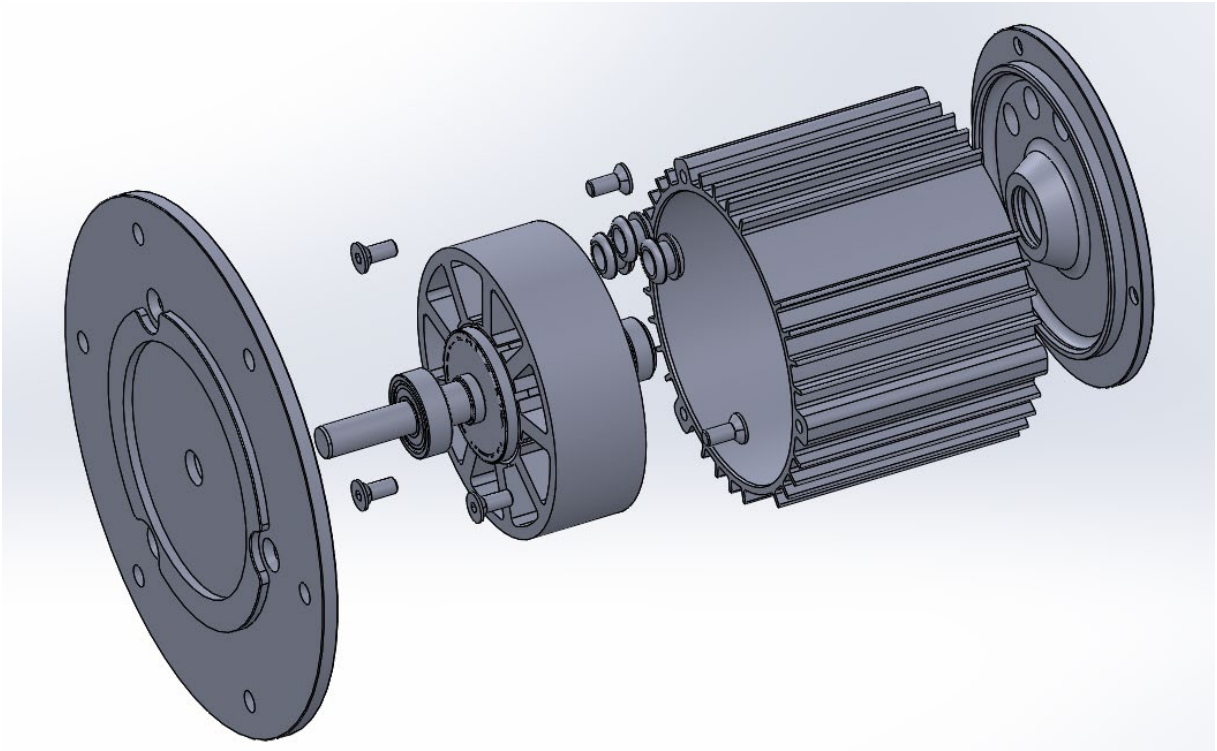

Fig.A.8. Explosive view of HSPMM.

Table A.1 Parameters of Prototype Machines

Stator slot number	6	9	12	9
Rotor pole number	4			6
Coil pitch	1	2	3	1
Stator bore diameter(mm)	34.08	35.1	38.6	43.3
Tooth body width(mm)	7.71	5.64	4.19	5.72
Stator yoke height(mm)	5.36	4.71	5.08	3.87
Slot opening(mm)	2.5	2.5	2.5	2.5
Stator outer diameter(mm)	90			
Stack length(mm)	30			
Air gap thickness(mm)	2			
Number of turns per phase	20			
Magnet thickness(mm)	6			
Magnet grade	N35H			
Silicon steel sheet	JFE G-core (0.2mm)			
Sleeve	Carbon fibre			

Appendix B: Publications

Journal papers published:

[J1] **Y. Wang**, J. H. Feng, S. Y. Guo, Y. F. Li, Z. C. Chen, Y. Wang, and Z. Q. Zhu, "Investigation of optimal split ratio for high-speed permanent-magnet brushless machines," *IEEE Trans. Magn*., vol. 54, no.11, Nov. 2018, Art no. 8105605.

[J2] J. H. Feng, **Y. Wang**, S. Y. Guo, Y. F. Li, Z. C. Chen, Y. Wang, and Z. Q. Zhu, **"**Split ratio optimization of high-speed permanent magnet brushless machines considering mechanical constraints," *IET Elect. Power Appl*., vol. 13, no. 1, pp. 81–90, Feb. 2019.

[J3] S. S. Xue, Z. Q. Zhu, **Y. Wang**, J. H. Feng, S. Y. Guo, Y .F. Li, Z. C. Chen, and J. Peng, "Thermal-loss coupling analysis of an electrical machine using the improved temperature-dependent iron loss model," *IEEE Trans. Magn*., vol. 54, no.11, Nov. 2018, Art no. 8105005.

Papers to be submitted

[J4] Y. Wang, Z.Q. Zhu, J.H. Feng, S.Y. Guo, Y. F. Li, and Y. Wang, "Rotor stress analysis of high-speed permanent magnet machines with segmented magnets retained by carbon-fibre sleeve," to be submitted to IEEE Transactions on Energy Conversion.

[J5] Y. Wang, Z.Q. Zhu, J.H. Feng, S.Y. Guo, Y. F. Li, and Y. Wang, **"**Investigation of unbalanced magnetic force in fractional-slot pm machines having odd number of stator slots," submitted to IEEE Transactions on Energy Conversion.

[J6] Y. Wang, Z.Q. Zhu, J.H. Feng, S.Y. Guo, Y. F. Li, and Y. Wang, **"**Analysis of rotor magnet loss of four-pole high-speed PM machines with alternate stator winding configuration," to be submitted to IEEE Transactions on Magnetics.